FY19

PROCEEDINGS OF THE U.S. ARMY
COMBAT CAPABILITIES DEVELOPMENT COMMAND
CHEMICAL BIOLOGICAL CENTER

IN-HOUSE LABORATORY INDEPENDENT RESEARCH AND SURFACE SCIENCE INITIATIVE PROGRAMS

U.S.ARMY

DEVCOM CHEMICAL BIOLOGICAL CENTER

Message from the Director of Research & Technology

It is my pleasure to present the eleventh annual edition of the Proceedings of the U.S. Army Combat Capabilities Development Command Chemical Biological Center (CCDC CBC) In-house Laboratory Independent Research (ILIR) and Surface Science Initiative (SSI) Programs.

In February 2019, the U.S. Army Research, Development, and Engineering Command (RDECOM) transitioned from the Army Materiel Command (AMC) to the Army Futures Command (AFC) and was renamed as the Combat Capabilities Development Command (CCDC). The three major elements of the AFC include Futures and Concepts, Combat Development, and Combat Systems. As part of the Combat Development element, CCDC focuses on fundamental scientific research, technology development, and engineering and analysis to support the Army's six modernization priorities. CCDC CBC activities span the life cycle of chemical and biological defense research and product development.

The CCDC CBC ILIR program funds innovative fundamental research projects that are high-risk with high potential for fulfilling future Army capability needs. Specifically designed to foster increased innovation, the ILIR program also aims to mentor junior investigators in the art and practice of initiating technological innovations and pursuing phenomenology at the boundaries of chemistry, biology, mathematics, or physics to gain insight and advances in support of CBRNE defense missions.

As always, this report includes a description of the ILIR program's rigorous project selection and evaluation process. A critical component of our program is the peer review of project proposals by external senior scientists from across the government. These reviews ensure that we not only fund projects with the greatest potential for fulfilling future Army capability needs, but that we receive an honest and unbiased assessment of our research efforts to hone the Basic Research program year after year.

Finally, the report concludes with a technical manuscript from each of the six ILIR, six SSI, and five internally funded Seedling projects from fiscal year 2019 (FY19). Together, these projects covered areas of interest across the chemical, biological, and physical sciences, including: *Rational Molecular Synthesis and Novel Materials*, *Synthetic Biology*, *Nano Chemical and Biological Sensing*, *Panomics and Molecular Toxicology*, *Aerosol Sciences*, *Algorithm Design and Development*, and *Surface Science*.

If you have questions about the ILIR Program or this report, please contact the CCDC CBC Public Affairs Office at usarmy.apg.ccdc-cbc.mbx.communications-office@mail.mil.

Sincerely,
Frederick J. Cox, Ph.D.
Director, Research and Technology Directorate
CCDC Chemical Biological Center

Strategic Mission and Vision

The U.S. Army Combat Capabilities Development Command Chemical Biological Center (CCDC CBC) is the Nation's principal research and development resource for non-medical chemical-biological (CB) defense. CCDC CBC's mission is to discover, develop, integrate, provide, and sustain technology solutions to enable the Joint Warfighter to assess, protect against, and mitigate chemical, biological, radiological, nuclear, and explosive (CBRNE) threats and hazards. CCDC CBC's vision is to be the premier provider of innovative CBRNE solutions for the Army, the Joint Warfighter, and our Nation. For more than 100 years, the Center has been a unique national asset, providing innovative and cost-effective CB defense technology solutions through our scientific and engineering expertise, coupled with our unique facilities and collaboration with partners.

CCDC CBC's mission and vision are supported by the Center's three Directorates: Research and Technology (R&T), Engineering, and Operations Applications. The R&T Directorate provides integrated science and technology (S&T) solutions that address CB defense knowledge gaps and vulnerabilities. Basic science research at CCDC CBC contributes valuable information to the fundamental science knowledgebase, enabling the development of technologies that directly benefit the Warfighter and further strengthen the Army's S&T mission. The Center's unique set of core research and technology capabilities position it to be the Army's fundamental source of research in chemistry and biology.

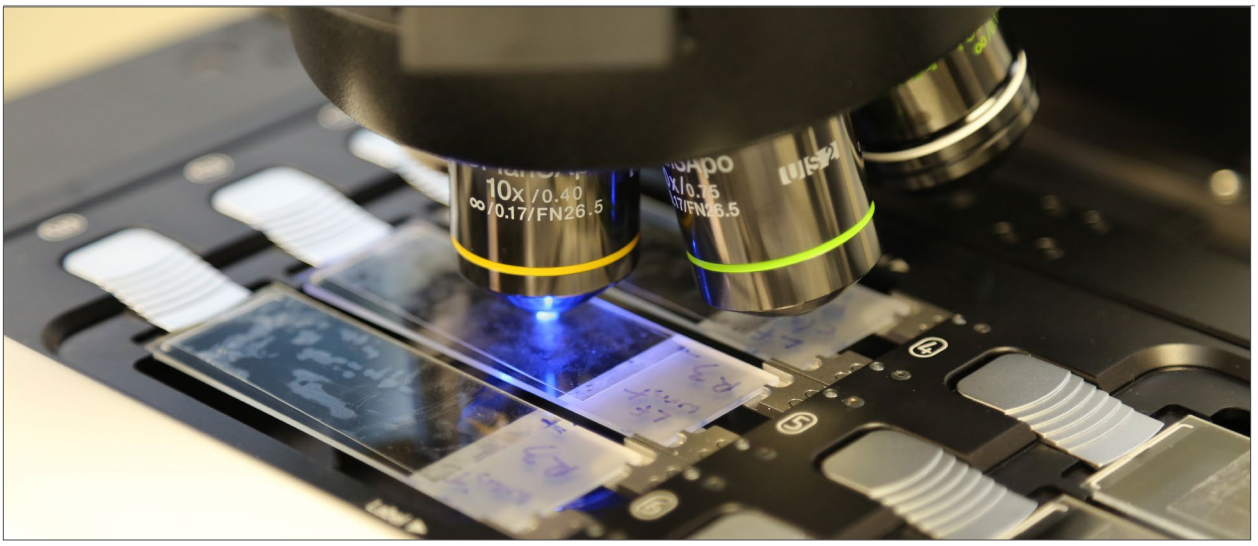

CCDC CBC Project: Researchers observe samples taken from protective suits under a fluorescing microscope after a simulated radioactive fallout test. (Photo credit: Jack Bunja, CCDC CBC)

CCDC CBC Collaboration Project: Deep Purple is a quad-rotor Unmanned Aircraft System developed by CCDC CBC that was integrated with chemical detection capability and tested during the Joint Warfighting Assessment 2019.(Photo credits: Jack Bunja, CCDC CBC)

CCDC CBC ILIR Project Selection and Evaluation Process

The purpose of the ILIR program is to fund innovative basic research projects that are high-risk but have high potential payoff for fulfilling future Army capability needs. The Department of Defense (DoD) defines basic research as "systematic study directed toward greater knowledge or understanding of the fundamental aspects of phenomena and of observable facts without specific applications toward processes or products in mind." The ILIR program is also specifically designed to foster increased innovation within CCDC CBC, where it is viewed as a critical part of the Center's efforts to ensure a high level of quality in basic science; to foster innovation in the areas of chemistry and biology; to mentor junior investigators in the art and practice of laboratory science; and to explore new technological innovations and phenomenology at the boundaries of chemistry, biology, mathematics, or physics to expand the state-of-the-possible in support of CBRNE defense missions.

The ILIR program solicits the Center's principal investigators for innovative proposals that correspond to topics highlighted in the CCDC CBC R&T Directorate's Strategic Roadmap. The FY19 ILIR topics were: *Rational Molecular Synthesis and Novel Materials*, *Synthetic Biology*, *Nano Chemical and Biological Sensing*, *Panomics and Molecular Toxicology*, *Aerosol Sciences*, *Algorithm Design and Development*, and *Surface Science*. The proposals are then reviewed and critiqued by a panel comprised of resident and external Department of the Army Senior Research Scientists (ST), Senior Scientists from other DoD organizations, and civilian and military faculty members at the United States Military Academy.

The review panel evaluates each proposal on its scientific objective, the scientific methods proposed, the qualifications of the investigator, and the budget; with the scientific objective and methods weighted as the most important criteria. The proposals are then ranked according to merit. Only proposals deemed by the panel as basic research are considered for funding.

Quality comments from the reviewers are compiled and used, along with the numerical score, as a critical assessment of the proposal. This written feedback is essential for the Center's mentoring of researchers and for justifying the elimination of research programs that are not competitive. Quarterly reviews of project performance provide guidance to the program's participants, ensuring that projects meet significant milestones and that substantive new knowledge is being produced and transferred to CCDC CBC and the broader scientific community. This cyclical review and assessment process were used to select and monitor the progress of six ILIR projects and six basic research projects under the SSI program. Internal funds were also used to support five "Seedling" projects, which are smaller scale projects of high-risk, high-reward basic research.

PROPOSAL SCORING CRITERIA

Exceptional (4): Comprehensive and complete in all areas; meets all significant objectives; offers a comprehensive project that exceeds the ILIR vision and is supportable by the proposed approach; has few weaknesses which are easily correctable.

Acceptable (3): Meets most of the significant objectives and is responsive to the ILIR vision; offers a feasible technical solution; weaknesses are readily correctable; proposal is complete to the extent that an award could be made in present terms.

Marginal (2): Minimally meets ILIR vision and objectives (i.e., offers a project vision that is marginally supported by the proposed approach, and/or claims are not documented or substantiated); significant deficiencies exist.

Unacceptable (1): Fails to meet significant characteristics of the ILIR vision and/or objectives stated in the Solicitation; has weaknesses and/or deficiencies that are significant and of such magnitude that they cannot be corrected without extensive discussion/major revision of the proposal.

	REVIEWERS							AVG
	1	2	3	4	5	6	7	
Scientific Objective	4.0	3.0	4.0	3.0	3.0	3.0	1.0	3.0
Methods and Approach	4.0	2.0	3.0	2.0	3.0	2.0	2.0	2.6
PI Qualifications	3.0	3.0	4.0	3.0	3.0	3.0	3.0	3.1
Budget	3.0	3.0	3.0	1.0	3.0	3.0	3.0	2.7
Overall Evaluation	**3.7**	**2.7**	**3.5**	**2.3**	**3.0**	**2.7**	**2.0**	**2.8**

[1] *DoD Financial Management Regulation, DoD 7000.14-R, Vol. 2B, Ch. 5*

While the U.S. Army mandated that independent annual reviews of all ILIR programs be conducted by a panel from the National Academies of Sciences, Engineering, and Medicine beginning in FY18, CCDC CBC continues to hold its annual external review in the fourth quarter to assess year-to-date performance of the funded ILIR and SSI projects. Comments and feedback from this review were used to support continued funding, or course corrections, of each ILIR/SSI project.

The annual CCDC CBC Technical Advisory Board (TAB) Review was held on Thursday, 26 September 2019. Five senior scientists from diverse federal defense and academic organizations (above) served on the TAB and reviewed the projects of the FY19 ILIR and SSI programs. The TAB panel also reviewed efforts from CCDC CBC's FY19 Seedling and Innovative Development of Employee Advanced Solutions (IDEAS) programs, providing their insights and direction on these smaller, short duration projects. The comments and insights from the TAB will be used to improve the quality and content of the individual research projects and to guide the overall mission of the programs into the future.

Members of the FY19 TAB review panel included:

- COL F. John Burpo, Ph.D., Academy Professor, United States Military Academy Department of Chemistry and Life Science
- Dr. Adam Rawlett, Senior Research Scientist (ST) for Materials Science, Combat Capabilities Development Command Army Research Laboratory
- Dr. Neil Jensen, Division Chief, CB Research Center of Excellence (CBR) Division, Defense Threat Reduction Agency
- Dr. Brian Cullum, Professor, Department of Chemistry and Biochemistry, University of Maryland Baltimore County
- Dr. Catherine Fenselau, Professor Emeritus Department of Chemistry and Biochemistry, University of Maryland, College Park

Upon conclusion of the review, the TAB convened to consolidate highlights of each project's strengths, recommend areas for improvement, and future considerations. The feedback was used to inform an out brief to the Director of CCDC CBC's Research and Technology (R&T) Directorate, provide feedback to the individual project principal investigators.

Overall, the TAB was pleased with the diversity and quality of projects across the portfolios, scoring both portfolios very well. Seven of the twelve projects received an acceptable quality score (3.00 or greater, on a scale of 1.00–4.00). The remaining five projects all scored above a 2.85—an improvement over the scores from previous TAB reviews.

The panel noted that the presented projects were being conducted at the basic research level, with most being clearly relevant to the CCDC CBC mission. The TAB was pleased that many of the ILIR and SSI projects were being led by early-to-mid career scientists. They commended the Center for its commitment to investing in its workforce—providing this valuable opportunity to gain experience in managing their own scientific projects is critical to developing future leaders. The panel also felt the most successful projects seamlessly integrated multiple scientific disciplines with appropriate modeling and experimental approaches that inform each other in a meaningful way. This was most evident in the SSI project, *"Characterization of opioid conformational changes and their effect on binding and reactivity on surfaces."*

The panel observed, however, that collaborations between principal investigators (PIs) or teams working on different projects in the same scientific domain were not readily apparent. For example, they noted there were several projects studying metal-organic frameworks (MOFs), but it was not evident how these projects were complementing each other, or how these projects were contributing to the large MOF "portfolio" at the Center. They reminded the Center that it is sufficient if work does not directly transition to a funded research project. All knowledge gained—so long as it is advancing the state-of-the-art in that field—is valuable. However, the Center should strive to capture this information so that unfruitful efforts are not repeated.

The panel found the twelve projects funded under the Seedling and IDEAS Programs were developing innovative approaches to challenging CB priorities. The panel felt the PIs of these projects were innovative, creative, articulate, and enthusiastic. The TAB panel noted the poster session was the best part of their day. Specific observations, comments, and recommendations on each reviewed project reviewed are provided in the TAB report.

This Proceedings Report contains the technical reports from all 17 CCDC CBC ILIR, SSI, and Seedling-funded projects.

FY19 Basic Research Program Highlights

FY19 BASIC RESEARCH PROGRAM PRODUCTIVITY

10 Presentations and posters

5 Peer-reviewed publications

3 Technical reports

3 Transitions

2 Patents filed

1 Award

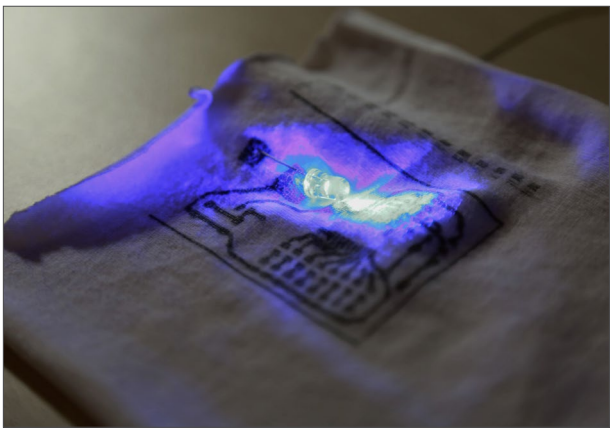

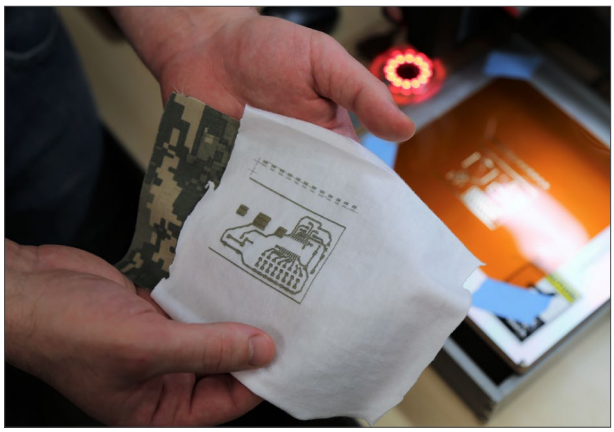

CCDC CBC Project: Conductive, flexible, silver ink circuitry printed on fabric will allow LEDs to be embedded within uniforms. The light initiates a chemical reaction that destroys chemical warfare agents, but is not visible to enemy forces. (Photo credits: Shawn Nesaw, CCDC CBC)

Center Researcher Acknowledged for Outstanding Presentation at International Conference

Dr. Erin Durke, Ph.D., a CCDC CBC ILIR PI presented her project, *Characterization of Particle Charge from Aerosol Generation Process: Impact on Infrared Signatures and Material Reactivity*, while attending her first International Conference on Aerosol Science and Technology in Prague, Czechia in September. Durke won an award for outstanding work out of approximately two dozen other presentations.

"We study it in a more non-traditional way than most aerosol researchers," Durke said. "We use transmission infrared spectroscopy, and we've been able to show differences in the spectra for powdered material versus aerosolized materials. We've also been able to use infrared spectroscopy to identify differences in the reactivity of the material as a function of aerosolization."

As Durke mentions, many researchers remove or neutralize the charge on aerosol particles before characterization, however, the charge is present in real-world samples and likely has an effect on the physical and chemical properties of an aerosolized material. On the battlefield, Warfighters may come into contact with aerosols in a number of ways.

Peer-reviewed Publications

- Garibay, S.J.; Iordanov, I.; Islamoglu, T.; DeCoste, J.B.; Farha, O.K. Synthesis and functionalization of phase-pure NU-901 for enhanced CO_2 adsorption: the influence of a zirconium salt and modulator on the topology and phase purity. *Cryst. Eng. Comm.* **2018**, *20* (44), pp 7066–7070.

- Hernandez, R.; Glaros, T.; Rizzo, G.; Ferreira, D.F. Purification and Proteomic Analysis of Alphavirus Particles from Sindbis Virus Grown in Mammalian and Insect Cells. *Bio-Protocol.* **2019**, *9* (10): e3239.

- Hudak, N.J.; Garrett, B.S.; DeLacy, B.G.; Mirotznik, M.S. Iterative design of multilayered dielectric microspheres with tunable transparency windows. *J. Opt. Soc. Am. A.* **2019**, *36* (5) pp 705–715.

- Peterson, G.W.; Au, K.; Tovar, T.M.; Epps, T.H., III. A Multivariate CuBTC Metal-Organic Framework with Enhanced Selectivity, Stability, Compatibility, and Processability. *Chem. Mater.* **2019**, *31* (20), pp 8459–8465.

- Peterson, G.W.; Browe, M.A.; Durke, E.M.; Epps, T.H., III. Flexible SIS/HKUST-1 Mixed Matrix Composites as Protective Barriers against Chemical Warfare Agent Simulants. *ACS Appl. Mater. Interfaces.* **2018**, *10* (49), pp 43080–43087

Technical Reports

- Jabbour, R.E.; Emmons, E.; Tripathi, A.; Kunkel, K. *Effect of Homoserine Lactones on the Physical Properties of Bacterial Nanocellulose Materials*; CCDC CBC-TR-1566; U.S. Army Combat Capabilities Development Command Chemical Biological Center: Aberdeen Proving Ground, MD, **2019**; UNCLASSIFIED Report.

- Jabbour, R.E.; Peterson, G.; DeCoste, J.; Jabaji, Y. *Matrix-Free Assisted Laser Desorption Ionization Using Metal-Organic Frameworks*; ECBC-TR-1550; U.S. Army Edgewood Chemical Biological Center: Aberdeen Proving Ground, MD, **2019**; UNCLASSIFIED Report.

- Myslinski, J.M.; Lux, M.W. *Impact of Crude Bacterial Cell Lysate on Performance of Commercial Cell-Free Expression*; ECBC-TR-1529; U.S. Army Edgewood Chemical Biological Center: Aberdeen Proving Ground, MD, **2018**; UNCLASSIFIED Report.

CCDC CBC Chemist Gregory Peterson spins engineered carbon with a polymer to make chemical warfare agent-resistant fabric. (Photo credit: Shawn Nesaw, CCDC CBC)

Presentations and Posters

- Angelini, D.; Horsmon, J.; Prugh, A.; Phillips, C. *Presented at the 58th Society of Toxicology Annual Meeting,* Baltimore, MD, **10–14 March 2019**.

- Calm, A.; Rizzo, G.; Glaros, T.; Gibbons, H.S. Epigenetic "Memory" During Bacterial Adaptation to Environmental Changes; Poster. *Presented at American Society for Mass Spectrometry Annual Conference,* Atlanta, Georgia, **2–6 June 2019**.

- Durke, E.M.; McEntee, M.L.; He, M.; Dhaniyala, S. Characterization of particle charge from aerosol generation process: Impact on infrared signatures and material reactivity. *Presented at the American Chemical Society National Meeting,* San Diego, CA, **25–29 August 2019**.

- Durke, E.M.; McEntee, M.L.; He, M.; Dhaniyala, S. Characterization of particle charge from aerosol generation process: Impact on infrared signatures and material reactivity. *Presented at the International Conference on Aerosol Science & Technology,* Prague, Czechia, **5–6 September 2019**.

- Kline, N.D.; Goetz, B.; Tripathi, A.; Ellis, C.; Serre, C.; Mendoza-Cortes, J. Probing the Connection Between Low-Frequency Vibrational Modes and Macroscopic Structural Behavior of Metal Organic Frameworks; *Presented at the ACS National Meeting and Exposition,* Orlando, Florida, **31 March–4 April 2019**.

- McEntee, M.; Winemiller, M.; Walz, A.; Fu-Lian, H.; Schenning, A.; Sheahy, M.; Iordanov, I.; Landers, J.; Peterson, G. Characterization of Opioid Conformers and Their Effect on Binding to Surfaces; *Presented at the ACS 47th Middle Atlantic Regional Meeting: Seeking Solutions Through Chemistry,* Baltimore, MD, **31 May 2019**.

- McEntee, M.; Winemiller, M.; Walz, A.; Fu-Lian, H.; Schenning, A.; Sheahy, M.; Iordanov, I.; Landers, J.; Peterson, G. Characterization of Carfentanil and Remifentanil in Solution and on Surfaces; *Presented at the ACS Fall 2019 National Meeting & Exposition,* San Diego, CA, **25– 29 August 2019**.

- Peterson, G.W.; Epps, T.H., III. MOFwich: Sandwiched Metal-Organic Framework-Containing Mixed Matrix Composite Polymers for Chemical Warfare Agent; *Presented at ACS National Meeting,* San Diego, California, **28 August 2019**.

- Peterson, G.W. MOFwich: Sandwiched Metal-Organic Framework-Containing Mixed Matrix Composite Polymers for Chemical Warfare Agent; *Presented at the Gordon Research Conference on Nanoporous Materials and Their Applications,* Andover, New Hampshire, **7 August 2019**.

- Peterson, G.W. MOFwich: Sandwiched Metal-Organic Framework-Containing Mixed Matrix Composite Polymers for Chemical Warfare Agent; *Presented at MOF2018,* Auckland, New Zealand, **12 December 2018**.

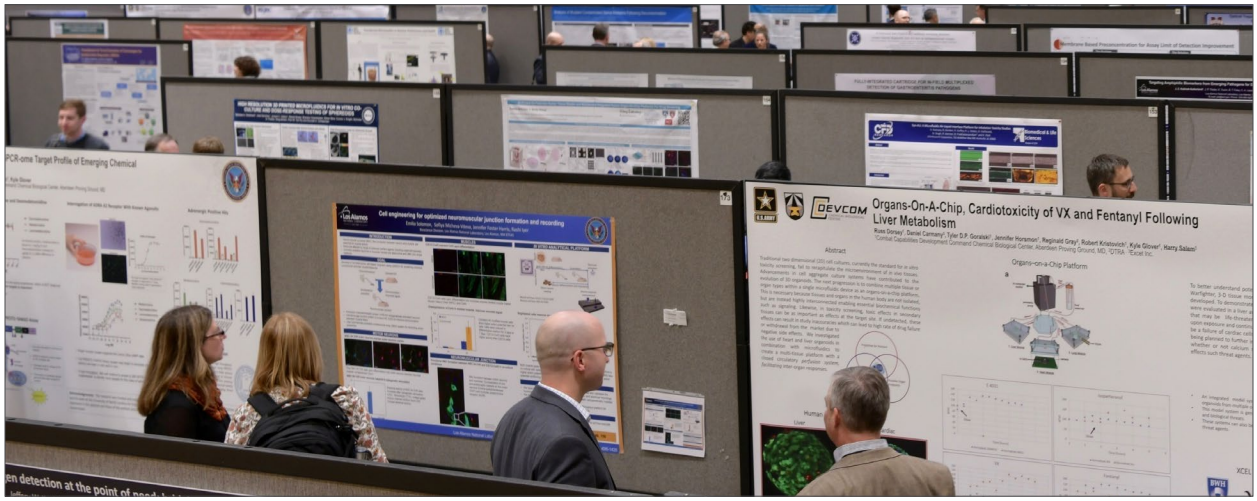

The Defense Threat Reduction Agency (DTRA) sponsored the 2019 Chemical and Biological Defense Science and Technology Conference—one of the largest gatherings of scientists, engineers, program managers, and leaders in the defense community—to discuss innovations that address the nation's chemical and biological threats. More than 350 posters were on display showcasing chemical and biological research from around the world. (Photo credit: Luis Palacios, DTRA)

Meet our FY19 Principal Investigators

Daniel J. Angelini, Ph.D.

Research Biologist, ***BioDefense Branch, CCDC CBC***

Dr. Angelini received his Ph.D. in Medical Pathology from the University of Maryland, Baltimore in 2004. He worked at Johns Hopkins University as both a post-doctoral fellow and a Research Associate from 2005–2011 and joined CCDC CBC in July 2011 as an NRC Senior Research Associate. He became a federal civilian employee in July 2015. Dr. Angelini has over 19 years of biological research experience. His current research focuses on several different areas including cell biology, the evaluation of biological sampling devices, and the development of prototype sampling devices.

Matthew A. Browe

Chemical Engineer, ***CBR Filtration Branch, CCDC CBC***

Mr. Browe received his bachelor's degree in Chemical Engineering from Pennsylvania State University in 2011 and is currently pursuing his master's degree in Chemical Engineering at the University of Delaware. Mr. Browe began working at CCDC CBC as a Chemical Engineer in 2011 focusing on permeation and micro-breakthrough testing and evaluation. His efforts include extensive analysis and data compilation of novel sorbents and MOF polymer hybrid films, identifying trends in performance with justification from theory, and materials characterization.

Jerry B. Cabalo, Ph.D.

Research Chemist, ***Sensors, Signatures, and Aerosol Technologies Branch, CCDC CBC***

Dr. Cabalo received his Ph.D. from the University of North Carolina, Chapel Hill in 1999. Dr. Cabalo has served as a chemist with the U.S. Army Research Laboratory and CCDC CBC since 2002. His primary duties include computational chemistry and basic research, energetic materials studies, and research and development of biological point detectors. Specifically, he has studied the near IR spectroscopy of energetic materials and has provided technical expertise on optics and UV solid state light sources. Additionally, he has been instrumental in testing prototypes with biological simulants using a variety of dispersal methods.

Shaun M. Debow

Research Chemical Engineer, ***Toxicology and Obscurants Branch, CCDC CBC***

Mr. Debow received his master's degree in Chemical & Biochemical Engineering from the University of Iowa in 2004. In 2006, Mr. Debow joined the CCDC CBC workforce as a Chemical Engineer managing lifecycle support for weapons systems. Mr. Debow's areas of expertise include basic and applied research of novel materials, development of novel solutions in anticipation of emerging needs, high-volume production and manufacturing, demilitarization, and systems engineering. Recent research interests include additive manufacturing, 2D materials, applications in surface science, warhead design, and gas adsorbents.

Erin M. Durke, Ph.D.

Research Chemist, *CBR Filtration Branch, CCDC CBC*

Dr. Durke received her doctorate in Analytical Chemistry from Virginia Tech in 2011. In 2011, she accepted a position at CCDC CBC where she studies the gas-surface interaction of chemical warfare environments. Dr. Durke led the design, development, and construction of two new systems created specifically to study agent aerosols and their interactions with atmospheric components and surfaces of interest.

Henry S. Gibbons, Ph.D.

Research Biologist, *Biotechnology Branch, CCDC CBC*

Dr. Gibbons received his Ph.D. in Biochemistry from Duke University in 2003 and conducted post-doctoral work at the University of North Carolina at Chapel Hill on protein export pathways in mycobacteria. Dr. Gibbons provided scientific and technical leadership for bacterial genetics and synthetic biology programs at CCDC CBC. His research group combines expertise in classical bacterial genetics with modern genomic and proteomic approaches to the characterization of fundamental biological phenomena in prokaryotes.

Ivan O. Iordanov, Ph.D.

Physicist, *Decontamination Sciences Branch, CCDC CBC*

Dr. Iordanov earned a Ph.D. in Physics from the Pennsylvania State University in 2012. Afterwards, he joined CCDC CBC as an NRC post-doctoral researcher in 2013 and was hired as a civilian employee in 2016. His area of expertise is the use of quantum mechanics based computational methods to improve understanding of adsorption within porous materials at the atomic level by creating models to visualize materials and their reactions.

Neal D. Kline, Ph.D.

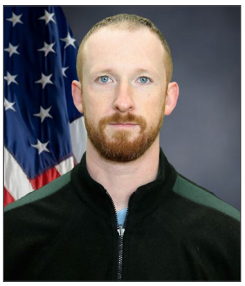

Research Chemist, *Spectroscopy Branch, CCDC CBC*

Dr. Kline received his Ph.D. in Physical Chemistry from Ohio State University in 2014. He began working at CCDC CBC in July 2014 as an ORISE post-doctoral research fellow and was hired as a government civilian at CCDC CBC in 2016. Since arriving at CCDC CBC, Dr. Kline has been working to develop a portable drug detection device capable of detecting illicit drugs in bodily fluids by combining surface-enhanced Raman spectroscopy (SERS) with a microfluidic platform. As a result of this SSI project, Dr. Kline has become very familiar with the principles underpinning normal Raman spectroscopy and SERS.

Ann M. Kulisiewicz

Research Chemist, *CBR Filtration Branch, CCDC CBC*

Ms. Kulisiewicz received her master's degree in Chemistry from the University of Delaware in 2015. Ms. Kulisiewicz began supporting the CCDC CBC in 2015 as a contractor and later transitioned to a civilian employee in 2018. Her work primarily focuses on MOFs for filtration applications and photocatalysis experiments.

Monica L. McEntee, Ph.D.

Research Chemist, *CBR Filtration Branch, CCDC CBC*

Dr. McEntee received her bachelor's degree in Chemistry and Mathematics with a minor in Biology in 2010 from Virginia Tech. She received her Ph.D. in Physical Chemistry in 2015 from the University of Virginia. In 2015, she was awarded an ORISE post doctoral fellowship in the Chemical, Biological, and Radiological (CBR) Filtration Branch at CCDC CBC studying the fundamental properties of environmental surfaces (sands and soils), as well as their interactions with chemical agent simulant vapors and aerosols and was subsequently hired as a civilian employee in 2017.

Gregory W. Peterson

Research Chemical Engineer, *CBR Filtration Branch, CCDC CBC*

Mr. Peterson received his bachelor's degree in Chemical Engineering from Bucknell University in 2003. He is currently pursuing his doctoral degree from the University of Delaware. Mr. Peterson joined CCDC CBC in 2003, and is responsible for the design, maturation, and integration of novel sorbent technologies into military respiratory systems. Mr. Peterson has authored and co authored 43 presentations at a variety of conferences, authored over 91 technical reports, 52 open literature publications, and holds or has submitted 21 patent applications.

Patrick C. Riley

Research Chemist, *Detection Spectrometry Branch, CCDC CBC*

Mr. Riley received his bachelor's degree in Chemistry from Salisbury University in 2010. He began working at CCDC CBC in November 2010 as a contractor before being hired on as a Research Chemist at CCDC CBC in January 2015. Mr. Riley has been evaluating the Joint Chemical Agent Detector Chemical Explosives Detector (JCAD-CED) and other relevant chemical detection technology and has served as the lead experimentalist for contact angle experimentation while performing data analysis and modeling of experimental results using MATLAB and COMSOL Multiphysics.

Bryan A. Rivers

Biologist, *BioChemistry Branch, CCDC CBC*

Mr. Rivers received his master's degree in Biology from the University of North Carolina, Charlotte in 1999. With more than 15 years of experience in government, industry, and academic laboratories, Mr. Rivers has applied his expertise in immunological molecular assay development and optimization at the CCDC CBC as a contractor since 2010 and as a civilian employee since 2016. Mr. Rivers has experience managing laboratory testing of bioidentification hardware evaluations, early assay development and evaluation of hand-held molecular devices, PCR assay design for biothreat agents, biological sample collection, and biosensor hardware evaluation, including live agent testing.

John A. Tokarz, III

Chemist, *CBR Filtration Branch, CCDC CBC*

Mr. Tokarz received his master's degree in Environmental Planning and Management from Johns Hopkins University in 2014. Mr. Tokarz has served as a chemist in the CBR Filtration Branch at CCDC CBC since July 2015. His work has largely focused on the testing, characterization, and performance evaluation of various types of cartridge filters and loose sorbent media against toxic industrial chemicals and toxic industrial materials, as well as ongoing efforts centered on method development and obtaining quality test results. His instrumentation expertise is in the area of mass spectroscopy, gas and liquid chromatography, and IR spectroscopy.

Ashish Tripathi, Ph.D.

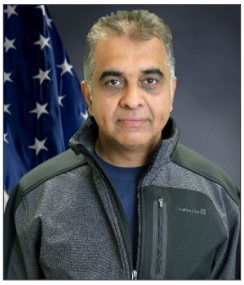

Research Physical Scientist, *Spectroscopy Branch, CCDC CBC*

Dr. Ashish Tripathi received a doctoral degree in Chemical and Fuels Engineering from the University of Utah in 1997. He has been a researcher at CCDC CBC since 1997, first as a contractor and transitioning to a civilian position in 2016. Dr. Tripathi has more than 20 years of experience in standoff and point threat detection research with 15 years supporting the Spectroscopy Branch of CCDC CBC. His expertise focuses on the application of Raman spectroscopy and imaging and surface-enhanced Raman spectroscopy to the detection of chemical, biological, and energetic materials.

Mark J. Varady, Ph.D.

Research Engineer, *Decontamination Sciences Branch, CCDC CBC*

Dr. Varady received a Ph.D. in mechanical engineering from the Georgia Institute of Technology in 2010 and has been working with CCDC CBC since 2012 as a contractor before transitioning to a civilian position in 2016. Dr. Varady primarily studies chemical transport mechanisms in polymer based materials, including multicomponent diffusion, viscoelastic response upon chemical exposure, and details of the polymer-particle interface in composite systems.

Table of Contents

In-house Laboratory Independent Research (ILIR) Projects

Surface Science Initiative (SSI) Projects

Seedling Projects

ILIR PROJECTS

Hierarchical systems through selective deposition and growth of metal-organic frameworks on block copolymers

Gregory W. Peterson
U.S. Army Combat Capabilities Development Command Chemical Biological Center, Research & Technology Directorate, 8198 Blackhawk Rd, Aberdeen Proving Ground, MD 21010

ABSTRACT

The use of polymers to template arrays of metal-organic frameworks has been an under-researched area. Previously, we explored the use of block copolymers to selectively deposit metal-organic framework constituents followed by *in situ* growth. We continued the modification of archetypal metal-organic framework HKUST-1 for enhanced compatibility with block copolymers. We investigated the incorporation of metal-organic polyhedral into block copolymers. Finally, we studied the growth of ZIF-8 into poly(styrene)-poly(ethylene oxide) electrospun fibers using zinc seeding. It was found that we were able to enhance compatibility using modification techniques, selectively deposit metal-organic polyhedral with poly(ethylene oxide) domains, and selectively grow ZIF-8 in poly(ethylene oxide) domains of poly(styrene)-poly(ethylene oxide) fibers.

Keywords: metal-organic framework, block copolymer, electrospinning, mixed-matrix membrane, acyl chloride, ZIF-8

1. INTRODUCTION

Metal-organic frameworks (MOF) are a relatively new class of highly porous materials that offer unprecedented control of porosity and chemistry.[1–3] By combining metal secondary building units with functionalized organic linkers, a wide variety of structures can be synthesized offering a wide range of properties. Over the past decade, the number of MOFs synthesized has grown, with well over 100,000 structures identified *in silico*.[4] Due to the ability to tune properties of MOFs, a wide range of potential applications have been identified, including gas storage,[5] catalysis,[6] toxic gas removal,[7] and sensing,[8] among others. However, although the chemistry of synthesis has been explored, tangible constructs other than crystalline powders have remained mostly unexplored.

Beyond simple growth of MOF crystallites, there have been some, albeit limited, investigations of hierarchical assembly of MOFs into thin films. MOFs are grown by connecting metal oxide secondary building units with organic linkers—by utilizing similar functional groups, such as oxygen centers, catechols, or carboxylic acids on polymer surfaces, nucleation and growth can occur. Layer-by-layer techniques using self-assembled monolayers have been investigated to create thin films, where MOFs are grown onto substrates, such as gold.[9] While thin films of MOFs are valuable in applications that require incorporating MOFs into devices, composite materials with MOFs on polymer substrates is far more advantageous for processability, flexibility, and reusability of the composite membrane. The two general approaches are the solution blending method (top-down approach), and *in situ* growth of MOFs in polymers (bottom-up approach). Various groups have employed the top-down approach of mixing different polymers with different MOFs. Specifically, the Cohen Group at the University of California has recently investigated mixing of polyvinylidene fluoride (PVDF) to integrate MOFs into films.[10] The same group has also used polymerization techniques to create pure MOF films, called polyMOFs.[11] Although these techniques show promise, they do not offer the ability to deposit or grow MOFs into hierarchical or systematic patterns.

Of primary importance for incorporating either starting constituents or preformed MOFs into block copolymers (BCP) is the interaction of these chemicals with the polymers. One way of estimating these interactions, and therefore choosing the right constituents and polymer systems, is the use of Hansen Solubility Parameters, which can be used to determine solubility of polymers, solvents, and small molecules within mixtures.[12] The underlying equation is

$$\delta_t^2 = \delta_d^2 + \delta_p^2 + \delta_h^2 , \quad (1)$$

where δ_d = London dispersion parameter, δ_p = polar interaction parameter, and δ_h = hydrogen bonding parameter.

Table 1. Hansen solubility radii of select functionalities and polymers.

Functionality	Interaction Radius ($MPa^{0.5}$)				
	PS	PI	PEO	PMMA	PVDF
Aniline (linker)	8.3	13.1	7.5	6.2	9.9
Decane	14.7	1.2	14.1	14.0	3.9
Benzene	5.5	10.9	8.2	5.9	8.5
Perfluoroheptane	21.8	8.3	17.1	18.5	9.2

When considering the interaction of two bodies, such as those described in Table 1, the interaction radius is calculated according to

$$R^2 = 4 * (\delta_{d1} - \delta_{d2})^2 + \left(\delta_{p1} - \delta_{p2}\right)^2 + (\delta_{h1} - \delta_{h2})^2 \, . \tag{2}$$

Using acyl chloride chemistry, we can modify the amine group to incorporate a variety of chemical functionalities to enhance compatibility with specific polymer systems.

Furthermore, taking advantage of interactions between metals and polymers, we can selectively seed poly(ethylene oxide) (PEO) with Zn through a chelation interaction and subsequently mix PEO with poly(styrene) (PS) and form various films and fibers for selective growth of ZIF-8 in the PEO phase. This concept is shown in Figure 1.

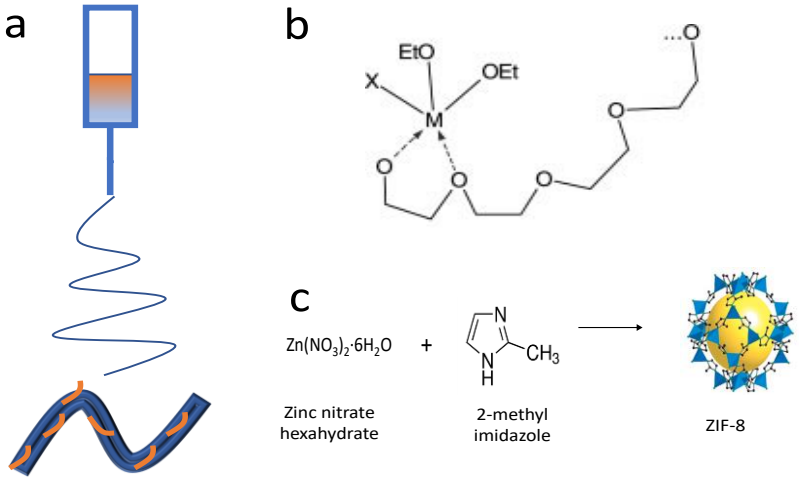

Figure 1. (a) Blend electrospinning concept. (b) Ability of metals to chelate to oxygen groups in PEG/PEO. (c) ZIF-8 precursors and crystal structure

2. METHODOLOGY

2.1 Metal-organic frameworks

2.1.1 Procurement and synthesis

Two MOFs were investigated in FY19: HKUST-1 (aka CuBTC), and variants thereof, as well as ZIF-8. For CuBTC, 250 mg (1.0 mmol) of $Cu(NO_3)_2 \cdot 3H_2O$ was added to an equal volume mixture of water/ethanol/dimethylformamide (DMF) (3 mL) in a 20 mL scintillation vial and stirred magnetically at 300 rpm. Separately, 140 mg (0.66 mmol) of 1,3,5-benzenetricarboxylic (BTC) was added to an equal volume mixture of water/ethanol/DMF (3 mL) in a 20 mL scintillation vial and stirred magnetically at 300 rpm. When all components were dissolved, the solutions were combined for 24 or 72 hours to study the effect of time on crystal formation. Crystallization was conducted at either 25, 50, or 85 °C. After synthesis, the solutions were decanted and washed with DMF two times, and then decanted and washed with ethanol two times. The crystals were vacuum-filtered and activated under vacuum (~1×10^{-2} bar) at 120 °C prior to characterization and testing. CuBTC 5-aminoisophthalic acid (AIA) composites were synthesized

using the same method with slight modifications. Combinations of BTC and AIA were dissolved at 50 °C, instead of 25 °C, due to the lower solubility of AIA in the water/ethanol/DMF solution. AIA was added at ~20 mol%, ~40 mol%, or ~60 mol% (with respect to total linker content).

ZIF-8 was grown on PS/poly (ethylene-glycol) (PEG) electrospun nanofibers with and without zinc pre-seeded in the PEG. In one example, 0.07 g (0.38 mmol) zinc acetate was dissolved in 5 mL of DMF and 2.5 mL of dichloromethane. Both 0.1 g PEG (M_n ~35,000 g/mol) and 1.0 g PS were dissolved in the solution which was subsequently electrospun (see procedure below). After electrospinning, the fibers were submerged in ~2 mL of a solution of 2-methyl imidazole (0.575 g) in 18 mL H_2O and 2 mL ethanol. After 1 hour, ~2 mL of a solution of zinc acetate (0.35 g) in 18 mL H_2O and 2 mL ethanol was added. The mixture was then allowed to sit for 24 hours, after which the fibers were taken out, washed with water, and dried.

2.1.2 Post-synthetic modification

CuBTC, CuBTC_20 AIA, and CuBTC_40 AIA were added into dichloromethane (5 mL, Sigma-Aldrich®) in a 20-mL scintillation vial. The MOFs were soaked for ~30 minutes and then sonicated for 30 seconds using a Fisher Scientific™ CL-18 probe sonicator at 70 % amplitude. Immediately after sonication, acyl chloride was added drop-wise to the solutions.

2.2 Polymer

CuBTC, CuBTC_40 AIA, and CuBTC_40 AIA_D (~40 mg) were mixed with DMF (4 mL) in a 20 mL scintillation vial and sonicated for 30 seconds. Polyacrylonitrile (PAN), (400 mg, Sigma-Aldrich®, M_n = 150,000 $g \cdot mol^{-1}$), was added to the vial, and the mixture was stirred magnetically at 50 °C until the PAN was dissolved. The resulting mixtures were electrospun using an MTI Corporation MSK-NFES-4 floor unit at a flow rate of 2 $mL \cdot h^{-1}$ through a 20-gauge needle and 15 kV electric field at 40 °C onto a mandrel rotating at 300 rpm.

CuBTC, CuBTC_40 AIA, and CuBTC_40 AIA_D (~20 mg) were mixed with tetrahydrofuran (3 mL) in a 20 mL scintillation vial and sonicated for 30 seconds. SIS (Poly(styrene-*block*-isoprene-*block*-styrene)) (300 mg, Sigma-Aldrich®), was added to the vial, and the mixture was stirred magnetically until the SIS was dissolved. Films were cast using a 10 mm blade.

CuBTC, CuBTC_20 AIA, and CuBTC_20 AIA_D (~200 mg) were mixed with 5 mL of tetrahydrofuran in a 20 mL scintillation vial and sonicated for 30 seconds. SEBS (Poly(styrene-*block*-ethylene-*ran*-butylene-*block*-styrene)) (1 g, Kraton™ G1642), was added to the vial, and the mixture was stirred magnetically until the SEBS was dissolved. Films were cast using a 10 mm blade.

2.3 Electrospinning

Electrospinning was conducted using a programmable floor-stand electrospinning unit (MSK-NFES-4 by MTI Corporation). Solutions were loaded into 6-mL plastic syringes equipped with a 20-gauge needle. The solutions were pumped at a flow rate of 2 mL/hour onto a rotating mandrel operating at 300 rpm. The electric field was set between 15–18 kV according to perceived solution viscosity.

2.4 Materials characterization

A variety of techniques was used to characterize electrospun nanofibers and films developed. This section summarizes each technique used.

2.4.1 Nitrogen isotherm

Nitrogen uptake was measured at 77 kelvin (K) using a Micromeritics® ASAP™ 2040. Samples were off-gassed at 60 °C overnight under vacuum. Surface area measurements were calculated using the Brunauer-Emmett-Teller method, and total pore volumes were calculated at a relative pressure of 0.975 atm.

2.4.2 Powder X-ray diffraction

Powder X-ray diffraction (PXRD) measurements were conducted using a Rigaku Miniflex 600 X-ray powder diffractometer with a D/Tex detector. Samples were scanned at 40 kV and 15 mA using Cu Kα radiation, a scan rate

of 5° min^{-1}, over a 2θ range of 3° to 50°. Data were plotted relative to the highest intensity peak and offset on the *y*-axis to show differences between each sample.

2.4.3 Scanning electron microscopy

Scanning electron microscopy (SEM) images were obtained using a Phenom GSR desktop SEM. Samples were supported on double-sided carbon tape and sputter-coated with gold prior to analysis. Typical settings for the instrument used an accelerating voltage of 5 kV at a nominal working distance of 10 mm. Specific operating conditions are listed with each image in Figure 6 for clarity.

2.4.4 Attenuated total reflectance-Fourier transform infrared spectroscopy

Attenuated total reflectance-Fourier transform infrared spectroscopy spectra of materials were collected with a Bruker Tensor 27 Fourier transform infrared spectrometer equipped with a Platinum ATR accessory and a single reflection diamond crystal. Sixteen scans over a range of 4,000–400 cm^{-1} were averaged with a resolution of 2 cm^{-1}.

2.4.5 Tensile testing

Tensile testing was conducted on the on the SEBS-based mixed matrix composites in accordance with ASTM D41216 using a Test Resources 220 Series instrument equipped with a 5,000 N load cell. Composites of ~2 cm height (between load clips), ~2 cm width, and ~150 µm thickness (measured with a Mitutoyo IP 65 micrometer) were strained at a rate of 50 cm/min. The modulus of elasticity, maximum load, and percent elongation were calculated in accordance with ASTM D412-16. At least three replicates were tested for each composite.

3. RESULTS AND DISCUSSION

3.1 Synthesis of isostructural CuBTC with reactive amine handle for post-synthetic modification

CuBTC has shown promise in a variety of applications, including ammonia filtration and distilled mustard (HD) uptake and reactivity. However, this material is not stable to moisture and thus potential applications are limited. In this year, we showed enhanced stability to moisture through incorporation of AIA as well as enhanced polymer compatibility through modification of the amine group with decanoyl chloride as shown in Figure 2.

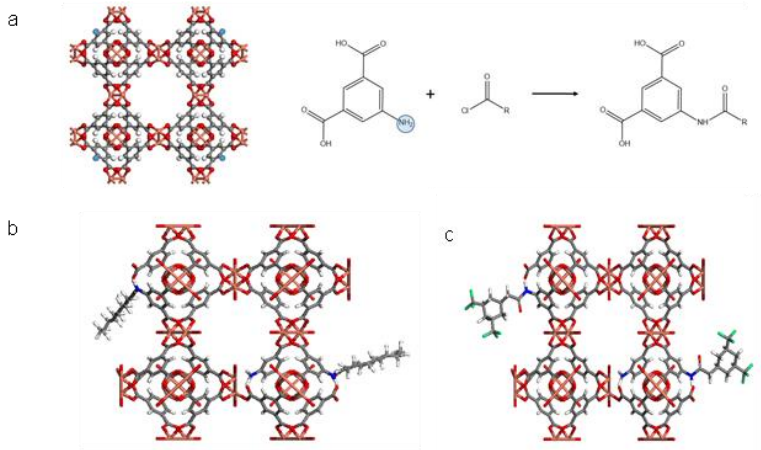

Figure 2. (a) Concept of CuBTC_AIA modification using acyl chlorides to form an amide. Proposed resulting structures after modification with (b) decanoyl chloride (CuBTC AIA_D) and (c) 3,5-bis(trifluoromethyl)benzoyl chloride (CuBTC AIA _B).

For over a month, CuBTC, CuBTC_20 AIA, and CuBTC_20 AIA_D were dispersed in liquid water. During this time, the CuBTC_20 AIA_D continued to float, and both CuBTC_20 AIA and CuBTC_20 AIA_D had no loss in crystallinity or nitrogen adsorption capacity after at least one day, as shown in Figure 3.

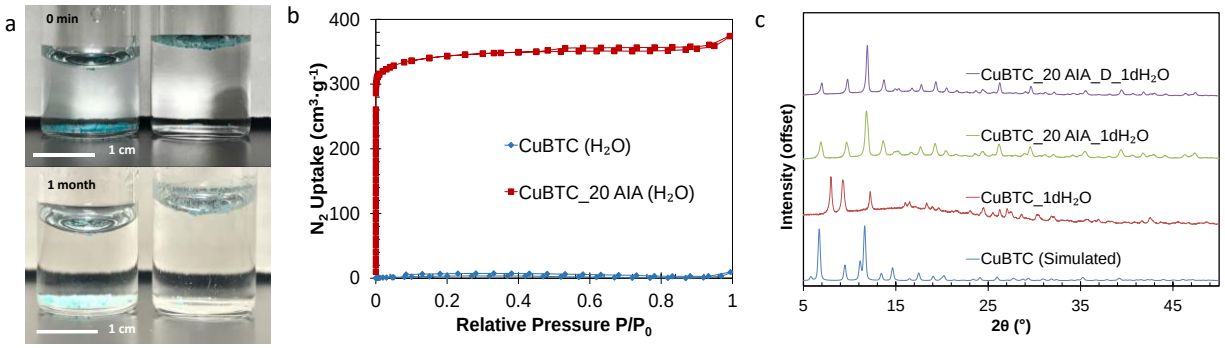

Figure 3. (a) CuBTC (left) and CuBTC_20 AIA_D (right) after 1 month in liquid water. (b) Nitrogen isotherm data for CuBTC and CuBTC_20 AIA after exposure to liquid water. (c) PXRD patterns of CuBTC, CuBTC_20 AIA, and CuBTC_20 AIA_D after exposure to liquid water.

Poly(acrylonitrile) (PAN) electrospun nanofibers and SIS and SEBS films were cast with CuBTC, CuBTC_40 AIA, and CuBTC_40 AIA_D MOFs, as shown in Figure 4. For all CuBTC composites (panels a, d, and h) large defects were present at the MOF-polymer interface. The CuBTC_40 AIA crystals had good compatibility with PAN nanofibers, but still had large defects with the SIS and SEBS polymers (panels b, e, and i). Incorporating decanoyl chloride resulted in better compatibility between the MOF crystal and polymer for both fibers and films (panels c, f, and j).

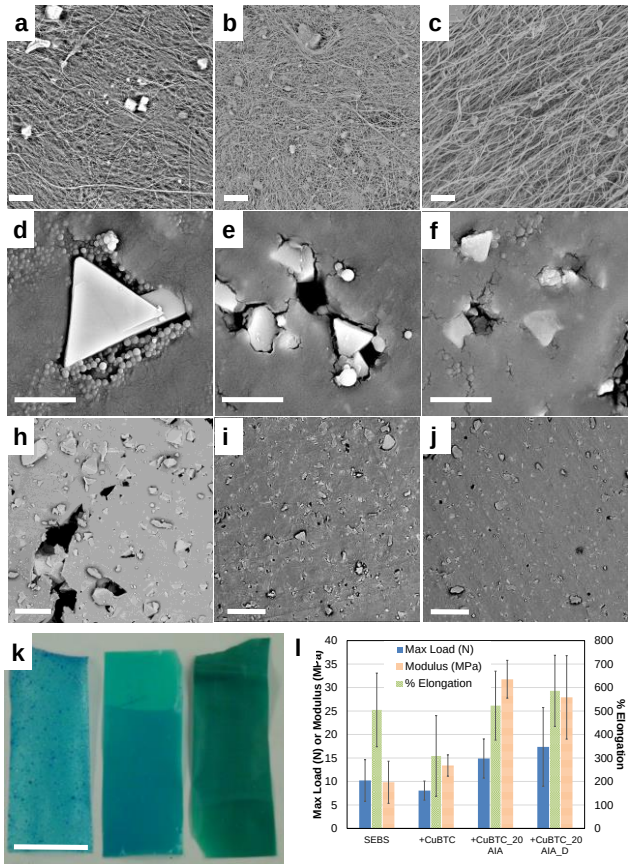

Figure 4. Electrospun PAN nanofibers containing (a) CuBTC, (b) CuBTC_40 AIA, and (c) CuBTC_40 AIA_D. Scale bars = 30 µm. 250 µm-thick SIS films containing (d) CuBTC, (e) CuBTC_40 AIA, and (f) CuBTC_40 AIA_D. Scale bars = 8 µm. 250 µm-thick SEBS films containing (h) CuBTC, (i) CuBTC_20 AIA, and (j) CuBTC_20 AIA_D. Scale bars = 100 µm. (k) Optical images of SEBS containing CuBTC (left), CuBTC_20 AIA (middle), and CuBTC_20 AIA_D (right). Scale bar = 2 cm. (l) Maximum load, elastic modulus, and percent elongation from tensile tests of SEBS-based materials.

3.2 ZIF-8 growth on PS/PEO fibers

The ability to grow MOFs selectively inside or outside of fibers has implications for potential end item applications. For example, in some cases, MOFs inside the fiber may be protected by the polymer shell such that it is shielded from degradation or contamination. On the other hand, particles located on the outside of the fiber may be more accessible and, therefore, more active toward degrading chemical warfare agents, for example.

We began investigating this selective deposition by incorporating low molecular weight PEO into PS fibers. We used a blending strategy such that varying amounts of PEG were mixed with PS in solvent. Zinc was also added with the idea that Zn will selectively chelate to PEG/PEO and therefore allow for selective growth of the ZIF. We investigated several formulations as outlined in Figure 5. In all cases except PS/PEG+Zn_40P_6:1, we were able to electrospin blended fibers. After electrospinning, we submerged the materials in an ethanol solution containing 2-methyl imidazole for 1 hour followed by the introduction of ethanol/zinc nitrate. After 24 hours, the fibers were removed from the solution, washed, and dried. In all cases, ZIF-8 was successfully grown on/in the fibers.

Sample	% PEO/PEG[1]	EO:Zn
PS/PEG+Zn_10P_6:1	10	6:1
PS/PEG+Zn_25P_6:1	25	6:1
PS/PEG+Zn_40P_6:1	40	6:1
PS/PEG+Zn_10P_12:1	10	12:1
PS/PEG+Zn_10P_24:1	10	24:1
PS/PEO+Zn_10P_6:1	10	6:1
PS+Zn	0	n/a

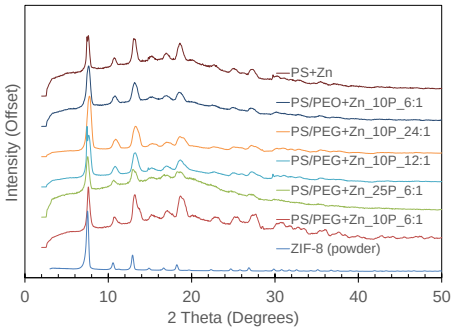

Figure 5. Table of composites electrospun and subsequently used to grow ZIF-8 (left). PXRD patterns for ZIF-8 composite fibers (right).

SEM images for the various samples are shown in Figure 6. Preliminary results indicate that the ZIF-8 crystal size can be controlled by the amount of PEG in the formulation (panels a and b). Furthermore, incorporating PEG into the fiber allows for etching within the fiber and subsequent growth of ZIF-8 within the fiber (panels c and d). When only PS is used, the fibers are not hollow and ZIF-8 grows exclusively on the outside of the fiber (panels e and f). The importance of Zn seeding within the fibers is shown in panels g and h. After sonication, those fibers seeded with Zn retain ZIF-8 crystals on the surface whereas, plain PS fibers do not retain crystals. These results are important design parameters for future work. In some cases, one may want robust ZIF-polymer materials whereas in other cases, it may be advantageous for the ZIF to fall off of the fiber.

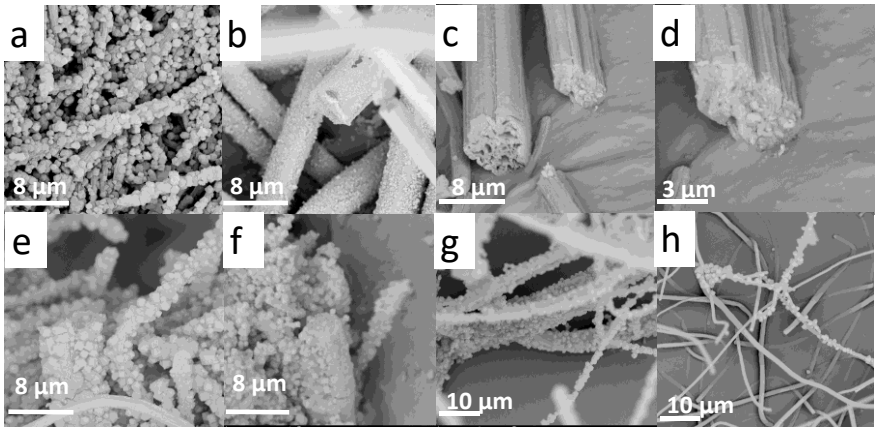

Figure 6. PS/PEG fibers electrospun with 6:1 EO:Zn and (a) 10 wt% and (b) 25 wt% PEG. PS/PEG fibers electrospun with 10 wt% PEG showing (c) etching due to water wash of PEG from fiber and (d) ZIF-8 growth in etched fibers. (e) PS fibers seeded with Zn and (f) PS fibers with no Zn seeding. (g) PS fibers seeded with Zn and (h) PS fibers with no Zn seeding after sonication.

4. CONCLUSIONS

A novel MOF containing AIA was synthesized such that post-synthetic modification could be conducted using the amine group. Acyl chlorides were used to convert the amine to amides to add functional groups to the MOF so that enhanced MOF-polymer compatibility could be achieved. The resulting materials were more stable to moisture and toxic gases and had better mechanical properties than composites formed from traditional CuBTC.

PS/PEG composite fibers were electrospun with zinc seeds to selectively grow ZIF-8 within or on the outside of the fiber. Crystal size varied based on PEG content, and zinc seeding led to more robust MOF attachment on the fiber as compared to MOFs grown on fibers without zinc seeding.

ACKNOWLEDGMENTS

Funding was provided by the U.S. Army via the In-house Laboratory Independent Research Program (PE0601101A Project 91A) at the Combat Capabilities Development Command Chemical Biological Center. The author thanks Dr. Hui Wang (CBR Filtration Branch), Dr. John Mahle (CBR Filtration Branch), Dr. Trent Tovar (NRC postdoctoral researcher, CBR Filtration Branch), Amedeo Napolitano (CBR Filtration Branch), Matthew Browe (CBR Filtration Branch), and Kathleen Au (CQL Summer Intern Student, University of Maryland, Baltimore County) for experimental support. The author thanks Prof. Thomas H. Epps, III from the University of Delaware for providing research guidance.

REFERENCES

[1] Eddaoudi, M.; Kim, J.; Rosi, N.; Vodak, D.; Wachter, J.; O'Keeffe, M.; Yaghi, O.M. Systematic Design of Pore Size and Functionality in Isoreticular MOFs and Their Application in Methane Storage. *Science.* **2002,** *295* (5554), pp 469–472.

[2] Eddaoudi, M.; Li, H.L.; Yaghi, O.M. Highly Porous and Stable Metal-Organic Frameworks: Structure Design and Sorption Properties. *J. Am. Chem. Soc.* **2000,** *122* (7), pp 1391–1397.

[3] Cavka, J.H.; Jakobsen, S.; Olsbye, U.; Guillou, N.; Lamberti, C.; Bordiga, S.; Lillerud, K.P. A New Zirconium Inorganic Building Brick Forming Metal Organic Frameworks with Exceptional Stability. *J. Am. Chem. Soc.* **2008,** *130* (42), pp 13850–13851.

[4] Wilmer, C.E.; Leaf, M.; Lee, C.Y.; Farha, O.K.; Hauser, B.G.; Hupp, J.T.; Snurr, R.Q. Large-scale screening of hypothetical metal-organic frameworks. *Nat. Chem.* **2011,** *4*, pp 83–89.

[5] Suh, M.P.; Park, H.J.; Prasad, T.K.; Lim, D.W. Hydrogen storage in metal-organic frameworks. *Chem. Rev.* **2012,** *112* (2), pp 782–835.

[6] Corma, A.; Garcia, H.; Llabres i Xamena, F.X. Engineering Metal Organic Frameworks for Heterogeneous Catalysis. *Chem. Rev.* **2010,** *110* (8), pp 4606–4655.

[7] DeCoste, J.B.; Peterson, G.W. Metal-Organic Frameworks for Air Purification of Toxic Chemicals. *Chem. Rev.* **2014,** *114* (11), pp 5695–5727.

[8] Kreno, L.E.; Leong, K.; Farha, O.K.; Allendorf, M.; Van Duyne, R.P.; Hupp, J.T. Metal-Organic Framework Materials as Chemical Sensors. *Chem. Rev.* **2012,** *112* (2), pp 1105–1125.

[9] Shekhah, O.; Wang, H.; Kowarik, S.; Schreiber, F.; Paulus, M.; Tolan, M.; Sternemann, C.; Evers, F.; Zacher, D.; Fischer, R.A.; Wöll, C. Step-by-Step Route for the Synthesis of Metal-Organic Frameworks. *J. Am. Chem. Soc.* **2007,** *129* (49), pp 15118–15119.

[10] Denny, M.S., Jr.; Cohen, S.M. In Situ Modification of Metal-Organic Frameworks in Mixed-Matrix Membranes. *Angew. Chem., Int. Ed.* **2015,** *54* (31), pp 9029–9032.

[11] Zhang, Z.; Nguyen, H.T.; Miller, S.A.; Cohen, S.M. polyMOFs: A Class of Interconvertible Polymer-Metal-Organic-Framework Hybrid Materials. *Angew. Chem., Int. Ed.* **2015,** *54* (21), pp 6152–6157.

[12] Hansen, C.M. Universality of Solubility Parameter. *Ind. Eng. Chem. Prod. Res. Dev.* **1969,** *8* (1), pp 2–11.

[13] Xin, C.; Zhan, H.; Huang, X.; Li, H.; Zhao, N.; Xiao, F.; Wei, W.; Sun, Y. Effect of various alkaline agents on the size and morphology of nano-sized HKUST-1 for CO_2 adsorption. *RSC Adv.* **2015,** *5* (35), pp 27901–27911.

[14] Venna, S.R.; Lartey, M.; Li, T.; Spore, A.; Kumar, S.; Nulwala, H.B.; Luebke, D.R.; Rosi, N.L.; Albenze, E. Fabrication of MMMs with improved gas separation properties using externally-functionalized MOF particles. *J. Mater. Chem. A.* **2015,** *3* (9), pp 5014–5022.

Deep learning for the prediction of experimental spectra

Patrick C. Riley[a], Samir V. Deshpande[b], Brian C. Hauck[b]
[a]U.S. Army Combat Capabilities Development Command Chemical Biological Center, Research & Technology Directorate, 8198 Blackhawk Rd, Aberdeen Proving Ground, MD 21010
[b]Science and Technology Corporation, 111 Bata Blvd, Suite C, Belcamp, MD 21017

ABSTRACT

Increasingly, the design of alarm algorithms to alert Soldiers of danger grows more complex as new threats emerge. These algorithms need to be robust enough to prevent false alarms to interferents yet sensitive enough to alarm to the incredibly small doses that prove lethal. Deep neural networks present a unique opportunity to improve current algorithms, predict experimental spectra of new threats, and potentially determine chemical species from spectra. Deep neural networks are a technique in machine learning that imitate the function of a human brain by passing inputs through a series of hidden layers, where a neuron—representative of a piece of data—is activated based on a mathematical function. While deep neural networks have been developed for predicting on laboratory instrumentation, no model has been demonstrated to translate to highly variable fielded chemical detectors. A model's training data set directly impacts its generalization to other like devices. A mature chemical detection technology with an existing large data set is ion mobility spectrometry, and past work has been done using neural networks to predict either chemical class based on spectra or spectra from molecular property inputs. However, in either case, the resulting network could not be generalized to additional detectors. Here, the design of a theoretical long short-term memory framework is presented that considers both instrument parameters and molecular properties to simulate the chemistry of a detection technology for which it was trained and to predict experimental spectra.

Keywords: deep neural network, machine learning, ion-mobility spectrometry, false alarm reduction

1. INTRODUCTION

The threat of harm from explosives, chemical warfare agents (CWA), and narcotics to civilian, Warfighter, and first responder safety has necessitated the development of small handheld analytical instrumentation or chemical detectors for the identification of these compounds. When shrinking lab bench sized analytical instrumentation, sacrifices in one or more of the following traits are made—size, response time, selectivity, or sensitivity. While size is a physical requirement posed on the design of the detector, selectivity and sensitivity are limitations of the analytical technique being used in the detector. Selectivity and sensitivity affect the chemical detector's ability to discern between chemicals and sense small quantities, respectively. These two factors directly impact the false alrm rate of a chemical detector—the probability of the detector alarming to an interferent (a false positive) or failing to alarm (a false negative).

One chemical detection technology often deployed for use in handheld design is ion mobility spectrometry (IMS). IMS is a technology easily shrunk to handheld size, has a rapid response, and is highly sensitive.[1] While IMS is highly sensitive, it lacks selectivity and will often false alarm to interferent chemicals.[2] IMS alarm algorithms function by calculating the reduced mobility (K_0) value of ions in the detector and comparing this to "detection windows"—a range of K_0 values where the ion of a chemical has previously been measured to appear.

To calculate the K_0, IMS detectors function by measuring the time it takes for ions to travel a discreet path within an electric field and a carrier gas. This discreet path in the instrument is referred to as the drift region and the time it takes for ions to travel in the drift region is referred to as the drift time (t_d). The K_0 value of the ions is calculated from the t_d of the ion, the path length of the drift region (L), the applied voltage (V), temperature (T), and pressure (P) of the drift gas, as shown in

$$K_0 = \frac{L^2}{V t_d}\left(\frac{273.15}{T}\right)\left(\frac{P}{760}\right). \quad (1)$$

To improve the false alarm rate of IMS-based chemical detectors, a variety of techniques are employed such as calibration or modeling. In calibration, highly accurate measurements of K_0 values are used to shrink and move detection windows when provided a chemical compound with a well-documented accurate K_0.[3,4] Modeling attempts to account for environmental conditions, instrument parameters, and molecular properties to improve the predictive nature of the alarm algorithms. One challenge of utilizing these techniques is the inherent non-linear behavior between the various parameters being measured. Selecting or measuring key values over others may introduce a bias into the model or reduce predictive capability when a key value is left out of the model.

One technique to minimize bias in a model is to utilize deep neural networks (DNN)—a sub-technique of machine learning (ML). ML is a field of computational science that uses several techniques for modeling a data set to allow computers to "learn" and make predictions or classify inputs. DNNs are a type of ML algorithm that uses a series of computations structured as interconnected nodes or "neurons" to model non-linear data. The network is formed by using data transform functions, called the activation function, in multiple hidden layers to determine the neurons that are passed from the input to the output layer. Research has shown that, when utilizing multiple hidden layers during backpropagation, the network is impeccable at removing this feature bias.[5] Backpropagation is where a DNN iteratively reweights features while attempting to reach a point where it is able to accurately predict from a training data set. Therefore, designing a DNN for predicting or classifying IMS spectra could improve false alarm rates.

The use of ML for the prediction or classification of analytical spectra is not uncommon.[6,7,8–11] In one study, a neural network (NN) was trained to predict the functional groups of analytes based on IMS spectra alone.[12,13] Another NN was trained with tandem ion mobility-mass spectrometry (IMMS) measurements to predict the IMS drift times of peptides and assist in protein identification.[6] More recent work has seen the development of a convolutional neural network (CNN) for classifying the collision cross section (CCS) of IMS ions or utilizing long short-term memory (LSTM) for making mass spectral substance detections.[8,9,11] CNN and LSTM are types of DNNs with differing approaches. CNN is often used in the classification of images and LSTM in natural language prediction. While each of these studies present a novel method for accurately predicting or classifying chemical information from spectra, none have demonstrated a network that is generalizable to multiple detection technologies utilizing the same analytical technique.

The manufacturing techniques and rugged use of handheld chemical detectors ensures that variance exists from instrument to instrument. This partly contributes to the wide detection windows seen across these devices. To accurately predict spectra or classify spectra of these instruments, a data set that appropriately captures all this variance would be required. The exact source of variance from detector to detector has not been well documented. Therefore, if a ML model was designed that can account for all potential instrument parameters and molecular properties that are the source of this variance, it was hypothesized that the network would be able to simulate the chemistry of a detection technology for which it is trained and predict the experimental result. Here this work describes the design of a data input stream and resulting network performance for an LSTM based DNN for predicting experimental spectra for an IMS detector by accounting for instrument parameters and molecular properties. The findings of this work would direct the design of features for modeling spectral variance in highly variable handheld chemical or biological detection devices.

2. METHODS

The training data set was acquired on the accurate ion mobility instrument (AIMI) which is an IMS in a stacked-ring design capable of measuring the variables affecting K_0 values to ± 0.1 % accuracy.[3,4] AIMI was selected because it is considered the "gold standard" of IMS data and recent work by DeepMind Technologies (London, UK) used high quality "gold standard" optical coherence tomography image input data before the DNN model was applied to a second platform. Training the model using this "gold standard" data set allowed the model to more accurately analyze lower quality and ambiguous optical coherence tomography scans during the testing phase.[14] Therefore, it was believed training the LSTM network on the "gold standard" in laboratory grade IMS would translate better prediction to lower grade handheld IMS detectors.

All chemicals used for the training data set were obtained from Sigma-Aldrich®. Dimethyl methylphosphonate (DMMP), di-*tert*-butylpyridine (D*t*BP), and triethyl phosphate (TEPO) were obtained as 97 %, 97 %, and 99.8 % pure standards, respectively. Di(propylene glycol) monomethyl ether (DPM), was obtained as a 99 % pure standard consisting of a mixture of isomers. All training data was collected in the positive ion detection mode and a

time-of-flight mass spectrometer (Ionwerks®, Inc.; Houston, TX) was used to mass identify all mobility peaks. Two different ionization sources were used for data collection—a ^{63}Ni ionization source for DMMP and a corona ionization source for all other chemicals.

A total of 111, 87, 83, and 89 data points were collected for DMMP, DtBP, TEPO, and DPM, respectively. A total of 32 features (shown in Table 1) was initially selected for each chemical compound ending in _1, _2, or _3 representing a feature specific to the reactant ion peak, monomer peak, or dimer peak, respectively.

Table 1. Feature set and corresponding correlation values. Blue highlighting represents features added to the model.

Feature (Feature#)	Positive Correlation Value	Feature (Feature#)	Negative Correlation Value
Molecular mass (amu)_3	9.96E-01	K0 (cm2V-1s-1)_3 (10)	-9.74E-01
Reduced mass w/air (g)_3	9.90E-01	K0 (cm2V-1s-1)_2 (9)	-9.66E-01
CCS_3 (cm2) (11)	9.70E-01	Ion source	-8.00E-01
Reduced mass w/air (g)_2	9.69E-01	ion mass protonated (amu)_3	-7.81E-01
Molecular mass (amu)_2	9.16E-01	Dipole Moment (Cm)_2	-5.10E-01
CCS_2 (cm2) (8)	8.71E-01	Electric Field (V/cm)	-3.96E-01
P (torr)	8.12E-01	radius gas (cm)	-3.39E-01
td (G1-G2)_3 (s)	8.01E-01	CCS_1 (cm2) (7)	-2.61E-01
td (G1-G2)_2 (s)	7.64E-01	radius ion (cm)_1	-2.41E-01
Drift gas Number Density (cm-3)	6.56E-01	[H2O] (ppmv)	-1.54E-01
td (G1-G2)_1 (s)	5.13E-01	Dipole Moment (Cm)_1	-1.11E-16
ion mass protonated (amu)_2	5.05E-01	Reduced mass w/air (g)_1	-1.05E-16
K0 (cm2V-1s-1)_1 (6)	2.71E-01	Molecular mass (amu)_1	-4.18E-17
Proton Affinity (kJ/mol)_2	2.20E-01		
Length (G1-G2) (cm)	1.64E-01		
drift gas T (K)	1.14E-01		
Proton Affinity (kJ/mol)_1	1.11E-16		
ion mass ammoniated (amu)	1.05E-16		
ion mass protonated (amu)_1	4.18E-17		

These features can be separated into categories of molecular properties, instrument parameters, or a combination of both, as shown in Figure 1.

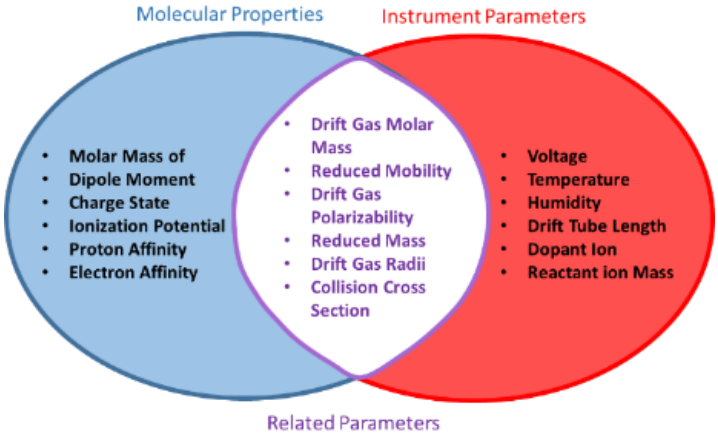

Figure 1. Venn diagram depicting features assigned to molecular properties, instrument parameters, or both.

A majority of data points were numerical in nature, and no feature engineering was performed before passing to any training models. Several features are considered "uncollected data points", or features that were not physically collected during testing or calculated from parameters determined during testing with the AIMI. One such data point—simplified molecular input line entry specification (SMILES), which uses the American Standard Code for Information Interchange (ASCII) characters to describe molecular structure—was added to the tensorflow pipeline by converting it into a 1-hot vector. To convert SMILES into a 1-hot vector, each ASCII character was assigned a numerical value, which was then represented by an array of vectors made of 0's and 1's. By designating a molecule

in this manner, as opposed to a traditional 1-hot vector, the structure represented by the SMILES is passed into the feature set.

Features of this dataset were down selected to prevent overfitting of the data and increase model run time. Features were assigned a binary predictor and a correlation matrix was generated to inform feature down-selection, as shown in Table 1. Several highly correlated features were determined to be sources of bias due to their discreet nature. For example, pressure *P* (torr) was considered an instrument parameter; but, as a feature, had two discreet values across the four chemicals collected. This occurred during data collection when DMMP was collected at high altitude and the other three compounds at sea level. Table 1 highlights the final select features in blue, but adds the addition of SMILES which is not listed in the table. As shown, many features were down-selected and mobility and CCS were primarily kept. K_0 and CCS equations contain many of the variables expressly written as discreet values in Table 1. The equation for K_0 is shown in equation 1 and the equation for CCS is

$$\Omega = \frac{3e}{16N}\left(\frac{2\pi}{\mu kT}\right)^{1/2}\left(\frac{1}{K}\right), \tag{2}$$

where e is the elementary charge, N is the drift gas number density, μ is the reduced mass of the ion-neutral pair, k is Boltzmann's constant, T is the neutral drift gas temperature, and K is the mobility of the ion (not normalized against standard pressure and temperature). Ions in an IMS separate based on the CCS, as larger molecules have an increased chance of collision with the drift gas and lower K_0 values. Therefore, by modeling initially on CCS and K_0, instrument parameters and molecular properties will be passed into the model, and training time will be reduced. The features for K_0, CCS, and SMILES were put into an LSTM network as described in Figure 2.

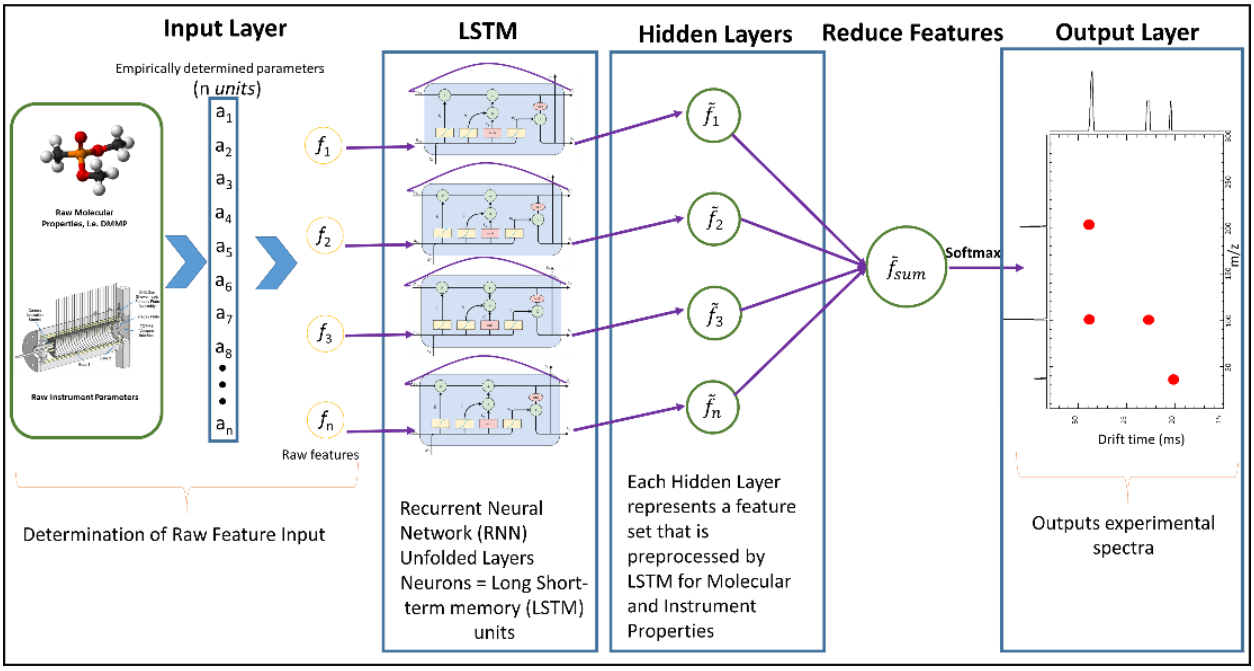

Figure 2. Proposed LSTM framework for predicting experimental spectra.

3. RESULTS

The LSTM network ran for 11 days and failed to converge on a solution. The resulting LSTM network behavior indicated an issue with the design of the framework, feature selection, or a lack of data. To determine which occurred an analysis was performed with a variety of decision trees, AdaBoost, and a feed-forward network by classifying the feature set. Running the networks in this fashion allowed rapid analysis of many architectures and the isolation of potential issues. Table 2 shows an analysis of many types of decision trees and AdaBoost by predicting based on two features—this would demonstrate any underlying issues with the selected features. Decision trees categorize well and function more efficiently on less data than a DNN. Therefore, low score values would indicate an issue with the feature selection.

Table 2. Decision tree and AdaBoost analysis displaying scores when classifying on two features.

Algorithm	# of Estimators	Feature 1	Feature 2	Scores
DecisionTree	N/A	9	11	0.5844595
RandomForest	17	9	11	0.5810811
ExtraTrees	17	9	11	0.5844595
AdaBoost	17	9	11	0.4864865
DecisionTree	N/A	9	10	0.6486486
RandomForest	17	9	10	0.6520270
ExtraTrees	17	9	10	0.7195946
AdaBoost	17	9	10	0.4966216
DecisionTree	N/A	9	8	0.7972973
RandomForest	17	9	8	0.7972973
ExtraTrees	17	9	8	0.7972973
AdaBoost	17	9	8	0.5168919
DecisionTree	N/A	9	6	0.9898649
RandomForest	17	9	6	0.9864865
ExtraTrees	17	9	6	0.9898649
AdaBoost	17	9	6	0.6216216
DecisionTree	N/A	9	7	0.9797297
RandomForest	17	9	7	0.9628378
ExtraTrees	17	9	7	0.9831081
AdaBoost	17	9	7	0.5912162

The resulting analysis of decision trees demonstrates high scores for classification indicating the features selected were appropriate for making predictions. A second analysis was performed utilizing all features simultaneously in a classification feed-forward network. Table 3 shows the results from the feed-forward network analysis where the number of epochs or backpropagations, batch size, type of output activation function, and number of hidden layers varied. Changes in accuracy due to a difference in these variables would indicate a potential issue with the LSTM network model. Lower accuracy, even with parameter modification, would indicate a lack of data.

Table 3. Tensorflow feed-forward network analysis depicting accuracy determined when classifying based on all features and manipulating network parameters, number of hidden layers, output activation function, batch size, and number of epochs.

# of Hidden Layers	Activation Function	Batch Size	#Epochs	Accuracy
3, 1 output	RELU, Output Relu	5	5	0.2167
		5	10	0.2167
		5	50	0.2830
		15	5	0.4667
		15	10	0.4333
		15	50	0.2833
		30	5	0.1833
		30	10	0.4167
		30	50	0.1833
2, 1 output	RELU, Output RELU	5	5	0.4000
		5	10	0.4000
		5	50	0.1333
		15	5	0.3167
		15	10	0.5000
		15	50	0.4333
		30	5	0.3500
		30	10	0.3167
		30	50	0.1833
2, 1 output	RELU, Output Sigmoid	5	5	0.4833
		5	10	0.4833
		5	50	0.4833
		15	5	0.5000
		15	10	0.5000
		15	50	0.5000
		30	5	0.2667
		30	10	0.5000
		30	50	0.5000

Table 3 shows that all reported accuracy was less than or equal to 0.5, indicating a lack of data. This is further demonstrated by the accuracy changes across batch size and outliers within the given data set. Since the final data set was split between training, testing, and validation at random a small data set would show higher variance and lower accuracy when predicting. For instance, if a random selection of data took more data points for DMMP, this would decrease accuracy because there are less DMMP rows to predict correctly and less training data for the other chemicals to accurately predict.

4. CONCLUSIONS

A feature set was designed utilizing the "gold standard" in IMS data to train an LSTM network to predict experimental spectra. The ideal solution is training a network to predict on lower quality data sets without being specifically trained

on that instrument. This work demonstrated a lack of "gold standard" data to properly train an LSTM network or to accurately classify with a feed forward network. Several decision trees demonstrated high accuracy when classifying on only two features—indicating a well-selected feature set, given more data for LSTM. Future work will curate data from Joint Chemical Agent Detectors—a handheld IMS chemical detector for which thousands of data points exist.

ACKNOWLEDGMENTS

Funding was provided by the U.S. Army via the In-house Laboratory Independent Research Program (PE0601101A Project 91A) at the Combat Capabilities Development Command Chemical Biological Center. The authors acknowledge Dr. Augustus W. Fountain III for his technical guidance and mentorship and Dr. Mary M. Wade for her general supervision, editing, and support.

REFERENCES

[1] Forbes, T.P.; Najarro, M. Ion mobility spectrometry nuisance alarm threshold analysis for illicit narcotics based on environmental background and a ROC-curve approach. *Analyst.* **2016,** *141* (14), pp 4438–4446.

[2] Eiceman, G.A.; Yuan-Feng, W.; Garcia-Gonzalez, L.; Harden, C.S.; Shoff, D.B. Enhanced selectivity in ion mobility spectrometry analysis of complex mixtures by alternate reagent gas chemistry. *Anal. Chim. Acta*. **1995,** *306* (1), pp 21–33.

[3] Hauck, B.C.; Siems, W.F.; Harden, C.S.; McHugh, V.M.; Hill, H.H., Jr., Construction and evaluation of a hermetically sealed accurate ion mobility instrument. *Int. J. Ion Mobility Spectrom.* **2017,** *20* (3–4), pp 57–66.

[4] Hauck, B.C.; Siems, W.F.; Harden, C.S.; McHugh, V.M.; Hill, H.H., Jr. High Accuracy Ion Mobility Spectrometry for Instrument Calibration. *Anal. Chem.* **2018,** *90* (7), pp 4578–4584.

[5] Hinton, G.E.; Salakhutdinov, R.R. Reducing the Dimensionality of Data with Neural Networks. *Science*. **2006,** *313* (5786), pp 504–507.

[6] Wang, B.; Valentine, S.; Plasencia, M.; Raghuraman, S.; Zhang, X. Artificial neural networks for the prediction of peptide drift time in ion mobility mass spectrometry. *BMC Bioinf.* **2010,** *11*, pp 1–11.

[7] Gastegger, M.; Behler, J.; Marquetand, P. Machine learning molecular dynamics for the simulation of infrared spectra. *Chem. Sci*. **2017,** *8* (10), pp 6924–6935.

[8] Liu, J.; Zhang, J.; Luo, Y.; Yang, S.; Wang, J.; Fu, Q. Mass Spectral Substance Detections Using Long Short-Term Memory Networks. *IEEE Access.* **2019,** *7*, pp 10734–10744.

[9] Plante, P-L.; Francovic-Fontaine, É.; May, J.C.; McLean, J.A.; Baker, E.S.; Laviolette, F.; Marchand, M.; Corbeil, J. Predicting Ion Mobility Collision Cross-Sections Using a Deep Neural Network: DeepCCS. *Anal Chem*. **2019,** *91* (8), pp 5191–5199.

[10] Riley, P.C.; Deshpande, S.V. Machine learning based spectral interpretation in chemical detection. In *Proceedings Volume 1106: Artificial Intelligence and Machine Learning for Multi-Domain Operations Applications.* SPIE Defense + Commercial Sensing. Baltimore, MD, 14–18 April 2019; Pham, T., Ed.; SPIE: Bellingham, WA, 2019; CID 11006-68.

[11] Kantz, E.D.; Tiwari, S.; Watrous, J.D.; Cheng, S.; Jain, M. Deep Neural Networks for Classification of LC-MS Spectral Peaks. *Anal. Chem*. **2019,** *91* (19), pp 12407–12413.

[12] Bell, S.; Nazarov, E.; Wang, Y.F.; Eiceman, G.A. Classification of ion mobility spectra by functional groups using neural networks. *Anal. Chim. Acta*. **1999,** *394* (2–3), pp 121–133.

[13] Bell, S.; Nazarov, E.; Wang, Y.F.; Rodriguez, J.E.; Eiceman, G.A. Neural Network Recognition of Chemical Class Information in Mobility Spectra Obtained at High Temperatures. *Anal Chem*. **2000,** *72* (6), pp 1192–1198.

[14] De Fauw, J.; Ledsam, J.R.; Romera-Paredes, B.; Nikolov, S.; Tomasev, N.; Blackwell, S.; Askham, H.; Glorot, X.; O'Donoghue, B.; Visentin, D.; van den Driessche, G.; Lakshminarayanan, B.; Meyer, C.; Mackinder, F.; Bouton, S.; Ayoub, K.; Chopra, R.; King, D.; Karthikesalingam, A.; Hughes, C.O.; Raine, R.; Hughes, J.; Sim, D.A.; Egan, C.; Tufail, A.; Montogmery, H.; Hassabis, D.; Rees, G.; Back, T.; Khaw, P.T.; Suleyman, M.; Cornebise, J.; Keane, P.A.; Ronneberger, O. Clinically applicable deep learning for diagnosis and referral in retinal disease. *Nat. Med*. **2018,** *24*, pp 1342–1350.

Characterization of aerosol particle charge and the impact of a high degree of charge on the particle's physical and chemical properties

Erin M. Durke[a*], Monica L. McEntee[a], Meilu He[b], Suresh Dhaniyala[b]
[a]U.S. Army Combat Capabilities Development Command, Chemical Biological Center, Research & Technology Directorate, 8198 Blackhawk Rd, Aberdeen Proving Ground, MD 21010
[b]Clarkson University, 8 Clarkson Ave, Potsdam, NY 13699

ABSTRACT

The metal oxide, TiO_2, was aerosolized expulsively with sonic nozzles, then integrated using transmission infrared spectroscopy. Specifically, the TiO_2 was exposed to methanol vapor within a vacuum chamber. The reaction was performed for both aerosolized TiO_2 and unmodified TiO_2 powder. The results for the reaction with the aerosolized sample differ drastically from those recorded for the methanol exposed powder. A high-flow dual-channel differential mobility analyzer was employed to determine the particle charge distribution for the polydisperse TiO_2 samples. The high-flow dual-channel differential mobility analyzer data indicates as many as 230 charges per particle for a 700 nm particle of TiO_2. Also, of note is the polarity of the aerosol particles. The concentration of positively charged particles versus negatively charged particles appears to be dependent upon the material being aerosolized, as opposed to the generation process simply resulting in an even bipolar distribution.

Keywords: aerosol, particle, charge distribution, infrared, metal oxide, reactivity

1. INTRODUCTION

Aerosol particles are ubiquitous in the atmosphere. In fact, the most significant variation observed for aerosol particles from one locale to the next is the overall concentration.[1–3] As a result of the omnipresence of aerosols, much focus is given to their impact—with respect to reactivity, exposure, and persistence, to name only a few considerations. However, within each of these topics, attention must be given to the basic characteristics or properties of the aerosols. It could be argued that the most important aerosol feature is the particle's inherent charge, because it has the potential to affect the physical and chemical properties. In fact, we have shown previously that the infrared spectra for several metal oxides is altered once the material has been aerosolized.[4] We have also reported a divergence in the interaction with several probe gases for aerosolized TiO_2.[5]

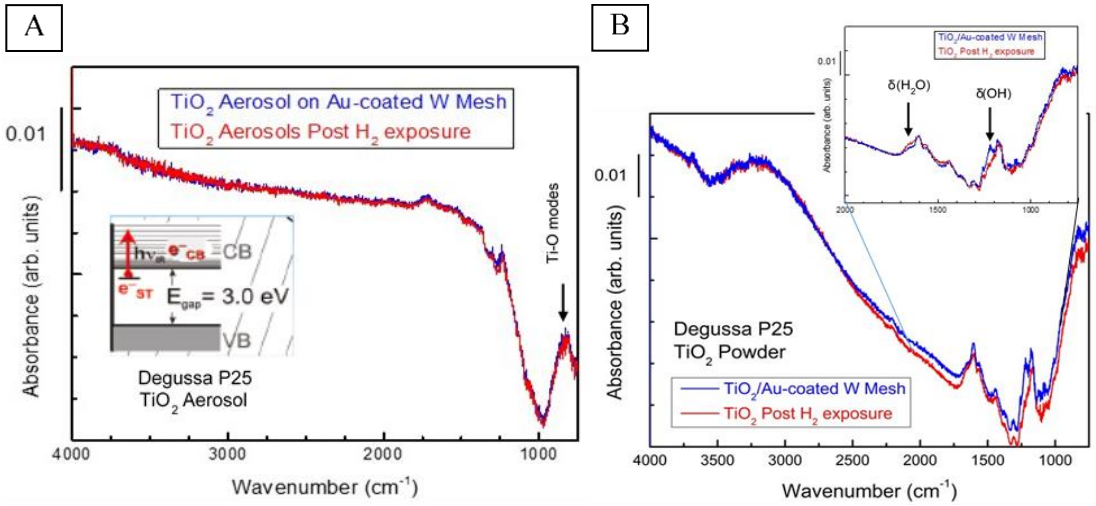

Figure 1. (A) TIR spectra of aerosolized TiO_2 exposed to H_2(g). (B) TIR spectra of unmodified TiO_2 exposed to H_2(g).

Figure 1B shows transmission infrared (TIR) spectra collected of aerosolized TiO_2 before and after exposure to H_2(g). Hydrogen was chosen as a probe molecule because its interaction with TiO_2 is well documented in the literature.[6,7]

Exposing the metal oxide, TiO_2, to H_2 results in the filling of shallow trapped states directly below the conduction band, and upon illumination with infrared (IR) light, promotion of those electrons occupying the shallow traps into the conduction band. These electrons, also known as conduction band electrons, are observed via a broad background rise ($\leq$ 2,000 cm^{-1}) seen in the IR spectrum. It is obvious in Figure 2A that no such background rise is present in the aerosolized TiO_2 spectrum. We concluded that, upon aerosolization, the shallow trapped states were filled, therefore once that sample is exposed to H_2, no further occupation of the shallow traps occurs. Contrarily, when the unmodified TiO_2 powder was exposed to H_2, a reaction was observed between the two species. While the characteristic background rise was not identified, the reaction was not unexpected. The reaction of TiO_2 powder and H_2 produced H_2O as a consequence of the presence of surface species, such as carbonates. Under standard procedures, the TiO_2 is pretreated to remove any contaminants, however, that step was not performed in the interest of maintaining similar sample preparations.

The TiO_2 samples, both powder and aerosol, were also exposed to CO. For the powder TiO_2, we were able to observe CO binding to the Ti^{4+} sites, as evidenced by the peaks in Figure 2B.[8] However, the aerosolized TiO_2 exposed to CO, shown in Figure 2A, showed no uptake at all. We hypothesized that the additional surface charge imparted via the aerosolization process inhibits the uptake and binding of CO to the Ti^{4+} sites.

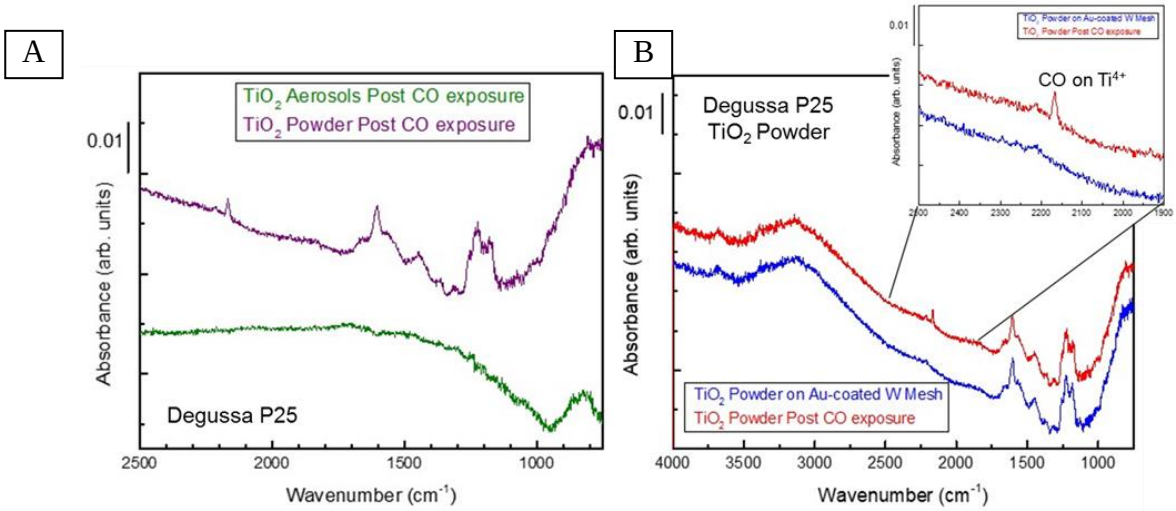

Figure 2. (A) TIR spectrum (green) of aerosolized TiO_2 exposed to CO(g). The purple spectrum was collected from TiO_2 powder after exposure to CO(g). (B) TIR spectra of unmodified TiO_2 exposed to CO(g) (red spectrum).

Traditional aerosol instrumentation was employed to determine the particle charge distributions (PCD) for the metal oxides understudy. Our collaborators at Clarkson University measured the PCD of monodisperse SiO_2 (200 nm spheres ± 10 % diameter) initially, as a monodisperse material is much more trivial to characterize than the polydisperse TiO_2.[5] The results of the PCD for SiO_2 showed as many as 30+ charges per particle for the 200 nm aerosols, see Figure 3.

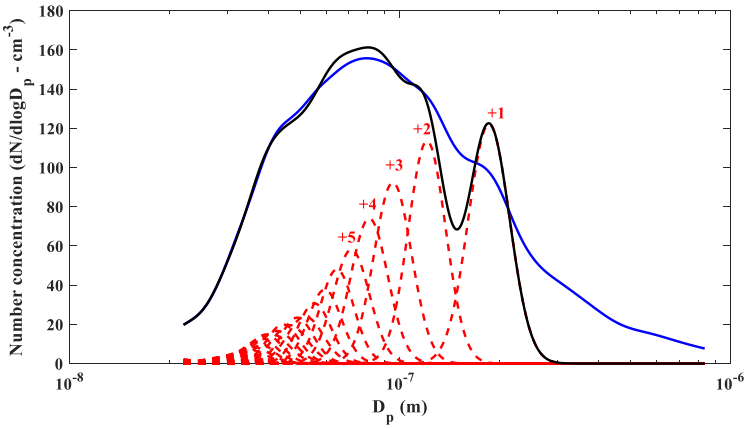

Figure 3. The final PCD determined for 200 nm SiO_2 aerosol particles. The results indicate as many as 30+ charges per particle were measured.

In the final year of this work, we explored the reactivity of TiO_2 and methanol, and how it is impacted by the aerosolization of TiO_2. The overall hypothesis states that any deviations in reactivity may be attributable to the excess charge resulting from the aerosol generation process.

2. EXPERIMENTAL

2.1 Materials

Aeroxide® P25 TiO_2 was purchased from Sigma-Aldrich® and used without further purification. Lanthanide-tagged SiO_2 particles were used without further purification. The SiO_2 particles were custom made by Fiber Optic Center, Inc. using AngströmSphere™ silica spheres. The SiO_2 particles characterized in these studies were 200 nm (± 10 %) in diameter.

2.2 Aerosolization

All materials were aerosolized using sonic nozzles based on the SRI International annular nozzle design, shown in Figure 4.[11] The sonic nozzle is comprised of an internal tube with a high-pressure air flow passing around said tube and exiting through an orifice. The configuration results in a Venturi effect, which pulls material from the sample reservoir and through the nozzle, where it will experience disruptive forces causing deagglomeration and aerosolization.

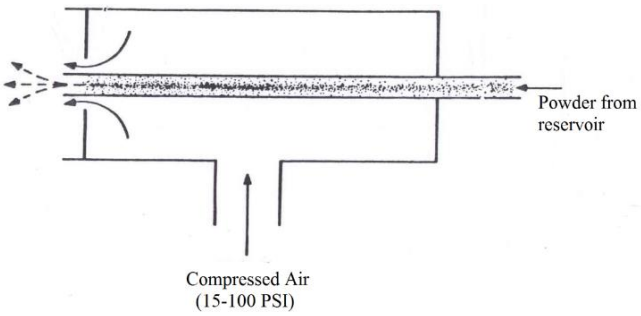

Figure 4. SRI International annular nozzle design. Modified picture from Calabrese and Ranade.[11]

For samples interrogated with transmission infrared (TIR) spectroscopy, the TiO_2 powder was aerosolized inside of a Lexan™ aerosol generation box. The samples (W mesh) were placed on the bottom of the box prior to aerosolization. Aerosols were generated for 2–5 seconds—depending on desired deposition concentration—then, the particles were allowed to settle on the sample surfaces for at least one hour. Some samples required higher deposited concentrations, so multiple aerosolizations were performed, with ample settling time allowed between generations.

For samples generated for particle size distribution (PSD) and PCD measurements (SiO_2 and TiO_2), the powders were contained inside sealed vials, and connected to the sonic nozzle via metal tubing. The powder was aerosolized into the sample drum, see Figure 5, from which samples were pulled for characterization.

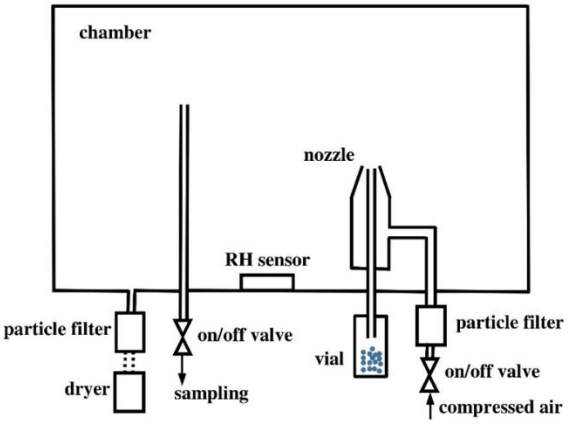

Figure 5. Sample drum utilized for PSD and PCD measurements.

2.3 Instrumentation

The aerosolized samples were interrogated with TIR spectroscopy inside of the custom mid-infrared aerosol chemistry chamber; sample mount schematic and picture shown in Figure 6. The TIR spectroscopy was performed using a Thermo Scientific™ Nicolet™ 6700 Fourier TIR spectrometer equipped with a mid-IR source and mercury cadmium telluride (MCT) Type A detector, allowing for an observable range of 4,000–650 cm^{-1}. Spectra are the sum of 1,024 scans acquired at a resolution of 2 cm^{-1}.[12]

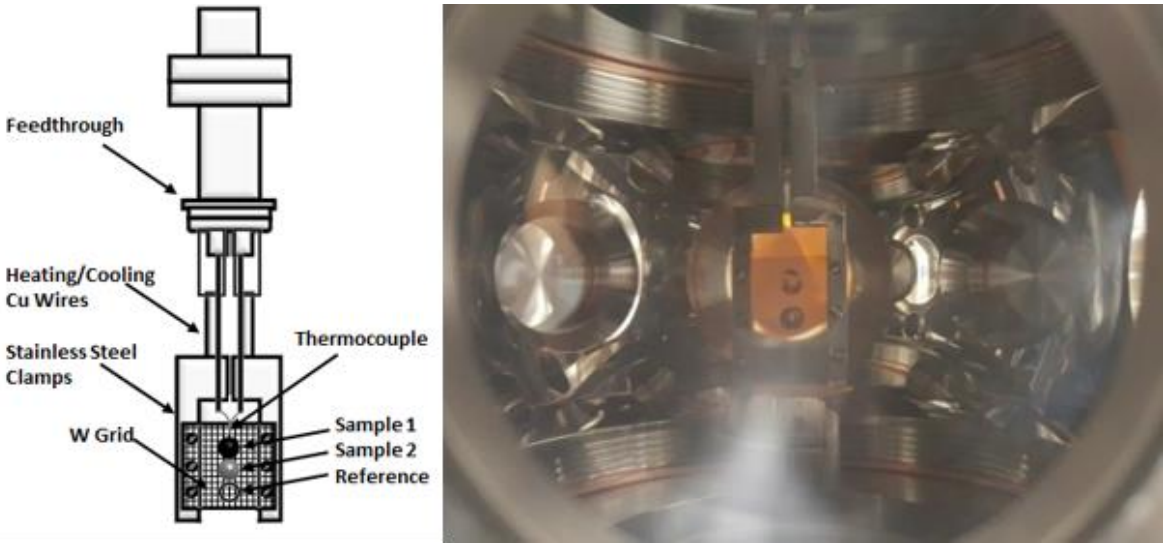

Figure 6. Schematic (left) and image (right) of the sample mount and W mesh used to perform TIR spectroscopy of the metal oxides (both powder and aerosols).

For size and charge distribution measurements, electrical mobility measurements were made using a scanning mobility particle sizer (SMPS). To determine the charge fraction of particles from the mobility measurements, the size distribution of particles must first be collected. Several instruments were utilized for PSD measurements. These instruments are based on different technologies; therefore, the PSD measurements were cross-validated using a customized high-flow SMPS, wide-range particle spectrometer, ultra-high sensitivity aerosol spectrometer, and aerodynamic particle sizer. The measurement range for each instrument is shown in Table 1.

Table 1. Instruments applied for PSD measurements.

	High-flow SMPS	**WPS**	**UHSAS**	**APS**
Technology	electrical mobility	electrical mobility	optical	aerodynamic
Size range (μm)	0.005 – 3	0.01 – 0.4	0.1 – 1	0.5 – 20

The schematic diagram of the experimental setup for PSD measurements is shown in Figure 7. The sonic nozzle was placed in a 20-gallon drum (Figure 5), compressed air was supplied to the nozzle at different pressures (e.g., 70 psi, 80 psi) and the aerosolized particles were dispersed into the drum. The concentrations of the dispersed particles were then measured using the four instruments listed in Table 1.

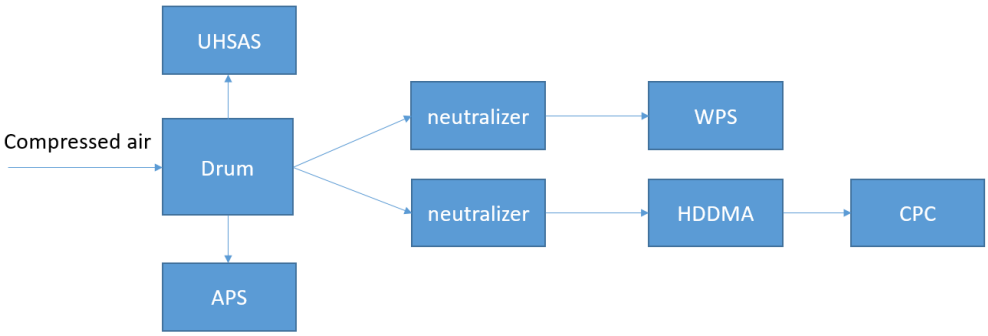

Figure 7. Schematic diagram of experimental setup for PSD measurements.

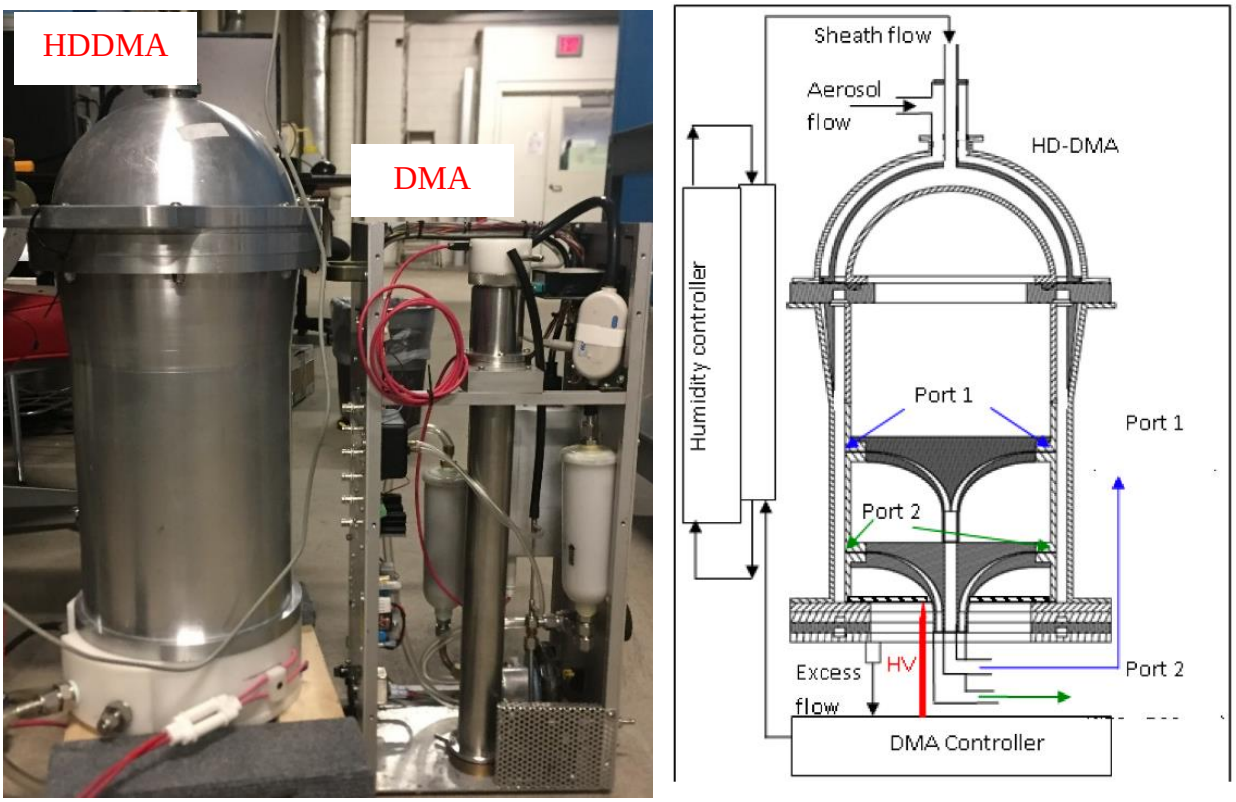

Figure 8. (a) High-flow dual-channel differential mobility analyzer (HDDMA) comparing with the conventional differential mobility analyzer (DMA); (b) inner diagram of HDDMA.

The high-flow SMPS was composed of a customized HDDMA for large size-range classification, and a condensation particle counter (CPC). The picture and schematic diagram of the HDDMA is shown in Figure 8. Compared with the conventional differential mobility analyzer, the HDDMA has a significantly larger radius which makes operation at high flow rates (sheath flow of ~100 l/min) possible. However, for the purposes of this study, to measure the size distribution of particles with a broad size range (< 100 nm up to 3 µm), the HDDMA is operated with a lower sheath flow rate (~20 l/min), much less than the sampling condition for which it was designed. The instrument was evaluated at the necessary sampling conditions for accurate data analysis.

2.4 HDDMA/multiple charge algorithm

The charge distribution is determined by first directly measuring the mobility distribution of the dispersed particles with HDDMA without the neutralizer in place, as shown in Figure 9. A CPC is used to measure total particle concentration, and the ultra-high sensitivity aerosol spectrometer (UHSAS) is employed to capture any changes in the PSD as a function of the experimental setup (i.e., removal of the charge neutralizer). The charge number and corresponding fractions can be obtained from the particle size and mobility distribution according to

$$Z_p = \frac{neC_c}{3\pi\mu D_p}, \tag{1}$$

where D_p is particle diameter, Z_p is electrical mobility, n is the number of elementary charges, e is the elementary charge, C_c is the Cunningham Correction factor, and µ is the air viscosity.

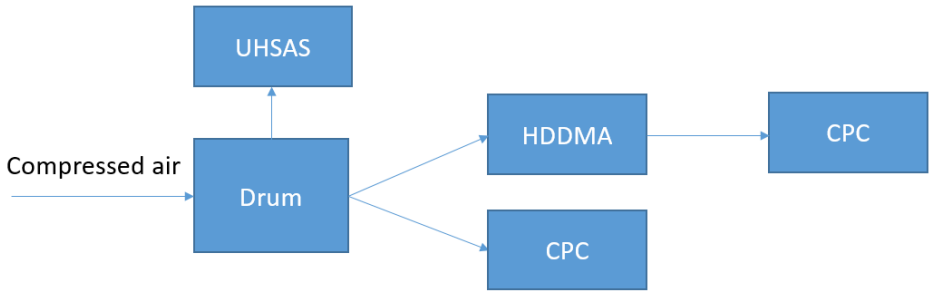

Figure 9. Schematic diagram of experimental setup for particle charge distribution measurements.

Upon removal of the charge neutralizer (see setup in Figure 9) upstream of the HDDMA, the mobility distribution is obtained. Using the PSD measurement, the charge distribution can be predicted. The charge fractions are then obtained from inversion of the matrix

$$S = \begin{bmatrix} N_{1,1} & N_{1,2} & \cdots & N_{1,P} \\ N_{2,1} & N_{2,2} & \cdots & N_{2,P} \\ \vdots & \vdots & \vdots & \vdots \\ N_{M,1} & N_{M,2} & \cdots & N_{M,P} \end{bmatrix} \begin{bmatrix} f_1 \\ f_2 \\ \vdots \\ f_P \end{bmatrix}, \quad (2)$$

where S is the mobility distribution measured by the HDDMA. For simplicity, the size distribution ($dN/d\log D_p$) is shown as N (with a size channel up to M and charge number up to P). The fraction f_i is then obtained from the inversion.[13]

3. RESULTS AND DISCUSSION

3.1 Chemical reactivity – TiO_2 exposed to methanol

In the previous experiments, we were able to show that aerosolizing the material under study affected the interaction with several different probe gases. While these initial studies were only exploring uptake and binding, not reaction, they showed notable differences even at this basic interaction. Therefore, it seemed plausible that the reactivity and final products could be affected as well. To test this premise, we exposed TiO_2, both powdered and aerosolized samples, to methanol vapor. The spectra shown in Figure 10 were collected for the methanol exposure of powdered TiO_2. Figure 10A shows the entire observable mid-IR spectrum (4,000–650 cm^{-1}) with the MCT detector employed in these studies. Figure 10B focuses specifically on the higher wavenumber region, highlighting both the molecular and dissociated adsorption of methanol.[14–16] Figure 10 clearly shows the uptake and subsequent reaction of methanol on the powdered TiO_2 sample.

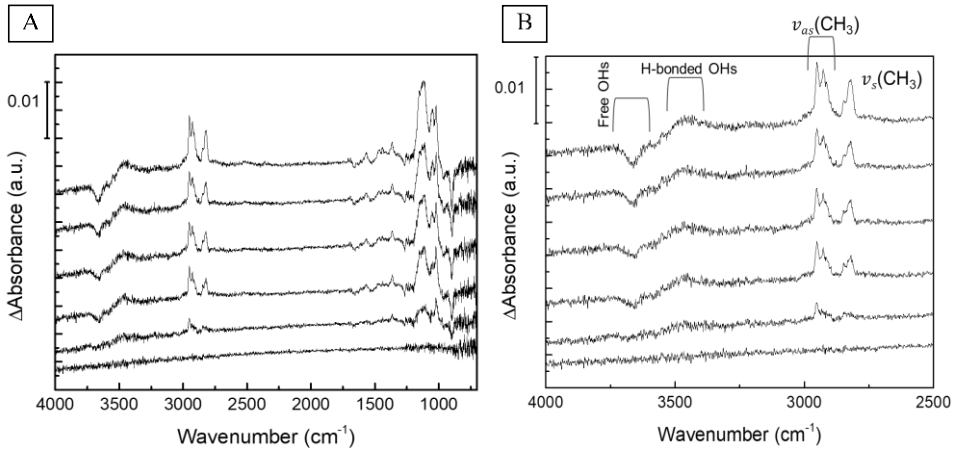

Figure 10. (A) TIR spectra for the exposure of powdered TiO_2 to methanol vapor. The methanol exposure increases as the spectra go from top to bottom. (B) The peaks observed in the hydrocarbon region indicate the binding of both molecular methanol and dissociated methanol (methoxy species) on the TiO_2 surface.

Next, the aerosolized TiO_2 was exposed to methanol vapor. The spectra shown in Figure 11 were collected before and after methanol exposure. The top spectrum in Figure 11 was recorded for the aerosolized TiO_2 prior to dosing. The two spectra directly below were acquired after exposure. The most interesting feature is the immediate and drastic decrease of the background below 2,000 cm^{-1}. Recall that the background rise seen in TiO_2 is indicative of electronic changes (i.e., filling of the shallow trapped states and their subsequent promotion to the conduction band). Previous research shows that the photocatalytic oxidation of methanol is induced by electron holes centered around the surface bound methoxy groups.[16] Based on the existing research, the likely explanation for the observed decrease is the lack of electron holes. Instead of methanol binding to the TiO_2 and reacting, the methanol appears to act as an electron acceptor, pulling the conduction band electrons out of the conduction band, resulting in a background decrease.

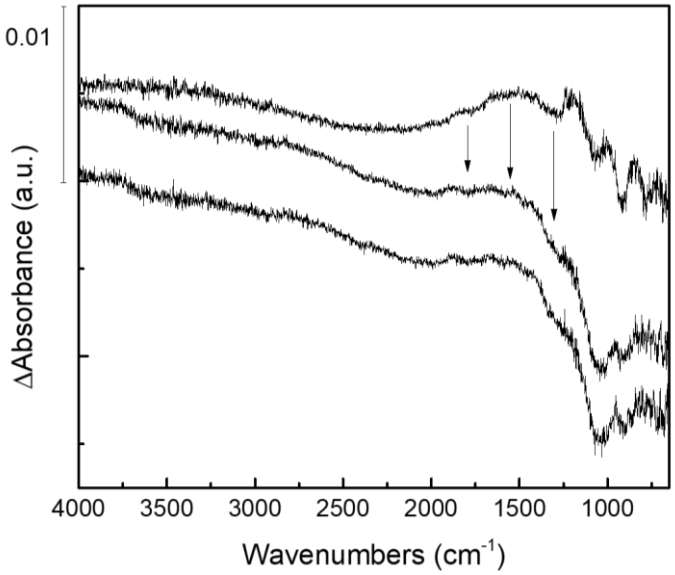

Figure 11. TIR spectra of aerosolized TiO_2 exposed to methanol vapor. Top spectrum was recorded before methanol exposure. Bottom two spectra were collected post-methanol exposure.

3.2 Particle charge distribution

In an attempt to accurately interpret the results from the methanol exposure of TiO_2 aerosols, and whether or not the observed outcome is attributable to excess surface charge, the particle charge distribution was measured. For the polydisperse sample, charge per particle was calculated for the most prominent size modes. Figure 12 shows the charge profile for 200 nm, 300 nm, 508 nm, and 708 nm aerosol particles of TiO_2. The 708 nm particles were determined to have upwards of 230+ charges per particle.

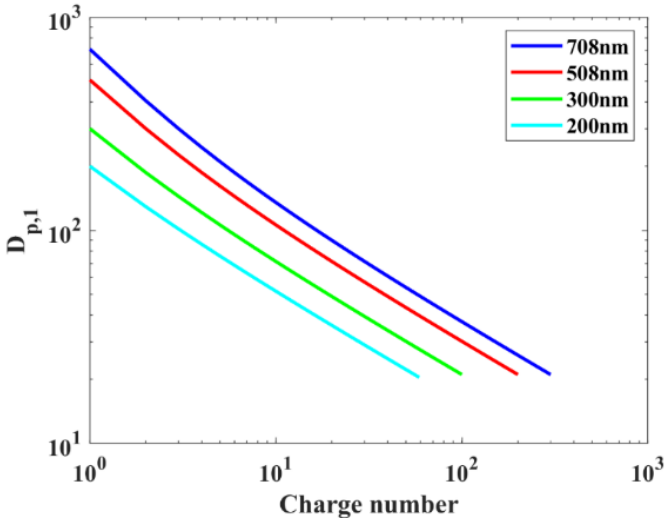

Figure 12. The charge profile for several mode sizes for TiO_2 aerosol particles.

4. CONCLUSIONS

The objective of this work was to investigate the charge imparted on an aerosol particle via the aerosol generation process, and to understand the impact of the additional charge on the material's physical and chemical properties. We were able to show, through our previous work, the differences in the IR spectra of powder versus aerosolized TiO_2 and SiO_2.[4] Our research also indicated a variation in the interactions of TiO_2 and several probe gases, upon aerosolization of the metal oxide.[5] Finally, in the most recent studies, the methanol reactivity of aerosolized TiO_2 was compared to that of the unmodified powder. As shown in Figures 10 and 11, the reactivity is drastically altered. We had hypothesized that the lack of electron holes on the TiO_2 (because they are presumably filled via the additional surface charge via aerosolization) would result in only molecularly bound methanol on the aerosolized TiO_2. However, what was observed was a significant divergence from that normal reactivity, with methanol appearing to act as an electron acceptor, see Figure 11, when it is generally seen as an electron donor. Perhaps it is a function of the magnitude of added charge. Historically, the charge per particle can be calculated based on the diameter of the particle, see Figure 13. The dashed line in Figure 13 shows the mathematical predication of the charge per particle. Yet, when the results from our studies are plotted on the same graph, one can note the obvious deviation from expected values. The most likely explanation for this departure is the influence of the material's specific chemical properties.

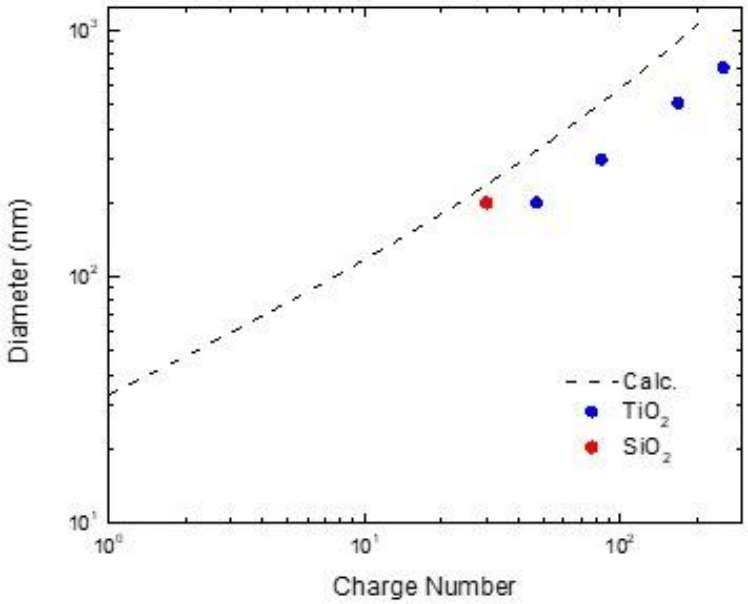

Figure 13. Charge per particle based on particle diameter. Red circle represents the measured charge per particle for 200 nm SiO_2 aerosols generated expulsively. The blue circles represent the measured charge per particle for 200 nm, 300 nm, 508 nm, and 708 nm TiO_2 aerosol particles generated expulsively.

If the basic values for the electron affinity and work function of TiO_2 (e^- affinity: 1.59 eV, ϕ: 4.13 eV) and SiO_2 (e^- affinity: 0.9 eV, ϕ: 4.6 eV) are compared, we can begin to explain why we see changes not only in the number of charges per particle, but also in the magnitude of positively charged particles versus negatively charged particles. Figure 14 shows that expulsive aerosolization of TiO_2 results in more positively charged particles overall. It also indicates that, for the same size aerosol particle of SiO_2, the TiO_2 will acquire more positive charge than the SiO_2 aerosols. If we tie these results to the work functions of each material, this is reasonable as SiO_2 has a value 0.5 eV greater than that of TiO_2.

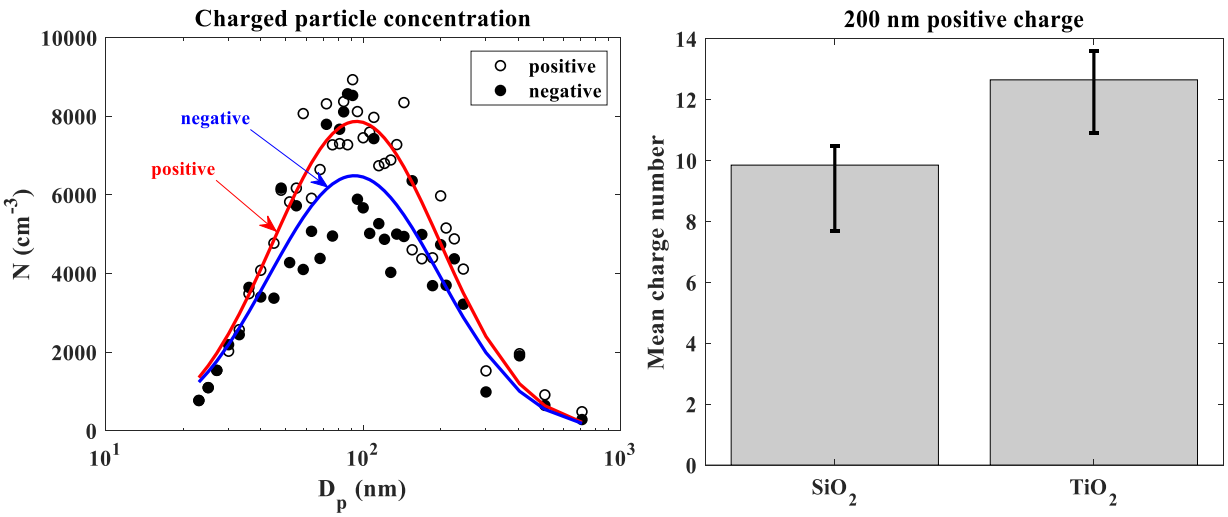

Figure 14. The graph on the left shows the varying concentrations of positively and negatively charged particles of aerosolized TiO_2. The graph on the right compares the concentration of positively charged 200 nm particles for both SiO_2 and TiO_2.

This work suggests that the charge on an aerosol particle is significantly more complex—in that, not only does the size of the particle and method of aerosolization play a role in the ultimate value for surface charge, but also, and probably more importantly, the material itself can have a noteworthy impact on the magnitude and polarity of the particle charge. Finally, the charge imparted via aerosolization is important to consider for objectives involving characterization and reactivity, as it is shown here to impact those features and properties in a noticeable way.

ACKNOWLEDGMENTS

Funding was provided by the U.S. Army via the In-house Laboratory Independent Research Program (PE 0601101A Project 91A) at the Combat Capabilities Development Command Chemical Biological Center.

REFERENCES

[1] Ng, N.L.; Canagaratna, M.R.; Jimenez, J.L.; Zhang, Q.; Ulbrich, I.M.; Worsnop, D.R. Real-Time Methods for Estimating Organic Component Mass Concentrations from Aerosol Mass Spectrometer Data. *Environ. Sci. Technol.* **2011,** *45* (3), pp 910–916.

[2] Drewnick, F.; Schwab, J.J.; Jayne, J.T.; Canagaratna, M.; Worsnop, D.R.; Demerjian, K.L. Measurement of Ambient Aerosol Composition During the PMTACS-NY 2001 Using an Aerosol Mass Spectrometer. Part I: Mass Concentrations Special Issue of Aerosol Science and Technology on Findings from the Fine Particulate Matter Supersites Program. *Aerosol Sci. Technol.* **2004,** *38* (S1), pp 92–103.

[3] Park, R.J.; Jacob, D.J.; Logan, J.A. Fire and biofuel contributions to annual mean aerosol mass concentrations in the United States. *Atmos. Environ.*, **2007,** *41* (35), pp 7389–7400.

[4] Durke, E.M.; McEntee, M.; Dhaniyala, S. Characterization of aerosol particle charge and the impact of a high degree of charge on the particle's physical and chemical properties. In *FY17 Proceedings of Edgewood Chemical Biological Center In-House Laboratory Independent Research and Surface Science Initiative Programs*; U.S. Army Edgewood Chemical Biological Center: Edgewood, MD, **2018;** pp 1–8.

[5] Durke, E.M.; McEntee, M.; Dhaniyala, S. Characterization of aerosol particle charge and the impact of a high degree of charge on the particle's physical and chemical properties. In *FY18 Proceedings of Edgewood Chemical Biological Center In-House Laboratory Independent Research and Surface Science Initiative Programs*; U.S. Army Edgewood Chemical Biological Center: Edgewood, MD, **2019;** pp 26–35.

[6] Panayotov, D.A.; Morris, J.R. Thermal Decomposition of a Chemical Warfare Agent Simulant (DMMP) on TiO_2: Adsorbate Reactions with Lattice Oxygen as Studied by Infrared Spectroscopy. *J. Phys. Chem. C.* **2009,** *113* (35), pp 15684–15691.

[7] Panayotov, D.A.; Burrows, S.P.; Yates, J.T., Jr.; Morris, J.R. Mechanistic Studies of Hydrogen Dissociation and Spillover on Au/TiO_2: IR Spectroscopy of coadsorbed CO and H-Donated Electrons. *J. Phys. Chem. C.* **2011,** *115* (45), pp 22400–22408.
[8] Linsebiger, A.; Lu, G.; Yates, J.T., Jr. CO chemisorption on TiO_2(110): Oxygen vacancy site influence on CO adsorption. *J. Chem. Phys.* **1995,** *103*, pp 9438.
[9] Rocker, G.; Göpel, W. Chemisorption of H_2 and CO on stoichiometric and defective TiO_2(110). *Surf. Sci.* **1986,** *175* (1), pp L675–L680.
[10] Linsebiger, A.; Lu, G.; Yates, J.T. CO photooxidation on TiO_2(110). *J. Phys. Chem.* **1996,** *100* (16), pp 6631– 6636.
[11] Calabrese, R.V.; Ranade, M.B. Pneumatic nozzle dissemination of powders into air; TCN 91291; U.S. Army Research Office: Research Triangle Park, NC, **1993;** UNCLASSIFIED Report.
[12] McEntee, M.L.; Durke, E.M.; Driscoll, D.; Morris, J.R. Mid-Infrared Aerosol Chemistry Chamber (MIRACC); ECBC-TN-072; U.S. Army Edgewood Chemical Biological Center: Aberdeen Proving Ground, MD, **2001**; UNCLASSIFIED Report.
[13] He, M.; Dhaniyala, S. A multiple charging correction algorithm for scanning electrical mobility spectrometer data. *J. Aerosol Sci.* **2013,** *61*, pp 13–26.
[14] Kim, K.S.; Barteau, M.A. Reactions of methanol on TiO_2(001) single crystal surfaces. *Surf. Sci.* **1989,** *223* (1–2), pp 13–32.
[15] Shen, M.; Henderson, M.A. Identification of the active species in photochemical hole scavenging reactions of methanol on TiO_2. *J. Phys. Chem. Lett.* **2011,** *2* (21), pp 2707–2710.
[16] Panayotov, D.A.; Burrows, S.P.; Morris, J. R. Photooxidation Mechanism of Methanol on Rutile TiO_2 Nanoparticles. *J. Phys. Chem. C.* **2012,** *116* (11), pp 6623–6635.

Effect of bacterial spore deactivation methods on bacteria chemical components as determined by Raman chemical imaging

Ashish Tripathi, Michael Kim, Phillip G. Wilcox, Erik D. Emmons
U.S. Army Combat Capabilities Development Command Chemical Biological Center, Research & Technology Directorate, 8198 Blackhawk Rd, Aberdeen Proving Ground, MD 21010

ABSTRACT

Recently, distribution of unreliably deactivated *Bacillus anthracis* spore samples created disruption in the defense, health, and disease control communities. Accurate and reliable determination of viability is critical to avoiding such incidents. Multiple technologies exist that can detect or identify an organism, but do not provide any information with regards to viability of the sample. Most often, one must rely on microbiological culture to confirm sample viability; however, this technique takes hours to days for confirmation. Recent work with *B. anthracis* Delta Sterne spores demonstrated that Raman spectroscopy could be used to discriminate between viable and gamma deactivated spores and provided initial insight into the probable source of discrimination found in the spores. From this previous work, we believe through Raman spectral analyses of viable and deactivated spore samples, significant changes in spectral response can be resolved and ascribed to classes of biomolecules affected by the deactivation processes. We expanded upon this study to include four different *Bacillus* spores (*B. anthracis*, *B. megaterium*, *B. thuringiensis*, and *B. atrophaeus*) and probe used de-activation techniques to include UV radiation, chemical, and thermal methodologies. Through this study, we hope to reveal via Raman spectroscopy relevant biomolecules that are critical in spectral determination of biological viability that could lead to reliable, non-contact, non-destructive, and rapid assessment of bacterial spores.

Keywords: bacterial spore viability, image segmentation, Raman spectroscopy, Raman microscopy, image cytometry, bright-field, microscopy

1. INTRODUCTION

Determining a spore's viability is traditionally performed using one of a few long-standing methods. The first, and most widely used method, is to culture the sample and wait to observe growth (or lack thereof); however, this method can take days to confirm lack of growth.[1,2] Other methods include polymerase chain reaction (PCR) or quantitative PCR (qPCR) to amplify DNA fragments. Although these methods do not always discriminate the DNA from viable and non-viable cells, sample preparation methods have been demonstrated which can prevent the DNA from nonviable cells from being replicated.[3,4] To perform PCR, the DNA needs to first be extracted from the sample with the PCR process itself taking minutes to hours to complete.[4,5] A third option involves the use of fluorescent stains or assays which can be used with flow cytometry[6] or optical microscopy.[7–11] In order to screen a large number of spores the ideal method would require minimal sample preparation and rapid acquisition of data. Using a method based on bright-field microscopy provides an approach that can be used to quickly measure a large number of spores. Combining this method with an additional analytical technique such as Raman spectroscopy improves the confidence in the final determination of viability. Previously, Raman microscopy has demonstrated the ability to discriminate between bacterial species and strains using both normal Raman[12–14] and surface-enhanced Raman spectroscopy.[15–17] Additionally, Raman spectral differences have been documented between viable and non-viable *Bacillus* spores that were inactivated using wet-heat,[18] cold atmospheric plasma,[19] and chemical (formalin)[17] methods. In this effort we will examine spores inactivated with gamma and ultraviolet C (UV-C) irradiation, autoclaving (thermal), and two chemical methods (bleach and aldehyde). The combination of bright-field and Raman imaging techniques is well suited for spore screening because they are both non-contact, non-destructive, and reagent-less. In this effort, we selected attenuated strains of *B. anthracis* Sterne, *B. atrophaeus*, *B. megaterium*, and *B. thuringiensis*.

To rapidly and automatically obtain cytometric measurements that, in part, include shape and size parameters of spores from bright-field images, requires a robust and accurate segmentation method. Manual characterization of spores in images is a slow, laborious, and subjective task. In addition to counting and determining morphological information, spore segmentation plays a valuable role in selective targeting of spores for further Raman imaging analysis. This type

of smart targeting has shown usefulness in forensic applications and leads to a reduction in the time required to analyze the sample by predetermining the location of the spores and interrogating only those locations.[20,21] In the case of Raman microscopy, spectral signatures are collected from the small region where the microscope objective focuses the laser and hyperspectral images are built by rastering the laser beam through the field of view (FOV). For sparse samples, such as deposited spores, a significant percentage of the overall collection time is spent on substrate regions of the image that contain no spore-like material. An additional complication can also occur when the raster scan takes equidistant steps which can result in the laser overlapping multiple spore edges on a single spectral scan. By identifying the spore regions before spectral acquisition, scans can be performed faster by ignoring regions where spore-like material is not present and spectral results can be linked back to a specific spore. These shortcomings are addressed by the approach presented in this report.

Specific software approaches to aid in the task of segmenting biological samples have been previously explored.[22,23] A variety of segmentation techniques have been applied on large cellular materials including white blood cells (which are in the 12–17 µm size range);[24–26] hematopoietic stem cells (~20–30 µm);[27] cancer cells;[28] bone marrow, blood, and cervical nuclei (~6 µm);[29,30] living *Spodoptera frugiperda* cells (~9–12 µm);[31] and fungal and bacterial spores (~2–60 µm depending on species).[32–38] These applications typically rely on a relatively small set of segmentation techniques—thresholding, edge/feature detection, morphological filtering, region growing, and deformable model fitting.[39,40] More advanced segmentation techniques such as neural networks require large amounts of training data to improve upon the accuracy[26] that can be achieved with traditional techniques.

In this effort, we use a combination of these traditional segmentation techniques to quickly and autonomously segment bright-field images of gram-positive spores. Gram positive spores are small (~1 µm in diameter) compared to the cells described in the previous paragraph, which can make them difficult to detect using bright-field imaging since it is close to the diffraction limit of optical microscopy. Using the microscope described later with a 100X objective, the image of a single spore is typically 11–16 pixels in length. Additionally, the spore deposition on a substrate is random, and the spores may be distributed individually or in clusters of varying sizes, which further complicates the segmentation process. To overcome these issues, a combined method incorporating watershed segmentation[38] and an unsupervised segmentation method[30] were previously proposed and demonstrated. The watershed based methods typically showed less than 90 % success in demarcation of individual spores,[30,38] whereas the unsupervised methods showed greater than 93 % success in demarcation;[30] but used an iterative process that came at a very high computational complexity and cost. The method used in this work employs the traditional watershed based segmentation[41] in conjunction with an optimized pre-processing methodology. Since this image processing technique segments images by finding local maxima contours around "catchment basins" of lower intensity,[41] it works well for both sparse (mono dispersed or well separated clusters of spores) and dense images (poorly separated clusters or large clusters of spores).

Using the image processing method, Raman spectra of multiple viable and deactivated spores is extracted. The Raman spectra of viable and deactivated spores is examined to obtain possible spectral differences between the two populations. These differences are compared with Raman spectra of various spore biomarkers to include calcium dipicolinate, DNA, protein surrogates, phospholipids, and peptidoglycan.

2. EXPERIMENTAL

2.1 Spore formation and growth study

2.1.1 Organism and growth medium

The *Bacillus* spore strains used in this study were *B. thuringiensis kurstaki* (ATCC 33679), *B. megaterium* (ATCC 9885), *B. anthracis* Sterne (34F2), and *B. atrophaeus* (ATCC 9372). A base of Difco™ sporulation medium (DSM) consisting of the following composition was used: 8 g/L nutrient broth (NB, Difco™), 2.15 g/L KH_2PO_4 (Sigma-Aldrich®) and 4.39 g/L K_2HPO_4 (Sigma-Aldrich®), which was sterilized at 121 °C for 30 minutes in an autoclave (Tomy ES-315). The sterilized base DSM was further supplemented with 40 mL of a 0.2 µm filtered pre-sterilized (Corning®) sporulation salt stock solution (CCY). The CCY stock consisted of 7.35 g/L $CaCl_2{\cdot}2H_2O$, 0.99 g/L $MnCl_2{\cdot}4H_2O$, 10.17 g/L $MgCl_2{\cdot}6H_2O$, 0.0081 g/L $FeCl_3$, and 0.34 g/L $ZnCl_2$. All CCY stock components were purchased from Sigma-Aldrich® except $ZnCl_2$, which was from Fisher Scientific™.

2.1.2 Culture conditions

A glycerol frozen stock of each strain was streaked onto a NB agar plate and incubated at 37 °C overnight (VWR® 3025 B). A single colony of each strain was inoculated into 1 L of DSM in a 4-L flask and incubated at 34 °C and 200 rpm. When the percentage of spores reached greater than 95 % under a phase-contrast microscope (Olympus BX51) after 2 to 3 days, the spore suspension was centrifuged (Beckman Avanti J-25I) at 10,000 rpm for 10 minutes and washed 3 times with pre-sterilized deionized water and concentrated to approximately 100 mL each.

2.1.3 Heat deactivation method

A 0.5-mL aliquot of each washed and concentrated strain was placed in a 2-mL screw cap glass vial and sterilized in an autoclave (Tomy ES-315) at 121 °C for 30 minutes. After sterilization, 0.1 mL of each inactivated strain was inoculated into 250 mL of DSM in a 1-L flask and incubated at 30 °C and 225 rpm for 2 weeks. No re-germination or growth was evident in each heat-inactivated strain.

2.1.4 Gamma radiation deactivation

The spore samples were irradiated utilizing a Cobalt-60 Irradiator (Model 484R) (JL Shepherd & Associates, San Fernando, CA). Four vials, each containing a 2 mL aliquot of water suspension with viable spores, were double-contained and packaged inside of a Saf-T-Pak™ (model QADOC-451) for the irradiation. The Saf-T-Pak™ was placed on a turntable and was rotated at 6 rpm for the duration of the irradiation. The samples were irradiated with a dose of 50 kGray. After deactivation, 0.1 mL of each inactivated strain was inoculated into 250 mL of DSM in a 1-L flask and incubated at 30 °C and 225 rpm for 2 weeks. No re-germination or growth was evident in each gamma radiation-deactivated strain.

2.2 Bright-field imaging and Raman measurements

All bright-field images and Raman hyperspectral cubes (RHSC) were collected utilizing an Alpha 300R confocal Raman imaging microscope (WITec, Ulm, Germany) using a 100X microscope objective and a 532 nm excitation laser. A UHTS300S_VIS spectrometer (WITec, Ulm, Germany) with a 600 lines/mm diffraction grating was used for Raman spectral measurements. Each spectrum was acquired with a 2-second integration time and 4 mW laser output in "continuous mode", where the sample stage was continuously moving over the length of the step size. No photo-bleaching was required as the fluorescence did not seem to deleteriously influence the Raman spectral information. The bright-field imaging option was used with the images on the 1-megapixel (1,000 x 1,000 pixels) setting. The images shown in this report are cropped from these original 1-megapixel images.

2.3 Microscopy slide preparation

For each type of spore and method of deactivation, two separate aluminum coated microscopy slides (EMF, AL136) were prepared. One was populated with only viable spores and the other with deactivated spores. To wash the spores, 4-µL aliquots of water suspension carrying the spores at various concentrations—colony forming units (CFU/mL)—were deposited on the aluminum slides at various locations. The water was allowed to dry, leaving a residue with spores on the microscopy slide surface.

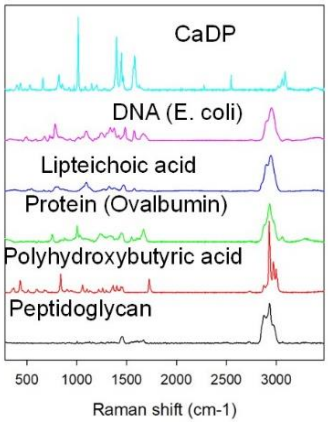

Figure 1. Raman spectra of various spore relevant biomarkers.

Additionally, aluminum-coated microscopy slides were prepared by depositing dry samples of various spore biomarkers to include calcium dipicolinate (CaDP), lipoteichoic acid, and peptidoglycan from *B. subtilis* and polyhydroxybutyric acid. Raman spectroscopy is not specific in discriminating large proteins, thus ovalbumin from chicken egg whites was added to the list of biomarkers as a surrogate for large proteins. Figure 1 shows the Raman spectra of these biomarker chemicals.

2.4 Data analysis

The "cosmic-ray" and baseline correction of the Raman spectral data was performed with the built-in functions in the WITec Project 5.2 version software. The post-acquisition imaging and spectral data analysis was performed using MATLAB® 2019a software (MathWorks; Natick, MA).

3. RESULTS AND DISCUSSION

3.1 Spore sample characterization

A comparison study of viable and deactivated spore mandates that the sample be comprised of mostly spore material and that the amount of non-spore debris (growth media and cellular debris) be minimized. The as-received spore samples were examined with the WITec microscope both visually and chemically. The cleanest spore sample was determined to be *B. anthracis* Sterne. The *B. anthracis* spore sample was comprised of over 95 % spore material with about 2 % of polyhydroxybutyric acid. This determination was made with the help of Raman chemical imaging analysis of a FOV containing the sample, as shown in Figure 2. The bright-field image of the FOV is shown in the top left panel of Figure 2. An overlay of the Raman chemical imaging map with green false-colored pixels showing a greater than 0.8 Pearson's cross correlation with the average spectrum of a viable *B. anthracis* spore (the determination of the average spectra of viable *B. anthracis* spores is discussed in Section 3.3.1) is shown in the bottom left panel of Figure 2. Additionally, red false-colored pixels show a greater than 0.8 Pearson's cross correlation with the spectrum of polyhydroxybutyric acid. The average spectra of anthracis spores (green), the average of all the spectra acquired at the red-pixel locations, and the polyhydroxybutyric acid spectrum (grey) is shown in the right panel of Figure 2.

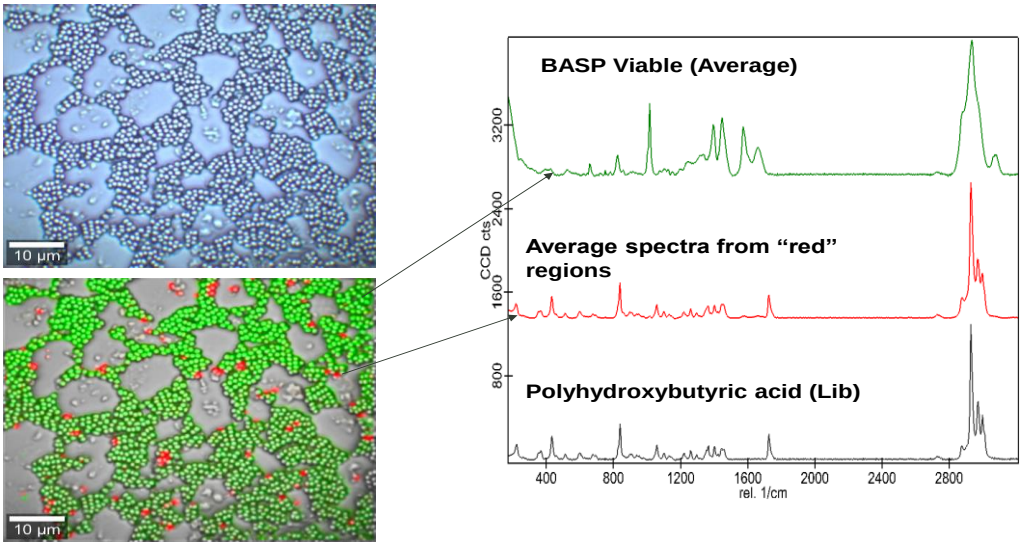

Figure 2. As-received *B. anthracis* spore sample purity determination.

The as-received *B. thuringiensis* spore sample had the least spore content by percentage. The *B. thuringiensis* spore sample was comprised of less than 40 % spore material. This determination was made with the help of Raman chemical imaging and bright-field image analysis of a FOV containing the sample, as shown in Figure 3. Spore-like material, characterized by about 1 micron oval shaped particles in the bright-field image of the FOV, were interspersed with smaller, irregularly shaped particles (shown in the top left panel of Figure 3). Raman chemical analysis showed that, indeed the 1-micron oval shaped particles presented Raman spectra that are typical of a spore (containing biomarker features from calcium dipicolinate, proteins, etc.). An overlay of the Raman chemical map with green false-colored pixels showing a greater than 0.95 Pearson's cross correlation with the average spectrum of a viable *B. thuringiensis*

spore (the determination of the average spectra of viable *B. thuringiensis* spores is discussed in Section 3.3.1, Figure 7) is shown in the bottom left panel of Figure 3. Additionally, false-colored red and blue pixels show a greater than 0.95 Pearson's cross correlation with extracted average spectrum as shown in the right panel of Figure 3.

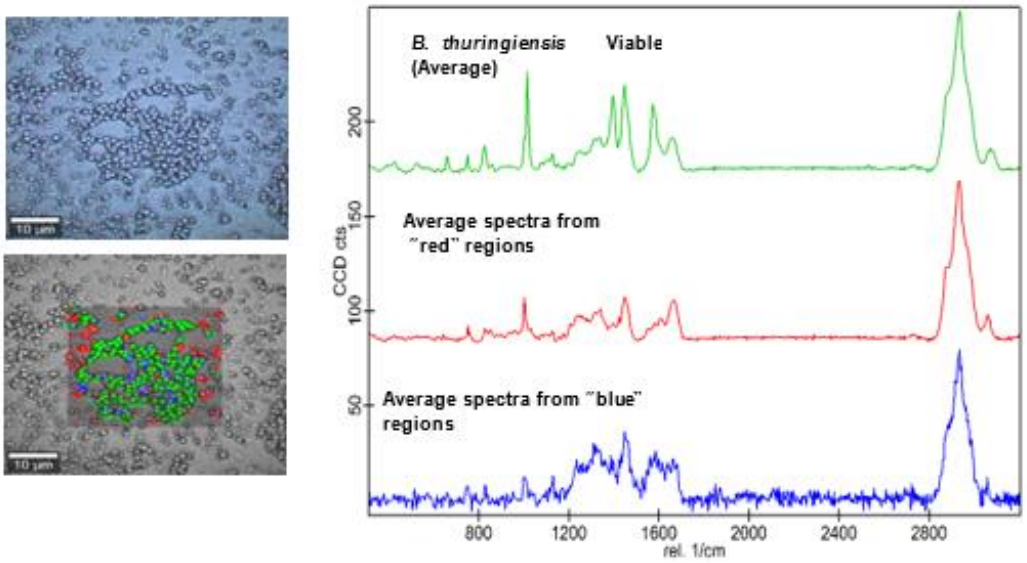

Figure 3. As-received *B. thuringiensis* spore sample purity determination.

The as-received sample of *B. thuringiensis* spores required purification. It was noticed that the suspension containing the spore tended to form "foam" when shaken. A small aliquot of the foam was deposited on a microscopy slide and the sample examined with the help of Raman chemical imaging and bright-field image analysis of a FOV containing the sample, as shown in Figure 4. Two FOVs were examined with the same methodology described in the last paragraph. The foam was comprised of 80 % spores with the rest being 20 % non-spore debris. The Raman and bright-field image analysis is shown in Figure 4. For the remainder of this effort, the foam of the *B. thuringiensis* spore suspension was used for analysis.

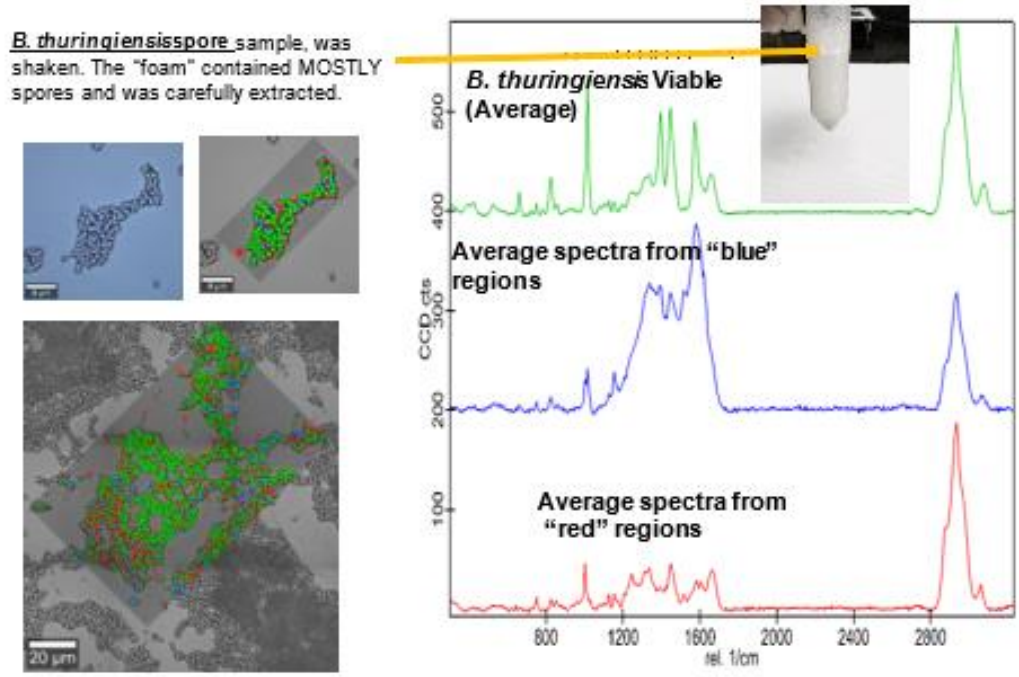

Figure 4. Foam of the shaken *B. thuringiensis* spore suspension contains mostly spores.

3.2 Segmentation overview

Raman chemical images are generated by raster scanning a laser over a sample to collect Raman spectra at each spatial coordinate. This generates a cube of data with spatial information stored along the *x*-axis, *y*-axis, and spectral information saved on the *z*-axis. Since the spatial resolution of bright-field imaging and Raman chemical imaging are both determined by the diffraction limit of visible light, it is technically feasible for Raman chemical imaging to reach image resolutions comparable to those obtained in bright-field images; however, because each pixel needs to be measured individually in an RHSC, the process of doing so is not practical due to the time required to sample each pixel. This means that Raman chemical images typically have significantly lower spatial resolution compared to bright-field images.

The step size for our RHSCs was typically 0.5 µm in both spatial dimensions. Since *Bacillus* spores are ~1 µm in diameter, measuring a RHSC over a larger region means that each spore could be interrogated multiple times in several pixels. Similarly, the laser could also interrogate an area where multiple spores are present in the FOV. Additionally, the Raman spectra collected over a single spore are not uniform and the fixed step size of the raster scan can lead to the interrogation of spore edges or multiple spores at a time which may not be representative of the spore as a whole. To build an average Raman spectra for a single and specific spore, a method was needed to map each point in the data cube to a pixel in the bright-field image.

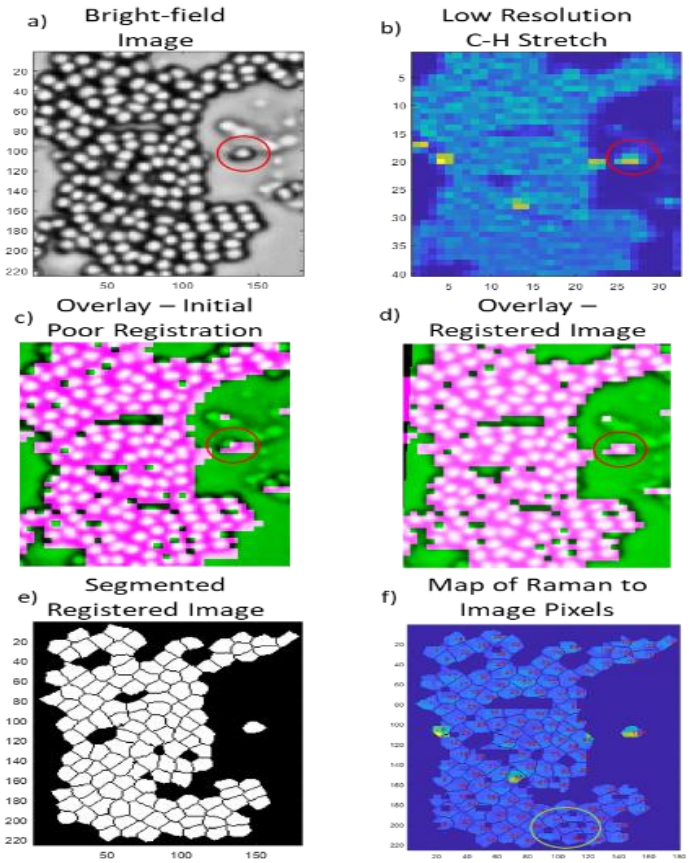

Figure 5. Process showing the registration of a bright-field image (a) and the C–H stretch segment of a RHSC (b) with initial poor alignment (c). After registration (d) the image is segmented (e) with each region being mapped back to a specific spectrum from the original data cube (f).

Image registration is a process where two different images of the same scene are aligned to overlap one another. Because the bright-field microscopy image is significantly higher resolution than the RHSC, straightforward registration techniques were unable to be used. To overcome these challenges, we developed a method to combine all measured Raman spectra from a single spore to obtain an average Raman spectrum for that spore. An example bright-field image of *B. atrophaeus* spores is shown in Figure 5a. First, the segment of the RHSC corresponding to the C–H stretch (2,938 cm^{-1}, C–H image), shown in Figure 5b, was extracted and resized to match the pixel size of the bright-field image using a nearest neighbor interpolation. Figure 5c shows an example of the misalignment present

between the bright-field and Raman images prior to registration. A singly dispersed spore is circled on the right side of the image to highlight this misalignment. Next, a non-reflective similarity transform was applied using the MATLAB® functions 'fitgeotrans' and 'imwarp' to translate, rotate, and scale the bright-field image into alignment with the results shown in Figure 5d. Third, the bright-field image was segmented using an algorithm based on the watershed technique to demarcate the spores as shown in Figure 5e. Finally, every pixel in each demarcated spore was then mapped back to a spectrum within the RHSC. Due to its higher spatial resolution, pixels in the bright-field image can map back to the same pixel within the RHSC which creates a weighted average spectrum being generated for each segmented region. In order to prevent background (non-spore) data from being included in the average, spectra without the C–H stretch spectral feature at 2,938 cm^{-1} were excluded. If more than 40 % of the pixels identified within any segmented region mapped to excluded spectra in the RHSC, then the region was considered blank, and an average was not calculated. The section circled in Figure 5f shows spores correctly identified in the segmentation, but not included in the average due to poor Raman signal. This data was collected from top to bottom and experienced a drift in focus as the scan progressed which caused more below-threshold pixels to be located toward the bottom of the data cube. The example shown in Figure 5 identified and generated spectra for 115 spores. The goal of this method was to generate a large number of high quality weighted average spectra that correspond to single spores, which will be discussed in the following sections.

3.3 Raman chemical imaging and spectroscopy

For each type of spore and method of deactivation, two separate aluminum-coated microscopy slides were prepared. The first was populated with only viable spores and the second with deactivated spores. Multiple FOVs from the two microscopy slides were interrogated with Raman chemical imaging microscopy. The Raman microscope was used in "continuous mode" where each spectra was acquired with a 0.5-µm step size over samples of all viable and deactivated spores to generate RHSCs. Preprocessing of all RHSCs was performed using WITec Project 5.2 analysis software by removal of "cosmic rays" using a filter size of 2 and dynamic factor of 5 (description of these terms is proprietary of WITec). Additionally, a baseline correction was performed using a rolling circle filter with a size of 100 spectral bins. Both viable and deactivated types of spores have strong Raman peaks associated with the C–H stretching vibrations around 2,938 cm^{-1}, which was used as a trigger to include that spectrum in the generation of representative average spectra for each of the two classes. Average spectra were created for each population.

3.3.1 Viable spores

Spectra from at least 300 spores were extracted for each species of spore in viable and deactivated states using the method described in Section 3.1 shows the collection of extracted single viable spore spectra in the fingerprint region and an overlay of the average of the single-spore Raman spectra from the four species of spores.

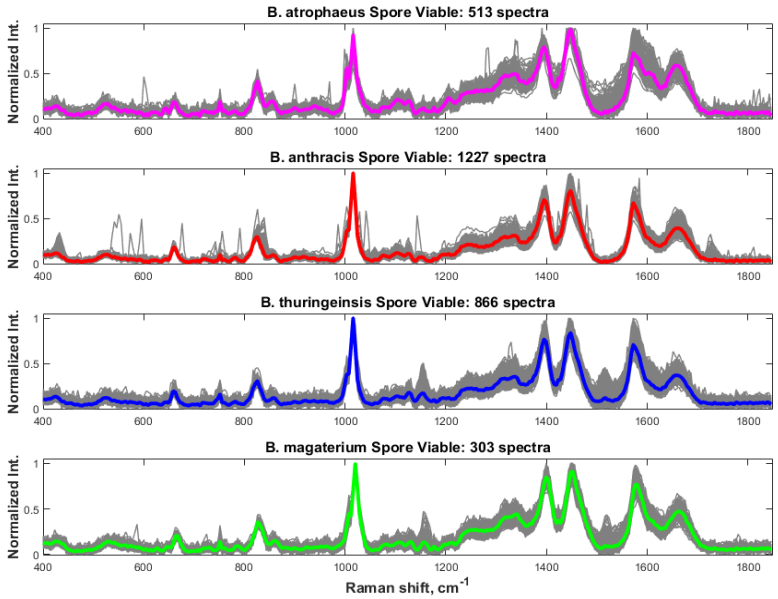

Figure 6. Collection of extracted single viable spore spectra in the fingerprint region and an overlay of the average of the single spore Raman spectra from the four species of spores.

A MATLAB® program was used to perform principal component analysis (PCA) on the collected viable spore spectral data in the fingerprint region. Figure 7 shows the results of the principal component analysis. The scores of the principal components 1, 2, and 3 for the four spores are shown in the left panel of Figure 7. A good degree of separation is obtained between the four species of spores, with *B. thuringiensis* and *B. anthracis* being the nearest neighbors. From the scree plot (shown in top right panel in Figure 7), it is evident that the first five components explain 90 % of the variance. The first five component loading vectors are shown in the bottom right panel of Figure 7.

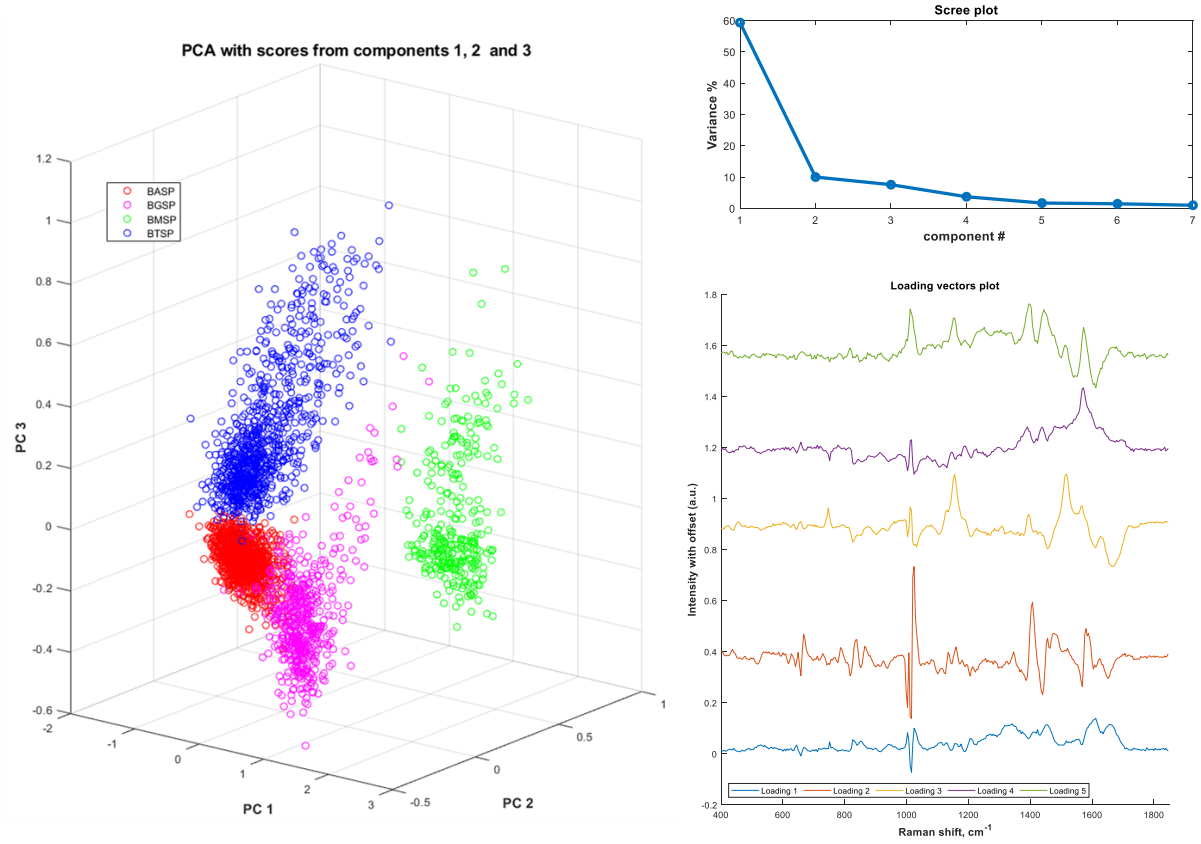

Figure 7. The results of the PCA on the fingerprint region of Raman spectra from single viable spores of four species of the *Bacillus* genus.

3.3.2 Autoclave deactivation of spores

The four species of spores were autoclave-deactivated using the method described in Section 2.1.3. At the time of writing this report, the Raman spectral data acquisition of at least 300 deactivated spores of each species was complete and preliminary data analysis was started. In this section we will show the preliminary multivariate data analysis of two of the four species. The previously mentioned MATLAB® program was used to perform PCA on the collected viable and autoclave deactivated spore spectral data in the fingerprint region for *B. anthracis* and *B. megaterium*.

Figure 8 shows the results of the PCA for the *B. anthracis* spores. The scores of the principal components 1, 2, and 3 for the viable spores (green) and autoclaved spores (red) are shown in the top left panel of Figure 8. A good degree of separation is noticed between the viable and autoclave deactivated spores. From the scree plot (shown in top right panel in Figure 8), it is evident that the first five components explain 90 % of the variance. The first five component loading vectors are shown in the bottom right panel of Figure 8. Clearly, principal components 1 and 2 explain most of the difference between the two groups. A deeper analysis of these results will be conducted to understand the biomarkers expressing these differences within the two groups. The collection of all the viable and autoclaved spore extracted Raman spectra along with the average spectra of the two groups is shown in the bottom left panel of Figure 8.

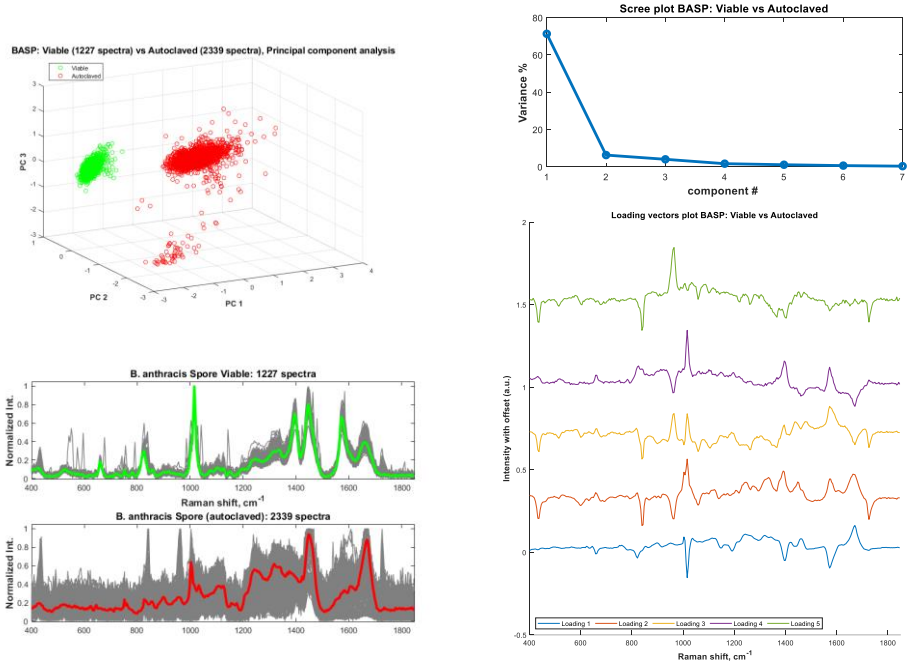

Figure 8. The results of the PCA on the fingerprint region of Raman spectra from single viable and autoclave-deactivated spores of *B. anthracis*.

Figure 9 shows the results of PCA analysis for the *B. megaterium* spores. The scores of the principal components 1, 2, and 3 for the viable spores (green) and autoclaved spores (red) are shown in the top left panel of Figure 9. A good degree of separation is noticed between the viable and autoclave-deactivated spores. From the scree plot (shown in top right panel in Figure 9), it is evident that the first five components explain 90 % of the variance. The first five component loading vectors are shown in the bottom right panel of Figure 9. Clearly, principal component 1 explains most of the difference between the two groups. Deeper analysis of these results will be conducted to understand the biomarkers expressing these differences within the two groups. The collection of all the viable and autoclaved spore extracted Raman spectra along with the average spectra of the two groups is shown in the bottom left panel of Figure 9.

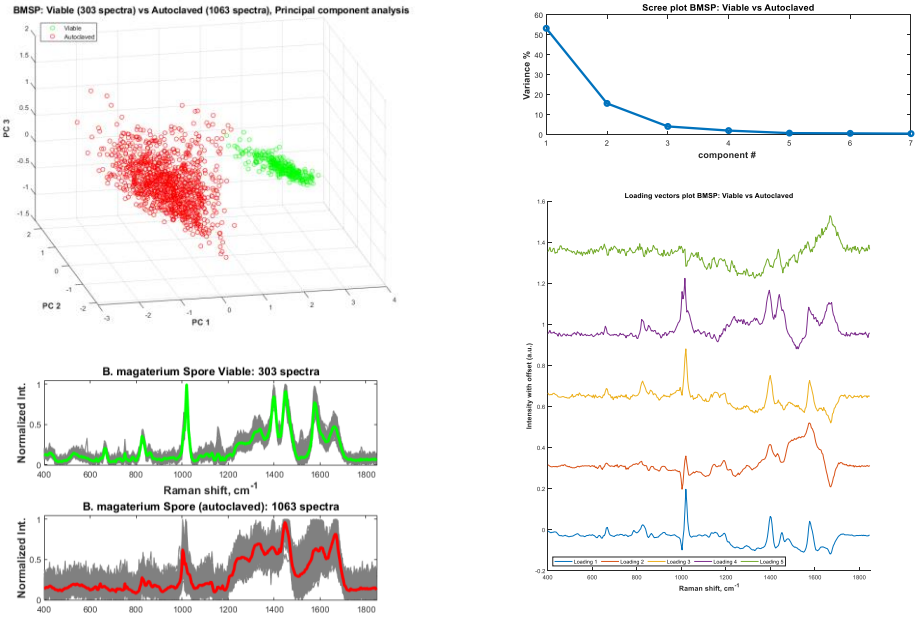

Figure 9. The results of the principal component analysis on the fingerprint region of Raman spectra from single viable and autoclave-deactivated spores of *B. anthracis*.

3.3.3 Gamma radiation deactivation of spores

The four species of spores were gamma radiation deactivated using the method described in the experimentation section. At the time of writing this report, the Raman spectral data acquisition of at least 300 deactivated spores of each species was completed and preliminary data analysis was started. We will report the results of this analysis upon completion.

ACKNOWLEDGMENTS

Funding was provided by the U.S. Army via the In-house Laboratory Independent Research Program (PE 0601101A Project 91A) at the Combat Capabilities Development Command Chemical Biological Center. The authors wish to thank Dr. Angela M. Zeigler for help in literature surveys, Ms. Rebecca Brown and Mr. Shawn Heinlein for performing the gamma radiation deactivation of spore samples, and Drs. Vipin K. Rastogi, Henry S. Gibbons, and Jason A. Guicheteau for helpful discussions.

REFERENCES

[1] ANSI/AMMI/ISO 11737-2:2009. Sterilization of medical devices – Microbiological methods, in Part 2: Tests of viability performed in the definition, validation and maintenance of a sterilization process. Association for the Advancement of Medical Instrumentation, Arlington, VA, 2014.

[2] Department of Defense. Review Committee Report: Inadvertant Shipment of Live Bacillus Anthracis Spores by DoD. Committee for Comprehensive Review of DoD Laboratory Procedures, Processes, and Protocols Associated with Inactivating Bacillus anthracis Spores. [Online], 13 July 2015, https://dod.defense.gov/Portals/1/features/2015/0615_lab-stats/Review-Committee-Report-Final.pdf.

[3] Rueckert, A.; Ronimus, R.S.; Morgan, H.W. Rapid differentiation and enumeration of the total, viable vegetative cell and spore content of thermophilic bacilli in milk powders with reference to Anoxybacillus flavithermus. *J. Appl. Microbiol*. **2005,** *99* (5), pp 1246–1255.

[4] Martinon, A.; Cronin, U.P.; Quealy, J.; Stapleton, A.; Wilkinson, M.G. Swab sample preparation and viable real-time PCR methodologies for the recovery of Escherichia coli, Staphylococcus aureus or Listeria monocytogenes from artificially contaminated food processing surfaces. *Food Control*. **2012,** *24* (1–2), pp 86–94.

[5] Murray, P.; Rosenthal, K.; Pfaller, M. *Medical Microbiology*, 8th ed; Elsevier Health Sciences: Philadelphia, PA, **2016**.

[6] Wilkinson, M.G. Flow cytometry as a potential method of measuring bacterial viability in probiotic products: A review. *Trends Food Sci. Technol*. **2018,** *78*, pp 1–10.

[7] D'Incecco, P.; Ong, L.; Gras, S.; Pellegrino, L. A fluorescence in situ staining method for investigating spores and vegetative cells of Clostridia by confocal laser scanning microscopy and structured illuminated microscopy. *Micron*. **2018,** *110*, pp 1–9.

[8] Firstencel, H.; Butt, T.M.; Carruthers, R.I. A fluorescence microscopy method for determining the viability of entomophthoralean fungal spores. *J. Invertebr. Pathol*. **1990,** *55* (2), pp 258–264.

[9] Green, L.C.; LeBlanc, P.J.; Didier, E.S. Discrimination between Viable and Dead Encephalitozoon cuniculi (Microsporidian) Spores by Dual Staining with Sytox Green and Calcofluor White M2R. *J. Clin. Microbiol*. **2000.** *38* (10), pp 3811–3814.

[10] Shafaat, H.S.; Ponce, A. Applications of a rapid endospore viability assay for monitoring UV inactivation and characterizing arctic ice cores. *Appl. Environ. Microbiol*. **2006,** *72* (10), pp 6808–6814.

[11] Yang, W.W.; Ponce, A. Rapid Endospore Viability Assay of Clostridium sporogenes spores. *Int. J. Food Microbiol*. **2009,** *133* (3), pp 213–216.

[12] Kalasinsky, K.S.; Hadfield, T.; Shea, A.A.; Kalasinsky, V.F.; Nelson, M.P.; Neiss, J.; Drauch, A.J.; Vanni, G.S.; Treado, P.J. Raman Chemical Imaging Spectroscopy Reagentless Detection and Identification of Pathogens: Signature Development and Evaluation. *Anal. Chem*. **2007,** *79* (7), pp 2658–2673.

[13] Tripathi, A.; Jabbour, R.E.; Treado, P.J.; Neiss, J.H.; Nelson, M.P.; Jensen, J.L.; Snyder, A.P. Waterborne Pathogen Detection Using Raman Spectroscopy. *Appl. Spectrosc*. **2008,** *62* (1), pp 1–9.

[14] Tripathi, A.; Jabbour, R.E., Guicheteau, J.A.; Christesen, S.D.; Emge, D.K.; Fountain, A.W.; Bottiger, J.R.; Emmons, E.D.; Synder, A.P. Bioaerosol Analysis with Raman Chemical Imaging Microspectroscopy. A*nal. Chem*. **2009,** *81* (16), pp 6981–6990.

[15] Cheng, H-W.; Chen, Y-Y.; Lin, X-X.; Huan, S-Y.; Wu, H-L.; Shen, G-L.; Yu, R-Q. Surface-enhanced Raman spectroscopic detection of Bacillus subtilis spores using gold nanoparticle based substrates. *Anal. Chim. Acta*. **2011,** *707* (1), pp 155–163.
[16] Jarvis, R.M.; Brooker, A.; Goodacre, R. Surface-enhanced Raman scattering for the rapid discrimination of bacteria. *Faraday Discuss*. **2006,** *132*, pp 281–292.
[17] Guicheteau, J.; Argue, L.; Emge, D.; Hyre, A.; Jacobson, M; Christesen, S. Bacillus Spore Classification via Surface-Enhanced Raman Spectroscopy and Principal Component Analysis. *Appl. Spectrosc*. **2008,** *62* (3), pp 267–272.
[18] Zhang, P.; Kong, L.; Setlow, P.; Li, Y.Q. Characterization of Wet-Heat Inactivation of Single Spores of Bacillus Species by Dual-Trap Raman Spectroscopy and Elastic Light Scattering. *Appl. Environ. Microbiol*. **2010,** *76* (6), pp 1796–1805.
[19] Wang, S.; Doona, C.J.; Setlow, P.; Li, Y.Q. Use of Raman Spectroscopy and Phase-Contrast Microscopy To Characterize Cold Atmospheric Plasma Inactivation of Individual Bacterial Spores. *Appl. Environ. Microbiol*. **2016,** *82* (19), pp 5775–5784.
[20] Kammrath, B.W.; Koutrakos, A.; Castillo, J.; Langley, C.; Huck-Jones, D. Morphologically-directed Raman spectroscopy for forensic soil analysis. *Forensic Sci. Int*. **2018,** 285, pp e25–e33.
[21] Tripathi, A.; Emmons, E.D.; Wilcox, P.G.; Guicheteau, J.A.; Emge, D.K.; Christesen, S.D.; Fountain, A.W., III. Semi-Automated Detection of Trace Explosives in Fingerprints on Strongly Interfering Surfaces with Raman Chemical Imaging. *Appl. Spectrosc*. **2011,** *65* (6), pp 611–619.
[22] Carpenter, A.E.; Jones, T.R.; Lamprecht, M.R.; Clarke, C.; Kang, I.H.; Friman, O.; Guertin, D.A.; Chang, J.H.; Lindquist, R.A.; Moffat, J.; Golland, P.; Sabatini, D.M. CellProfiler: image analysis software for identifying and quantifying cell phenotypes. *Genome Biol*. **2006,** *7* (10), pp R100.1–R100.11.
[23] Schindelin, J.; Ignacio, A.C.; Frise, E.; Kaynig, V.; Longair, M.; Pietzsch, T.; Preibisch, S.; Rueden,S.; Saalfeld, S.; Schmid, B.; Tinevez, J.Y.; White, D.J.; Hartenstein, V.; Eliceiri, K.; Tomancak, P.; Cardona, A. Fiji: an open-source platform for biological-image analysis. *Nat. Methods*. **2012,** *9*, pp 676–682.
[24] Fatichah, C.; Purwitasari, D.; Hariadi, V.; Effendy, F. Overlapping white blood cell segmentation and counting on microscopic blood cell images. *Int. J. Smart Sens. Intell. Syst*. **2014,** *7* (3), pp 1271–1286.
[25] Jiang, K.; Liao, Q-M.; Dai, S-Y. A novel white blood cell segmentation scheme using scale-space filtering and watershed clustering. In *Proceedings of the 2003 International Conference on Machine Learning and Cybernetics*. 2–5 November 2003; Institute of Electrical and Electronics Engineers, Inc.: Danvers, M.A., 2003; *5*, pp 2820–2825.
[26] Fang, Y.; Chongxun, Z.; Chen, P.; Li, L. White blood cell image segmentation using on-line trained neural network. Presented at the 27th Annual International Conference of the IEEE Engineering in Medicine and Biology, Shanghai, China, **3 Jan 2005**.
[27] Buggenthin, F.; Marr, C.; Schwarzfischer, M.; Hoppe, P.; Hilsenbeck, O.; Schroeder, T.; Theis, F.J. An automatic method for robust and fast cell detection in bright field images from high-throughput microscopy. *BMC Bioinf.* **2013,** *14*, pp 1–12.
[28] Simon, I.; Pound, C.R.; Partin, A.W.; Clemens, J.Q.; Christens-Barry, W.A. Automated image analysis system for detecting boundaries of live prostate cancer cells. *Cytometry*, **1998,** *31* (4), pp 287–294.
[29] Malpica, N.; de Solórzano, C.O.; Vaquero, J.J.; Santos, A.; Vallcorba, I.; García-Sagredo, J.M.; del Pozo, F. Applying watershed algorithms to the segmentation of clustered nuclei. *Cytometry*. **1997,** *28* (4), pp 289–297.
[30] Jung, C.; Kim, C.; Chae, S.; Oh, S. Unsupervised segmentation of overlapped nuclei using bayesian classification. *IEEE Transactions on Biomedical Engineering*. **2010,** *57* (12), pp 2825–2832.
[31] Tscherepanow, M.; Zöllner, F.; Hillebrand, M.; Kummert, F. Automatic segmentation of unstained living cells in bright-field microscope images. In *Advances in Mass Data Analysis of Images and Signals in Medicine, Biotechnology, Chemistry, and Food Industry*: Third International Conference, MDA 2008, Leipzig, Germany, 14 July 2008; Perner, P., Salvetti, O. Eds.; Springer: Berlin, 2008; pp 158–172.
[32] Jones, C.L.; Lonergan, G.T.; Mainwaring, D.E. The use of image analysis for spore counts of white-rot fungi. *Biotechnol. Tech*. **1992,** *6* (5), pp 417–422.
[33] Korsnes, R.; Westrum, K.; Fløistad, E.; Klingen, I. Computer-assisted image processing to detect spores from the fungus pandora neoaphidis. *MethodsX*. **2016,** *3*, pp 231–241.
[34] Oh, K.; Chen, Y.; Matsuoka, H.; Yamamoto, A.; Kurata, H. Morphological recognition of fungal spore germination by a computer-aided image analysis and its application to antifungal activity evaluation. *J. Biotechnol*. **1996,** *45* (1), pp 71–79.
[35] Perner, P.; Jänichen, S.; Perner, H. Case-based object recognition for airborne fungi recognition. *Artificial Intelligence in Medicine*. **2006,** *36* (2), pp 137–157.

[36] Xu, P.; Li, J. Computer assistance image processing spores counting. Presented at the 2009 International Asia Conference on Informatics in Control, Automation and Robotics, Bangkok, Thailand, 1–2 February 2009.
[37] Wagner, J.; Macher, J. Automated spore measurements using microscopy, image analysis, and peak recognition of near-monodisperse aerosols. *Aerosol Sci. Technol*. **2012,** *46* (8), pp 862–873.
[38] Nasr-Isfahani, S.; Mirsafian, A.; Masoudi-Nejad, A. A new approach for touching cells segmentation. In *Proceedings of the First International Conference on BioMedical Engineering and Informatics (BMEI 2008), Volume I*, Sanya, China, 27–30 May 2008; Peng, Y., Zhang, Y., Eds.; the IEEE Computer Society: Los Alamitos, CA, 2008; pp 816–820.
[39] Bengtsson, E.; Wählby, C.; Lindblad, J. Robust cell image segmentation methods. *Pattern Recognition and Image Analysis*. **2004,** *14* (2), pp 157–167.
[40] Meijering, E. Cell segmentation: 50 years down the road. *IEEE Signal Processing Magazine*. **2012,** *29* (5), pp 140–145.
[41] Beucher, S.; Meyer, F. The morphological approach of segmentation: the watershed transformation. In *Mathematical Morphology in Image Processing, 1st Edition*; Dougherty, E.R., Ed.; Optical Engineering Series; Marcel Dekker, Inc.:New York, 1993; 34, pp 433–481.

Epigenetic "memory" during bacterial adaptation to environmental changes

Alena M. Calm[a], Gabrielle M. Rizzo[b], Trevor G. Glaros[a], Henry S. Gibbons[a]*
[a]U.S. Army Combat Capabilities Development Command Chemical Biological Center, Research & Technology Directorate, 8198 Blackhawk Rd, Aberdeen Proving Ground, MD 21010
[b]Excet, Inc., 6225 Brandon Ave Ste 360, Springfield, VA 22150

ABSTRACT

Bacteria encounter numerous stresses in the environment for which they must respond rapidly and appropriately to in order to ensure survival. *Salmonella typhimurium,* an enteric bacterium, survives a variety of hostile environments in the stomach, intestinal tract, and gastric-associated lymphoid tissue during infection by coordinating and modulating gene expression patterns critical for survival. We hypothesized that *S. typhimurium* retains epigenetic "memories" of prior growth conditions that influence virulence gene expression even upon transfer to a new environment, and that these heritable DNA methylation patterns, epigenetic mechanisms, or both, affect protein expression long after any triggering stimulus is removed. Using a simple *in vitro* model of adaptation to intracellular conditions, we asked whether protein expression patterns differed after bacterial populations grown in a different media were shifted to a common medium. Using high-coverage liquid chromatography-tandem mass spectrometry-based proteome analysis, we compared an abundance of proteins from cultures originally grown in Luria-Bertani broth and high-Mg^{2+} minimal media and subsequently transferred to a liquid culture continuously grown in low-Mg^{2+} medium. We have sought over the past year to generate and stabilize baseline protein expression levels in unshifted cultures. We report baseline stability of the proteome over multiple passages, and now establish a basis dataset against which shifted cultures may be compared. Enteric pathogens represent a significant impediment to battlefield readiness—understanding the effects of culture conditions prior to infection on the expression of virulence factors may provide insights into the infectious process and yield new forensic biomarkers that facilitate differentiation of lab-grown from wild-acquired bacterial infections.

Keywords: epigenetics, *Salmonella typhimurium,* virulence factors, microbial forensic signatures, proteomics, DNA methylation, serial passage

1. INTRODUCTION

During the life and infection cycle of bacterial pathogens, sudden changes in the ambient environment are routine, resulting in metabolic, physical, and oxidative stresses on the organism as it transits from one environmental niche to another. The Enterobacterium *Salmonella enterica* serovar Typhimurium—commonly referred to as *S. typhimurium*—has served as a robust, well-characterized model organism for both intestinal and systemic infection modes, mimicking the symptoms and disease course of Typhoid fever in the mouse model.[1] During the course of infection, *S. typhimurium* must pass from the extremely acidic environment of the stomach to the basic, oxygen-poor, microbe-rich and hyperosmotic environment of the intestinal tract, and finally to the hostile, acidic, magnesium (Mg^{2+})-depleted, iron-poor, and inherently antimicrobial environment of the macrophage phagolysosome.[2] In addition to its life cycle in the mammalian host, *S. typhimurium* encounters many external environmental stresses, as it can persist in soils and infect plant leaves, seeds, and fruits.[3] Throughout this cycle, the organism survives by coordinating gene and protein expression patterns to ensure rapid and appropriate adaptation to new environments. The orderly progression during the mammalian infection cycle is likely to contrast dramatically with the highly variable outdoor environment, in which the passage from one condition may be seemingly random as a bacterium encounters nutrient-rich conditions, predation by amoeba, infection of alternative vertebrate hosts, dilute and ion-poor conditions, etc. Thus, it is likely that coordinated gene expression patterns during a given stage of mammalian infection might be influenced by previous conditions, thereby decreasing the likelihood of triggering a niche-inappropriate pattern of gene expression during subsequent phases of infection. We hypothesized *S. typhimurium* preserves a "memory" of previous growth conditions that can influence subsequent gene and protein expression patterns. Here, we report elevated expression of several proteins in the *S. typhimurium* chemotaxis and motility system that is detectable over

at least 10 doublings following a shift from growth in two different media into a single common medium. If confirmed during the upcoming project period, we believe that this observation would represent the first report of potential long-term hysteresis or "memory" in the chemotaxis signaling pathway.

2. MATERIALS AND METHODS

2.1 Culturing and passaging

S. typhimurium strain SL1344 was streaked out onto Luria-Bertani broth (LB) agar and incubated overnight at 37 °C. From the plate, a single colony was selected and used to inoculate 10 mL cultures in 50 mL conical tubes (CELLTREAT®, Inc.) in triplicate. The following media was used for three different culture conditions in triplicate: LB, and two variations of N-minimal medium:[4] high-magnesium (HMg) containing 100 mM HEPES pH 7.5, 10 mM $MgCl_2$, 1X N-minimal salts, 0.1% casamino acids, 0.4 % glucose; and low-magnesium (LMg) containing 100 mM MES pH 6.0, 8 µM MgCl2, 1X N-minimal salts, 0.1 % casamino acids, 0.4 % glucose). The cultures were incubated at 300 rpm and 37 °C. After 24 hours in culture, 10 µL of each culture were used to inoculate a fresh 10-mL culture in the same media (1:1,000 dilution). Cultures were grown as before. After 24 hours in culture, all tubes were collected and centrifuged at 4,000 rpm (3,320 x g) on a table-top centrifuge for 20 minutes. All pellets were suspended in 25 mL LMg media, centrifuged as before, and suspended in 10 mL of LMg media. 250 µL of the washed bacteria were then used to inoculate 250 mL of LMg media in 1-L Nalgene® non-baffled plastic flasks with vent cap (Thermo Fisher Scientific, Inc.; Waltham, MA), in triplicate. They were cultured as before, but the agitation was adjusted to 250 rpm in a floor-model shaking incubator. After 24 hours, all cultures were collected by centrifugation and washed 3 times in sterile phosphate buffered saline (PBS) (Thermo Fisher Scientific, Inc.; Waltham, MA). Before the last wash, cultures were split 5 ways so that for each replicate there were 5 x 50 mL tubes of washed bacteria. A 1.8-mL tube was also collected for each replicate for use in the QIAGEN® AllPrep® purification. All of the collected samples were centrifuged and the pellets were snap frozen on liquid nitrogen and stored at -80 °C. The tubes were all labeled to capture their replicate number as well as their original culture condition and how many times they were passaged into LMg media (i.e., LB1 P_0, LB2 P_0, LB3 P_0, LMg 1 P_0, etc.). In two experiments, cultures were collected after the first transfer into LMg-minimal media (P_0). In a third experiment, cultures were passaged four times (to P_4) in the LMg media. In the latter case, cultures were diluted 1:1,000 every 24 hours by transferring 250 µL of the culture directly into the fresh medium without washing. Cultures were not washed between passages, and a 1:1,000 dilution passage was performed into fresh media. Cultures were always grown for 24 hours between passages.

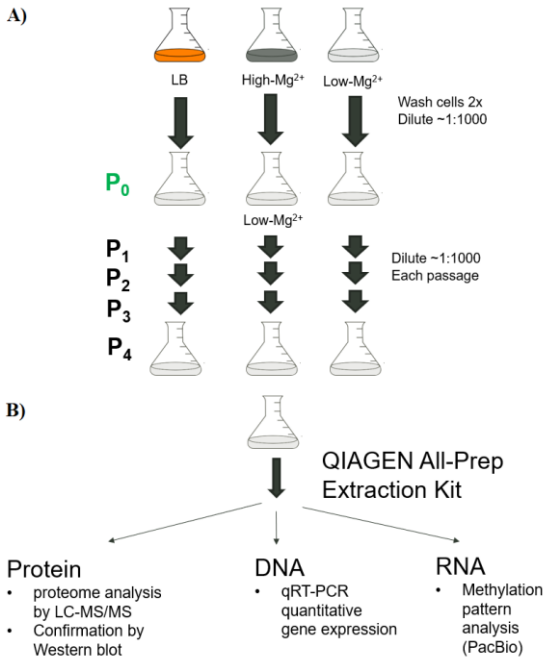

Figure 1. Experimental scheme. A) Growth and passaging scheme for *S. typhimuirium* cultures. B) Single sample utilized for extraction of nucleic acids and proteins.

2.2 Extraction of nucleic acids and protein

The AllPrep® Bacterial DNA/RNA/Protein Kit (QIAGEN®) was utilized for the extraction of protein and nucleic acids from bacterial cell cultures. A 1.8 mL sample of culture was collected, centrifuged, and pellets were snap frozen and stored at -80 °C. Tubes were thawed and re-suspended according to the manufacturer's instructions. All purified samples were collected and stored at -80 °C.

2.3 Cell lysis for proteomic analysis

Bacterial pellets were each resuspended in 500 µL of lysis buffer (4 % SDS [Sigma-Aldrich®; St. Louis, MO] + 25 mM Tris HCl pH 7.6 [Bioland Scientific, LLC; Paramount, CA]), then transferred into Eppendorf® LoBind protein tubes and boiled at 95 °C for 5 minutes. Each sample was then lysed using a Branson probe sonicator set at 50 % power with a pulse setting of 5 seconds on, 5 seconds off, for a total of 25 seconds. Lysates were then clarified via centrifugation at 21,130 x g for 10 minutes, and the clarified lysates were transferred into new Eppendorf® LoBind tubes. The protein concentration of each sample was determined using a Pierce™ BCA® protein assay kit, and 1 mg was removed from each sample for digestion.

2.4 Filter-aided sample preparation digestion

Dithiothreitol (DTT) (Sigma-Aldrich®; St. Louis, MO) was added to each sample to a final concentration of 10 mM. Samples were then boiled at 90 °C for 15 minutes, then cooled to room temperature. Amicon® 15 mL 10 K molecular weight cut-off filter units were pre-washed with 4 mL UA buffer (8 M urea [Thermo Scientific™] + 100 mM Tris HCl pH 8.6 [Bioland Scientific, LLC; Paramount, CA]) and spun down at 3,220 x g for 20 minutes. The 1-mg samples were then transferred into respective filter units. 10 mL of UA buffer were added to each unit, and they were spun for 30 minutes. 100 µL of 0.5 M iodoacetamide (Sigma-Aldrich®; St. Louis, MO) were added to each filter, and the samples incubated in the dark at room temperature for 30 minutes. Filter units were then centrifuged for 20 minutes, then washed two times with 4 mL of UA buffer and centrifuged for 20 minutes both times, to remove iodoacetamide. Following the second rinse, 4 mL of 0.1 M triethylammonium bicarbonate (TEAB) (Sigma-Aldrich®; St. Louis, MO) was added to each filter and centrifuged for 20 minutes. This wash step was repeated 2 times. Lyophilized trypsin (Promega Corporation; Madison, WI) was resuspended to a concentration of 1 µg/µL in 50 mM TEAB and 17 µL was deposited into each 1 mg sample for a protein:enzyme ratio of ~60:1. The top of each filter unit was wrapped in Parafilm® M and incubated overnight at 37 °C.

2.5 Desalting and creating master mix sample

The next day, the filter units were cooled to room temperature and the filtrates were transferred to separate Eppendorf® LoBind tubes. Each filter was then rinsed with 50 µL of 50 mM TEAB twice and 50 µL of 0.5 M NaCl (Sigma-Aldrich®; St. Louis, MO) once. Each rinse was pooled together with their respective sample, and then each sample was acidified with 10 % formic acid to a final concentration of 1 %. Oasis HLB 1-cc 30 mg SPE cartridges (Waters Corporation; Milford, MA) were used for desalting. The cartridges were attached to a vacuum apparatus and activated by adding 1 mL of activation buffer (50 % water + 50 % acetonitrile (ACN)); the activation step was repeated once more. The columns were then washed twice each with 1 mL of wash buffer (5 % ACN + 0.5 % trifluoroacetic acid in water) and each column was then loaded with their respective sample. Columns were then rinsed twice with wash buffer, followed by elution with 1 mL of elution buffer (70 % ACN + 30 % water). Eluents were collected in clean Eppendorf® LoBind tubes and 30 µL of each desalted eluent was taken and combined into a master mix tube. The master mix is intended to normalize samples across all 5 passages in order to form a vertical comparison of P_0–P_4. All samples, including the master mix, were dried down in a Savant™ SpeedVac™ (Thermo Fisher Scientific, Inc.; Waltham, MA) and resuspended in 30 % ACN + 70 % water to ~2 mg/mL (estimated concentration based on initial protein assay results). A Thermo Scientific™ Pierce™ Quantitative Colorimetric Peptide Assay kit was used to assess peptide concentration of each sample. 30 µg of each sample was transferred into Eppendorf® LoBind tubes and 30% ACN + 70% water was added to each sample to reach 45 µL total volume. An additional 5 µL of 1 M TEAB was then added to each sample for a final concentration of 30 µg in 50 µL. For the master mix sample in particular, 12 of these 30-µg aliquots were made.

2.6 Tandem mass tag labeling

The 30-µg aliquots were each labeled using a 5 mg Thermo Scientific™ TMT10plex™ Isobaric Label Reagent Set following the manufacturer's instructions. Briefly, each tag was resuspended in 256 µL of 100 % ACN (DriSolv®),

and 20 µL of each tag was mixed with its corresponding sample (see labeling scheme, Figure 2). For the master mix sample, all 12 aliquots were labeled in this fashion; 5 master mix aliquots were then paired with each of the 5 passages. After labeling samples in accordance with the manufacturer's instructions, each passage was pooled together. The 5 pools were then dried down.

2.7 Basic reverse phase fractionation

Each pool underwent basic reverse phase fractionation on an XBridge C18 5 µm, 4.6 x 250 mm column (Waters Corporation; Milford, MA). A 65-minute gradient from 100 % mobile phase A (10 % ACN + 90 % water + 20 mM ammonium formate, pH 10) to 100 % mobile phase B (90 % ACN + 10 % water + 20 mM ammonium formate, pH 10) was run, and fractions were collected. Following fractionation, the fractions were concatenated into 3 early "Start" fractions, 28 "mid-phase" fractions, and 5 late "End" fractions. These fractions were acidified with 100 µL of 10 % formic acid, then dried down and resuspended in 20 µL of 5 % ACN + 0.1 % formic acid in water, and finally transferred into autosampler vials. The three "Start" fractions and five "End" fractions were combined into respective vials, for a total of 30 samples. This was repeated for all five passage pools.

2.8 Q Exactive™ analysis

The 30 fractions of each passage (a total of 150 fractions) were analyzed on a Thermo Scientific™ Q Exactive™ Plus mass spectrometer on a Thermo Scientific™ EASY-Spray™ column (PepMap RSLC C18, 2 µm, 100 Å, 75 µm x 50 cm). Each fraction was run on a 182-minute gradient from 95 % buffer A (0.1 % formic acid in water) to 90 % buffer B (80 % ACN + 90 % water + 0.1 % formic acid), and then back to 95 % buffer A. Full MS resolution was set at 70,000 with a scan range of 300–1,700 *m/z*, and data-dependent MS/MS resolution was set at 35,000.

2.9 Data analysis

The proteomics data software PEAKS® Studio 8.5 (Bioinformatics Solutions, Inc.; Waterloo, ON, Canada) was used to process the 150 raw files collected from P_0–P_4 MS analysis. The master mix sample from each passage was used to normalize data between passages to create a vertical comparison between them. The LMg sample from P_0 was used as the base sample, and the LMg channel 129C from P_0 in particular was used as the reference label, so that all expression ratios compare the HMg and LB media conditions of every passage to the LMg media condition from P_0. ANOVA-significant proteins (with false-discovery rate set to 1 %) were selected and their expression levels were monitored within each media type and through each passage.

2.10 Methods for sample prep and analysis of P_0 triplicates

Two additional sets of P_0 bacterial pellets were processed as described above. These P_0 samples were not passaged further, and so a master mix sample was not assembled for them. The two P_0 sets were labeled with two separate Thermo Scientific™ TMT10plex™ Isobaric Label Reagent Sets and were compared to the P_0 pellets from the P_0–P_4 sample set. To perform this comparison, the master mix channel 131 was removed from the data analysis software, so that only the triplicates of LMg, HMg, and LB conditions were observed in each P_0. ANOVA-significant proteins (with a false-discovery rate of 1 %) that showed a 2-fold or greater expression change when comparing LB or HMg media to LMg media were selected. These proteins were further filtered to include only those that were present in all three P_0 sets, as they were presumed to be the most highly reproducible. These proteins' expression patterns were then observed in the larger P_0–P_4 data set.

3. RESULTS

To test our hypothesis, we designed a simple *in vitro* experimental scheme (Figure 1) in which bacterial populations grown in several media types were passaged into a low-Mg^{2+} medium that is designed to mimic phases of the host infection cycle.[5] Briefly, the laboratory strain of *S. typhimurium* SL1344 was grown in rich medium (LB) and in two variants of a glucose minimal medium containing either mM or µM concentrations of Mg^{2+} (HMg and LMg media, respectively). In addition to the variance in Mg^{2+} concentrations, the HMg media is also moderately alkaline (pH 7.5), whereas the LMg medium is moderately acidic (pH 6.0). The HMg medium represses genes involved in the intracellular lifecycle, whereas the LMg media condition mimics the phagolysosomal life stage of *S. typhimurium.* During its intracellular stage, the bacterium encounters an environment rich in antimicrobial compounds—including

antimicrobial peptides, reactive oxygen, and nitrogen species—and poor in divalent cations, iron, and other important nutrients. Micromolar concentrations of Mg^{2+} are known to induce expression of the major intracellular virulence regulon of *S. typhimurium*[5] which is regulated by the PhoP/PhoQ 2-component response regulator system.[6] We passaged all three cultures by diluting 1:1,000 into LMg, grew them for several generations to optical densities (OD_{600}) of 0.3–0.5, and examined their protein profiles by LC-MS/MS-based proteomics.

We previously reported the development of an isobaric tagging method based on tandem mass tagging (TMT) labeling (Figure 2). This technique allows us to quantitate simultaneously the abundance of proteins in three biological replicates in each of three experimental conditions. A "master mix" was generated by mixing equal amounts of all samples from a single experiment together. The abundance of a given protein in each individual sample was normalized to the abundance in the "master mix."

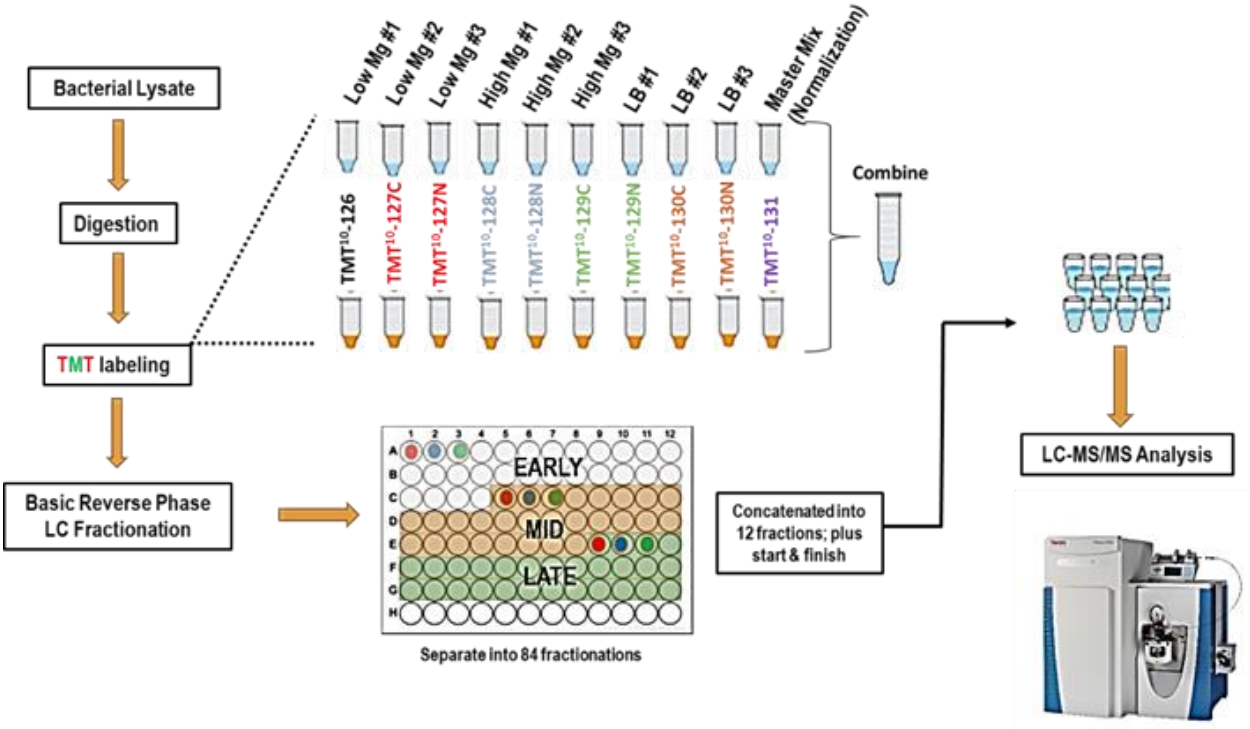

Figure 2. Proteomic extraction, labeling, and analysis pipeline.

Previously, we had reported a set of six proteins whose expression appeared to shift under the passage scheme outlined in Figure 1. Most of these proteins were either structural or regulatory components of the chemotaxis/motility system of *Salmonella*, which raised the possibility that this system was indeed differentially expressed. We sought to confirm the abundance of these proteins in extracts using Western blots. The blots from that experiment revealed significant problem with one of the passages that skewed the results (not shown). We proceeded to repeat the experiment with the goal of confirming the earlier results and providing the orthogonal verification that biochemical analysis would provide.

In this experiment, shown in Figure 3, many proteins appeared to shift in abundance, which was not explained by any obvious difference in the optical density of the cultures at harvest. Subsequent analysis revealed that one of the sets of biological replicates was significantly altered relative to the other extracts, with altered global mobility and abundance shifts shown by subsequent SDS-PAGE and Western analysis (not shown).

We therefore attempted yet another passaging experiment and analyzed all of the P_0–P_4 fractions that had been initially grown in LMg medium without a shift from LB or HMg medium. We separated proteins by SDS-PAGE and blotted for two constitutively expressed proteins—LpxC and GroEL (Figure 3A). These proteins are not thought to vary during normal growth and served as loading controls; as expected both were evenly expressed across all lanes, consistent with results of a stain for total protein (not shown). In 1D-SDS-PAGE analysis, no differences were noted, suggesting that the number of proteins whose expression changed was quite small. Furthermore, proteomic analysis of the unshifted (LMg) extracts showed very limited changes even when later passages were compared to P_0 (Figure 3B),

with the larger numbers of proteins exhibiting 2-fold changes relative to P_0 at later passages, and with much smaller numbers of proteins showing such shifts when successive passages are directly compared. The identity of proteins that showed a 2-fold trend relative to P_0 are shown in Figure 3C. Importantly, very few proteins showed statistically significant fold-changes. This is expected and provides a baseline against which the pending dataset consisting of the shifted conditions will be compared.

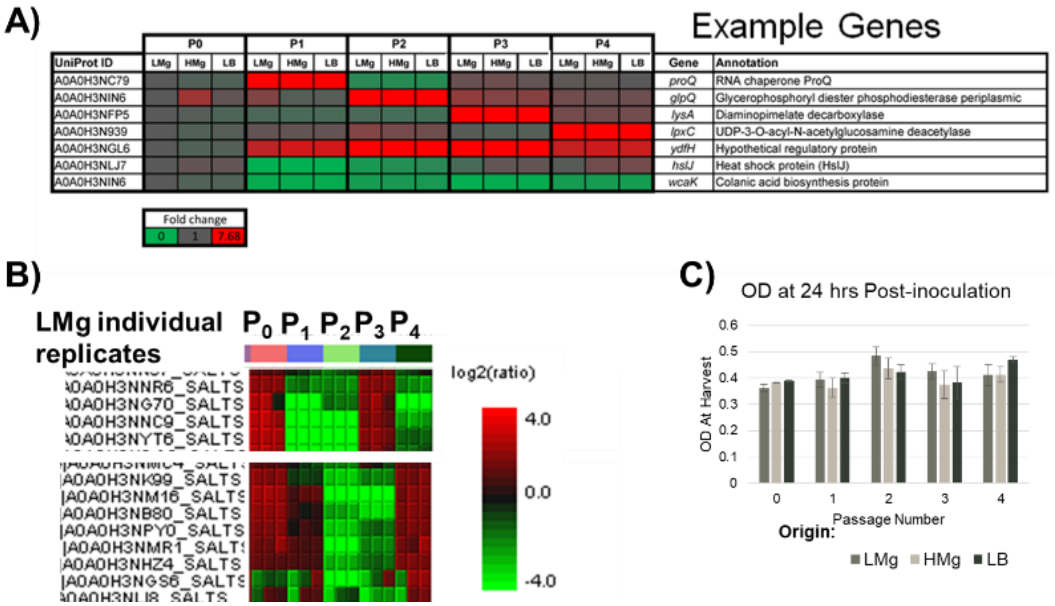

Figure 3. Passage of isolates results in shifting expression patterns in proteins. A) Proteins shown were selected to represent seven different patterns of altered expression. B) Biological replicates from each passage show similar expression levels. C) Culture density at harvest does not vary over multiple passages. Western blot analysis revealed significant deviations in one of the four passages that may have skewed overall results in the experiment, which has since been repeated (see Figure 4).

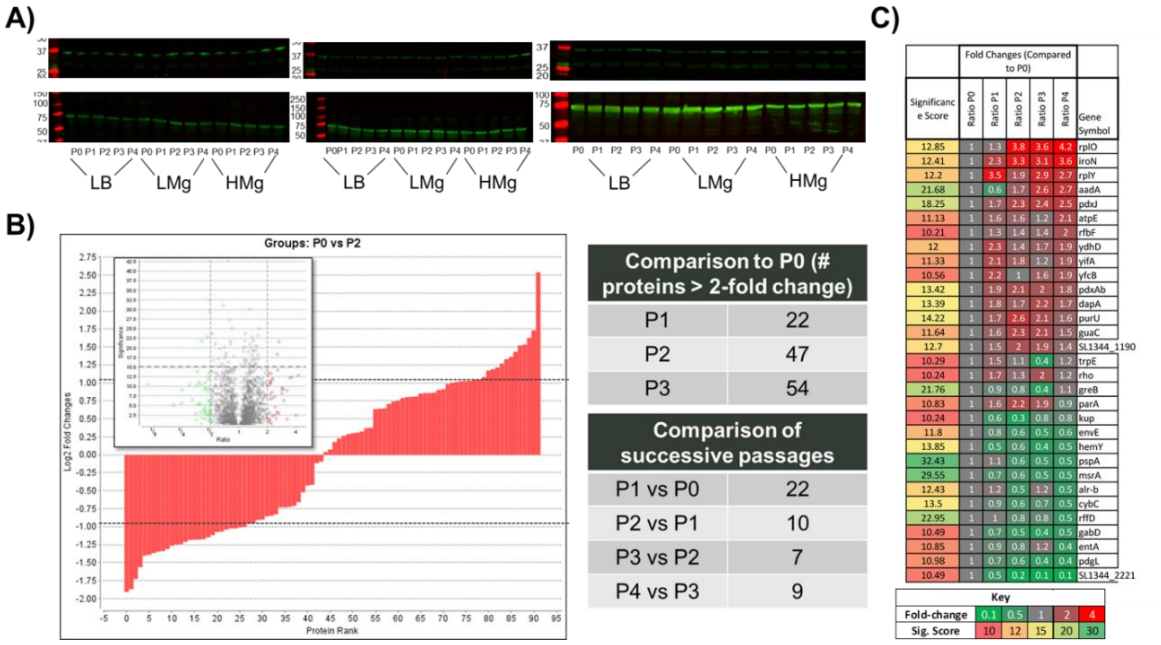

Figure 4. Proteomic analysis of medium shift experiment as of October 2019. A) Western blot analysis of LpxC (top) and GroEL (bottom) across shifts from LB and HMg relative to LMg controls. B) A very small number of proteins shifts abundance in unshifted controls with comparison of passages to P_0 and comparison of successive passages. C) Identities of proteins whose abundance shifts >2-fold and significance scores >10 (equivalent to $p \sim 0.05$) to show potential weak trends. True significant cutoff is at a score of 20 (equivalent to $p = 0.01$).

4. DISCUSSION

Previously, other groups have reported a “memory” or “hysteresis” response in a two-component regulatory system that bacteria use to sense environmental phosphate levels.[7] Cultures starved of phosphate express basal levels of phosphate-sensing system, and exposure to transient high-phosphate conditions triggered elevated expression of the PhoBR system that persisted following removal of phosphate, such that subsequent exposure to a high-phosphate growth condition triggered a quicker response.[8] In the shifted fractions expected to be available, we hope to confirm the results from our initial studies of this system, published in previous reports to this body, which implicated changes to proteins involved in chemotaxis and motility. The previously published work, along with our current work, suggests that the overall signal generated by shifts in medium composition is likely to be small, and may be difficult to distinguish from the baseline with the sensitivity needed.

ACKNOWLEDGMENTS

Funding was provided by the U.S. Army via the In-house Laboratory Independent Research Program (PE 0601101A Project 91A) at the Combat Capabilities Development Command Chemical Biological Center.

REFERENCES

[1] Garai, P.; Gnanadhas, D.P.; Chakravortty, D. Salmonella enterica serovars Typhimurium and Typhi as model organisms: revealing paradigm of host-pathogen interactions. *Virulence.* **2012,** *3* (4), pp 377–388.
[2] Monack, D.M.; Mueller, A.; Falkow, S. Persistent bacterial infections: the interface of the pathogen and the host immune system. *Nat. Rev. Microbiol.* **2004,** *2* (9), pp 747–765.
[3] Silva, C.; Calva, E.; Maloy, S. One Health and Food-Borne Disease: Salmonella Transmission between Humans, Animals, and Plants. *Microbiol. Spectr.* **2014,** *2* (1), pp Oh-0020–2013.
[4] Snavely, M.D.; Gravina, S.A.; Cheung, T.T.; Miller, C.G.; Maguire, M.E. Magnesium transport in Salmonella typhimurium. Regulation of mgtA and mgtB expression. *J. Biol. Chem.* **1991,** *266* (2), pp 824–829.
[5] García Véscovi, E.; Soncini, F.C.; Groisman, E.A. The role of the PhoP/PhoQ regulon in Salmonella virulence. *Res. Microbiol.* **1994,** *145* (5–6), pp 473–480.
[6] García Véscovi, E.; Soncini, F.C.; Groisman, E.A. Mg^{2+} as an Extracellular Signal: Environmental Regulation of Salmonella Virulence. *Cell.* **1996,** *84* (1), pp 165–174.
[7] Bourret, R.B. Learning from Adversity? *J. Bacteriol.* **2017,** *199* (18), pp 1–4.
[8] Hoffer, S.M.; Westerhoff, H.V.; Hellingwerf, K.J.; Postma, P.W.; Tommassen, J. Autoamplification of a two-component regulatory system results in "learning" behavior. *J. Bacteriol.* **2001,** *183* (16), pp 4914–4917.

Effect of toxicants on the regulation of endothelial barrier function

Daniel J. Angelini*, Jennifer R. Horsmon, Amber M. Prugh, Christopher S. Phillips
U.S. Army Combat Capabilities Development Command Chemical Biological Center, Research & Technology Directorate, 8198 Blackhawk Rd, Aberdeen Proving Ground, MD 21010

ABSTRACT

Endothelial cells line the internal portion of the vasculature and are responsible for maintaining homeostasis within the body. This function is accomplished through tightly regulating the passage of both fluid and nutrients from the bloodstream to various tissues. When this regulation is disrupted by inflammation or exposure to specific toxic compounds, fluids and macromolecules accumulate in the surrounding tissues, resulting in edema. This accumulation of fluids is typically regulated through the paracellular pathway, which is defined as the movement of fluids and macromolecules through gaps formed at intercellular junctions. Several chemical warfare agents have been shown to disrupt the endothelium and induce edema following sub-lethal exposures in experimental animals. In these studies, we examined the effects of different toxicants on the immortalized dermal microvascular endothelial cells (HMEC-1). We then compared these results to those obtained from primary cultured microvascular endothelial cells from skin, lung, and heart. This assessment will demonstrate that HMEC-1 could be suitable for assessing the vascular toxicity and allow for more rapidly generated toxicity estimates. The data gathered in this study will provide fundamental knowledge regarding the regulation of endothelial barrier function for both immortalized and primary endothelial cells.

Keywords: barrier function, edema, endothelial cells, paracellular pathway

1. INTRODUCTION

1.1 Endothelial barrier function

Endothelial cells (EC) play a crucial role in maintaining homeostasis; these cells tightly regulate the passage of fluid, nutrients, and immune cells from the intravascular compartment to tissues throughout the body.[1,2] Transendothelial flux of molecules occurs through either the paracellular pathway (intercellular gaps) or the transcellular pathway (transcytosis or vesicular transport). Edema formation, or fluid accumulation within tissues, typically occurs through the paracellular pathway[3]—regulated at the cell-cell level by at least two distinct junctional complexes: adherens junctions (AJ), and tight junctions (TJ).[2] The number of these specific junctions in an EC is dependent on its location within the vascular tree. For example, brain microvascular endothelial cells (MVEC) contain many more TJs than ECs from any other regional vascular bed.[2] AJs and TJs are both tethered to the actin cytoskeleton, but AJs play a prominent role in the regulation of barrier function throughout almost the entire vasculature.[4] AJs consist of the membrane-spanning vascular endothelial (VE)-cadherin, and the cytosolic proteins, α-, β-, γ-, and p120 catenins.[2] The VE-cadherin ectodomain participates in calcium-dependent, homophilic cell-cell adhesion, and is tethered to the actin cytoskeleton through the catenin proteins. Both rapidly acting (e.g., thrombin, histamine) and late acting regulators (e.g., tumor necrosis factor-α (TNFα), endotoxin) of barrier function increase tyrosine phosphorylation of VE-cadherin; these phosphorylation events induce a loss of cell-cell adhesion and actin depolymerization leading to intercellular gap formation and increased paracellular permeability.[2,5,6]

1.2 CWAs and vascular injury

Several chemical warfare agents (CWA)—including nerve agents (e.g., VX) and vesicants (e.g., HD)—have been shown to disrupt the endothelium and induce edema in experimental animals.[7–10] Choking agents, such as chlorine and phosgene, have also been shown to disrupt the endothelial barrier, particularly within the lungs.[11,12] It is interesting to note, that biological toxins of military importance have also been shown to disrupt the endothelial barrier (e.g., ricin and staphylococcal enterotoxin B).[13,14] In many of these cases, it is unknown whether these alterations in endothelial barrier function are due to necrosis/apoptosis or alterations of the EC cytoskeleton. Additional studies are necessary

to address the knowledge gap that exists concerning the mechanisms of action of these compounds/toxins on the endothelium.

2. METHODOLOGY

2.1 Human endothelial cell culture

The human MVEC line HMEC-1[15] was obtained from ATCC® (Manassas, VA) and cultured at 37 °C and 5 % CO_2 in MCDB131 culture media (ATCC®) supplemented with 10 ng/mL epidermal growth factor, 1 µg/mL hydrocortisone, 10 mM L-glutamine, 1 % penicillin-streptomycin, and 10 % fetal bovine serum (all supplements were obtained from ThermoFisher Scientific™; Waltham, MA). Even though this is an immortalized cell line, we only examined these ECs within a 10-passage window. This cell line was chosen due to its EC origin and its usefulness as a generalized MVEC. HMEC-1s have been shown to express all of the typical EC markers, have EC morphology, and form consistent EC barriers.[15] Also, these ECs have been shown to be responsive to classical regulators of endothelial barrier function (e.g., histamine).[15] For comparison, we examined primary MVECs from three different areas of the body that are all major CWA targets: skin (human dermal MVEC, HMVEC-D), lung (human lung MVEC, HMVEC-L), and heart (human cardiac MVEC, HMVEC-C) (Lonza; Walkersville, MD). All primary MVECs were cultured at 37 °C and 5 % CO_2 in Endothelial Cell Growth Medium MV (PromoCell GmbH; Heidelberg, Germany) supplemented with 5 % fetal calf serum, human recombinant epidermal growth factor (5 ng/mL), human recombinant basic fibroblast growth factor (10 ng/mL), insulin-like growth factor (20 ng/mL), human recombinant vascular endothelial growth factor 165 (0.5 ng/mL), ascorbic acid (1 µg/mL), and hydrocortisone (0.2 µg/mL) (all supplements were from PromoCell GmbH). To reduce potential contamination, the media was also supplemented with GA-1000 (125 µg amphotericin B/5 mg gentamicin; ThermoFisher Scientific™). Only primary MVECs from passages 5–10 were used for these studies.

2.2 Preparation of experimental chemicals

Stock solutions of the organophosphate pesticide malathion (ULTRA® Scientific; N. Kingstown, RI) and its metabolite, malaoxon (Sigma-Aldrich®; St. Louis, MO), were prepared (500 mM) in 100 % ethanol (EtOH) and stored at 4 °C.[16] A stock solution of bis(2-chloroethyl)amine hydrochloride (BCAH; Sigma-Aldrich®) was prepared in distilled H_2O (100 mM) and stored at 4 °C for up to 72 hours. A stock solution of lipopolysaccharide (LPS) was prepared in sterile PBS (5 mg/mL), aliquoted, and stored at -20 °C until use.[17]

2.3 Evaluation of endothelial cell viability

EC viability was assessed using an MTT viability assay (Roche Applied Science; Indianapolis, IN) following treatment with increasing concentrations of the experimental compound(s) for 24 hours. This assay was performed as we have previously described.[16,18] Viability results were used to determine the toxicity of the selected compound(s) and indicate the optimal concentrations for examining changes in endothelial barrier function.

2.4 Evaluation of cellular impedance

Cellular impedance was measured using the ACEA xCelligence® Real-Time Cell Analyzer (RTCA) as described.[19,20] HMEC-1, HMVEC-C, HMVEC-D, or HMVEC-L were plated on the specially designed impedance plates and grown to a post-confluent state (72 hours). Once confluent, the ECs were exposed to the selected compound with impedance readings recorded every 15 minutes. Results were reported as normalized cell index (CI). Evidence of endothelial barrier dysfunction was indicated by a decrease in the normalized CI compared to simultaneous media and/or vehicle control.

2.5 Vascular permeability imaging

The *In Vitro* Vascular Permeability Imaging Assay (EMD Millipore; Temecula, CA) was used to image the endothelial barrier dysfunction induced by the selected compound(s). Initially, the surfaces of an 8-well chamber slide (Millicell® EZ Slide; Millipore) were coated with biotinylated-gelatin. The wells of the chamber slide were then sterilized using 70 % ethanol and dried. HMEC-1 or HMVEC-D were cultured at a concentration of ~8 x 10^4 cells/mL on the coated chamber slides. The ECs were then grown to confluence (typically 48–72 hours) then treated with media, malathion (300 µM or 1,000 µM), or malaoxon (300 µM or 1,000 µM) for 24 hours. Following treatment, the media was removed

and the ECs were exposed to a fluorescein-streptavidin reagent for 5 minutes at room temperature to stain the areas of the slide that are not covered by ECs. The chambers were then washed with PBS and fixed with 3.7 % formaldehyde for 30 minutes at room temperature. The ECs were then washed with PBS, counterstained with DAPI, coverslipped, and visualized using a fluorescence microscope. Images were then recorded by a digital camera and processed using ImageJ software (National Institutes of Health; Bethesda, MD).

2.6 Evaluation of cytoskeletal changes

Actin reorganization is a key component of endothelial barrier dysfunction.[2] Several agonists are known to alter the cytoskeleton during loss of barrier function.[6,17,21] Using fluorescence microscopy, we examined filamentous-actin (F-actin) following exposure to the test compounds versus vehicle controls. ECs were grown to confluence on either 4- or 8-well chamber slides (Millicell® EZ Slide) for 48–72 hours and then treated with the compound(s) of interest for 24 hours. Following exposure, the ECs were washed with PBS and fixed with 3.7 % formaldehyde for 30 minutes. Following fixation, the ECs were washed with PBS, permeabilized with 0.5 % Triton X-100 in PBS, and then stained with fluorescein phalloidin (1.65 x 10^{-7} M, 20 minutes at room temperature) as described.[6] The ECs were then counterstained with DAPI, coverslipped, and visualized through a fluorescence microscope.

2.7 Statistical analysis

All quantifiable results are reported as mean ± standard error of the mean. Statistical analysis was performed using GraphPad Prism 8 software (GraphPad Software, Inc.; La Jolla, CA). A one-way analysis of variance (ANOVA) was used to compare the mean responses among the experimental and control groups. The Dunnett's multiple comparisons test was used to determine whether significant differences between groups existed. A *p*-value of <0.05 was considered significant.

3. DATA

3.1 Effect of malathion/malaoxon on MVEC viability

ECs were plated at a density of 5.0 x 10^4 cells/well in 96-well tissue culture plates and allowed to attach for 24 hours. The cells were then exposed to media, vehicle (EtOH), or increasing concentrations of malathion or malaoxon (1–10,000 µM) for 24 hours at 37 °C. The exposures were evaluated using the MTT Viability Assay (Figure 5).

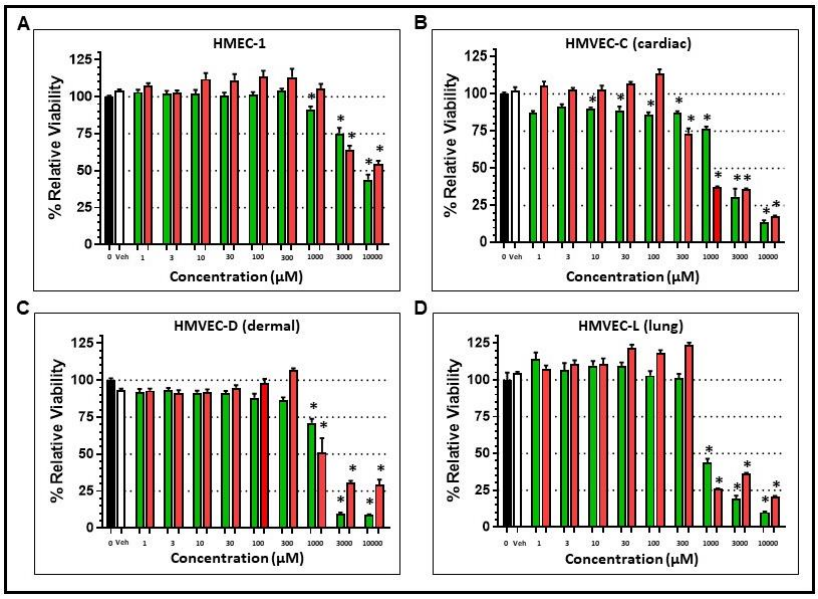

Figure 5. Effects of malathion and malaoxon on MVEC viability. (A) HMEC-1, (B) HMVEC-C, (C) HMVEC-D, and (D) HMVEC-L were exposed to increasing concentrations of malathion (1–10,000 µM; green bars), malaoxon (1–10,000 µM; red bars), media alone (closed bars), or vehicle (EtOH; open bars) for 24 hours. Following exposure, the ECs were assayed for viability using the MTT Viability Assay. The results are reported as mean standard error of the mean (SEM) as % Relative Viability; $n \geq 8$ for each condition tested. *$p < 0.05$ compared to vehicle.

Following exposure to malathion, significant reductions in viability were seen at concentrations ≥1,000 µM in HMEC-1, HMVEC-D, and HMVEC-L. Malathion concentrations as low as 10 µM induced losses in HMVEC-C viability. Treatments with the metabolite of malathion and malaoxon induced reductions in EC viability in concentrations ≥3,000 µM in HMEC-1, but ≥1,000 µM for HMVEC-D and HMVEC-L. HMVEC-C appeared to be the most sensitive to the effects of malaoxon, with ≥300 µM inducing cellular death in these cells.

3.2 Effect of LPS on MVEC viability

ECs were plated at a density of 5.0 x 10^4 cells/well in 96-well tissue culture plates and allowed to attach for 24 hours. The cells were then exposed to media, vehicle (PBS), or increasing concentrations of LPS (0.03–10 µg/mL) for 24 hours at 37 °C. The ECs were evaluated using the MTT Viability Assay. Following exposure to LPS, no concentration of this compound induced any visible cell death in any of the ECs examined (HMEC-1, HMVEC-C, HMVEC-D, HMVEC-L; data not shown).

3.3 Effect of BCAH on MVEC viability

ECs were plated at a density of 5.0 x 10^4 cells/well in 96-well tissue culture plates and allowed to attach for 24 hours. The cells were then exposed to media, vehicle (H_2O), or increasing concentrations of BCAH (0.01–100 µg/mL) for 24 hours at 37 °C. The ECs were evaluated using the MTT Viability Assay (Figure 6). Following exposure to BCAH, significant cell death was seen at concentrations ≥300 µM in HMEC-1. Significant cell death was observed in BCAH-treated HMVEC-D at concentrations ≥100 µM. HMVEC-L appeared to be the most sensitive ECs to BCAH; concentrations ≥10 µM induced significant cell death in these cells.

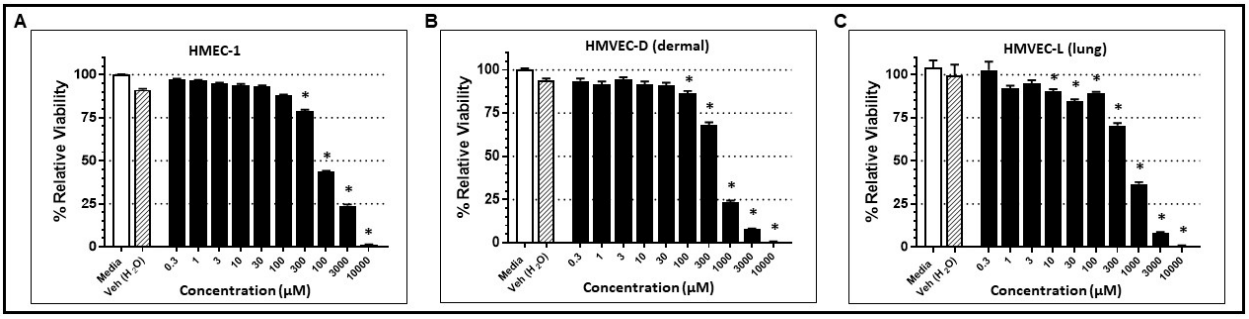

Figure 6. Effects of BCAH on MVEC viability. (A) HMEC-1, (B) HMVEC-D, and (C) HMVEC-L were exposed to increasing concentrations of BCAH (0.03–10,000 µM; closed bars), media alone (open bars), or vehicle (H_2O; cross-hatched bars) for 24 hours. Following exposure, the ECs were assayed for viability using the MTT Viability Assay. The results are reported as mean standard error of the mean as % Relative Viability; $n \geq 8$ for each condition tested. *$p < 0.05$ compared to vehicle.

3.4 Effect of selected toxicants on cellular impedance in HMEC-1

The HMEC-1 cells were grown to confluence on E-Plate® 16s for 72 hours at 37 °C and then exposed to increasing concentrations of malathion (100–300 µM), malaoxon (100–300 µM), LPS (10–3,000 ng/mL), BCAH (0.003–3 mM), vehicle, or media alone for 16 hours. Cellular impedance was measured every 15 minutes, using the ACEA instrument, following the exposures (Figure 7). Reductions in normalized CI were observed following malathion (100 µM) treatment at 5–6 hours post-exposure, while exposures to an increased concentration of malathion (300 µM) induced reductions at 1–3 hours post-exposure (Figure 7A). With both concentrations examined, this loss in normalized CI stabilized between 8–10 hours post-exposure remaining until the end of the experiment. A similar timeline of a reduced normalized CI was observed with both concentrations of malaoxon (Figure 7B), although the reduction was slightly more pronounced with this compound. The effects of LPS on normalized CI were also examined in these cells (Figure 7C). All of the concentrations of LPS (10–3,000 ng/mL) caused a reduction in normalized CI. Reductions were observed at approximately 1–2 hours following initial exposure and never returned to baseline during the 16-hour experiment. When examining the effect of BCAH on HMEC-1s, only concentrations of 1 mM and 3 mM induced any reductions in normalized CI (Figure 7D). Both of these concentrations of BCAH caused cellular death in these cells, suggesting that the observed reduction in normalized CI is due to cell death and not the formation of cellular gaps.

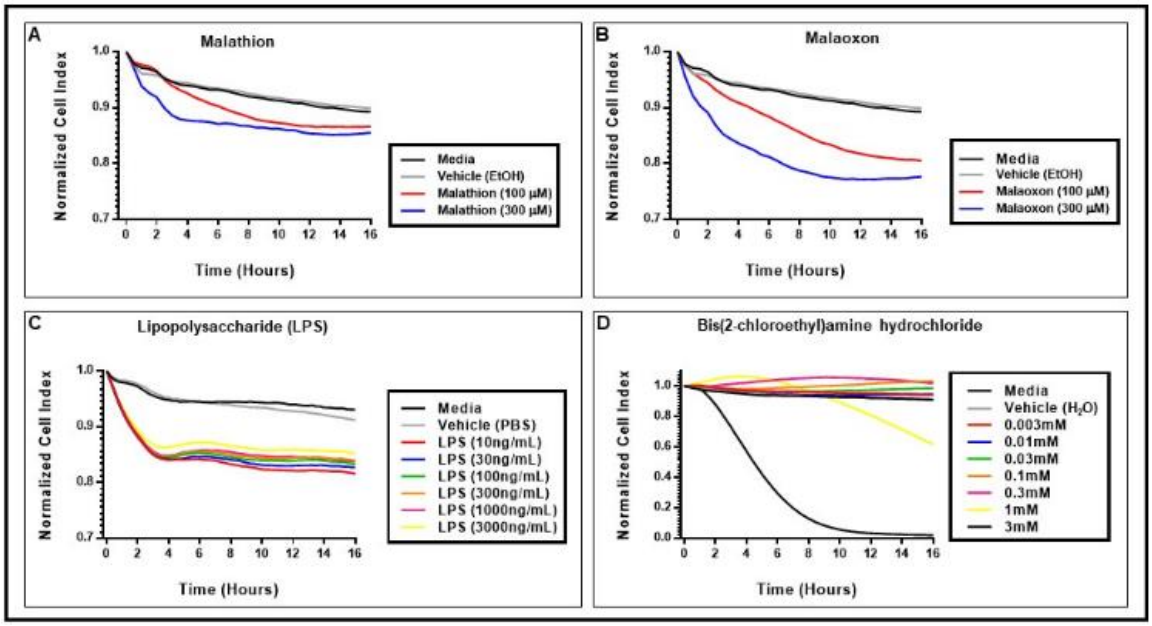

Figure 7. Cellular impedance changes in cultured HMEC-1 following treatment with selected toxicants. HMEC-1 cells were exposed to increasing concentrations of (A) malathion (100–300 µM), (B) malaoxon (100–300 µM), (C) LPS (10–3,000 ng/mL), or (D) BCAH (0.003–3 mM), media alone, or vehicle for 16 hours. The results are expressed as mean of the normalized cell index ($n \geq 5$ for each experimental condition).

3.5 Effect of selected toxicants on cellular impedance in HMVEC-D

The HMVEC-D cells were grown to confluence on E-Plate® 16s for 72 hours at 37 °C and then exposed to increasing concentrations of malathion (100–1,000 µM), malaoxon (100–1,000 µM), LPS (10–3,000 ng/mL), BCAH (0.01– 0.3 mM), vehicle, or media alone for 16 hours. Cellular impedance was measured every 15 minutes following the exposures (Figure 8).

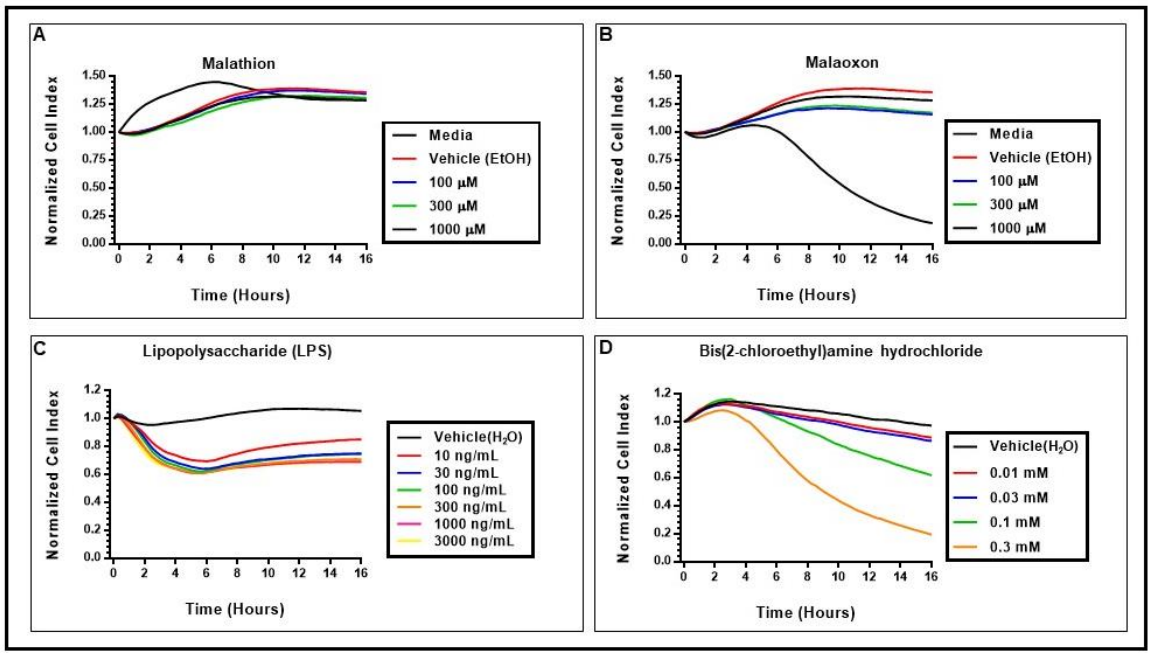

Figure 8. Cellular impedance changes in cultured HMVEC-D following treatment with selected toxicants. HMVEC-D cells were exposed to increasing concentrations of (A) malathion (100–1,000 µM), (B) malaoxon (100–1,000 µM), (C) LPS (10–3,000 ng/mL), or (D) BCAH (0.01–0.3 mM), media alone, or vehicle for 16 hours. The results are expressed as mean of the normalized cell index ($n \geq 6$ for each experimental condition).

Following exposure to malathion or malaoxon, there were no observable reductions in normalized CI with the exception of the 1,000 µM malaoxon exposure (Figure 8A and Figure 8B). This reduction was likely due to the induction of cellular death in response to malaoxon treatment; this concentration of malaoxon reduced cellular viability as shown in the MTT assay (Figure 5). We also examined the effects of LPS (10–3,000 ng/mL) on normalized cell index in HMVEC-D (Figure 8C). The results from these experiments were very similar to those seen with HMEC-1 cells. There was an approximate 1–2 hour time lag following initial exposure and reduction in normalized CI. This reduction lasted several hours and only slightly recovered from peak reductions. As seen with HMEC-1s, there did not appear to be a dose-dependent relationship between LPS and reductions in normalized CI. In addition to malathion, malaoxon, and LPS, we also examined the effect of BCAH (0.01–0.3 mM) on normalized CI (Figure 8D). In these treatments, we did observe a dose-dependence between BCAH concentration and reductions in normalized CI, but these concentrations seemed to correlate with BCAH concentrations that induced cellular death. These results suggest that BCAH does not induce cellular retraction and the formation of intercellular gaps, but alters the endothelial barrier through cell death.

3.6 Effect of selected toxicants on cellular impedance in HMVEC-L

The HMVEC-L cells were grown to confluence on E-Plate® 16s for 72 hours at 37 °C and then exposed to increasing concentrations of malathion (100–1,000 µM), malaoxon (100–1,000 µM), BCAH (0.01–1 mM), vehicle, or media alone for 16 hours. Cellular impedance was measured every 15 minutes following the exposures of the selected toxicants (Figure 9). Similar to HMVEC-D, treatment with malathion or malaoxon failed to reduce the normalized CI with the exception of the 1,000 µM concentration of malaoxon (Figure 9A and Figure 9B). This change appears to be related to the induction of cell death following treatment based on the results of the MTT assay on the cells. Following treatment with BCAH (0.01–1 mM), only a concentration of 1 mM induced any changes in normalized CI. As with malaoxon, this concentration is associated with the loss of cell viability as shown in the previous MTT assays.

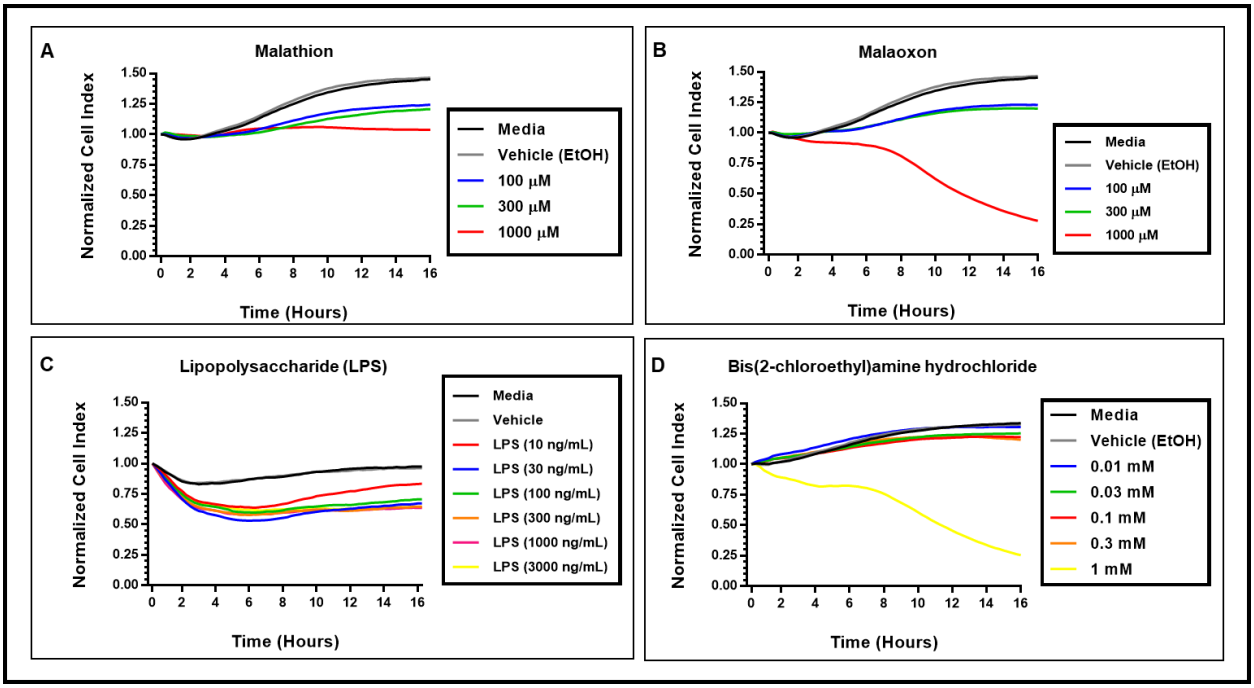

Figure 9. Cellular impedance changes in cultured HMVEC-L following treatment with selected toxicants. HMVEC-L cells were exposed to increasing concentrations of (A) malathion (100–1,000 µM), (B) malaoxon (100–1,000 µM), (C) lipopolysaccharide (LPS, 10–3,000 ng/mL), or (D) BCAH (0.01–0.3 mM), media alone, or vehicle for 16 hours. The results are expressed as mean of the normalized cell index ($n \geq 6$ for each experimental condition).

3.7 Visualization of intercellular gaps

EC retraction and the formation of intercellular gaps is one of the major pathways of barrier disruption. In these experiments, HMEC-1 (Figure 10) or HMVEC-D (Figure 11) were grown to confluence on glass slides that were coated with biotinylated gelatin. The cells were then exposed to malathion (1,000 µM), malaoxon (1,000 µM) or media alone for 24 hours. ECs (either HMEC-1 or HMVEC-D) displayed increased numbers of intercellular gaps with either malathion or malaoxon treatment. In these experiments, there were more intercellular gaps associated with malaoxon treatment compared to malathion treatment.

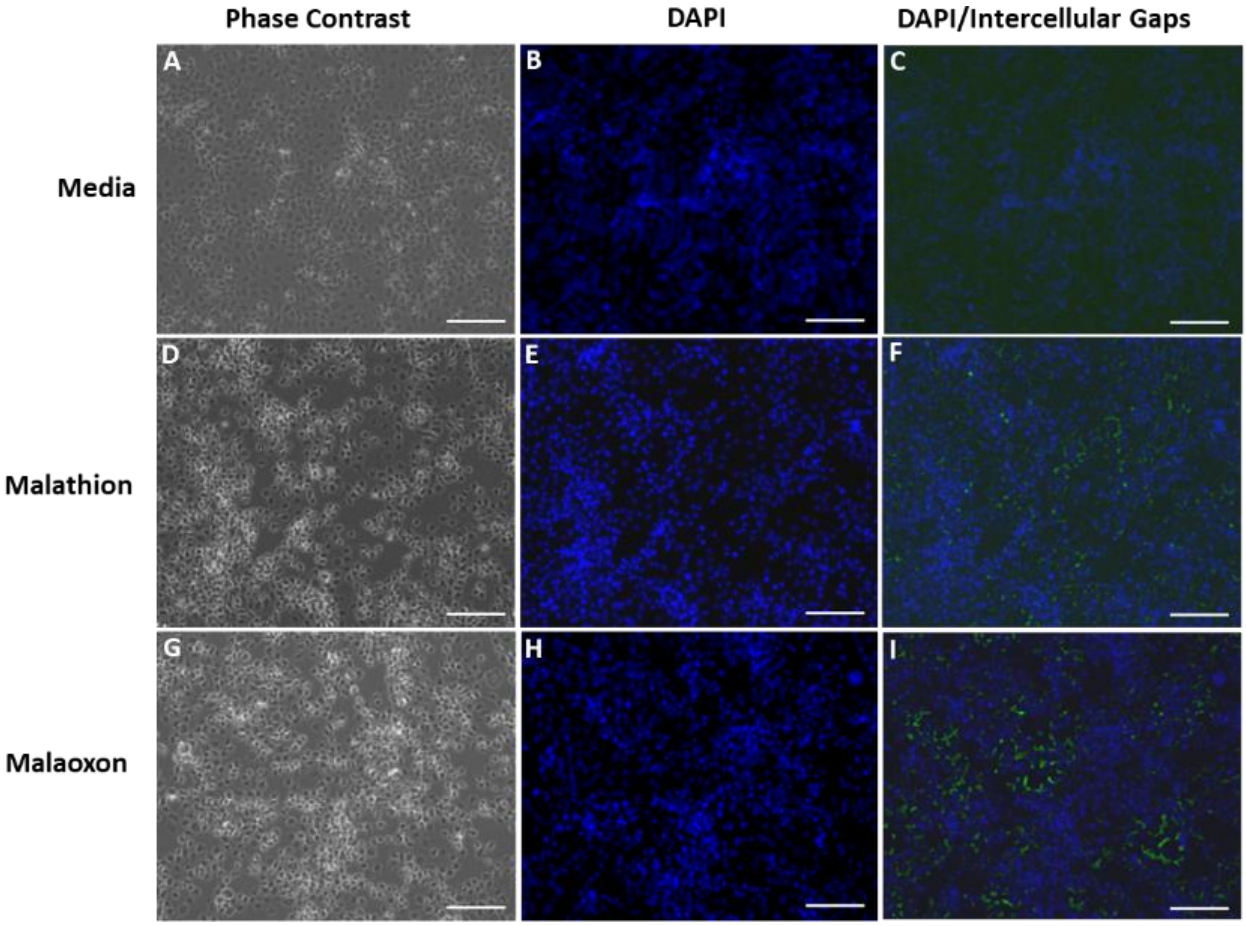

Figure 10. Intercellular gap formation in HMEC-1 following treatment with malathion or malaoxon. Confluent HMEC-1 cells were exposed to (A–C) media, (D–F) malathion (1,000 µM), or (G–I) malaoxon (1,000 µM) for 24 hours.

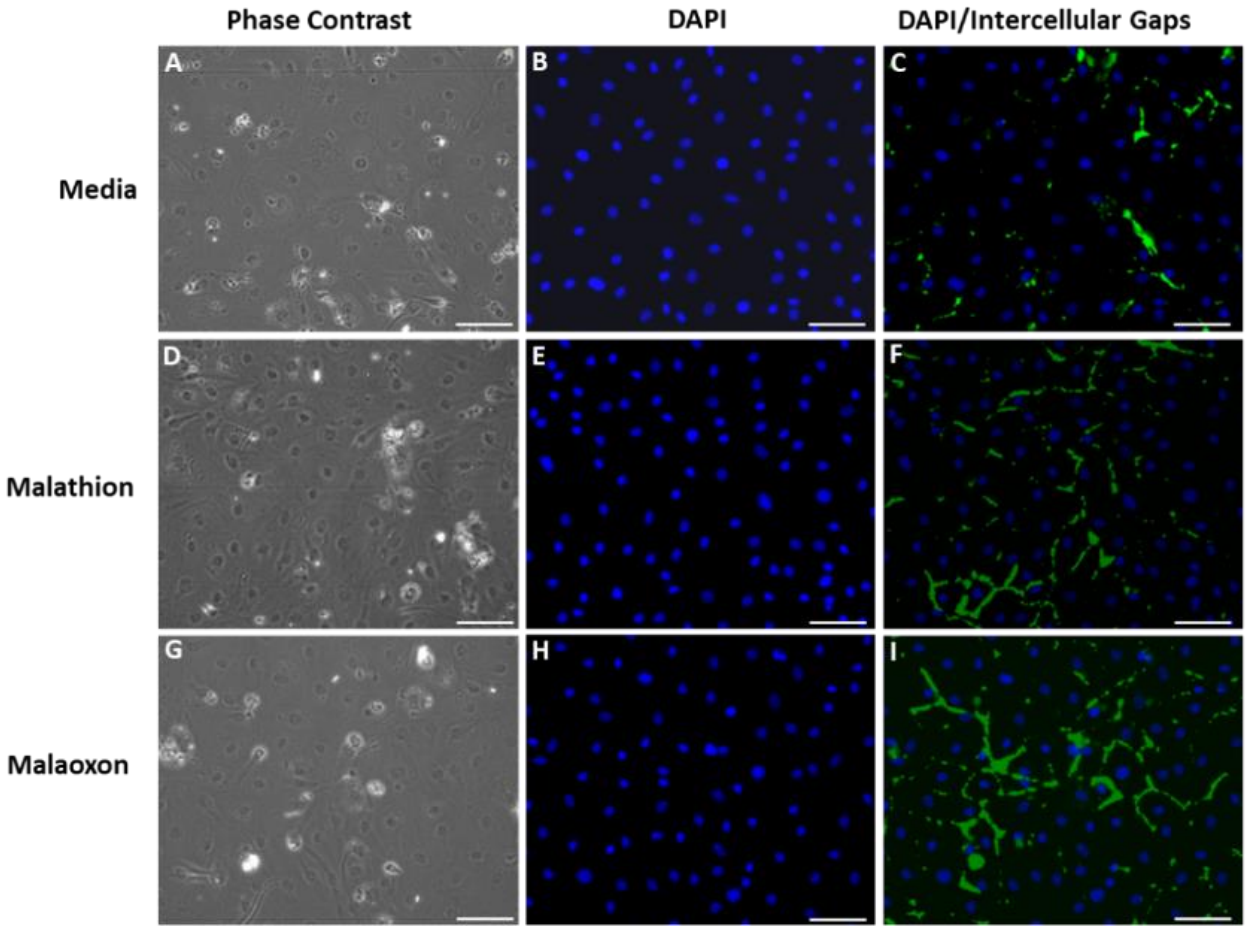

Figure 11. Intercellular gap formation in HMVEC-D following treatment with malathion or malaoxon. Confluent HMVEC-D cells were exposed to (A–C) media, (D–F) malathion (1,000 µM), or (G–I) malaoxon (1,000 µM) for 24 hours.

3.8 Effect of selected toxicants on actin reorganization

Postconfluent HMVEC-D were exposed to malathion (1,000 µM), malaoxon (1,000 µM), or media alone for 24 hours. The monolayers were then fixed, permeabilized, stained with fluorescein-phalloidin, and examined by fluorescence microscopy (Figure 12). The media control ECs contained continuous transcytoplasmic microfilaments and tight cell-to-cell contacts with no intercellular gaps. Malathion- or malaoxon-exposed ECs displayed actin reorganization; exposed ECs had increased expression of actin stress fibers. More stress fibers were observed with malaoxon treatment compared to malathion. In addition, malathion- or malaoxon-exposed EC monolayers displayed intercellular gaps.

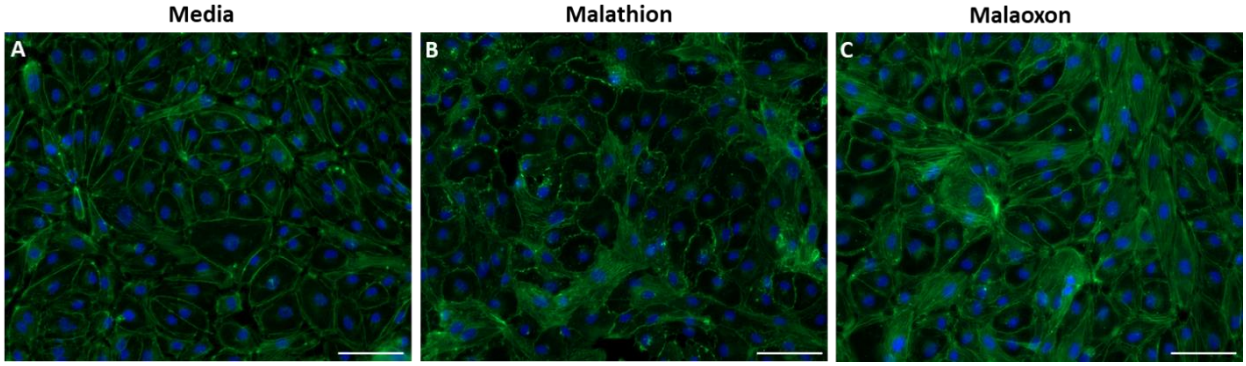

Figure 12. Actin reorganization in HMVEC-D following treatment with malathion or malaoxon. Confluent HMVEC-D cells were exposed to (A) media, (B) malathion (1,000 µM), or (C) malaoxon (1,000 µM) for 24 hours.

4. CONCLUSIONS

In the current study, we have examined the effects of four different toxicants on a MVEC line (HMEC-1) as well a primary MVECs (HMVEC-C, HMVEC-D, and HMVEC-L). Treatment with the organophosphate compounds malathion and malaoxon and the chemotherapeutic compound BCAH induced a dose-dependent reduction in cell viability in all cells examined. Treatment of the MVECs with LPS failed to produce any toxicity at concentrations as high as 10 µg/mL. Overall, it appears that the HMEC-1s are more resistant to the toxic effects of the compounds tested compared to the primary MVECs that were used in this study. In HMEC-1, malathion or malaoxon disrupted the endothelial barrier in concentrations that did not induce cell death. This was different than the primary MVECs examined, wherein only concentrations of malathion or malaoxon that were shown to be toxic caused any changes in barrier function as demonstrated by normalized CI. Our results also show that BCAH only disrupted the endothelial barrier at concentrations that caused cellular death in all cells examined. It is interesting to note that LPS disrupted the endothelial barrier in all MVECs examined in a time-dependent manner. This effect does not appear to be dose-dependent. All concentrations of LPS examined (10–3,000 ng/mL) induced similar reductions in normalized cell index regardless of concentration. Throughout this study, we have observed that HMVEC-C are very difficult to culture and have an extremely limited number of cell doublings. Due to this, we have concluded that these cells should only be used in specific circumstances when trying to answer specific questions regarding the cardiac endothelium.

ACKNOWLEDGMENTS

Funding was provided by the U.S. Army via the In-house Laboratory Independent Research Program (PE0601101A Project 91A) at the Combat Capabilities Development Command Chemical Biological Center. The authors would also like to thank Dr. Augustus W. Fountain, Ms. Rebecca Braun, Dr. Kelly Basi, Dr. Kyle Glover, and Mrs. Davi Kristovich for continued scientific and administrative support.

REFERENCES

[1] Garcia, J.G.; Schaphorst, K.L. Regulation of endothelial cell gap formation and paracellular permeability. *J Investig. Med.* **1995,** *43* (2), pp 117–126.

[2] Sukriti, S.; Tauseef, M.; Yazbeck, P.; Mehta, D. Mechanisms regulating endothelial permeability. *Pulm. Circ.* **2014,** *4* (4), pp 535–551.

[3] Lucas, R.; Verin, A.D.; Black, S.M.; Catravas, J.D. Regulators of endothelial and epithelial barrier integrity and function in acute lung injury. *Biochem. Pharmacol.* **2009**, *77* (12), pp 1763–1772.

[4] Gavard, J. Endothelial permeability and VE-cadherin: a wacky comradeship. *Cell. Adh. Migr*. **2013,** *7* (6), pp 455–461.

[5] Angelini, D.J.; Hasday, J.D.; Goldblum, S.E.; Bannerman, D.D. Tumor Necrosis Factor-α-Mediated Pulmonary Endothelial Barrier Dysfunction. *Curr. Respir. Med. Rev.* **2005,** *1* (3), p 14.

[6] Angelini, D.J.; Hyun, S.W.; Grigoryev, D.N.; Garg, P.; Gong, P.; Singh, I.S.; Passaniti, A.; Hasday, J.D.; Goldblum, S.E. TNF-alpha increases tyrosine phosphorylation of vascular endothelial cadherin and opens the paracellular pathway through fyn activation in human lung endothelia. *Am. J. Physiol. Lung Cell Mol. Physiol.* **2006,** *291* (6), pp L1232–L1245.

[7] Angelini, D.J.; Dorsey, R.M.; Willis, K.L.; Hong, C.; Moyer, R.A.; Oyler, J.; Jensen, N.S.; Salem, H. Chemical warfare agent and biological toxin-induced pulmonary toxicity: could stem cells provide potential therapies? *Inhal. Toxicol.* **2013,** *25* (1), pp 37–62.

[8] Peng, X.; Perkins, M.W.; Simons, J.; Witriol, A.M.; Rodriguez, A.M.; Benjamin, B.M.; Devorak, J.; Sciuto, A.M. Acute pulmonary toxicity following inhalation exposure to aerosolized VX in anesthetized rats. *Inhal. Toxicol.* **2014,** *26* (7), pp 371–379.

[9] Poursaleh, Z.; Ghanei, M.; Babamahmoodi, F.; Izadi, M.; Harandi, A.A.; Emadi, S.E.; Taghavi, N.O.; Sayad-Nouri, S.S.; Emadi, S.N. Pathogenesis and treatment of skin lesions caused by sulfur mustard. *Cutan. Ocul. Toxicol.* **2012,** *31* (3), pp 241–249.

[10] Testylier, G.; Lahrech, H.; Montigon, O.; Foquin, A.; Delacour, C.; Bernabé, D.; Segebarth, C.; Dorandeu, F.; Carpentier, P. Cerebral edema induced in mice by a convulsive dose of soman. Evaluation through diffusion-weighted magnetic resonance imaging and histology. *Toxicol. Appl. Pharmacol.* **2007,** *220* (2), pp 125–137.

[11] Massa, C.B.; Scott, P.; Abramova, E.; Gardner, C.; Laskin, D.L.; Gow, A.J. Acute chlorine gas exposure produces transient inflammation and a progressive alteration in surfactant composition with accompanying mechanical dysfunction. *Toxicol. Appl. Pharmacol.* **2014,** *278* (1), pp 53–64.

[12] Werrlein, R.J.; Madren-Whalley, J.S.; Kirby, S.D. Phosgene effects on F-actin organization and concentration in cells cultured from sheep and rat lung. *Cell Biol. Toxicol.* **1994,** *10* (1), pp 45–58.

[13] Lindstrom, A.L.; Erlandsen, S.L.; Kersey, J.H.; Pennell, C.A. An in vitro model for toxin-mediated vascular leak syndrome: ricin toxin A chain increases the permeability of human endothelial cell monolayers. *Blood.* **1997,** *90* (6), pp 2323–2334.

[14] Campbell, W.N.; Fitzpatrick, M.; Ding, X.; Jett, M.; Gemski, P.; Goldblum, S.E. SEB is cytotoxic and alters EC barrier function through protein tyrosine phosphorylation in vitro. *Am. J. Physiol.* **1997,** *273* (1 Pt 1), pp L31–L39.

[15] Ades, E.W.; Candal, F.J.; Swerlick, R.A.; George, V.G.; Summers, S.; Bosse, D.C.; Lawley, T.J. HMEC-1: establishment of an immortalized human microvascular endothelial cell line. *J. Invest. Dermatol.* **1992,** *99* (6), pp 683–690.

[16] Angelini, D.J.; Moyer, R.A.; Cole, S.; Willis, K.L.; Oyler, J.; Dorsey, R.M.; Salem, H. The Pesticide Metabolites Paraoxon and Malaoxon Induce Cellular Death by Different Mechanisms in Cultured Human Pulmonary Cells. *Int. J. Toxicol.* **2015,** *34* (5), pp 433–441.

[17] Gong, P.; Angelini, D.J.; Yang, S.; Xia, G.; Cross, A.S.; Mann, D.; Bannerman, D.D.; Vogel, S.N.; Goldblum, S.E. TLR4 signaling is coupled to SRC family kinase activation, tyrosine phosphorylation of zonula adherens proteins, and opening of the paracellular pathway in human lung microvascular endothelia. *J. Biol. Chem.* **2008,** *283* (19), pp 13437–13449.

[18] Prugh, A.M.; Cole, S.D.; Glaros, T.; Angelini, D.J. Effects of organophosphates on the regulation of mesenchymal stem cell proliferation and differentiation. *Chem. Biol. Interact.* **2017,** *266*, pp 38–46.

[19] Bischoff, I.; Hornburger, M.C.; Mayer, B.A.; Beyerle, A.; Wegener, J.; Fürst, R. Pitfalls in assessing microvascular endothelial barrier function: impedance-based devices versus the classic macromolecular tracer assay. *Sci. Rep.* **2016,** *6*, pp 1–11.

[20] Ke, N.; Wang, X.; Xu, X.; Abassi, Y.A. The xCELLigence system for real-time and label-free monitoring of cell viability. *Methods Mol. Biol.* **2011,** *740*, pp 33–43.

[21] Young, B.A.; Sui, X.; Kiser, T.D.; Hyun, S.W.; Wang, P.; Sakarya, S.; Angelini, D.J.; Schaphorst, K.L.; Hasday, J.D.; Cross, A.S.; Romer, L.H.; Passaniti, A.; Goldblum, S.E. Protein tyrosine phosphatase activity regulates endothelial cell-cell interactions, the paracellular pathway, and capillary tube stability. *Am. J. Physiol. Lung Cell Mol. Physiol.* **2003,** *285* (1), pp L63–L75.

SSI PROJECTS

Environmental effects on carfentanil binding on surfaces

Monica L. McEntee*, Mark D. Winemiller, Andrew J. Walz, Fu-Lian Hsu,
Amanda M. Schenning, Michelle L. Sheahy, Ivan O. Iordanov, Gregory W. Peterson
U.S. Army Combat Capabilities Development Command Chemical Biological Center, Research & Technology Directorate, 8198 Blackhawk Rd, Aberdeen Proving Ground, MD 21010

ABSTRACT

Drug overdoses involving opioids have risen exponentially for the past decade. One way to combat this opioid crisis is to understand the interactions between opioids and surfaces, which can provide help in other fields in order to develop better decontamination procedures, new antidotes, and protection protocols to help first responders and the Warfighter. One important opioid of interest, carfentanil, was studied here in different environments (solvents and pH) in order to understand how environmental factors affect the binding of carfentanil to a SiO_2 surface. Both the carfentanil citrate salt and freebase showed similar binding uptakes. The results also showed water, chloroform, hexane, and pH buffers ranging from 2–8 did not hinder the uptake of carfentanil citrate salt on SiO_2. However, methanol, ethanol, and isopropanol alcohols all removed carfentanil from the surface. Density functional theory calculations revealed the cohesive energy between water molecules is stronger than water with carfentanil, while the cohesive energy of methanol is closer to the cohesive energy of methanol with the opioid. Thus, carfentanil prefers to interact in the alcohol solution compared to binding to the surface.

Keywords: carfentanil, conformational changes, surface binding, opioid, freebase, salt, nuclear magnetic resonance

1. INTRODUCTION

The opioid crisis has emerged as a growing threat to civilians, first responders, and the military. In 2017, synthetic opioids were the main driver of 47,600 overdose deaths in the United States, which is 67.8 percent of all drug overdose deaths.[1] Maryland, West Virginia, California, Florida, and many other states showed significant (as high as 9.6 percent) increases in drug overdose death rates from 2016 to 2017.[2] Previous and current studies have focused on combating the opioid crisis by trying to hinder opioid binding to pain receptors in the human body.[3,4] Our work takes a different approach and focuses on understanding the interactions between the opioid and surfaces before even coming into contact with the human body.

Janssen et al. developed the synthetic class of fentanyl opioids in the 1960s in order to replace morphine for pain relief.[5–7] Further research led to improved synthesis procedures and the creation of new opioids with varying functions ranging from increased potency to faster onset rates in the body.[8] From there, studies were performed to try and understand how these opioids bind to the μ-, δ-, and κ-opiate receptors in the body.[3,4] Both experimental and theoretical calculations have shown the structural orientation of the opioid can affect how the opioid binds to the receptor site.[4,9] Therefore, understanding the impact of changing the conformational structure on binding and reactivity on surfaces cannot be overemphasized.

The opioid of interest in this study is carfentanil, which is 10,000 times more potent than morphine.[10] Providing a knowledge base about how this opioid interacts in solution and on surfaces can help generate better protection protocols in order to help civilians, first responders, and the military. In our previous work,[11] we studied carfentanil and remifentanil, which has a fast onset time, in water and methanol solutions. The results showed carfentanil produced conformers in water, but not in methanol; on the other hand, remifentanil produced only one structure in solution. Additionally, when comparing the opioid salts to the neutral (freebase) molecules through density functional theory (DFT) calculations, the salts formed stable conformers compared to the neutral molecules in solution.[11] From these results, the uptake was measured of these opioids on a surface, and the update was higher in water than in methanol. Here we try to change the environment of the solution to force the opioid into one structure or the other to compare how each structure would affect binding on the surface. We study the impact environmental factors such as solvents and pH have on opioid binding and reactivity on surfaces in order to see if the conformers change with

environment, which can help in the future understanding of these class of molecules in many different research fields such as synthesis, decontamination, toxicology, aerosols and obscurants, and medicine.

2. METHODS

2.1 Synthesis and characterization of carfentanil in solution

The synthesis procedure for carfentanil salt and freebase were performed from a derivation from the literature[12] and described in more detail elsewhere.[11] Conformational changes in different solvents and pH ranges were measured using nuclear magnetic resonance spectroscopy (NMR). All ^{1}H NMR spectra were recorded on a Bruker Avance III HD 500 MHz instrument and referenced to the residual solvent peaks. A macro was used so that gradient shimming would be performed before the collection of each ^{1}H spectrum after a specified time interval. At the conclusion of a run, another macro was used to process and integrate all the ^{1}H NMR spectra back against the internal standard allowing for a greater number of points to be collected and eliminating bias during analysis. The following pH solutions were used: a pH of 2 solution of HCl was prepared using an Accumet Research AR25 Dual Channel pH/Ion Meter that had been calibrated with Thermo standard solutions at a pH of 4, 7, and 10; all other buffers were prepared to 0.3 M and measured with the pH meter—a pH of 4 was prepared using acetic acid/sodium acetate, a pH of 6 was prepared using acetic acid/ammonium acetate, and a pH of 7.5 was prepared using sodium dihydrogen phosphate/disodium hydrogen phosphate.

2.2 Uptake studies using liquid chromatography-mass spectrometry

Uptake studies were performed by preparing aqueous solutions of carfentanil citrate in water, chloroform, hexane, methanol, ethanol, and isopropanol solvents. Approximately 10 mg of solid material (porous SiO_2) was added to each set of solutions and stirred at ambient temperature for 18–24 hours. The samples were then centrifuged to drive the surface material to the bottom of the vial. The top aqueous portion was pipetted into a vial and transferred into the liquid chromatography-mass spectrometry (LC-MS). A control set of vials was made for carfentanil with no solid material for comparison.

2.3 Density functional theory calculations

Plane wave DFT calculations were done using the Quantum Espresso software package. Core electrons were approximated using projector augmented wave (PAW) pseudopotentials with a 40/400 Ry corresponding wavefunction/electron density cutoff. The exchange correlation was approximated using the Perdew–Burke-Ernzerhof (PBE) functional. All presented structures were geometry optimized with convergence thresholds of $10^{-5}/10^{-4}$ Ry for the energies/forces. All calculations included only the Γ-point due to size constraints.

3. RESULTS AND DISCUSSION

3.1 Environmental effects on carfentanil in solution

Previous studies showed carfentanil salts (both oxalate and citrate salts) in methanol generated only one structure, while the opioid salts in water showed two distinct geometrical structures.[11] Based on these previous findings, carfentanil oxalate in various solvents were studied. Figure 1 (left) shows the NMR spectra of 0.16 M carfentanil oxalate in methanol (black curve), chloroform (red curve), dimethyl sulfoxide (green curve), deuterated water (purple curve), and water (blue curve). The doubling effect of each split peak became more apparent as the polarizability of the solvent increased, which resulted in the presence of a second carfentanil conformer. Before introducing the SiO_2 surface to the solvent solutions, pH effects due to the solvent needed to be understood, which could convolute the results.

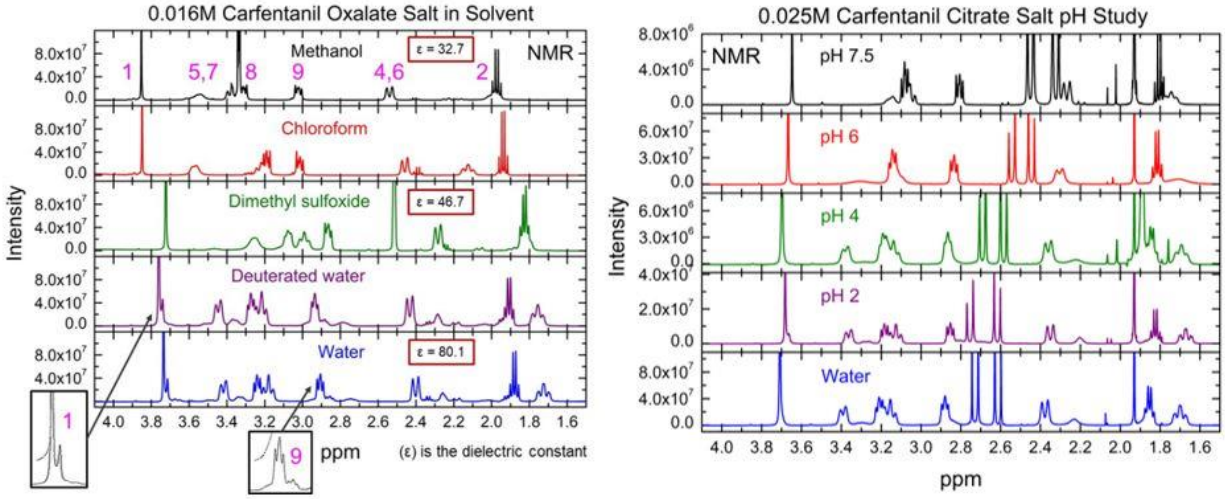

Figure 1. NMR spectra of carfentanil salts in solvent (left) and pH (right) solutions. Left: Carfentanil oxalate (0.16 M) in methanol (black curve), chloroform (red curve), dimethyl sulfoxide (green curve), deuterated water (purple curve), and water (blue curve). This figure is modified from McEntee et al.[11]. Right: Carfentanil citrate (0.25 M) in a solution with a pH of 7.5 (black curve), 6 (red curve), 4 (green curve), 2 (purple curve), and water (blue curve).

Therefore, a pH study was performed using buffer solutions with a pH of 2, 4, 6, and 7.5. Figure 1 (right) shows 0.25 M carfentanil citrate in each pH solution. Previous work has shown the opioid salts behave the same regardless of the salt anion (oxalate, citrate, and HCl).[11] The low pH solutions—2 and 4—show similar results to the opioid in water with two distinct conformers presence in the solution. Interestingly, at pH 6, several of the peaks broadened or even disappeared suggesting one of the conformers became unstable and transformed into the other conformer. At the higher pH of 7.5, the second conformer reemerged at shifted ppm values. The shifts could be due to a new conformer that is different from the previous two conformers or due to interactions with the buffer solution. The cause is still being investigated. The results of the pH study suggest future studies should focus on the uptake of carfentanil at a mid-level pH range of 5–7 on the SiO_2 surface, since only one conformer was observed, compared to the carfentanil uptake at a low pH or in water, which showed two conformers in solution.

3.2 Freebase versus salt uptake on SiO_2

One avenue to take in order to determine if different conformers could affect binding to the surface was to compare the carfentanil salt to the neutral freebase. Previous theoretical calculations proposed the freebase was more labile and preferred to stay as one structure.[11] On the other hand, the salt—with its proton on the nitrogen atom on the piperidine ring of the carfentanil molecule—could have multiple stable conformers at favorable energies at room temperature.[11] Therefore, a study was performed to keep the surface, solvent, concentration of the opioid, and all other parameters constant, and only change the salt to the freebase. Figure 2 shows the uptake of carfentanil citrate and the freebase in two different solutions, a low pH of 1.68 and a 1:1 mixture of pH 1.68/methanol. The green circles show how much opioid was recovered from the solution with the porous SiO_2 present in the solution. In the pH 1.68 solution with SiO_2, all of the opioid was bound to the SiO_2 surface and could not be removed; conversely, with methanol present in the mixture, the majority of the opioid was removed from the SiO_2 surface. As a control, the purple circles show how much opioid was present in the solution with no SiO_2. The results showed binding to the SiO_2 surface was independent of the type of opioid, freebase or salt, and that the solvent played a major role in opioid uptake on the surface. Since the type of opioid did not play a major role in binding and was only theorized to play a large role, further study into the environmental effects on the opioid uptake were explored below in the next sections.

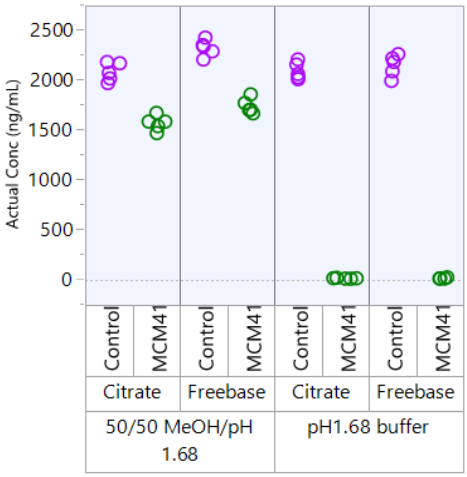

Figure 2. Uptake studies of carfentanil citrate and freebase in either a pH of 1.68 or a mixture of a pH of 1.68/methanol alone (purple circles) or on SiO_2 (green circles).

3.3 Environmental effects on carfentanil binding on SiO_2

After determining that the type of opioid present in solution had no effect on the binding, the next step was to determine if the solvents and pH had any effect on binding as well. Figure 3 illustrates the uptake of carfentanil citrate on the SiO_2 surface (blue circles) in pH buffer solutions ranging from 1.68 to 10 and in various solvents such as hexane, chloroform, deionized water (DIW), and methanol. The control experiments without the SiO_2 surface are depicted with red circles. The red circles shown for carfentanil citrate in a pH 10 solution were unusually low due to the opioid precipitating out of solution at that pH range. Surprisingly, all of the pH and solvent solutions showed that the opioid stayed on the surface, except when methanol was present in the solution. Methanol must have a unique interaction either with the opioid or with the surface that the other solvents did not possess regardless of polarity or pH range. The results from this study confirmed the earlier conclusion that the structure of carfentanil does not affect the binding on the SiO_2 surface.

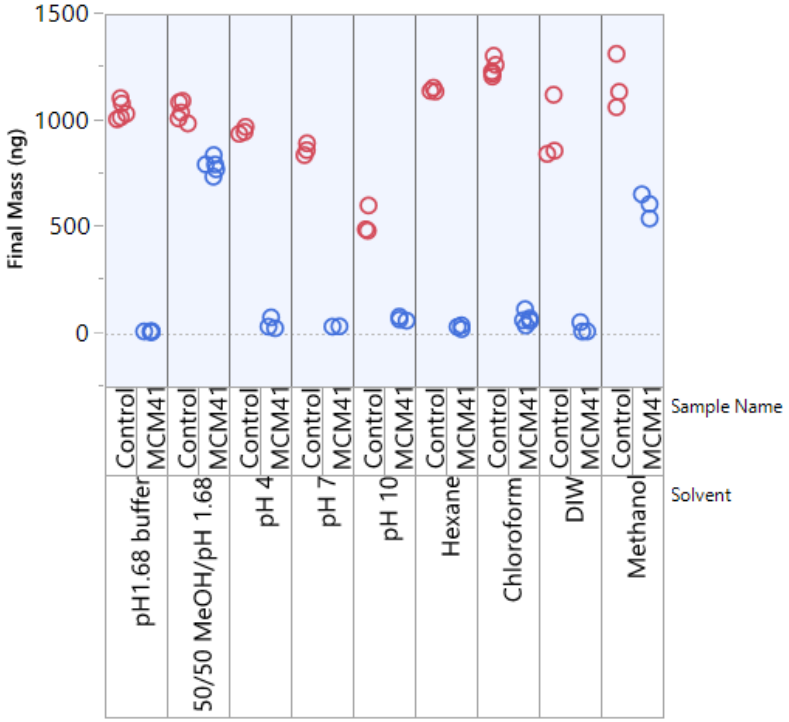

Figure 3. Uptake studies of carfentanil citrate in a pH of 1.68, 4, 7, and 10 solutions and in hexane, chloroform, DIW, and methanol solutions with SiO_2 present (blue circles) and with SiO_2 absent (red circles).

3.4 Passivation verses solubility effects

Since methanol significantly removed carfentanil from the surface, it was important to understand the reason why only methanol had an effect in order to drive future decontamination protocols and procedures. There were two possible reasons for the extraction of the opioid with methanol from the surface: 1) the methanol passivated the surface (i.e., blocked surface sites) or 2) carfentanil citrate was more soluble in methanol than the other solutions studied. A methanol wash step was added to the experimental method procedure to determine if passivation was the leading cause of opioid removal from the SiO_2 surface. The uptake procedure involved washing the dry SiO_2 surface with methanol, evaporating the excess methanol not bound to the surface, and then adding the desired opioid and solvent solution to the surface. The solution was then mixed for 24 hours, centrifuged, and the extractant was placed in the LC-MS for quantitative analysis. Figure 4 shows various solvents and solvent mixtures with both washed and unwashed experiments for comparison. The N/A experiments were the control experiments with the SiO_2 surface absent from the vial. The washed and unwashed experiments showed the same results. Therefore, the methanol did not passivate the surface, and the blocking of surface sites was not the reason for low opioid binding to the surface in the methanol solution.

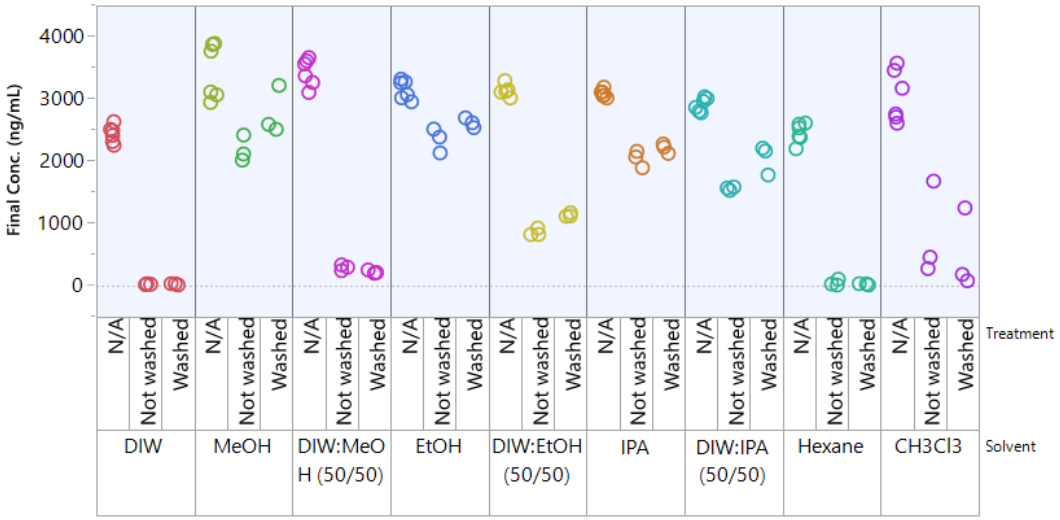

Figure 4. Uptake studies of carfentanil citrate in DIW (red circles), methanol (light green circles), DIW/methanol (magenta circles), ethanol (blue circles), DIW/ethanol (yellow circles), isopropanol (orange circles), DIW/isopropanol (cyan circles), hexane (green circles), and chloroform (purple circles) with SiO_2 present and a wash step, with SiO_2 present without a wash step, and with SiO_2 absent.

The other possible factor for the minimal opioid binding was the solubility of the opioid with methanol. In order to determine if solubility was indeed the cause of less binding, other solvents with similar solubilities with carfentanil should produce the same results. Therefore, other alcohols such as ethanol and isopropanol were studied to not only see if they performed similarly to methanol, but also to see if a trend would emerge as the nonpolar group of the alcohol molecule increased. The uptake results showed all three alcohols performed similarly with very little opioid uptake to the SiO_2 surface (Figure 4). Additionally, the alcohols were mixed with water because these particular alcohols are miscible in water in decreasing order as the nonpolar moiety of the alcohol molecule increases. If the opioid is more soluble in alcohol than water, then the more miscible the alcohol becomes in water, the more interaction the opioid has with the water. Thus, more opioid binding can occur in the water/alcohol mixture. Figure 4 confirmed this trend as the alcohol changed from methanol to ethanol to isopropanol in water, more of the carfentanil citrate was bound to the SiO_2 surface as the alcohol molecule increased in size. The results revealed that solubility plays a large role in the binding of carfentanil to the surface.

3.5 Density functional theory calculations of carfentanil on SiO_2 in solution

DFT calculations were performed to confirm the experimental results as well as provide more insight into why solubility plays such as large role in the binding of carfentanil on the SiO_2 surface. A model system was created of a carfentanil molecule binding to a SiO_2 surface with either water or methanol molecules present in the simulation (Figure 5). The interaction energies were calculated for the whole system and found to be -3.19 eV in water and -3.46 eV in methanol. These energies are similar and do not account for the large opioid binding differences

between water and methanol found experimentally. Thus, the interaction energies for the individual components such as the solvent or surface alone with the opioid were calculated. In order to compare to the total interaction energies, only the solvent molecules that were not bound or dissociated on the surface after relaxation were removed from the simulation (Figure 5). The interaction energies for the opioid and the surface without the solvent present for water and methanol were -1.15 and -1.70 eV, respectively. Furthermore, the interaction energies for the opioid without the surface in water and methanol were -2.28 and -1.73 eV, respectively. These results contradict the experimental results; however, two factors were not accounted for in the calculations. The two factors were the density of the solvent molecules and the solvent-solvent interactions compared to the solvent interactions with the opioid.

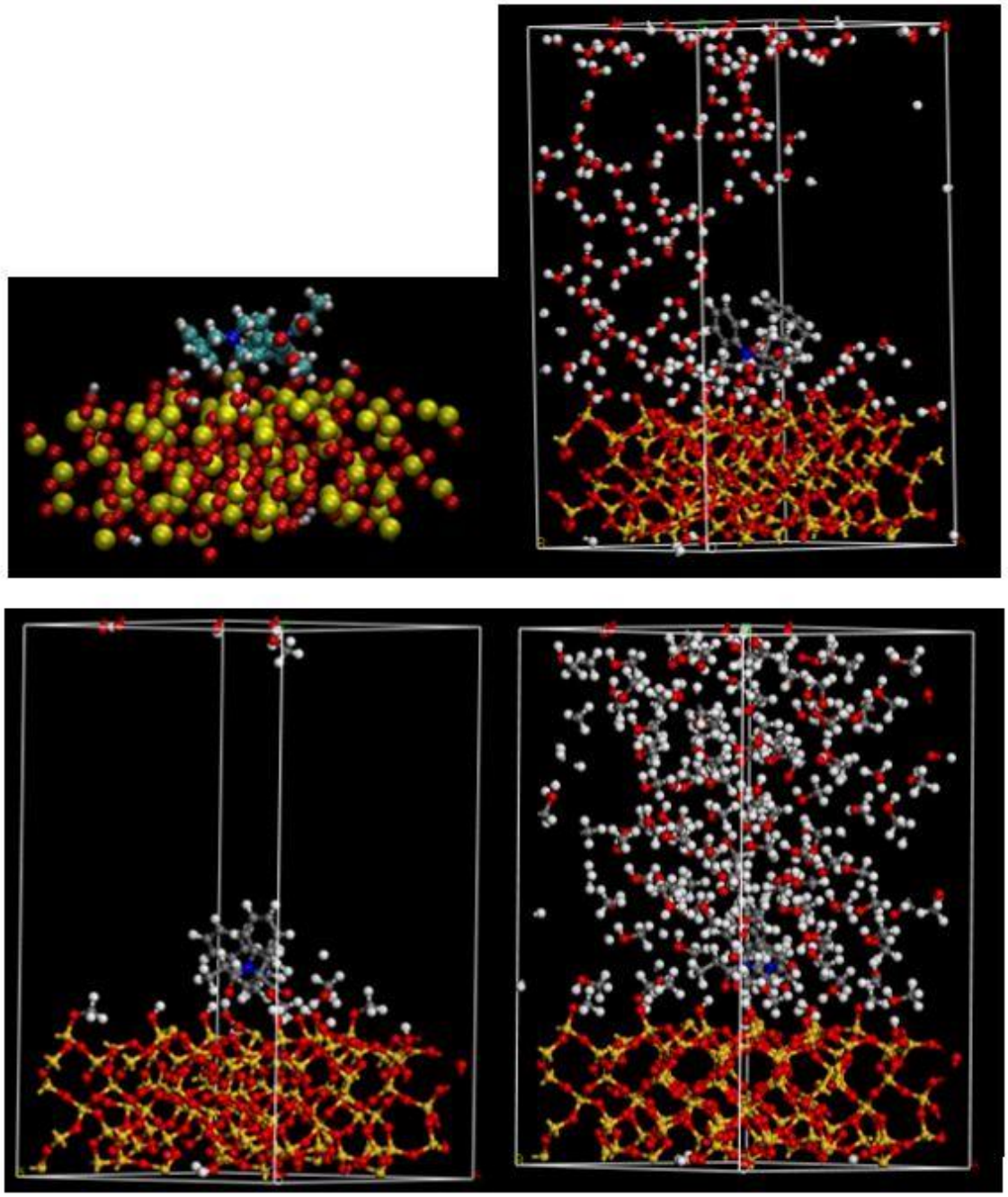

Figure 5. DFT models of a carfentanil molecule bound to SiO_2 in water (top) and in methanol (bottom). (Left) Each system has the solvent molecules that were not bound to the surface removed. (Right) Each system shows all of the components in the model present. The Si, O, C, N, and H atoms are represented in yellow, red, grey, blue, and white, respectively.

The solvent-solvent interactions could play a significant role in the solubility of carfentanil with the solvent. Here, we determined the diameter of one carfentanil molecule and calculated the cohesive energy loss if a sphere of solvent molecules were removed from the solution to accommodate that one carfentanil molecule (Figure 6). The cohesive energy is related to the forces that keep the solvent molecules close together in a condensed state. Thus, the higher the cohesive energy loss, the more the solvent prefers to interact with itself than with the opioid. Figure 6 shows a range of diameters for one carfentanil molecule due its non-spherical shape. The cohesive energy loss for water is in the range of 1–9 eV, and the cohesive energy loss for methanol is in the range of 0.4–3 eV. The significantly higher energy losses for water compared to methanol signify that water prefers to interact with itself more than methanol wants to interact with itself. Additionally, the large cohesive energy loss eV values also overshadow the ~0.5 eV differences in the interaction energies—indicating the cohesive energy is the driving factor for carfentanil binding to the surface in solution. The results confirm that carfentanil is more soluble in methanol than in water, and thus would stay in the methanol solution instead of bind to the SiO_2 surface.

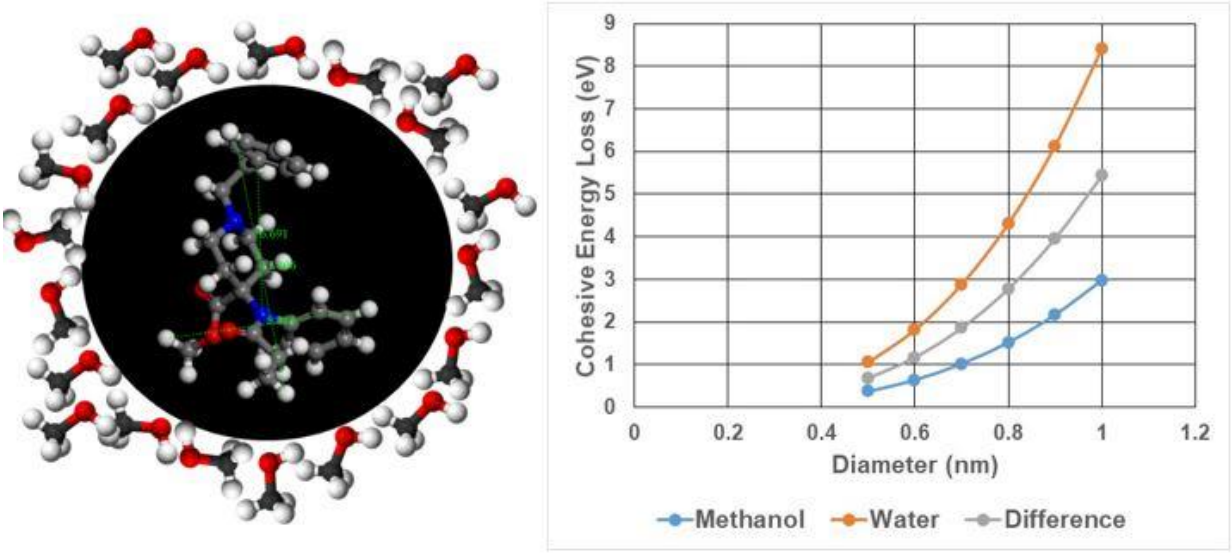

Figure 6. Left: Schematic of one carfentanil molecule surrounded by methanol molecules to represent the amount of cohesive energy loss from one opioid molecule. The O, C, N, and H atoms are represented in red, grey, blue, and white, respectively. Right: Cohesive energy loss (eV) versus the diameter of a carfentanil molecule using methanol (blue curve) and water (orange curve) as the solvents. The grey curve represents the difference between the water and methanol curves.

4. CONCLUSIONS

Carfentanil binds to the SiO_2 surface in solution based on the solubility of the opioid in solvent and not based on the structure or type of the opioid molecule. In solution, the conformational structure of carfentanil changes with both solvent interactions and changes in pH; however, the structural changes are independent of binding to the SiO_2 surface. In polar and nonpolar solvents and a wide range for pH buffers (2–10), carfentanil will bind to the SiO_2 surface, except when alcohols are present. Carfentanil binds less to SiO_2 in the present of methanol, ethanol, and isopropanol. DFT calculations show that the cohesive energy loss is higher for water than for methanol, which shows water prefers to interact with itself compared to methanol interacting with itself. Therefore, the opioid is more soluble in methanol and does not want to bind to the SiO_2 surface.

ACKNOWLEDGMENTS

Funding was provided by the U.S. Army via the Surface Science Initiative Program (PE 0601102A Project VR9) at the Combat Capabilities Development Command Chemical Biological Center

REFERENCES

[1] Scholl L.; Seth P.; Kariisa M.; Wilson N.; Baldwin G. Drug and opioid-involved overdose deaths – United States, 2013–2017. *Morbidity and Mortality Weekly Report.* **2019,** *67* (5152), pp 1419–1427.

[2] Multiple Cause of Death 1999–2017 on CDC Wide-ranging Online Data for Epidemiologic Research (CDC WONDER). Atlanta, GA: CDC, National Center for Health Statistics, **2018**. https://wonder.cdc.gov/wonder/help/mcd.html. (accessed September 28, 2019).

[3] Maguire, P.; Tsai, N.; Kamal, J.; Cometta-Morini, C.; Upton, C.; Loew, G. Pharmacological profiles of fentanyl analogs at μ, δ and κ opiate receptors. *Eur. J. Pharmacol*. **1992,** *213* (2), pp 219–225.

[4] Weltrowska, G.; Lemieux, C.; Chung, N.N.; Guo, J.J.; Wilkes, B.C.; Schiller, P.W. 'Carba'-carfentanil (trans isomer): a μ opioid receptor (MOR) partial agonist with a distinct binding mode. *Bioorg. Med. Chem.* **2014,** *22* (17), pp 4581–4586.

[5] Van Daele, P.G.; De Bruyn, M.F.; Boey, J.M.; Sanczuk, S.; Agten, J.T.; Janssen, P.A. Synthetic analgesics: N-(1-[2-arylethyl]-4-substituted 4-piperidinyl) N-arylalkanamides. *Arzneimittelforschung.* **1976,** *26* (8), pp 1521–1531.

[6] Niemegeers, C.J.; Schellekens, K.H.; Van Bever, W.F.; Janssen, P.A. Sufentanil, a very potent and extremely safe intravenous morphine-like compound in mice, rats and dogs. *Arzneimittelforschung.* **1976,** *26* (8), pp 1551–1556.

[7] Janssens, F.; Torremans, J.; Janssen, P.A. Synthetic 1, 4-disubstituted 1,4-dihydro-5H-tetrazol-5-one derivatives of fentanyl: alfentanil (R 39209), a potent, extremely short-acting narcotic analgesic. *J. Med. Chem*. **1986,** *29* (11), pp 2290–2297.

[8] Feldman, P.L.; Brackeen, M.F. A novel route to the 4-anilido-4-(methoxycarbonyl)piperidine class of analgetics. *J. Org. Chem.* **1990,** *55* (13), pp 4207–4209.

[9] Feinberg, A.P.; Creese, I.; Snyder, S.H. The opiate receptor: a model explaining structure-activity relationships of opiate agonists and antagonists. *Proc. Natl. Acad. Sci. U.S.A.* **1976,** *73* (11), pp 4215–4219.

[10] Stanley, T.H. New developments in opioid drug research for alleviation of animal pain. *J. Am. Vet. Med. Assoc.* **1987,** *191* (10), pp 1252–1253.

[11] McEntee, M.L.; Winemiller, M.D.; Walz, A.J.; Hsu, F-L.; Schenning, A.M.; Sheahy, M.L.; Iordanov, I.O.; Landers, J.M.; Peterson, G.W. Characterization of opioid conformational changes and their effect on binding and reactivity on surfaces. *FY18 Proceedings of the Edgewood Chemical Biological Center In-House Laboratory Independent Research and Surface Science Initiative Programs*; U.S. Army Edgewood Chemical Biological Center: Edgewood, MD, **2019,** pp 69–76.

[12] Walz, A.J.; Hsu, F-L. Synthesis of 4-anilinopiperidine methyl esters, intermediates in the production of carfentanil, sufentanil, and remifentanil. *Tetrahedron Lett.* **2014,** *55* (2), pp 501–502.

Cooperative interactions between functionalized particles and binders in polymer composites and their effect on chemical transport

Mark J. Varady[a]*, Devon A. Boyne[b], Melissa S. Hulet[b], Yossef A. Elabd[c]
[a]U.S. Army Combat Capabilities Development Command Chemical Biological Center, Research & Technology Directorate, 8198 Blackhawk Rd, Aberdeen Proving Ground, MD 21010
[b]Leidos, P.O. Box 68, Gunpowder Branch, Aberdeen Proving Ground, MD 21010
[c]Department of Chemical Engineering, Texas A&M University, College Station, TX 77843

ABSTRACT

Protective coatings on military assets are complex polymer composites consisting of a high loading of several different particle types to achieve the desired coating functionality. The transport properties at the particle-polymer interface can differ significantly from those in the polymer bulk, and when the interfacial regions overlap, undesirably fast chemical transport pathways can open up. Improving the chemical resistance of protective coatings while maintaining the desired properties requires a detailed understanding of how the interface can be tuned to improve the interfacial transport properties. Colloidal force spectroscopy using atomic force microscopy offers a useful technique to study the details of the polymer-particle interaction *ex situ* at the scale of a single particle in the composite system. In this work, the influence of different particle surface modifications—including chemical functionalization and polymer grafting—on the polymer particle adhesion are assessed and corresponding changes in transport properties are measured. We find that modifications to the standard force spectroscopy technique is necessary to ensure that the particle-polymer interface is representative of that in the composite material. Preliminary results for silica-polyurethane composite systems show evidence of increased transport rate in the composite compared to the pure polymer, but further work is needed on modified particle surfaces.

Keywords: transport phenomena, diffusion, polymer composites, atomic force microscopy, colloidal force spectroscopy, interface adhesion, chemical resistance

1. INTRODUCTION

Protective coatings on military assets are complex polymer composites consisting of different solid particle types and sizes bound together by a polymer binder matrix. The particles provide rheology modification for processing and application, required optical and signature management properties of the coating, and camouflage. To achieve all of these functions, the particle (or solids) loading in the polymer binder must be relatively high, up to 60 wt%. In these high-loading composite coatings, it has been observed that the breakthrough of a chemical is significantly faster than the corresponding pure polymer. Since the particles used in these systems are non-porous, this suggests that the transport properties of the polymer are modified by the presence of the particles. At the polymer-particle interface, the arrangement of polymer chains can be different than it is in the bulk, and the nature of the interface is mediated by interactions between the polymer and particle. Thus, to understand and control chemical transport in polymer composites, it is necessary to determine how changes in the polymer-particle interface manifest as changes in the overall transport properties of the system.

Mixed matrix membranes (MMM) for chemical separations and proton and anion exchange membranes for fuel cells are two other industrially significant applications where polymer composites are used in the context of chemical transport. In MMMs, porous materials—such as zeolites and metal-organic frameworks (MOF)—are incorporated into a polymer membrane to improve the membrane permeability and selectivity for a given separations process. Galizia et al. provided a comprehensive overview of MMMs for separation processes.[1] Separation of CO_2/CH_4 mixtures is one application where MMMs have been extensively studied using polyimide-MOF composites.[2,3] In proton and anion exchange membranes, particles are incorporated to improve membrane hydration as well as mechanical and thermal stability.[4] For example, Nafion™-silica nanocomposites have been shown to improve water

retention over pure Nafion™ membranes and increase the operating range.[5] In both chemical separations and ion transport, the importance of tuning the polymer-solid interface to prevent undesirable transport pathways has been noted. Bachman et al. showed that ethane/ethylene separation using composites of 6FDA-DAM polymer with M2(dobdc) MOF was non-selective in cases where there was poor integration of the MOF in the polymer, suggesting undesirable fast transport pathways along the polymer-MOF interface.[6] The interface in MMMs is so important that it has resulted in a review article dedicated solely to the effect of polymer-solid interface on membrane performance and perspectives on improving the interface morphology.[7] Molecular dynamics calculations have also been employed to investigate details of the interface during chemical transport—for example, CO_2 and CH_4 diffusion near a polyimide-zeolite interface.[8]

Details of the polymer-particle interface are difficult to access, and transport properties at the interface are even more difficult. There have been many studies on the effect of the particle-polymer interface on mechanical properties. For example, atomic force microscopy (AFM),[9] nanoindentation,[10,11] and nanoscratch[12] techniques have been used to show that the polymer exhibits different mechanical properties near a solid interface compared to the bulk. Most studies assessing transport properties in polymer composites have focused on the behavior of the overall composite with no detailed study of the interface. Su et al. showed a broadening of the glass transition for polyethylene glycol (PEG)-silica composites with increasing particle loading using differential scanning calorimetry and related this to the permeation behavior of the composite membranes.[13] Another example is the study of gas permeability in composites high free-volume polymers and fumed silica, showing vast increases in permeation with no detailed mechanistic understanding. However, there have been studies using specialized experimental techniques on specially prepared model systems; for example, the use of neutron reflectivity to study changes in polymer morphology and chemical accumulation at interfaces in planar systems.[14,15] Positron annihilation lifetime spectroscopy is another technique that has been used to probe the details of the polymer-solid interface during chemical transport,[16,17] but is available at few laboratories around the world.

Details of the interactions between particles and polymer surfaces have been studied using so-called colloidal force spectroscopy using AFM.[18,19] In colloidal force spectroscopy, a small particle (~1–50 µm diameter) is attached to the end of an AFM cantilever as shown in Figure 1. This particle is brought in contact with the surface, pressed in, then pulled off. During this process, the deflection, δ, of the cantilever is recorded and converted to a force, F, with knowledge of the cantilever spring constant, k ($F = k\delta$). The adhesion between the particle and the surface is captured during the retraction, or pull-off, of the cantilever. Pham et al. examined deformation and adhesion of rubbery polydimethylsiloxane (PDMS) with a silica colloidal probe, and illustrated the need to account for capillary forces due to the liquid-like behavior of the soft PDMS.[20] Feldman et al. measured the adhesion of both polar and non-polar colloidal probes on an array of polymers, providing general suggestions to achieve quantitative data.[21]

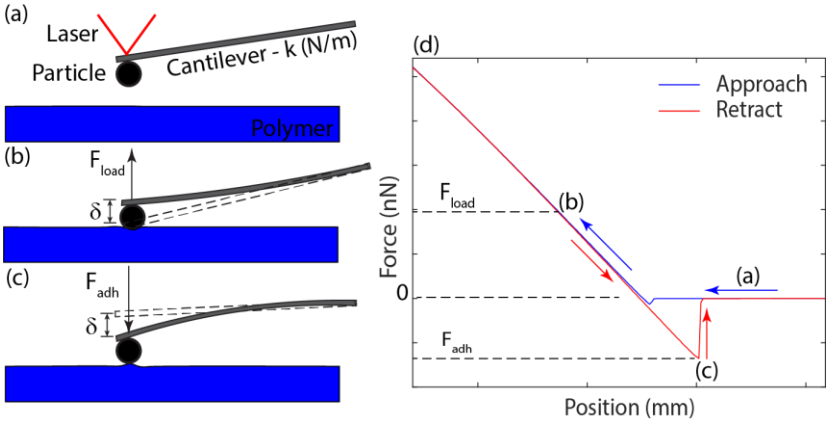

Figure 1. Schematic of colloidal force spectroscopy using an atomic force microscope: (a) the cantilever with attached particle in a retracted (from the surface) position, (b) the particle pressed into the surface resulting in a positive cantilever deflection, and (c) the particle adhering to the surface during pull-off resulting in a negative cantilever deflection. (d) Plot of the force on the particle versus vertical cantilever position.

This work focuses on utilizing the colloidal force spectroscopy technique to characterize the polymer-particle interface and how it changes with different particle surface modifications and chemical exposure. Corresponding measurements of chemical transport through the composite materials are used to correlate changes in the interface to corresponding changes in transport properties. Additionally, chemical imaging techniques are employed to access details of chemical

transport near the particle-polymer interface. The particle surface is modified by functionalizing the surface and by grafting polymers onto the particle surface.

2. METHODOLOGY

2.1 Materials

Polyurethane (PU) and polyhydroxyurethane (PHU) polymers were synthesized by the Combat Capabilities Development Command Army Research Laboratory and described in a previous publication.[22] PDMS was obtained as a two-part kit (Dow Corning Sylgard 184). Polyamic acid solution was obtained from Sigma-Aldrich® (12 wt% in 80 % NMP/20 % xylene).

Silica and functionalized silica particles were obtained from Sigma-Aldrich® (9–13 µm glass spheres) or Polysciences, Inc.® (0.5 µm and 5 µm silica, carboxyl functionalized silica, and amine functionalized silica).

For the PU and PHU films, solutions of 100 mg/mL polymer in cyclopentanone (Sigma-Aldrich®, >99 % purity) were prepared and spin cast onto attenuated total reflectance (ATR) crystals (Pike Technologies™, Germanium 45 deg, 80 mm x 10 mm x 4 mm) or glass slides (Fisher Scientific™, 1-inch diameter). For the ATR crystals, 200 µL of solution were spread onto the ATR crystal and rotated at 300 rpm for 5 minutes in a spin coater (WS-650 Series Spin Processer, Laurell Technologies®). For the glass slides, 200 µL of solution were spread onto the glass slide and rotated at 1,500 rpm for 5 minutes in a spin coater.

For the PDMS films, ten parts A and one-part B by mass were added to hexane (Sigma-Aldrich®, >95 % purity) to obtain a 25 % PDMS/75 % hexane solution by mass. 200 µL of this solution was spread onto the glass slide and rotated at 3,000 rpm for 2 minutes in a spin coater. PU and PHU films were dried in a 70 °C oven at least overnight while PDMS films were dried in a 50 °C oven at least overnight.

Polyimide (PI) films were made by depositing 100–200 µL of polyamic acid solution on a glass slide and spin casting at 820 rpm for 1 minute, followed by baking in a 70 °C oven at least overnight.

Polyaniline (PAni) films were made by dissolving in N-methyl-2-pyrrolidone (NMP) to make a 5 mg/mL solution, then depositing 100–200 µL on a glass slide and spin casting at 1,000 rpm for 2 minutes, followed by baking in a 70 °C oven at least overnight.

Silica-polymer composites were created by dispersing varying masses of 0.5 µm particles in 1 mL of cyclohexanone using a homogenizer (Scilogex D160) operating at ~9,000 rpm for 10 minutes before preparing the 100 mg/mL polymer solutions as described above.

Colloidal AFM probes with bare particles were acquired from AppNano (5 µm silica particle on k ~20 N/m cantilever, ACTA-SiO_2-A). Colloidal probes with functionalized particles were obtained from Novascan Technologies, Inc. (Ames, IA) (~5 µm amine or carboxyl functionalized polystyrene (PS) or silica particle on end of k ~16 N/m cantilever).

2.2 Methods

Imaging and colloidal force spectroscopy were performed with a Nanosurf (Liestal, Switzerland) Flex Axiom AFM equipped with the Advanced Force Spectroscopy software option. Each colloidal AFM probe was calibrated prior to use by using the thermal tuning capability of the instrument to obtain the resonant frequency and spring constant of the cantilever. Additionally, the deflection sensitivity (relating photodetector voltage to cantilever deflection) of each colloidal probe was obtained by measuring the photodetector voltage as a function of z-position as the colloidal probe is pressed into a rigid silicon wafer. Both the cantilever spring constant and deflection sensitivity are required for obtaining quantitatively accurate measurements of the particle-polymer interaction force. Standard force spectroscopy was performed by approaching the colloidal probe to the polymer surface using default settings, performing a 2 µm indentation over 1 second followed by a pull-off over 1 second. Modifications to the standard force spectroscopy procedure were also investigated and are described in the Results and Analysis section.

Details of the chemical breakthrough experiments have been described in previous publications.[22] Briefly, a controlled vapor concentration was created by flowing dry N_2 gas through a custom blown, glass saturator cell (Glassblowers.com, Inc., Turnersville, NJ) that was saturated with the desired liquid chemical. The vapor

concentration delivered (i.e., effective partial pressure or activity) was modulated by combining the saturated vapor flow with dry N_2 and setting the corresponding mass flow controllers in the desired ratio with a total flow rate of 50 SCCM in all cases. This flow was passed over the top of the polymer-coated ATR crystal and IR light was shone through the backside of the crystal, creating an evanescent wave at the polymer-crystal interface. Monitoring the intensity of the reflected IR light as a function of wavelength allows the presence of species with corresponding absorption bands to be detected. Because the evanescent wave penetrates less than 600 nm into the polymer, this measurement only detects species near the polymer-crystal interface. Integration over the absorption band(s) corresponding to a particular species of interest allows quantification of the amount of species absorbed as a function of time.

3. RESULTS AND ANALYSIS

3.1 Particle-polymer adhesion

Initial force spectroscopy experiments were performed for PS particles (bare, COOH, and NH_3 functionalized) on PU, PHU, PAni, and PI polymers. Each particle-polymer combination was measured for three different samples, and each sample was measured at 16 equally spaced points on a 100 µm x 100 µm grid. The adhesion and snap-in forces obtained from these experiments are plotted in Figure 2.

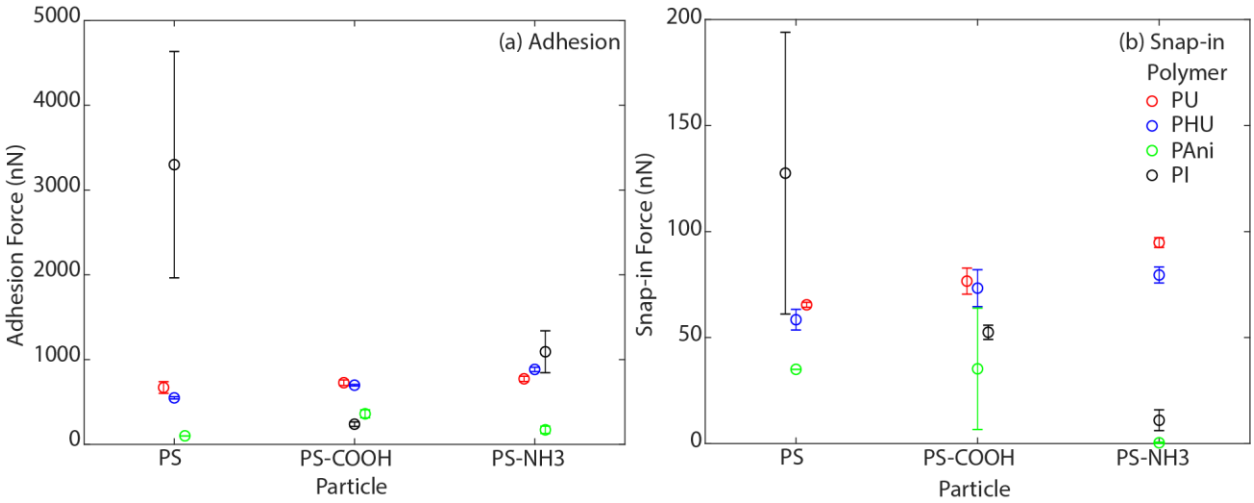

Figure 2. (a) Adhesion and (b) snap-in forces between PS and functionalized PS particles and different polymer surfaces: PU (red), PHU (blue), PAni (green), and PI (black).

Besides the large adhesion force observed for the pure PS particle on PI, there was not a lot of differentiation between the adhesion forces for different particle functionalizations. This result was unexpected and led to questioning whether the particle-polymer interface in the standard force spectroscopy experiment was truly representative of the corresponding interface in the polymer composite.

In typical polymer composites, the particles are put into solution with the polymer, cast into the desired form, then dried to remove the solvent, leaving the polymer composite. In this process, the interface between the particle and polymer naturally evolves as the solvent is removed from the mixture. By simply bringing an external particle into contact with the polymer surface, the interface formed is not necessarily the same, and the measured adhesion forces are not the same as they would be in the composite. Several options were explored for ensuring that the polymer-particle interface in the force spectroscopy experiments was representative of the interface in the composite materials.

The first option was to bring the colloidal probe into contact with a thin-film polymer solution and allow the solvent to evaporate. As long as the particle maintains contact with the polymer solution throughout the drying process, the resulting interface should be equivalent to that of the actual composite material. Thus, the force required to pull the particle out of the cured polymer should be an accurate representation of the particle-polymer adhesion force in the composite. Figure 3 shows a schematic of the process with an optional step for exposing the system to penetrant vapor prior to performing the pull-off test.

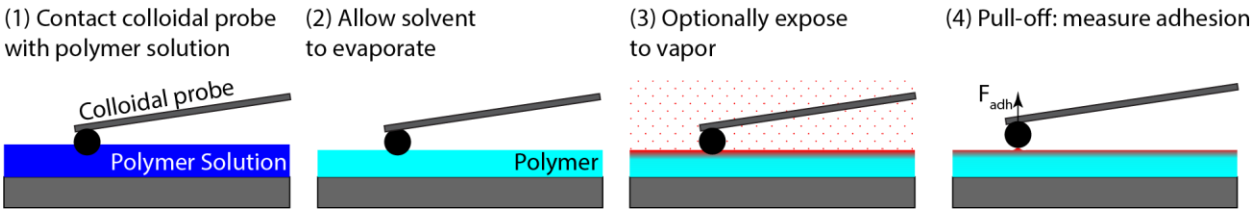

Figure 3. Modification of force spectroscopy in which a colloidal probe is brought into contact with a polymer solution and the solvent is driven off with the particle in contact. Optional vapor exposure before pull-off is also shown.

This procedure was employed for 5 µm silica colloidal probes (Novascan Technologies, Inc.) and PDMS-hexane solutions, allowing the solvent to evaporate 24–72 hours before performing pull-off. The results were variable with the most common difficulty being the colloidal probe losing contact with the polymer solution before complete drying occurred. In this case, no force was detected upon pull-off. Another problem was saturation of the photodetector signal due to the adhesion force being too large and the cantilever deflection going beyond the detectable limit before separation occurred. This occurred in particular cases where the polymer solution covered part of the cantilever, and not just the particle. An example of this case is shown in Figure 4, where the larger interaction area increased the force required to separate the cantilever from the polymer. Furthermore, the residual polymer on the cantilever and size of the deformed region of the polymer after the pull off indicate that the separation not only occurred at the polymer-particle interface, but over a much larger area, and so was not representative of the polymer-particle interface.

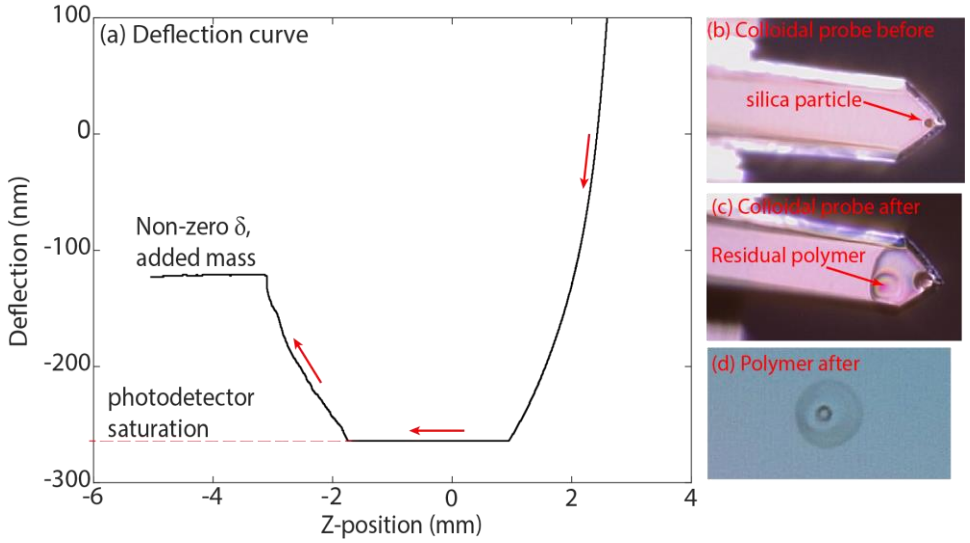

Figure 4. (a) Deflection curve for pull-off of silica colloidal probe from a PDMS film after bringing the colloidal probe into contact with PDMS-hexane solution and waiting for hexane to evaporate. Also shown are optical microscope images of the colloidal probe (b) before and (c) after the experiment and (d) the polymer after the experiment.

Due to the low success rate and low throughput of the method (one sample every 24–72 hours depending on the solvent evaporation time), this method was not further pursued.

Another modification of colloidal force spectroscopy involved partially embedding particles in a polymer so that a portion of the particle protruded from the polymer surface. In this case, a tipless cantilever with an adhesive applied to its end could be brought into contact with the protruding particle, the adhesive cured, and the particle pulled out of the polymer as shown schematically in Figure 5.

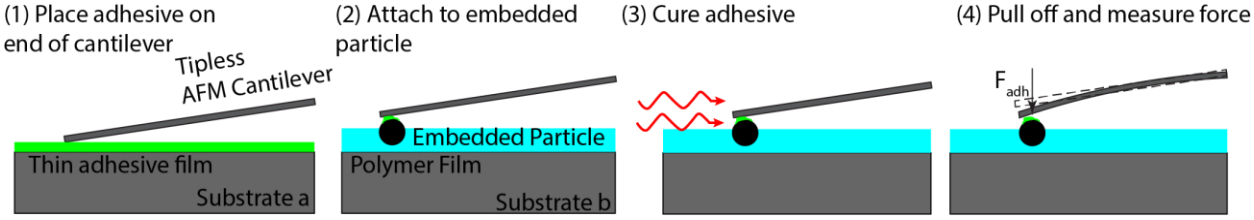

Figure 5. Modification of force spectroscopy in which the particle is embedded in the polymer film, then pulled out by attaching to a tipless AFM cantilever using an adhesive.

Silica particles (9–13 µm diameter) were embedded in a PU film by first spin coating a PU/cyclohexane solution on a glass slide as described in the Materials and Methods section, then spin coating an ~5 mg/mL suspension of silica particles in MeOH on top of the polymer solution, followed by baking in a 70 °C oven overnight. This resulted in silica particles protruding from the PU film as shown in Figure 6. The optical microscope clearly shows individual silica particles that have not agglomerated. To determine how much the particles were protruding from the film, AFM imaging was performed on a single particle in contact mode (ContAl-G cantilever, BudgetSensors®, k = 0.2 N/m). The resulting height map shows that the particles were indeed embedded in and protruding from the PU film. To pull out a particle, a tipless cantilever (ACTA-TL, AppNano, k = 20 N/m) was contacted with a thin layer of UV curable adhesive (Loctite® AA349) and applied to an aluminum substrate with a razor blade. The adhesive coated cantilever was then positioned over a single particle and brought into contact. While in contact, the setup was exposed to 349 nm UV light (Analyt) for 2 hours. Performing the pull off test resulted in no detected cantilever deflection, indicating the particle was not attached. The optical microscope image of the cantilever after the test shows that there was indeed adhesive on the cantilever and it appears that the particle left an indentation in the adhesive. Further attempted runs gave similar results, indicating that either insufficient UV light made it to the interface to cure the adhesive or that the adhesive provided an insufficient bond to the particle.

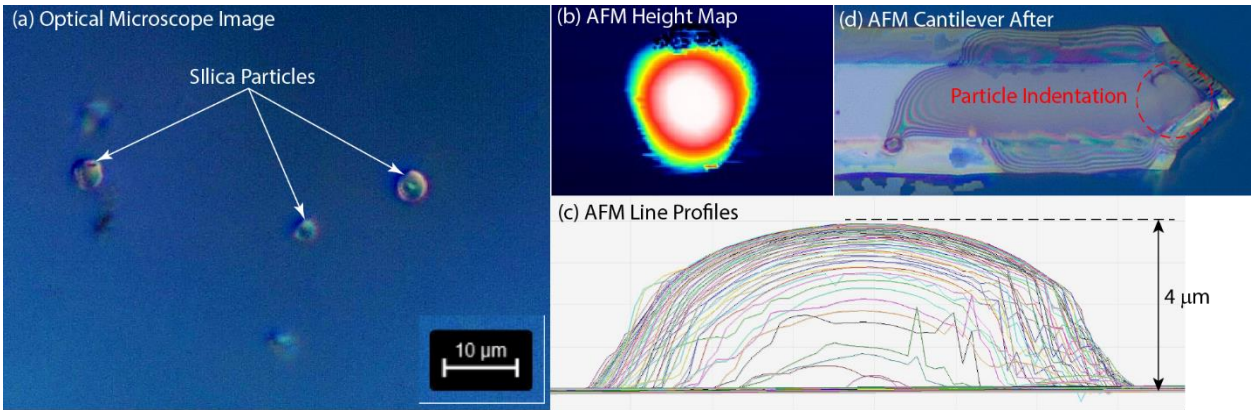

Figure 6. (a) Optical microscope image of silica particles embedded in PU film, (b) AFM height contours and (c) AFM line profiles of a single particle, and (d) optical microscope image of tipless AFM cantilever after applying glue and attempting to pull off a particle.

Although not yet successful, pulling out particles embedded in a polymer appears to be a viable way to determine the adhesion force between particle and polymer in a composite. Processing conditions can be tuned to change the depth the particles are embedded in the material and different adhesives can be used to optimize the particle-cantilever bond strength.

One of the key features of the formation of the particle-polymer interface is that the polymer solution is above its glass transition temperature, allowing the polymer to relax to a (near) equilibrium configuration relatively quickly. In a polymer solution, the glass transition temperature (T_g) is much lower than that for the pure polymer and is often below the processing temperature. When this is the case, the polymer chains are free to arrange themselves and to accommodate the particle interface before the solvent evaporates. For a polymer that has a T_g above the processing temperature, the chains are effectively locked into place and a near-equilibrium interface with a particle cannot form on an experimentally viable time scale. This is why the standard force spectroscopy method yielded adhesion forces that did not differ between particle functionalizations as expected. One possible way to address this is to heat the polymer above its T_g and perform standard force spectroscopy. Experiments were performed for PU, PHU, and PI polymers and 5 µm silica colloidal probes (AppNano, ACTA-SiO2-A) over a temperature range 25–100 °C (OMEGA® flexible heater, KHRA-2/10-P), with the results shown in Figure 7. Also shown are results for a 5-µm amine functionalized silica colloidal probe that was made in-house with a tipless cantilever (AppNano, ACTA-TL) and functionalized particles from Polysciences, Inc.

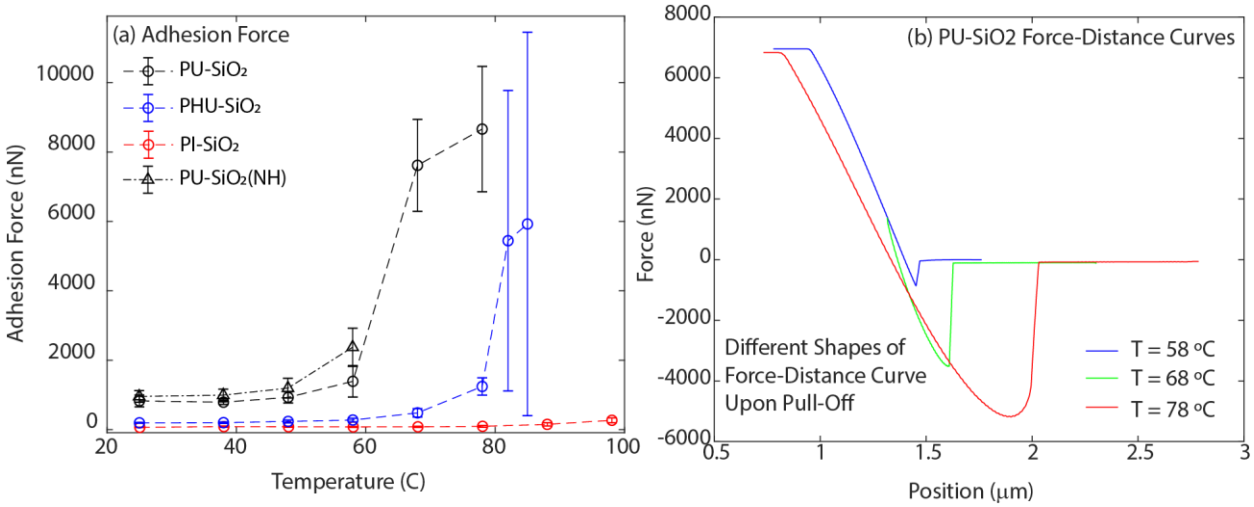

Figure 7. (a) Adhesion force at different temperatures for silica colloidal probe (circles) and amine functionalized silica colloidal probe (triangles) with PU (black), PHU (blue), and PI (red). (b) Force-distance curves for silica-PU at 58 °C (blue), 68 °C (green), and 78 °C (red).

The results clearly show a transition in adhesion force behavior between 60–70 °C for PU and ~80 °C for PHU. This is presumably the glass transition temperature; although, it should be noted that the measured temperature is on the surface of an aluminum substrate on which the polymer-coated glass slide sits, so the actual polymer temperature could be somewhat lower. Once above the glass transition temperature, the polymer chains are able to relax and adjust to the presence of the particle surface, forming a stronger attachment. In the case of PI, the T_g was too high to observe the transition in this experiment. The results are preliminary in that the temperature control must be improved, so no definitive conclusions can be drawn. However, it appears as if adhesion force after transition is larger for PU compared to PHU, which could be due to the additional hydroxyl groups on PHU strengthening the interchain hydrogen bonds and decreasing the polymer-particle interaction. Also, the amine-functionalized silica particle is potentially showing a stronger interaction with PU than the bare silica particles at 58 °C, but the particle-cantilever adhesive bond failed above this temperature, so no additional data could be obtained. The shape of the force-displacement curve also changes with increasing temperature, and this could hold important information about how the interactions change in different regimes. This will be studied in the future, and great care must be taken to accurately separate the contact mechanics from the adhesion forces in the measurement.[20,23]

The large error bars above T_g for PHU arise from the fact that an on/off temperature controller was used in this experiment, causing the temperature to oscillate up to 4 °C around the setpoint and the interface to move during the force spectroscopy experiment due to thermal expansion of the underlying aluminum substrate. A specialized temperature control stage designed specifically for the Flex-Axiom AFM (Nanosurf, Liestal, Switzerland) has been ordered and will be used for future experiments.

To make the amine-functionalized silica colloidal probe in-house, a 0.5 mg/mL suspension of particles in MeOH was spin cast onto a glass slide, then placed in a 70 °C oven for 1 hour to dry. UV cure adhesive was applied to the end of a tipless cantilever and excess glue was “wiped off” by bringing the end into contact with a dry glass surface and dragging the cantilever across it. Then, the cantilever was positioned over a single isolated particle and brought into contact. The particle-adhesive-cantilever system was then removed and exposed to UV light (349 nm) for 30 minutes to cure the adhesive. Figure 8 shows the different steps involved in creating the colloidal probe. The colloidal probe appeared to function as expected up to about 60 °C when the adhesive bond failed. Different adhesives will be explored to achieve higher temperatures.

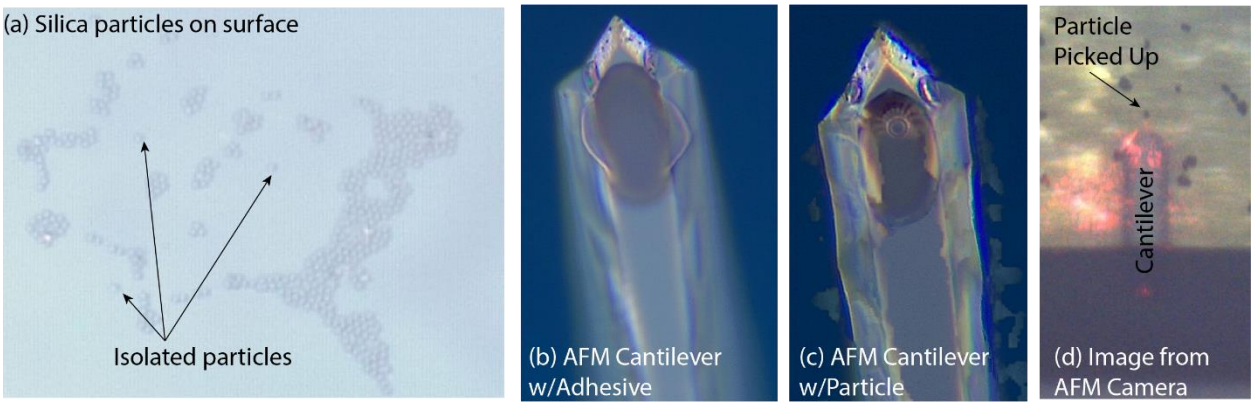

Figure 8. Colloidal probe made in-house: (a) 5 µm amine functionalized silica particles on glass slide, (b) tipless AFM cantilever with UV cure adhesive on end and (c) with particle attached, (d) view of positioning single particle under cantilever end before attachment.

3.2 Chemical breakthrough in polymer composites

Chemical breakthrough experiments were performed on pure PU and silica-PU composite films with different loadings (10 wt%, 20 wt%, and 30 wt% particles). In all cases, the films were exposed to saturated methyl salicylate (MeS) in N_2 at 38 °C for 24 hours. Figure 9a shows the normalized (to equilibrium value) difference spectrum integrated over 1,665–1.685 cm^{-1}, which corresponds to the band for MeS. The breakthrough of MeS appears to be slower for the pure PU compared to the composites, suggesting that there may not be good adhesion between the PU chains and silica particles. To further investigate this, the IR spectra were plotted for the C=O (~1,700 cm^{-1}) and NH (~3,330 cm^{-1}) regions of the PU spectra both before and after MeS exposure. If there was significant particle-polymer interaction, it is expected that there would be a significant shift in the NH or C=O peaks of PU or a change in the relative magnitudes of the corresponding free and bound species when silica particles were added. However, there is no evidence of either of these, further indicating that the polymer-particle interaction is relatively weak in this case.

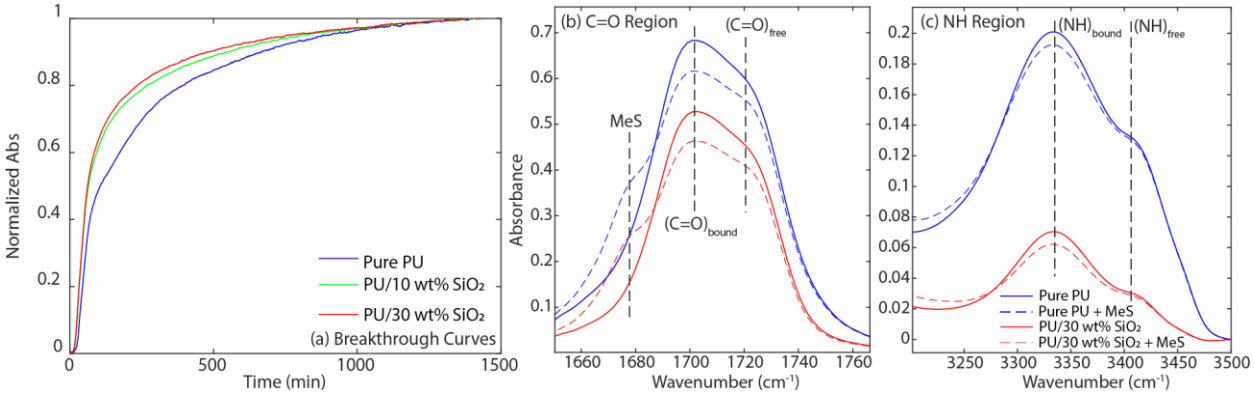

Figure 9. (a) Breakthrough curves for MeS in pure PU (blue), and 10 wt% (green) and 30 wt% (red) silica-PU composites. Corresponding spectra in (b) C=O region and (c) NH region both before (solid lines) and after (dashed lines) MeS exposure.

4. CONCLUSIONS

Significant progress was made on measuring ex-situ particle-polymer adhesion that is representative of the corresponding interface in a polymer composite. Two viable paths forward are (a) partially embedding a particle in a polymer and pulling it out using a tipless AFM cantilever dipped in adhesive, and (b) heating the polymer above T_g so that the polymer chains form a near-equilibrium interface with the particle. For the first option, the primary obstacles are controlling the depth the particle is embedded in the polymer (to limit the interaction area) and finding a viable adhesive to ensure good particle-cantilever contact. For the second option, better temperature control is needed, and the implications of measuring the adhesion force at elevated temperature for correlation to breakthrough

measurements at lower temperatures need to be fully considered. Additionally, the ability to safely expose the polymer-particle interface to different chemical vapors is needed to study changes in the interface upon chemical exposure. An environmental chamber has been implemented that encloses the space around the AFM cantilever and has a flow inlet. Further measures need to be taken to ensure that the enclosure is properly sealed before proceeding with vapor exposure experiments.

Composites were also made with different particle loadings and breakthrough testing was performed on these. The breakthrough curves showed faster transport for higher particle loadings, possibly indicating poor interface adhesion, which is supported by analysis of the polymer IR spectrum. To ensure good particle distribution in the composite, higher magnification imaging techniques such as scanning electron microscopy or transmission electron microscopy might be employed. Future work will include breakthrough tests on composites made with particles of varying functionalization and different polymers.

ACKNOWLEDGMENTS

Funding was provided by the U.S. Army via the Surface Science Initiative Program (PE 0601102A Project VR9) at the Combat Capabilities Development Command Chemical Biological Center. The authors would like to thank Mikaela Boynaich who worked on this project as a summer student through the College Qualified Leaders program administered by the Army Educational Outreach Program and Dr. Melissa Sweat who provided valuable advice and assistance in making colloidal probes and performing force spectroscopy measurements, and Dr. Thomas Pearl and Dr. Brent Mantooth for their insights on transport in polymer composites.

REFERENCES

[1] Galizia, M.; Chi, W.S.; Smith, Z.P.; Merkel, T.C.; Baker, R.W.; Freeman, B.D. 50th Anniversary Perspective: Polymers and Mixed Matrix Membranes for Gas and Vapor Separation: A Review and Prospective Opportunities. *Macromolecules.* **2017,** *50* (20), pp 7809–7843.

[2] Bae, T.H.; Lee, J.S.; Qiu, W.; Koros, W.J.; Jones, C.W.; Nair, S. A high-performance gas-separation membrane containing submicrometer-sized metal-organic framework crystals. *Angew. Chem., Int. Ed.* **2010,** *49* (51), pp 9863–9866.

[3] Guo, A.; Ban, Y.; Yang, K.; Yang, W.S. Metal-organic framework-based mixed matrix membranes: Synergetic effect of adsorption and diffusion for CO_2/CH_4 separation. *J. Membr. Sci.* **2018,** *562*, pp 76–84.

[4] Zhang, H.W.; Shen, P.K. Recent Development of Polymer Electrolyte Membranes for Fuel Cells. *Chem. Rev.* **2012,** *112* (5), pp 2780–2832.

[5] Tang, H.L.; Wan, Z.; Pan, M.; Jiang, S.P. Self-assembled Nafion-silica nanoparticles for elevated-high temperature polymer electrolyte membrane fuel cells. *Electrochem. Commun.* **2007,** *9* (8), pp 2003–2008.

[6] Bachman, J.E.; Smith, Z.P.; Li, T.; Xu, T.; Long, J.R. Enhanced ethylene separation and plasticization resistance in polymer membranes incorporating metal-organic framework nanocrystals. *Nat. Mater.* **2016,** *15*, pp 845–849.

[7] Lin, R.J.; Hernandez, B.V.; Ge, L.; Zhu, Z.H. Metal organic framework based mixed matrix membranes: An overview on filler/polymer interfaces. *J. Mater. Chem. A.* **2018,** *6* (2), pp 293–312.

[8] Dutta, R.C.; Bhatia, S.K. Structure and gas transport at the polymer-zeolite interface: Insights from molecular dynamics simulations. *ACS Appl. Mater. Interfaces.* **2018,** *10* (6), pp 5992–6005.

[9] Zhang, M.; Askar, S.; Torkelson, J.M.; Brinson, L.C. Stiffness Gradients in Glassy Polymer Model Nanocomposites: Comparisons of Quantitative Characterization by Fluorescence Spectroscopy and Atomic Force Microscopy. *Macromolecules.* **2017,** *50* (14), pp 5447–5458.

[10] Gibson, R.F. A review of recent research on nanoindentation of polymer composites and their constituents. *Compos. Sci. Technol.* **2014,** *105*, pp 51–65.

[11] Kalidindi, S.R.; Mohan, S.; Rossi, A. Mechanical Characterization of Mesoscale Interfaces Using Indentation Techniques. *JOM.* **2017,** *69* (1), pp 22–29.

[12] Schöneich, M.; Zamanzade, M.; Stommel, M. Fiber-matrix interphase in applied short glass fiber composites determined by a nano-scratch method. *Compos. Sci. Technol.* **2015,** *119*, pp 100–107.

[13] Su, N.C.; Smith, Z.P.; Freeman, B.D.; Urban, J.J. Size-Dependent Permeability Deviations from Maxwell's Model in Hybrid Cross-Linked Poly(ethylene glycol)/Silica Nanoparticle Nembranes. *Chem. Mater.* **2015,** *27* (7), pp 2421–2429.

[14] Kim, S.; Dura, J.A.; Page, K.A.; Rowe, B.W.; Yager, K.G.; Lee, H-J.; Soles, C.L. Surface-Induced Nanostructure and Water Transport of Thin Proton-Conducting Polymer Films. *Macromolecules.* **2013,** *46* (14), pp 5630–5637.
[15] Lin, E.K.; Kolb, R.; Satija, S.K.; Wu, W.L. Reduced Polymer Mobility near the Polymer/Solid Interface as Measured by Neutron Reflectivity. *Macromolecules.* **1999,** *32* (11), pp 3753–3757.
[16] Butt, H.J.; Duran, H.; Egger, W.; Faupel, F.; Harmandaris, V.; Harms, S.; Johnston, K.; Kremer, K.; Lin, F.Y.; Lue, L.; Ohrt, C.; Raetzke, K.; Ravelli, L.; Steffen, W.; Vianna, S.D.B. Interphase of a Polymer at a Solid Interface. *Macromolecules.* **2014,** *47* (23), pp 8459–8465.
[17] Ohrt, C.; Rätzke, K.; Oshima, N.; Kobayashi, Y.; O'Rourke, B.E.; Suzuki, R.; Uedono, A.; Faupel, F. Free Volume Profiles at Polymer-Solid Interfaces Probed by Focused Slow Positron Beam. *Macromolecules.* **2015,** *48* (5), pp 1493–1498.
[18] Kappl, M.; Butt, H-J. The Colloidal Probe Technique and its Application to Adhesion Force Measurements. *Part. Part. Syst. Charact.* **2002,** *19* (3), pp 129–143.
[19] Leite, F.L.; Herrmann, P.S.P. Application of atomic force spectroscopy (AFS) to studies of adhesion phenomena: a review. *J. Adhes. Sci. Technol.* **2005,** *19* (3–5), pp 365–405.
[20] Pham, J.T.; Schellenberger, F.; Kappl, M.; Butt, H-J. From elasticity to capillarity in soft materials indentation. *Phys. Rev. Mater.* **2017,** *1*, pp 015602–015610.
[21] Feldman, K.; Tervoort, T.; Smith, P.; Spencer, N.D. Toward a force spectroscopy of polymer surfaces. *Langmuir*. **1998,** *14* (2), pp 372–378.
[22] Boyne, D.A.; Varady, M.J.; Lambeth, R.H.; Eikenberg, J.H.; Bringuier, S.A.; Pearl, T.P.; Mantooth, B.A. Solvent-Assisted Desorption of 2,5-Lutidine from Polyurethane Films. *J. Phys. Chem. B.* **2018,** *122* (7), pp 2155–2164.
[23] Leite, F.L.; Bueno, C.C.; Da Róz, A.L.; Ziemath, E.C.; Oliveira, O.N. Theoretical models for surface forces and adhesion and their measurement using atomic force microscopy. *Int. J. Mol. Sci.* **2012,** *13* (10), pp 12773–12856.

Novel MXene/titania nanocomposite fibers for enhanced charge injection

Shaun M. Debow[a*], Brendan G. DeLacy[a], Yury Gogotsi[b], Yi Rao[c], William R. Creasy[d]
[a]U.S. Army Combat Capabilities Development Command Chemical Biological Center, Research & Technology Directorate, 8198 Blackhawk Rd, Aberdeen Proving Ground, MD 21010
[b]Drexel University, 3141 Chestnut St, Philadelphia, PA 19104
[c]Utah State University, 0300 Old Main Hill, Logan, UT 8432
[d]Leidos, P.O. Box 68, Gunpowder Branch, Aberdeen Proving Ground, MD 21010

ABSTRACT

MXenes are a recently discovered class of materials with exceptional electrical, thermal, mechanical, and electromagnetic properties. They were first discovered by Gogotsi and co-workers in 2011 at Drexel University. This class of materials is produced by selective etching and delaminating early transition metal compounds to form nanoparticles with two dimensional structures. MXenes have the ability to 1) efficiently absorb light of varying wavelengths (visible through infrared), 2) efficiently store charge and act as supercapacitors, and 3) exhibit photoluminescence. We hypothesized that MXenes efficiently grown or attached to a semiconductor substrate (with suitable band gap) will efficiently absorb light, generate excited electrons, and inject that charge into the semiconductor. In order to test this hypothesis, we fabricated novel Ti_3C_2-MXene-TiO_2 fiber nanocomposites and subsequently measure their charge injection properties using transient absorption measurements. This project provides the Combat Capabilities Development Command Chemical Biological Center with a new and exciting material to be explored in a range of applications including filtration, decontamination, energy conversion, and obscuration. In addition, we are correlating the charge transfer properties to chemical reactivity using test reactions involving photoreaction of methylene blue and photoreduction of CO_2. Preliminary results have been obtained.

Keywords: MXene, photoexcitation, nanofibers, nanoparticles

1. INTRODUCTION

MXenes are a recently discovered a class of materials. They are two-dimensional in structure and made of transition metal carbides, carbonitrides, and nitrides.[1] They exhibit exceptional electrical, thermal, mechanical, and electromagnetic properties. The first class of two-dimensional transition metal carbides were originally discovered and characterized by Dr. Yury Gogotsi and co-workers in 2011 at Drexel University[2] and referred to as MXenes. These materials have since expanded to include carbonitride and nitride materials, all produced by selective etching and delaminating layers using a range of early transition metal compounds.[2,3] Large material diversity contributes to their wide-ranging properties. Theoretical and experimentally created MXenes were previously discussed in the FY18 Proceedings of the Edgewood Chemical Biological Center ILIR and SSI Programs annual report.[4]

Recently, MXenes have found applications in water purification and desalination,[5] microwave absorbing and shielding,[6,7] water splitting,[8] methane adsorption,[9] transparent conductors,[10] photocatalysis,[11,12] chemical sensing,[13] photoluminescence quantum dots,[14] flexible and conducting films,[15] and super capacitors.[15–19]

Due to the above MXene characteristics, we anticipated that this exciting class of materials should also exhibit superior charge injection characteristics. This is supported by the material's ability to efficiently absorb incident radiation, the ability to store charge (e.g. as a supercapacitor), its high conductivity, and the ability to transfer charge and exhibit photoluminescence. The ability to store energy could also affect the ability to chemically react in reactions that require energy storage, such as photoreactions.

Assuming an efficient electron acceptor is near or adjacent to the MXene, it was hypothesized that the excited electron should hop or inject into an acceptor substrate, e.g. a semiconductor material. Photoluminescence would be quenched in this scenario. Hence, our central hypothesis in this study was that a MXene nanostructure efficiently grown or

attached to a semiconductor substrate (with suitable band gap) will efficiently absorb light, store that charge in a controllable fashion, and inject that charge into the adjacent semiconductor substrate. Furthermore, we hypothesized that the way in which the 2D sheets of MXene are prepared or attached to the semiconductor substrate will greatly impact the charge injection process.

To test this hypothesis, we identified TiO_2 as a suitable semiconductor substrate that could be used to study the charge carrier transfer dynamics between the Ti_3C_2 MXene and the TiO_2 substrate. TiO_2 is an ideally suited material for this study due to its inherent band gap, its ease of fabrication, and its ability to grow or attach to other nanostructures, such as MXenes. Hence, a primary goal during the previous year of this study was to fabricate and characterize MXene-TiO_2 composites.

Several aspects of this study may have direct-transition application to the U.S. Army and the Warfighter. Two particularly interesting properties are: 1) they could provide advantages as a new type of catalyst for decontaminating chemicals, and 2) they may also serve as attenuating aerosols for use in a complex electromagnetic environment.[1,5–7] MXenes have the property of being hydrophilic after suitable processing, which reduces the organic solvent waste burden that is inherent with hydrophobic materials. Their hydrophilic characteristic indicates that they can be suspended in a water solution; this may facilitate their dispersal as an aerosol fog, rather than needing incendiary or energetic dispersal methods. Previous research, available in the scientific literature, has described a method to achieve specific lateral size distributions through the use of gradient centrifugation.[20] This selectivity may allow better performance by properly matching the flake size with intended wavelengths of electromagnetic radiation to absorb or reflect. Alternatively, the flakes could be used in a broad, lateral-size distribution—this may produce a broadband absorber covering a wider range of wavelengths (e.g., from microwave to visible radiation). In comparison to MXenes, graphitic materials, such as graphene, are well-studied two-dimensional conductive materials; however, their electrical efficiencies are reduced through lattice and surface defects that are an inherent byproduct in their synthesis. In addition to defect-related performance degradation, graphitic materials are typically hydrophobic, and this hydrophobicity increases their processing costs by requiring potentially hazardous organic solvents for forming dispersions.

MXenes may enable or enhance photoreactions which have a potential application, for example, to decontaminate chemical warfare agents. TiO_2 is a well-known material for promoting photoreactions due to its ability to form electron-hole pairs; however, it has a large bandgap that drives photo absorption to the near UV radiation range.[21–24] The addition of MXene to TiO_2 may significantly increase the absorbance of radiation into the visible to infrared bands—attributed to the broadband absorbance of radiation by MXene over a wide frequency range. Alternatively, the MXene may provide a capability for energy storage, so reactions may occur faster than with TiO_2 alone, or reactions may occur that were otherwise energetically unfavorable.

2. METHODS

The following approach was used to fabricate and characterize Ti_3C_2-MXene-TiO_2 nanocomposites:

2.1 TiO_2 fiber substrates

Our laboratory has both the expertise and equipment to electrospin titania fibers with controllable dimensions. These fibers were used as the substrate for embedding and attaching MXene nanostructures. The fibers were characterized in terms of composition and size via transmission electron microscopy and scanning electron microscopy.

2.2 MXene fabrication

MXene fabrication involved collaboration with Dr. Yury Gogotsi and his laboratory group at Drexel University; Dr. Gogotsi is the preeminent leader in the field of MXene synthesis and preparation. This expertise reduced the time and labor needed to produce usable MXene. We focused on Ti_3C_2 MXene in this study, but a wide range of other compounds, made by varying the transition metal, are options for future studies.

2.3 Charge injection

Charge injection studies were performed in collaboration with Dr. Yi Rao and his research group at Utah State University. Dr. Rao's expertise in pump-probe transient absorption spectroscopy allowed us to evaluate the movement of excited charge carriers in ways we could not have otherwise. Further details are described in Section 3.3. Dr. Rao

was funded to assist with the characterization of the MXene-TiO_2 nanocomposite fibers. Transient absorption spectroscopy is a pump/probe technique where the injection of charge into a substrate is monitored by pumping the composite with a femtosecond laser of a given wavelength and power, and subsequently probing/monitoring the absorption properties of the substrate (at a different wavelength) to determine whether excited charge carrier transfer occurs.

2.4 TiO_2/Ti_3C_2 nanocomposite fabrication

An approach to quickly fabricate Ti_3C_2 MXene-TiO_2 nanocomposites is by electrospinning TiO_2 fibers containing the MXene using a sol-gel process. This approach is based upon a prior study in which electrospun polymer-only fibers and thin films were loaded with MXenes. These composites were shown to have greater electrical conductivity, when compared with the corresponding neat polymer.[25,26] The electrical conductivity of polymers loaded with MXene increased by three-orders of magnitude when compared with the neat polymer.[24]

3. EXPERIMENTAL

3.1 Synthesis of MXene-TiO_2 and TiO_2 composite nanofibers

A laboratory quantity of Ti_3C_2 MXene was fabricated by Gogotsi's group following procedures similar to those previously disclosed by Ghidiu et al.[27] In brief, this method involves etching a Ti_3AlC_2 MAX phase with an acid, followed by sonication or vigorous shaking to delaminate into monolayers.

The resulting Ti_3C_2 monolayers from Gogotsi were incorporated into electrospun TiO_2 fibers at the Combat Capabilities Development Command (CCDC) Chemical Biological Center (CBC) following electrospinning procedures reported by Liu et al.,[26] with modifications to incorporate Ti_3C_2-MXene and applying concepts similar to those implemented by Mayerberger et al.[25] and Kiennork et al.[28] Mayerberger discovered that the polymer jet ejection characteristics vary depending upon Ti_3C_2 concentration, due to changes in viscosity and electrical conductivity. They determined the ideal concentration for electrospun Ti_3C_2 in a polymer solution is a 1 % w/w. This concentration was the starting point for TiO_2 electrospinning; however, these parameters, in addition to electrospinning voltage potentials, needle size, and pump rate, required tuning to be optimized.

As a control, pristine TiO_2 fibers (without MXene) also were fabricated using a simple a sol-gel synthesis process. This sol-gel process disperses MXene and Titanium isopropoxide (TTiP) into a uniform suspension containing polymethyl methacrylate (PMMA) that is ideal for electrospinning. Fibers were electrospun using the sol-gel suspension, then thermally treated in a controlled environment to evaporate PMMA and convert the TTiP to TiO_2.

A brief description of the procedure follows: 320 mg of PMMA was slowly added to 2 mL of chloroform while stirring, the solution was stirred until the PMMA was completely dissolved, for approximately 30 minutes. TTiP was added dropwise to the stirring solution, the volume varied from 0.29 mL to 0.67 mL, depending upon the desired MXene to TTiP concentration. The solution was allowed to stir for an additional 30 minutes. Following the addition of TTiP, a variable volume of MXene/N,N–dimethylformamide (DMF) suspension (20 mg/mL MXene/DMF) was added and allowed to stir for 2 hours. Fibers were electrospun using an MTI KJ Group Electrospinning cabinet, model MSK-NFES-3LDV (Richmond, CA). The solution was drawn into a syringe with an 18-gauge needle attached. The syringe was clamped into a syringe pump, with the needle positioned 8 cm away from a horizontally-rotating drum mandrel. The following process parameters were used: the mandrel operated at 400 rpm, the syringe pump flow was set to a nominal 0.12 mL/min, and a 10-kV potential was applied to the syringe tip. Pristine TiO_2 nanofibers were electrospun by applying the sol-gel synthesis process previously described for MXene-TiO_2 fibers, but without the addition of any MXene, and were produced using 0.67 mL of TTiP and 320 mg of PMMA.

The resulting MXene-TTiP-PMMA and TTiP-PMMA nanofibers mats were allowed to stand for 24 hours under ambient conditions. This allowed the TTiP in the electrospun fibers to hydrolyze into $Ti(OH)_4$ and then further condensate to amorphous TiO_2 prior to thermal treatment.[29]

Fibers were thermally treated by calcining in a Thermo Scientific™ Lindberg/Blue M™ Mini-Mite™ TF55035A-1 Tube Furnace (White Deer, PA) for four hours at 400 °C under an Ar–H_2 (10 % H_2) atmosphere or under air. A weight difference was noted between the pre-calcined and post-calcined fibers, this difference was consistent with the evaporation of PMMA and water. A list of the fiber samples and fabrication conditions are presented in Table 1.

Table 1. Sample numbers and conditions for fiber synthesis.

Sample #	Conditions for MXene addition	Amt. PMMA (g)	Amt. TTiP (mL)	Calcination Cond.
180607-1	0.275 g MXene flake, 2 mL $CHCl_3$, 2 mL DMF	0.320	0.29	Calcined in Ar-H_2 (10% H2) 4 h @ 400C
190313-01	1 mL MXene-DMF Suspension, 2 mL $CHCl_3$, 1 mL DMF	0.320	0.67	Calcined in Ar-H_2 (10% H_2) 4 h @ 400C
190712-01	NO MXene – control, 2 mL $CHCl_3$, 2 mL DMF	0.320	0.67	Annealed in Air 4 h @ 400C
190715-01	NO MXene, 2 mL $CHCl_3$, 2 mL DMF	0.320	0.67	Annealed in Air 4 h @ 400C
190715-01-01	NO MXene in electrospinning, 2 mL $CHCl_3$, 2 mL DMF	0.320	0.67	Annealed in Air 4 h @ 400C
	Step 3.2: MXene Self-Assembled using 1 mL MXene-Water Supernatent Suspension + 10 mL Deionized Water. Vacuum filtered to remove water			
190718-01	1 mL MXene-DMF Suspension, 2 mL $CHCl_3$, 2 mL DMF	0.320	0.67	Annealed in Air 4 h @ 400C
190724-01	0.1 mL MXene-DMF Suspension, 2 mL $CHCl_3$, 2 mL DMF	0.320	0.67	Annealed in Air 4 h @ 400C
190722-01	1 mL MXene-DMF Suspension, 2 mL $CHCl_3$, 1 mL DMF	0.320	0.67	Annealed in Air 4 h @ 400C
190722-01-01	1 mL MXene-DMF Suspension, 2 mL $CHCl_3$, 1 mL DMF	0.320	0.67	Annealed in Air 4 h @ 400C
	Step 3.2: MXene Self-Assembled using 1 mL MXene-Water Supernatent Suspension + 10 mL Deionized Water. Vacuum filtered to remove water			
190722-A-01	0.5 mL MXene-DMF Suspension, 2 mL $CHCl_3$, 2 mL DMF	0.320	0.67	Annealed in Air 4 h @ 400C
190726-01	1.1 mL MXene-DMF Suspension, 2 mL $CHCl_3$, 1.4 mL DMF	0.320	0.67	Annealed in Air 4 h @ 400C
190726-01-01	1.1 mL MXene-DMF Suspension, 2 mL $CHCl_3$, 1.4 mL DMF	0.320	0.67	Annealed in Air 4 h @ 400C
	Step 3.2: MXene Self-Assembled using 1 mL MXene-Water Supernatent Suspension + 10 mL Deionized Water. Vacuum filtered to remove water			
190729-01	1.5 mL MXene-DMF Suspension, 2 mL $CHCl_3$, 1 mL DMF	0.320	0.67	Annealed in Air 4 h @ 400C
190730-01	0.7 mL MXene-DMF Suspension, 2 mL $CHCl_3$, 1.8 mL DMF	0.320	0.67	Annealed in Air 4 h @ 400C
190731-01	0.6 mL MXene-DMF Suspension, 2 mL $CHCl_3$, 1.9 mL DMF	0.320	0.67	Annealed in Air 4 h @ 400C

3.2 Synthesis of MXene-TiO_2 composite nanofibers with self-assembled surface MXene

MXene flake was self-assembled to the surface of some electrospun TTiP-PMMA and MXene-TTiP-PMMA fibers. The self-assembly process started with as-spun fiber mats—electrospun following procedures outlined in section 3.1—prior to the calcination step. Briefly, a colloidal suspension of MXene in water was produced by adding 0.0330 g of MXene to 40 mL of deionized water. This solution was sonicated at 24 W for 70 minutes using a Misonix Sonicator 3000 (Cole-Parmer ®, Farmingdale, NY) with a horn having a one-inch diameter tip operating at 20 kHz. Following sonication, 0.129 g of electrospun fibers were added to the colloidal suspension and stirred for 15 minutes. During this time, MXene self-assembled onto the fiber surface. The resulting fibers were centrifuged at 4,100 rpm for 15 minutes, then filtered. Coated fibers were thermally treated using the previously-described procedures.

3.3 Visible pump-transient infrared absorption spectroscopy

The experimental setup includes an integrated Ti:sapphire regenerative amplifier laser system (UpteK Solutions; Bohemia, NY) operating at 1 kHz and 800 nm, producing 100 fs pulses of 4.0 mJ. The first 20 % of the 800 nm output

was attenuated to a pulse energy of 10 µJ and used as the pump beam. The remaining 80 % of the output laser pulse was used to pump a Palitra-FS IR Optical Parametric Amplifier (Quantronix Inc., San Jose, CA) with a different frequency generator to produce an infrared (IR) pulse of 5,000 nm (1,900 cm^{-1}) having a pulse energy of 18 µJ. The IR beam was attenuated by more than 1,000 times before the samples were pumped. The IR probe was detected by a Teledyne Judson liquid nitrogen cooled HgCdTe detector, model, MCT-13-4.0 (Stuart, FL), followed by an amplifier. The pump pulse was modulated by a New Focus (Santa Clara, CA) modulated chopper operating at 500 Hz. The amplified signal from the detector was sent to a lock-in amplifier (Stanford Research, SR830). The digitized outputs were processed and recorded by a home-made Labview (National Instruments; Austin, TX) program. The instrumentation response function for the transient IR pulse was 300 fs. As mid-IR is sensitive to intraband transitions of free carriers in the conduction band or valance band of semiconductors, the change in the IR absorption is used for probing electron injection.

3.4 Reactivity studies

Ti_3C_2 MXene-TiO_2 fibers were studied to determine their catalytic or reactive capabilities, particularly with a goal toward chemical warfare agent decontamination. After survey studies were completed, two reactions were selected for in-depth study and to compare different formulations.

3.4.1 Methylene blue bleaching

The first reaction evaluated methylene blue (MB) in an acidic aqueous solution. This reaction was used to compare the reactivity of several MXene fiber preparations in solution. MB is a blue indicator dye that indicates either oxidation or reduction reactions. Hydrogen peroxide (30 % H_2O_2) was added to the solution, this allowed catalytic conversion of H_2O_2 into OH radicals, which then reacted with the MB. Reactions were carried out in 40 mL glass vials using 10 mL of solution (having a 1 cm path length). A typical reaction solution was composed of 1–3 mg of a fiber sample, 2.5×10^{-5} M MB, 2.62 M acetic acid (25 µL added to 10 mL), and 0.03 % H_2O_2. Concentrations were selected to allow the reactions to nearly reach completion in 60–90 min. Residual MB was detected using a UV-vis spectrometer (JASCO). A methylene blue ISO test was used as a guide.[30]

MXene-containing composites were shown to cause a MB photoreaction with simulated sunlight and with 400 nm light. Simulated sunlight was generated using a solar simulator calibrated to 1 kW/m^2. The 400 nm light source was a 50 W diode array. The reactivity of samples is being correlated to the photoexcitation studies of the Yao group.

3.4.2 CO_2 reduction

The other reaction that was studied was gas-phase (or surface-phase) CO_2 reduction. Publications have suggested that MXene materials are capable of CO_2 photoreduction with H_2O under simulated solar radiation to produce CH_4 or other products.[31–33]

Studies were performed using a few different MXene-TiO_2 fiber samples prepared with varying concentrations of MXene for CO_2 photoreduction. Reactions were carried out in 20 mL volume headspace vials with Teflon™-lined screwcaps. An amount of 3 mg of the fiber samples was pre-suspended in 0.1 mL of water and added to the headspace vial. An amount of 10 µL of diethylamine was then added to the headspace vial, since an amine was found to promote reaction with other TiO_2 studies.[32] A slurry of the solid and liquid was made by vortexing the suspension for 30 seconds. The vial was swirled to coat the bottom and side of the vial with the slurry. Solid-phase CO_2 (dry ice), made in-house from a CO_2 gas cylinder, was added to the vials. The vials were purged with Ar gas to expel some air while the CO_2 evaporated. The reaction products were detected by gas injection of 0.25 mL of gas using a gas-tight syringe from the headspace vial into an Agilent gas chromatographer/mass spectrometer with a Gerstel autosampler. The vials were held at room temperature. The gas chromatographer was operated in split injection mode, with a 50:1 ratio, and the mass spectrometry was scanned over 5–200 atomic mass unit (amu) with no solvent delay. Samples were prepared using D_2O rather than H_2O to determine the incorporation of deuterated hydrogen into the reaction products.

4. RESULTS AND DISCUSSION

4.1 Electrospun MXene-TTiP-PMMA fibers

The primary goal for the first year of this multi-year project was to develop methods and procedures to attach MXene to a semiconductor substrate that would efficiently absorb light. During the second year, at least 14 MXene composites were fabricated for testing using the general method, shown in Table 1. It was unknown at the inception of this project if MXene could actually form an intermediate or composite that would allow for easily handling and processing (e.g., electrospinning) to produce a MXene-semiconductor composite. No literature references were found to indicate this had been done before. Method development began by trying a 2.5 wt% loading of MXene to TTiP solution for electrospinning. The concentration of MXene was gradually increased over several electrospinning experimental runs. Ultimately MXene pre-suspended in DMF at a concentration of 20 mg/mL (MXene/DMF) was determined to produce the best electrospun fibers. PMMA polymer was selected as the support matrix because it provided an inert matrix that allowed the fibers to be electrospun. In post processing, PMMA was subsequently removed during thermal treatment. The electrospun fibers were examined by electron microscopy. Images obtained in year one of this study are shown in the FY18 Proceedings of the Edgewood Chemical Biological Center In-House Laboratory Independent Reearch and Surface Science Initiative Programs.[4]

4.2 Transient absorption measurements (pump-probe)

In collaboration with Dr. Rao at Utah State University, studies of two laser pump-probe optical properties were studied on several films. Electron injection studies were done for the samples using transient absorption spectroscopy.

4.2.1 Carrier relaxation of photoexcited MXene

The MXene alone exhibits broad spectral absorption from 300–1,000 nm. The IR absorbance at 5,000 nm is transparent to any chemical groups, but sensitive to the change in the absorption of free carriers. Therefore, the transient IR absorption measures the intra-band transition of free carriers. At a fluence of 130 μJ/cm^2, the photoexcitation increases the transmission of the mid-IR probe. Photoexcitation suppresses conductivity of the MXene film, indicating that the MXene has metallic characteristics. This phenomenon has been observed in graphene in other work.[34]

Photoexcitation of metallic MXene does not result in an increase in carrier density. Instead, carrier scattering rate increases as hot carriers are strongly coupled with phonons, resulting in a transient decrease in $\Delta T/T$. The scattering time was found to be from 3–10 ps. The increased THz transparency of a graphene sample after photoexcitation corresponds to a photoinduced decrease in the THz conductivity. This result is expected in the context of photoexcitation of a metal. In a semiconductor, photoexcitation normally generates free carriers and increases conductivity, that is, it produces a positive photoconductivity.

4.2.2 Charge flow in MXene-TiO_2 composites

We measured fluence-dependent kinetics for MXene-TiO_2 under the photoexcitation of 800 nm from 279–13,021 μJ/cm^2, as presented in Figure 1. The change in the IR transmission at $t = 0$ as a function of the applied fluence was plotted. There is an approximately linear dependence on fluence, shown in Figure 1c, indicating that multiphoton effects are not important in the carrier generation. Both the fast and slow time constants for the carrier relaxation remain almost constant across the fluence. These intensity-independent results suggest that the cooling of excited carriers by phonon emission is not screened efficiently leading to high density-independent carrier-phonon scattering rates in MXene-TiO_2.

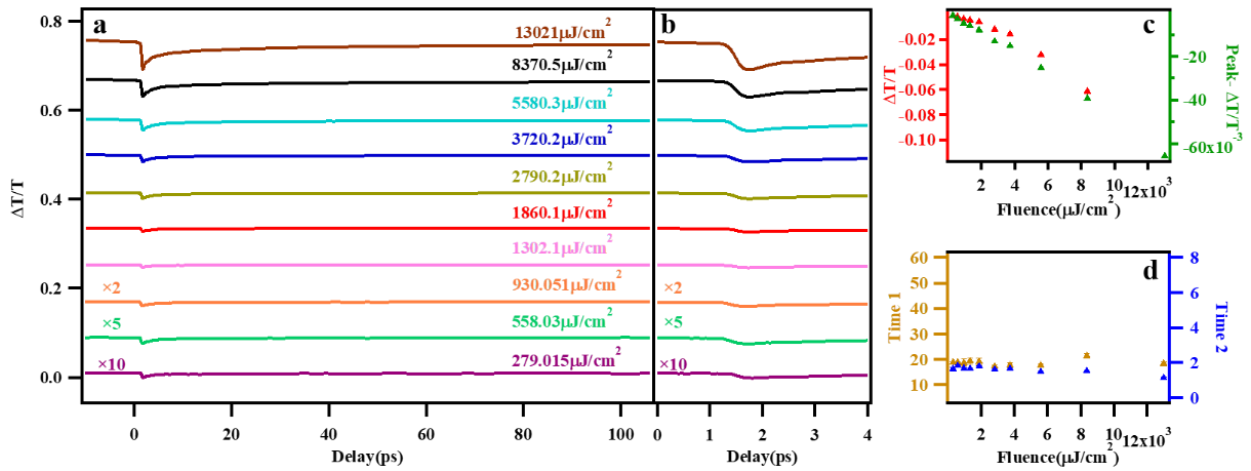

Figure 1. Kinetics traces of MXene-TiO_2 under 800 nm at different excitation fluence values from 279 μm/cm² to 13,021 μm/cm² with a long (a) and short time scale (b), respectively. (c) The transient IR peak (t = 0) as a function of excitation fluence. (d) The two time constants with a function of excitation fluence.

With the knowledge of carrier dynamics in the MXene pellet, we now switch attention to carrier flow in MXene-TiO_2 composites. Figure 2 shows the kinetic traces of photo-induced changes in transmission at 5,000 nm by photoexcitation at 400 nm and 800 nm for MXene-TiO_2 and pristine TiO_2, in a short time scale of 2 ps (A) and a long time scale of 100 ps (B), respectively. The kinetic traces show a decrease in the transient IR transmission for the MXene-TiO_2 and TiO_2.

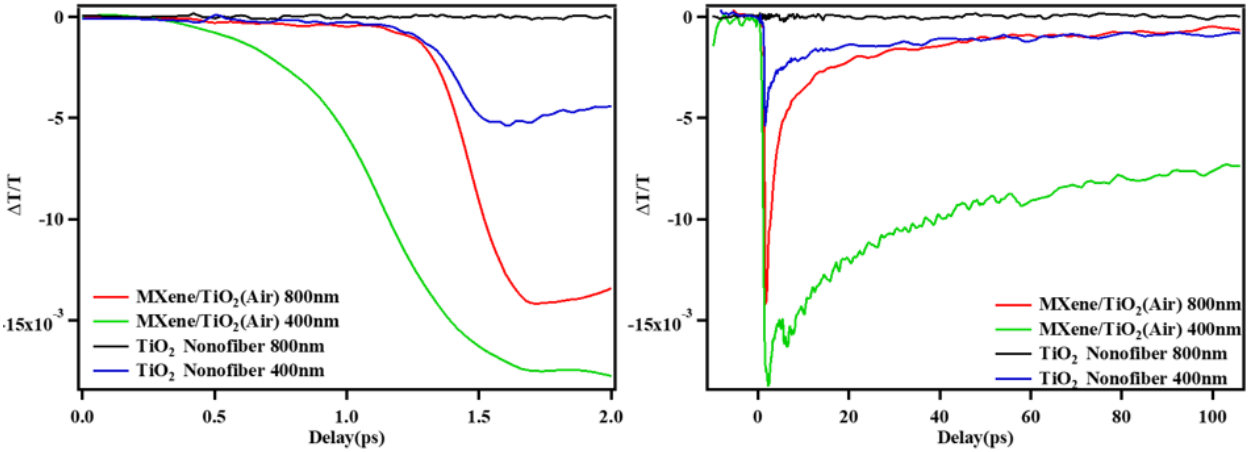

Figure 2. Kinetic traces of photo-induced IR transmission (5,000 nm) change ΔT/T under 400 nm and 800 nm at a short time scale of 2 ps (left), and at a long-time scale of 100 ps (right).

In the early time scale of Figure 2, we examined charge transfer in MXene-TiO_2. The photoexcitation of MXene-TiO_2 exhibits a much slower formation of under 400 nm than that under 800 nm. Carriers are generated only from MXene under the photoexcitation of 800 nm since the excitation is below the onset of TiO_2 transition, while photogenerated carriers are from both MXene and TiO_2 but dominated by TiO_2 under 400 nm. As expected, no photo-induced IR transmission was observed for TiO_2 alone at 800 nm since the pump energy was below the band gap of TiO_2. Carriers in TiO_2 are generated instantaneously under the photoexcitation of 400 nm, with a formation time constant as fast as 120–150 fs. These results indicate that photogenerated carriers transfer from MXene to TiO_2 in a more efficient way than from TiO_2 to MXene.

Fitting the data to a biexponential function yields two relaxation processes of 1.66 ps and 17.73 ps for MXene-TiO_2 under 800 nm shown in the longer time scale (right) in Figure 2. The fast process was attributed to back carrier transfer from the accepting TiO_2 to MXene and the slow process to trap-assisted recombination in the TiO_2. The slow recombination in TiO_2 was also evidenced by that under 400 nm in Figure 2.

4.2.3 Plasmonic carrier injection from photoexcited MXene to TiO_2

When a semiconductor having a band gap larger than 3.1 eV is coupled with a metal with the plasmon resonance band in the visible light or near-IR light range, only hot electron injection can be used for the transfer of plasmonic energy. Upon absorption of that radiation, MXene electrons are excited. After photoexcitation of the plasmon from the MXene, an athermal distribution of electron-hole pairs is created with a maximum energy separation with the photon energy. The energy redistribution through electron-electron scattering results in a Fermi-Dirac distribution of excited charge carriers around the Fermi level. On the other hand, TiO_2 is known as a good electron-accepting metal oxide. The excellent electron-accepting property, or the very fast electron injection, can be understood from the high density of states in the conduction band of TiO_2. When MXene comes in close contact with the semiconductor, band bending occurs inside the semiconductor to achieve Fermi level equilibrium between the metal and the semiconductor. Such bending leads to the formation of a Schottky barrier in the contact.

The Schottky barrier is a way to store excess photoexcitation energy in the material or prevent holes from recombining with electrons. The results indicate that it is formed at the interface or the electrical contact between the TiO_2 and the MXene. The energy storage raises the question of whether the energy can be utilized for productive work, such as to drive a chemical reaction.

4.3 Reactivity studies

The MXene-TiO_2 composite fibers listed in Table 1 were studied to determine catalytic or reactive capabilities. The reactivity depends not only on stored energy, but also the type of available reaction mechanisms, which in turn guide the selection of which specific reaction to use. Several surveys of reactions were examined at various pHs, concentrations, and with different additives. However, the initial survey was not comprehensive; it is likely that the best reaction remains. Even so, the results appear promising, and indicate that the materials will provide useful results in the future. After the initial screening, MB and CO_2 reactions were selected for an in-depth study.

4.3.1 Methylene blue reactions

The first reaction investigated using MB in aqueous acidic solution. MB was chosen as an indicator because it is well studied in the scientific literature, and it is possible to draw some conclusions about the nature of the reaction based on comparison to previous work.[36] MB also is easily detected using UV-vis spectrometry, although other instrumental methods such as liquid chromatography/mass spectrometry are also available at CCDC CBC. MB is a blue indicator dye that indicates either oxidation or reduction reactions. Hydrogen peroxide (30 % H_2O_2) was added to the solution, so the reaction mechanism likely involved converting H_2O_2 into hydroxyl radicals (·OH), which then reacted with the MB.[36] This conversion to ·OH can be an oxidation or reduction, but it still indicates the reactive contribution from the MXene.

The MB reaction was used to compare reactivity in solution from MXene-TiO_2 composite fiber preparations. By comparing the fiber samples, we can determine the presence or absence of a reaction and develop a correlation with the amount of MXene present. Reaction rates were determined by making a reaction solution, exposing it to visible or 400 nm radiation for a known amount of time, and then sampling the solution and analyzing it on a UV-vis spectrometer. The kinetics data indicate a good correlation between the amount of radiation received by the sample and the amount of MB reacted; neglecting any potential exponential fit error due to a pseudo-first order reaction of the MB. A sample kinetic plot for three runs is shown in Figure 3. The run from 7/26C (fiber sample 190715-01, pristine TiO_2 fibers) is not significantly different from the blank run (MB solution with no fiber sample), while the 7/25B (fiber sample 190718-01, fabricated using MXene flake pre-suspended in DMF) run is significantly faster.

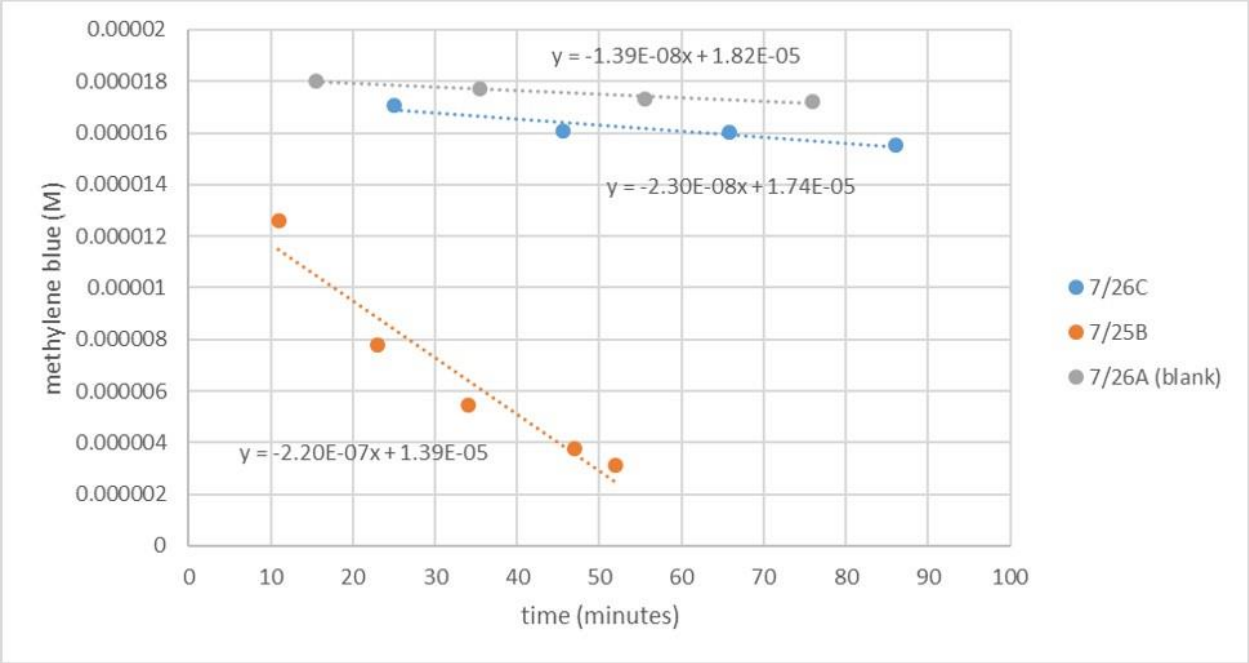

Figure 3. Kinetic plot of three reaction runs, showing the concentration of MB in solution versus time (minutes). Trend lines 7/26C and 7/25B correspond to samples 190715-01 and 190718-01, respectively. Trend line 7/26A corresponds to a MB baseline containing only MB.

Table 2 shows the relative rates of reaction of MB in the presence of the fiber samples using 400 nm irradiation. Although there is a lot of variation, the fibers with MXene react faster than those without. The fastest reaction is with 190726-01, used as the reference for the relative rates. This sample had almost the highest amount of MXene, although 190729-01 was higher. The treatment with 1 mL supernatant MXene solution in water was done to allow MXene sheets to attach to the outside of the fibers. This may have improved the rate for sample 190722-01-01.

It was not possible to determine the kinetic dependence on the concentrations of all the components or all of the fiber samples. That information could be useful to determine the reaction. A few studies to examine the rate dependence based upon the amount of fiber present were completed, and these resulted in a limited number of data points. The results of these studies are presented in Table 3. An extensive, detailed characterization of all the reagents in the reaction was not possible. In general, there did not appear to be a strong dependence of the reaction rate to the amount of fiber present. A change in the amount of fiber present, by a factor greater than 50 produced a change in reaction rate of less than 3 times, for specimen 190722-01-01. For specimen 190726-01, increasing the amount of fiber by 7.75 times the original mass doubled the reaction rate. For specimens 190729-01 and 190730-01, increasing the amount of fiber by 3 or 6 times, respectively, produced little change in the rate. This type of behavior is preliminary evidence that the fiber has catalytic effects on the reaction, but more study is needed to identify the sources of variation and find ways to optimize the rates.

4.3.2 CO_2 reduction studies

The composite MXene-TiO_2 fibers were evaluated for their photocatalytic potential to reduce CO_2. This potential application was guided by several journal articles which indicated that TiO_2, with or without MXene, may significantly improve reaction rates in CO_2 reduction.[31,32] Reducing CO_2 has recently gained a significant amount of interest due to its application in the solar energy industry, to decrease the amount of CO_2 released into the environment from industrial processes, or to make hydrocarbon fuels. This is typically a difficult reaction because it involves both reduction and oxidation steps.[32,33]

Preliminary studies did not show any reaction with fiber samples alone. Liu et al. utilized an amine modifier to produce amine-functionalized titanate nanosheets by adding diethylenetriamine.[32] As a result, we added the related compound diethylamine (Sigma-Aldrich® reagent grade) to the reaction mixture. With this amine modifier, interesting reaction products were observed. At present, the exact mechanism is not clear, the modifier may have helped couple with CO_2

so that it remained available, in close proximity, to the fiber material. Another amine modifier, ethylenediamine, did not show any reaction.

Table 2. Relative rates of MB reaction with the fiber samples.

Samples run (25 µL acetic acid + 100 µL 3% H_2O_2 in 10mL H_2O)					
Run name	**Fiber specimen**	**Weight of fiber (mg)**	**Rate (M-1 min-1)**	**Relative rate**	**Amt. MXene (Table 1)**
7/25 A	180607-1	1	3.80E-08	0.136	275 mg Mxene (dry flake)
7/25 B	190718-01	1.4	2.20E-07	0.788	1 mL DMF susp.
7/26 B	190712-01	4.65	4.49E-08	0.161	None
7/26 C	190715-01	1.2	2.30E-08	0.083	None
7/26 D	190718-01	1.9	8.46E-08	0.303	1 mL DMF susp.
7/26 E	190313-01	1.8	3.44E-08	0.123	1 mL DMF susp.
7/26 F	190722-01	2.1	7.83E-08	0.281	1 mL DMF susp.
7/26 G	190722A-01	2.5	8.12E-08	0.291	0.5 mL DMF susp.
7/26 H	190724-01	2.6	7.13E-08	0.256	0.1 mL DMF susp.
7/29 A	190715-01-01	3.7	9.45E-08	0.339	No DMF susp., 1 mL water supernatant
7/29 B	190722-01-01	3.8	1.94E-07	0.696	1 mL DMF susp, 1 mL water supernatant
7/31 B	190726-01	3.1	2.79E-07	1	1.1 mL DMF susp.
7/31 C	190726-01-01	1.6	7.51E-08	0.269	1.1 mL DMF susp, 1 mL water supernatant
8/1 A	190729-01	1.2	1.15E-07	0.413	1.5 mL DMF susp.
8/1 B	190730-01	2.4	1.61E-07	0.576	0.7 mL DMF susp.
8/5 A	190729-01	0.4	1.24E-07	0.445	1.5 mL DMF susp.
8/5 B	190730-01	0.4	1.35E-07	0.485	0.7 mL DMF susp.
8/5 C	190726-01	0.4	1.44E-07	0.516	1.1 mL DMF susp.

Table 3. Comparison of the reaction rates for various amount of fiber sample.

Run name	Fiber prep. Name	Weight (mg)	Rate	Relative rate
7/29 B	190722-01-01	3.8	1.94E-07	0.696
7/30 A	190722-01-01	0.38	1.54E-07	0.551
7/30 B	190722-01-01	0.76	9.70E-08	0.348
7/30 D	190722-01-01	0.076	6.87E-08	0.246
7/31 B	190726-01	3.1	2.79E-07	1
8/5 C	190726-01	0.4	1.44E-07	0.516
8/1 A	190729-01	1.2	1.15E-07	0.413
8/5 A	190729-01	0.4	1.24E-07	0.445
8/1 B	190730-01	2.4	1.61E-07	0.576
8/5 B	190730-01	0.4	1.35E-07	0.485

A series of fiber samples were compared using the headspace vial method with 400 nm radiation. Formation of a product identified as acetaldehyde was observed for all the fiber samples, this identification was made through analysis of the corresponding electron impact mass spectra. Acetaldehyde may be a possible reaction product from CO_2 reduction, but a literature search indicates it has never been previously reported as a product. Forming acetaldehyde involves a large number of reaction steps, including the formation of a C–C bond, compared with products that have

been reported such as formate, methanol, or methane, that do not involve production of a C–C bond but only reduction to add C–H bonds.

Blank runs were performed using the exact procedure and light exposure, but without adding any solid fibers. acetaldehyde was observed in only trace amounts. As a result, it appears that the product is not a contaminant, but it is not possible to rule out that it originates from the pristine or composite fibers. Diethylamine decomposing on the fibers could produce a byproduct, such as ethylamine, that would have a similar mass spectrum to acetaldehyde and could be the source.

Studies using D_2O rather than H_2O indicate that isotopically labeled water contributes to hydrogen in the product, although not all of it. Mass spectra of the products are shown in Figure 4, these show a shift in the mass spectral peaks for the ^1H and ^2H labels on the products from 44–47 amu. The shift indicates that the methyl group may be partially deuterated, since the M^+ peak moves from 44 amu to 47 amu, suggesting that three ^1H atoms have been replaced by two ^2H atoms. The envelope of peaks from 44–47 amu has a peak at every mass, rather than a peak only at every other mass, indicating that some ^1H are present. Both mass spectra have a peak at 29 amu, indicating that the CHO^+ fragment from the molecule has ^1H in both cases. At this time, the reaction does not appear to be catalytic, since the CO_2 reduction was never observed to go to completion. Even after several days on the light source, there was residual CO_2 remaining in the vial.

Further studies are underway to compare different MXene composite fiber samples. It may be possible to change the reaction conditions or to use different reagents to make the reaction go to completion. A study using isotopically labeled CO_2 is also possible.[14]

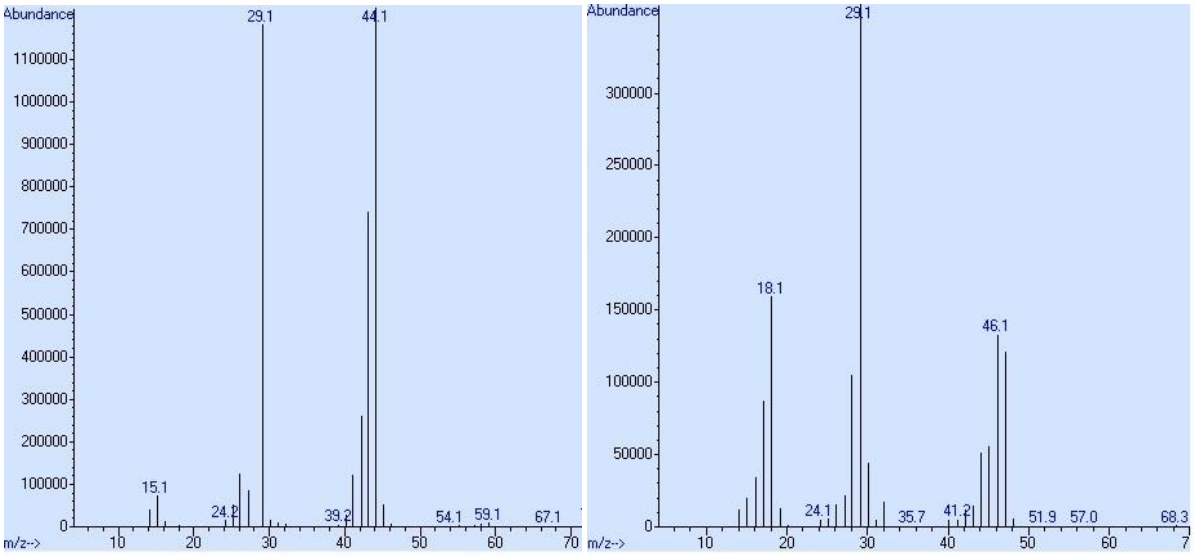

Figure 4. Acetaldehyde mass spectra observed from CO_2 reduction experiment mass spectral analysis. Left panel, using H_2O reagent as source of hydrogen (run 9/23 F); right panel, same reaction with D_2O as source of the hydrogen (run 9/13 A).

5. CONCLUSIONS

During the second year of this three-year effort, we confirmed our original hypothesis, that charge carriers would be excited at relatively long wave lengths (800 nm) and transferred to an adjacent semiconductor (titania). This phenomenon had previously been unreported in the scientific literature. We initiated photocatalytic and photochemistry studies to investigate potential application space for the composite materials, in particular we focused on CO_2 reduction to produce methane and photocatalytic degradation of dyes. This area of study appears to be fruitful, and there are several aspects that we will continue to study in order to explore possible applications of the materials. For the remainder of this study, we will explore novel methods to fabricate electrospun and composite materials to enhance the contact area between the TiO_2 fibers and MXene sheets; survey different ways to fabricate TiO_2 nanocomposites, including spin casting, to produce larger diameter fibers in a scalable process, and a new "yolk@shell" process[33] to produce spherical particles; characterize the materials using transient absorption

measurements to identify the highest performing materials, delivering the highest excitation; and gain a better understanding of the charge separation process through continued reactivity studies with MB reactions and the CO_2 reduction method, optimizing the reaction conditions to identify the best materials and understand the reaction mechanisms, and study reactions at longer wavelengths.

ACKNOWLEDGMENTS

Funding was provided by the U.S. Army via the Surface Science Initiative Program (PE 0601102A Project VR9) at the CCDC CBC. The authors further extend their gratitude to the Senior Research Scientists, internal and external senior scientists, and professionals who invested their time to evaluate the initial proposal and participate during the year-end Technical Advisory Board review. The authors acknowledge and thank the professionals at the W. M. Keck Center for Advanced Microscopy and Microanalysis at the University of Delaware for use of their instrumentation and support of this project.

REFERENCES

[1] Naguib, M.; Mochalin, V.N.; Barsoum, M.W.; Gogotsi, Y. 25th Anniversary Article: MXenes: A New Family of Two-Dimensional Materials. *Adv. Mater*. **2014,** *26* (7), pp 992–1005.

[2] Naguib, M; Kurtoglu, M.; Presser, V.; Lu, J.; Niu, J.; Heon, M.; Hultman, L.; Gogotsi, Y.; Barsoum, M.W. Two-Dimensional Nanocrystals Produced by Exfoliation of Ti_3AlC_2. *Adv. Mater*. **2011,** *23* (37), pp 4248–4253.

[3] Anasori, B.; Lukatskaya, M.R.; Gogotsi, Y. 2D metal carbides and nitrides (MXenes) for energy storage. *Nat. Rev. Mater*. **2017,** *2*, pp 1–27.

[4] Debow, S.M.; DeLacy, B.G.; Gogotsi, Y.; Rao, Y. Novel MXene/titania nanocomposite fibers for enhanced charge injection. *FY18 Proceedings of the Edgewood Chemical Biological Center In-House Laboratory Independent Research and Surface Science Initiative Programs*; U.S. Army Edgewood Chemical Biological Center: Edgewood, MD, **2019,** pp 77–88.

[5] Li, R.; Zhang, L.; Shi, L.; Wang, P. MXene Ti_3C_2: An Effective 2D Light-to-Heat Conversion Material. *ACS Nano*. **2017,** *11* (4), pp 3752–3759.

[6] Han, M.; Yin, X.; Li, X.; Anasori, B.; Zhang, L.; Cheng, L.; Gogotsi, Y. Laminated and Two-Dimensional Carbon-Supported Microwave Absorbers Derived from MXenes. *ACS Appl. Mater. Interfaces.* **2017,** *9* (23), pp 20038–20045.

[7] Li, X.; Yin, X.; Han, M.; Song, C.; Xu, H.; Hou, Z.; Zhang, L.; Cheng, L. Ti_3C_2 MXenes modified with in situ grown carbon nanotubes for enhanced electromagnetic wave absorption properties. *J. Mater. Chem. C.* **2017,** *5* (16), pp 4068–4074.

[8] Le Formal, F.; Pendlebury, S.R.; Cornuz, M.; Tilley, S.D.; Grätzel, M.; Durrant, J.R. Back Electron-Hole Recombination in Hematite Photoanodes for Water Splitting. *J. Am. Chem. Soc*. **2014,** *136* (6), pp 2564–2574.

[9] Liu, F.; Zhou, A.; Chen, J.; Jin, J.; Zhou, W.; Wang, L.; Hu, Q. Preparation of Ti_3C_2 and Ti_2C MXenes by fluoride salts etching and methane adsorptive properties. *Appl. Surf. Sci*. **2017,** *416*, pp 781–789.

[10] Mariano, M.; Mashtalir, O.; Antonio, F.Q.; Ryu, W-H.; Deng, B.; Xia, F.; Gogotsi, Y.; Taylor, A.D. Solution-processed titanium carbide MXene films examined as highly transparent conductors. *Nanoscale*. **2016,** *8* (36), pp 16371–16378.

[11] Pan, X.; Zhao, Y.; Liu, S.; Korzeniewski, C.L.; Wang, S.; Fan, Z. Comparing Graphene-TiO_2 Nanowire and Graphene-TiO_2 Nanoparticle Composite Photocatalysts. *ACS Appl. Mater. Interfaces*. **2012,** *4* (8), pp 3944–3950.

[12] Peng, C.; Yang, X.; Li, Y.; Yu, H.; Wang, H.; Peng, F. Hybrids of Two-Dimensional Ti_3C_2 and TiO_2 Exposing {001} Facets toward Enhanced Photocatalytic Activity. *ACS Appl. Mater. Interfaces*. **2016,** *8* (9), pp 6051–6060.

[13] Xiao, B.; Li, Y-C.; Yu, X-F.; Cheng, J-B. MXenes: Reusable materials for NH_3 sensor or capturer by controlling the charge injection. *Sens. Actuators, B.* **2016,** *235*, pp 103–109.

[14] Xue, Q.; Zhang, H.; Zhu, M.; Pei, Z.; Li, H.; Wang, Z.; Huang, Y.; Huang, Y.; Deng, Q.; Zhou, J.; Du, S.; Huang, Q.; Zhi, C. Photoluminescent Ti_3C_2 MXene Quantum Dots for Multicolor Cellular Imaging. *Adv. Mater*. **2017,** *29* (15), p 1604847.

[15] Ling, Z.; Ren, C.E.; Zhao, M-Q.; Yang, J.; Giammarco, J.M.; Qiu, J.; Barsoum, M.W.; Gogotsi, Y. Flexible and conductive MXene films and nanocomposites with high capacitance. *Proc. Natl. Acad. Sci. U.S.A.* **2014,** *111* (47), pp 16676–16681.

[16] Tian, Y.; Yang, C.; Que, W.; Liu, X.; Yin, X.; Kong, L.B. Flexible and free-standing 2D titanium carbide film decorated with manganese oxide nanoparticles as a high volumetric capacity electrode for supercapacitor. *J. Power Sources*. **2017,** *359*, pp 332–339.
[17] Wen, Y.; Rufford, T.E.; Chen, X.; Li, N.; Lyu, M.; Dai, L.; Wang, L. Nitrogen-doped $Ti_3C_2T_x$ MXene electrodes for high-performance supercapacitors. *Nano Energy*. **2017,** *38*, pp 368–376.
[18] Xin, Y.; Yu, Y-X. Possibility of bare and functionalized niobium carbide MXenes for electrode materials of supercapacitors and field emitters. *Mater. Des*. **2017,** *130*, pp 512–520.
[19] Xu, S.; Wei, G.; Li, J.; Ji, Y.; Klyui, N.; Izotov, V.; Han, W. Binder-free $Ti_3C_2T_x$ MXene electrode film for supercapacitor produced by electrophoretic deposition method. *Chem. Eng. J.* **2017,** *317*, pp 1026–1036.
[20] Maleski, K.; Ren, C.E.; Zhao, M-Q.; Anasori, B.; Gogotsi, Y. Size-Dependent Physical and Electrochemical Properties of Two-Dimensional MXene Flakes. *ACS Appl. Mater. Interfaces.* **2018,** *10* (29), pp 24491–24498.
[21] Yu, J.; Jaroniec, M.; Lu, G. TiO_2 Photocatalytic Materials. *Int. J. Photoenergy*. **2012,** *2012*, pp 1–5.
[22] Guo, Q.; Ma, Z.; Zhou, C.; Ren, Z.; Yang, X. Single molecule photocatalysis on TiO_2 surfaces. *Chem. Rev*. **2019,** *119* (20), pp 11020–11041.
[23] Schneider, J.; Matsuoka, M.; Takeuchi, M.; Zhang, J.; Horiuchi, Y.; Anpo, M.; Bahnemann, D.W. Understanding TiO_2 Photocatalysis: Mechanisms and Materials. *Chem. Rev.* **2014,** *114* (19), pp 9919–9986.
[24] Linsebigler, A.L.; Lu, G.; Yates, J.T., Jr. Photocatalysis on TiO_2 surfaces: Principles, Mechanisms, and Selected Results. *Chem. Rev*. **1995,** *95* (3), pp 735–738.
[25] Mayerberger, E.A.; Urbanek, O.; McDaniel, R.M.; Street, R.M.; Barsoum, M.W.; Schauer, C.L. Preparation and characterization of polymer-$Ti_3C_2T_x$ (MXene) composite nanofibers produced via electrospinning. *J. Appl. Polym. Sci.* **2017,** *134* (37), pp 1–7.
[26] Liu, J.; McCarthy, D.L.; Cowan, M.J.; Obuya, E.A.; DeCoste, J.B.; Skorenko, K.H.; Tong, L.; Boyer, S.M.; Bernier, W.E.; Jones, W.E., Jr. Photocatalytic activity of TiO_2 polycrystalline sub-micron fibers with variable rutile fraction. *Appl. Catal., B.* **2016,** *187*, pp 154–162.
[27] Ghidiu, M.; Lukatskaya, M.R.; Zhao, M-Q.; Gogotsi, Y.; Barsoum, M. Conductive two-dimensional titanium carbide 'clay' with high volumetric capacitance. *Nature*. **2014,** *516*, pp 78–81.
[28] Kiennork, S; Nakhowong, R; Chueachot, R; Tipparach, U. Preparation and Characterization of Electrospun TiO_2 Nanofibers via Electrospinning. *Integr. Ferroelectr*. **2015**, *165* (1), pp 131–137.
[29] Mahshid, S.; Askari, M.; Ghamsari, M.S. Synthesis of TiO_2 nanoparticles by hydrolysis and peptization of titanium isopropoxide solution. *J. Mater. Process. Technol.* **2007,** *189* (1–3), pp 296–300.
[30] Mills, A. An overview of the methylene blue ISO test for assessing the activities of photocatalytic films. *Appl. Catal., B.* **2012,** *128*, pp 144–149.
[31] Low, J.; Zhang, L.; Tong, T.; Shen, B.; Yu, J. TiO_2/MXene Ti_3C_2 composite with excellent photocatalytic CO_2 reduction activity. *J. Catal*. **2018,** *361*, pp 255–266.
[32] Liu, S.; Xia, J.; Yu, J. Amine-Functionalized Titanate Nanosheet-Assembled Yolk@Shell Microspheres for Efficient Cocatalyst-Free Visible-Light Photocatalytic CO_2 Reduction. *ACS Appl. Mater. Interfaces*. **2015,** *7* (15), pp 8166–8175.
[33] Morris, A.J.; Meyer, G.J.; Fujita, E. Molecular Approaches to the Photocatalytic Reduction of Carbon Dioxide for Solar Fuels. *Acc. Chem. Res.* **2009,** *42* (12), pp 1983–1994.
[34] Jnawali, G.; Rao, Y.; Yan, H.; Heinz, T. Observation of a transient decrease in terahertz conductivity of single-layer graphene induced by ultrafast optical excitation. *Nano Lett*. **2013,** *13* (2), pp 524–530.
[35] Mowry, S.; Ogren, P.J. Kinetics of methylene blue reduction by ascorbic acid. *J. Chem. Educ.* **1999,** *76* (7), pp 970–973.
[36] Salem, I.A.; El-Maazawi, M.S. Kinetics and mechanism of color removal of methylene blue with hydrogen peroxide catalyzed by some supported alumina surfaces. *Chemosphere*. **2000,** *41* (8), pp 1173–1180.

Towards understanding the role of material voids and porosity on transport

Jerry B. Cabalo[a*], Angela M. Zeigler[a], Roseanna N. Zia[b], Brian K. Ryu[b], Mark J. Varady[a], Devon A. Boyne[c], Melissa S. Hulet[c], Erica R. Valdes[a], Bradley R. Ruprecht[d]
[a]U.S. Army Combat Capabilities Development Command Chemical Biological Center, Research & Technology Directorate, 8198 Blackhawk Rd, Aberdeen Proving Ground, MD 21010
[b]Stanford University, Department of Chemical Engineering, 443 Via Ortega, Stanford, CA 94305
[c]Leidos, P.O. Box 68, Gunpowder Branch, Aberdeen Proving Ground, MD 21010
[d]U.S. Army Combat Capabilities Development Command Chemical Biological Center, Engineering Directorate, 8198 Blackhawk Rd, Aberdeen Proving Ground, MD 21010

ABSTRACT

The fundamental study of how material porosity affects transport is closely related to additive manufacturing. While the transport properties and permeability of bulk samples of polymeric material are well known, the effect of porosity and defects on the permeability of such materials is not. This knowledge is highly desirable for energy storage, energy exploration, and the Army-specific environmental protective equipment against chemical and biological agents. This knowledge potentially permits use of additive manufacturing for protective equipment, thus greatly reducing the logistics burden while building equipment readiness. Although the interaction between an analyte chemical and a bulk material dominate transport across the bulk, it is hypothesized that the vapor pressure of the analyte contributes significantly to transport rates in the presence of voids and porosity. The construction of the necessary infrastructure to perform this study is reported here. Parts fabricated using three types of additive manufacturing techniques were characterized quantitatively using micro-computed tomography imaging, and qualitatively with scanning electron microscopy and optical microscopy. A specialized test set-up with mass spectrometer was utilized to measure solvent vapor breakthrough as a function of time. Quantitative measurements were used to construct physically realistic simulations and these results were compared to simulations.

Keywords: transport, voids, porosity, mesoscale, additive manufacturing, 3D printing, microscopy, micro-computed tomography

1. INTRODUCTION

The effect of transport across porosity and voids within a material is of great importance to the Army and is worthy of study. This phenomenon is closely related to additive manufacturing or 3D printing. 3D printing is an emerging technology that is of interest to the Army because it potentially greatly reduces the logistics and supply chain burden. 3D printing affects a number of application areas, such as weapons and body armor,[1] or protective equipment. For example, the Stars and Stripes reported that airmen had modified air masks using 3D-printed parts.[2] This demonstrates how additive manufacturing provides the capability to custom form protective equipment for individual Warfighters, reducing the need to transport and maintain large inventories of many sizes to ensure a good fit to every Warfighter. A strong advantage of 3D-printed parts is the ability to manufacture complex parts without any additional burden. This capability contributes to equipment readiness, which in turn contributes to the battle readiness line of effort in the 2018 Army Strategy.[3]

However, there is a significant technical barrier to the implementation of 3D printing, especially with respect to protective equipment. The ability of materials formed by additive manufacturing to provide protection from chemical warfare agents or other toxic chemicals is not well known, due to porosity and voids inherent in many additive manufacturing processes.[4,5] In other words, how these defects affect material permeability is not well known. To enable the Army to fully exploit the potential of additive manufacturing, there is a need for a fundamental understanding of how porosity and voids (i.e., defects) affect transport through material in general.

The presence of voids or other subsurface defects in 3D-printed parts are inherent to the methods utilized. For example, with laser sintering, a bed of powdered material, either metal or thermoplastic, is presented to a high-powered laser. The laser heats the powder and fuses particles together. To add additional material, the part is built up with additional layers of powder, which are then subsequently heated by a laser, thus fusing the additional powder, and melting a thin layer that fuses the new layer to the growing part. Creating a continual cycling of heating/melting, vaporization, and cooling that results in porosity and voids that would not be otherwise present in a conventionally manufactured part.[6]

The fundamental phenomenon of transport through porous media affects other application areas that are relevant. The energy industry fully explores the transport of hydrocarbons through porous stone, which is a similar problem. The fundamental knowledge gap is how voids and porosity affect the transport of chemicals or liquids through a "solid" material. The work reported here also affects the study of the flow of analytes through homogeneous or heterogeneous coating materials, as well as naturally porous ones (e.g., rock).[7–10]

The objective is to understand the mechanism of transport through porous polymeric materials. In the case of metals, it is expected that diffusion through the solid particles is too slow for relevant study, and so the focus is on polymers. Although the interaction between an analyte and the polymer control transport in the case of a bulk sample, it is hypothesized that vapor pressure of the analyte controls the transport rate across voids and through pores. A number of possible factors are considered in the transport process. The first factor is percolation through the solid, that is, transport through interconnected pores. We do not expect interconnection of pores and voids unless enough material is vaporized in the buildup process by the fusing laser such that vapor must escape. Only in very foam-like materials do we expect this property. The second factor that is considered is the strength of attraction between chemicals or solvents of interest and the bulk polymer, analogous to fast wetting of hydrophilic materials versus slow diffusion through hydrophobic matrices. The third factor to consider is the vapor pressure of the transported chemical. If the vapor pressure is low, then when a void is encountered in the bulk material it acts like a barrier and may slow transport. If the vapor pressure is high, then voids may enhance transport as the material could "jump" across the void. Varady et al.[11] considered this possibility with a continuum-based model that predicts an enormous effect on transport based on porosity parameters. A fourth factor to consider is surface transport within voids and reabsorption into the bulk after a void is crossed. Lastly, there may be other interfaces within polymeric materials other than voids, analogous to metal crystal grains found in bulk metals. These interfaces may also influence transport.

The first-year progress described in this report focuses on the building of the experimental and modeling infrastructure. This infrastructure is the foundation for the investigation of the influence of voids and porosity on transport of a chemical of interest through a bulk polymer.

2. METHODS

To achieve the goal of testing the role of solvent vapor pressure in its ability to permeate a void or porous medium, especially of the length scales encountered with additive manufacturing, the overall approach is a combined experimental and modeling effort. In this first year of the program, the necessary experimental and modeling tools were established. Measurements of the subsurface structure of 3D-printed parts with microscopy established the precise length scales involved. Thin samples with similar substructure were also produced and characterized. Using these samples, breakthrough measurements of solvent were performed. Using the measurements of subsurface voids and pores, physically realistic mesoscale models were constructed and used for initial simulations.

2.1 3D printing methods

At this time, additive manufacturing—3D printing technology—is rapidly expanding. A wide range of materials are currently available that include polymers, metals, and even ceramics. To limit this study to a reasonable scope, the materials were limited to polymer "inks" and three main printing methods were used.

The first printing method considered was fused deposition modeling (FDM) of a black polycarbonate acrylonitrile butadiene styrene (PC-ABS) thermoplastic. The polymer is heated until it melts or fuses and is extruded through the print nozzle. The nozzle is rastered across the desired cross section of the part to build that part layer-by-layer. The direction of the print rastering is rotated 90 ° for each layer to ensure maximum strength. As the melted thermoplastic is deposited, it fuses with the layer below as well as the adjacent bead to build up the part. There is potential for voids or defects between subsequent layers as well as between beads within a single layer. The speed at which the printing head is moved can affect the structure of subsurface voids.

The second printing method examined was selective laser sintering (SLS) with glass-filled nylon. The feedstock consisted of a powdered mixture of nylon and glass beads. The glass beads typically provide desired strengthened structural properties. The powdered mixture was spread in a thin layer, and a focused high-power CO_2 laser was used to melt and fuse the powder together. The laser is only rastered across the desired cross section of the part. A fresh layer of feedstock powder is spread over the growing part, and the laser fuses the next layer to the previous layer as well. A part is thus constructed layer-by-layer. Upon completion of the part, it is suspended in a bed of the unfused, leftover feed stock and must be removed. Voids potentially can arise between grains of the feedstock powder. Additive manufacturing of metal and other non-polymeric materials often use a similar powdered bed approach. It is likely voids observed for the glass-filled nylon 3D-printed parts will be observed in other materials.

The third printing method examined involves stereolithography (SLA or stereolithography apparatus). This method is limited to polymers that can be optically cured, typically with a 355 nm or 405 nm laser, or imaging of a high-power UV lamp. The monomeric resin resides in a bath or reservoir. The cross section of the part is selectively cured with the UV light. For the laser light sources, the focused laser spot is rastered across the cross section of the part to make a solid slice of the part. In newer printers, the output of a UV lamp can be imaged to form the cross section of the part. To form the next layer, a fresh layer of monomer is spread over the previous slice, and a subsequent layer is built by UV curing. In this method, there is potential for the presence of voids between layers. For this study, an SLA elastomeric material was used.

Samples were printed using all three methods. To enable breakthrough measurements, 1-inch x 1-inch-thin samples of varying thickness were produced. In addition, parts were designed to capture different print conditions—including pyramids with a 2-inch x 2-inch base by 2-inch height, and a prism shape with a cylindrical handle (2-inch x 2-inch by 1-inch base and a handle with a 0.5-inch diameter, 1 inch in height).

2.2 Microscopy methods

Three microscopy methods were performed to capture the dimensions of pores and voids in the 3D-printed material. First, confocal optical microscopy in visible wavelengths was performed. However, it was difficult to extract quantifiable data, even though the system used the capability to produce 3D data. Characterization of the materials via optical microscopy was discontinued.

Scanning electron microscopy (SEM) was also performed to characterize the materials. It was expected that this method would capture, at least, porosity visible on the surfaces imaged. However, it proved difficult to capture many measurements, and of these measurements, all were confined to the surfaces of the material.

The third method of microscopy performed was micro computed tomography (micro-CT) X-ray microscopy. This technology is essentially the same as computerized axial tomography X-ray imaging—CAT scans. A series of X-ray images are recorded around an axis of an object to be imaged. The data is reconstructed into a 3D image using computerized algorithms. For micro-CT, spatial resolution of ~100 nm is possible. The parts for this study were characterized at the Combat Capabilities Development Command (CCDC) Army Research Laboratory (ARL). The data was encoded as an MPEG movie file, where each movie frame was an image of the slice of the 3D-printed part. Thus, in reality, each pixel in an image represented a voxel—a volume element in the data. A length scale was present in the data that permitted the determination of the length of each voxel.

2.3 Software for quantitative measurement of pores and voids from micro-CT data

Quantitative data was extracted from the movie file using software written in MATLAB® version R2016b. First, the movie data was read into MATLAB® as a 3D array of voxel intensities from the images. The value of each voxel was directly proportional to the density of the respective volume element. A threshold value was determined from an analysis of the intensities to determine the difference between voids and solid material.

For statistical measurements of voids in the 3D materials, 10,000 measurements were taken in a Monte Carlo approach. The coordinates of a point within the part were randomly selected, targeting points that lay inside the internal void structure of the part. If the point selected was outside of the part, then that point was ignored and not counted as a measurement and another random point was selected. To determine if a point lay inside or outside, measurements were taken along all six directions along the three Cartesian axes. If the outside of the data box was encountered in any direction, the point was counted as outside the part. Next, the value of the randomly selected point was evaluated whether its value was greater or less than the threshold value used to differentiate solid from void. If counted as solid, a count was recorded, but no measurement taken or counted. If the point lay inside a void, three measurements were

taken. First, a count was recorded for voids rather than solid. A ratio of void counts to total number of counts within the part would give a ratio of void volume to solid volume for the part. Second, a diameter measurement was recorded. The distance from the point to the walls along all six directions of the three Cartesian axes was taken. It was assumed that the lengths along each axis corresponded to the axes of an ellipse within each of the three Cartesian planes, namely the *xy*, *xz*, and *yz* planes. The area of each ellipse, using the lengths of the axes *A* and *B*, was computed via

$$Area = 1/4\,(A)(B)\pi \tag{1}$$

resulting in three ellipse area values. The minimum value was selected resulting in selection of the plane with the minimal area. For the sake of simplification, the radius of a circle that equaled the area thus determined was reported as the radius of the void. This approach is justified because the voids can assume arbitrary shapes, and approximation of complex shapes with simple shapes is a common practice.

Length measurements were performed in the following manner. For each random point found to reside in a void or pore, the maximum length measurement along the Cartesian axes from the point to a wall was determined. At the point of a wall, additional measurements were taken along the four orthogonal directions. If additional length was encountered, that length was added to the measurement. When a wall was encountered, another set of measurements ensued. Measurements ceased when a dead end was reached—when a wall was encountered in any direction. These lengths were then recorded. To avoid infinite loops in the event a measurement without voids was encountered, if 1,000,000 measurements were attempted before the limit of 10,000 was reached, the measurements ceased as well.

The result of the measurement process was typically 10,000 measurements of void diameters and void lengths. The distribution of the measurements as a function of diameter and void length were determined by binning the measurements and summing the results by bin.

2.4 Laboratory measurements of breakthrough

Two methods of recording saturated chemical vapor breakthrough time were attempted. The first used attenuated transmission (ATR) IR spectroscopy. A film or sample of the 3D-printed material was brought into contact with the surface of the ATR crystal. The opposite side was exposed to saturated vapor of isopropyl alcohol (IPA). Breakthrough time was determined between the time of IPA introduction on one side and observation of IPA IR absorption signature on the other side. This method was abandoned when it became clear that the 3D-printed sample did not remain in close enough contact with the ATR crystal to record a measurement.

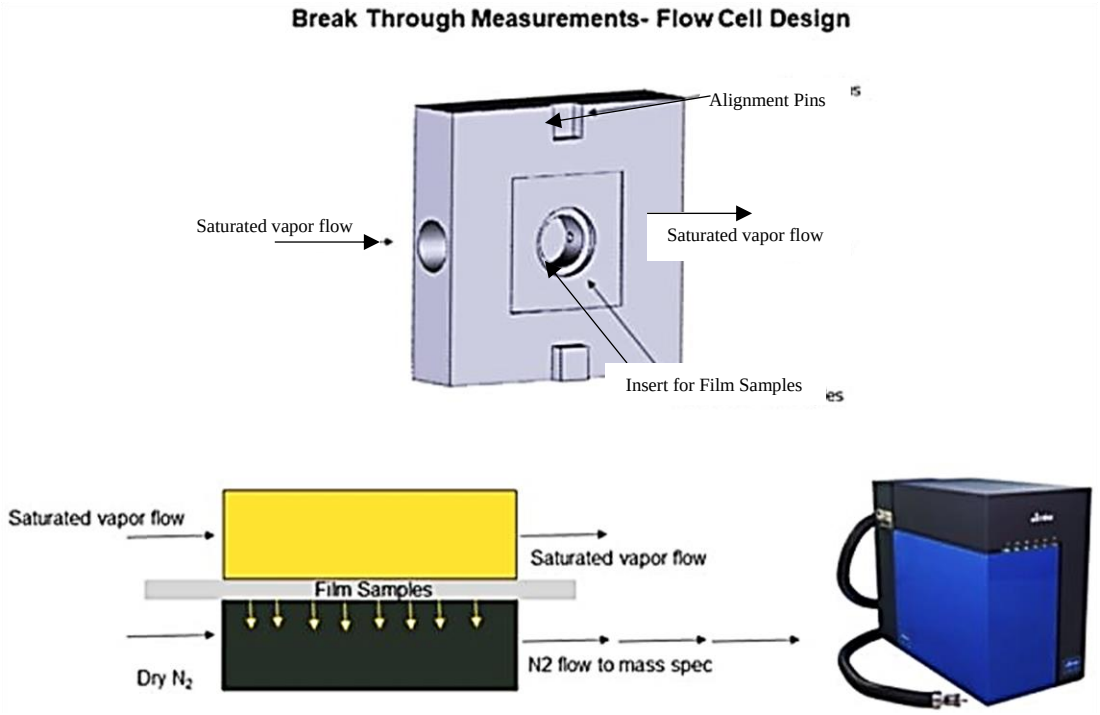

Figure 1. Design for breakthrough measurements. Design for flow cell composed of two halves that are identical pieces as shown (top). Schematic for operation (bottom).

The second method used a special mount for the sample made from acrylic-based photopolymer. The measurement has to limit the pressure differential across the sample to accommodate thin samples. The top of Figure 1 shows half of the sample holder, with channels to introduce saturated vapor flow. A recessed area accepts the polymeric sample with a channel for an O-ring to make a seal. An identical corresponding part completes the seal with a corresponding channel for dry nitrogen. Flows are adjusted to minimize the pressure differential across the sample. The dry nitrogen flow is connected to the inlet of a mass spectrometer that detects very low levels of vapor as it permeates the sample. The mass spectrometer signal is monitored as a function of time after release of the IPA vapor to determine the breakthrough measurements.

2.5 Simulation method

Simulations are performed using a unified atom approach in order to enable work at the micrometer scale. When atoms are explicitly included and the simulation length scale is greater than 10 nm, then the number of individual atoms becomes computationally intractable. To extend the length scale to relevant lengths, it becomes necessary to treat groups of atoms as a single particle. Instead of a force field that describes interactions between atoms, an approximate force field must be used to describe interactions between these unified atoms. A force field describes all possible interactions between particles in the simulation, including the bonding force between atoms, the force between angular and torsional motions, as well as weaker interactions such as van der Waals interactions. As shown in Figure 2, polymer molecules were approximated as a single spherical particle, and packed into a simulation box with a length scale of tens of micrometers. Voids were created by removal of polymer particles from randomly selected spheres, where the sphere sizes were made to mirror micro-CT measurements. The volume fraction of voids could also be made to mirror the experimental measurements. Figure 2 shows examples of the resulting simulation box.

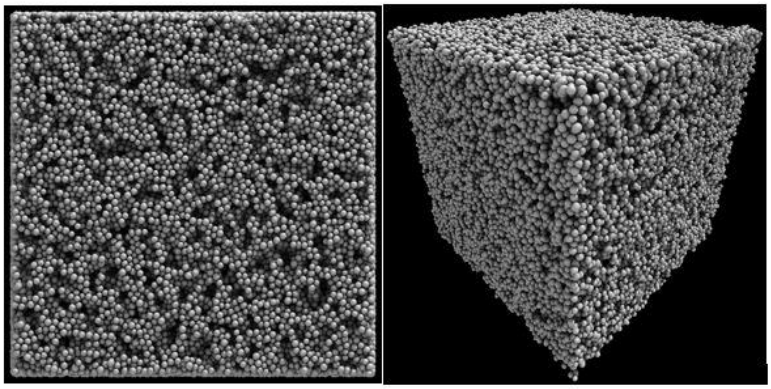

Figure 2. Representations of the simulation box with pore network. The left panel shows a side-on view, and the right panel shows a 3D edge-on view of the simulation box.

The Large-scale Atom/Molecule Massively Parallel Simulator (LAMMPS)[12] software platform was used to perform the simulations. Several thousand particles representing vapor solvent molecules were introduced on one side of the simulation box. A constant force simulating pressure was applied to each solvent particle and the particles were then allowed to percolate through the pore/void network. Tracking of the particles as they reached the opposite side of the simulation box permitted simulation of the breakthrough time.

3. RESULTS AND DISCUSSION

Progress was made during the first year of performance in several areas. Quantitative microscopy was performed and used to build realistic models for simulations. At the same time, a capability was made to measure solvent breakthrough across 3D-printed samples of varying thickness. Preliminary simulations were performed and qualitatively compared to laboratory breakthrough measurements.

3.1 Quantitative measurements of void structures with microscopy

Samples of FDM, SLS, and SLA 3D printing techniques were examined with SEM microscopy, while measurements of FDM and SLS samples were performed with micro-CT X-ray microscopy. Figure 3 shows an example of an SEM image compared to a micro-CT micrograph, both of an FDM-manufactured part. The SEM qualitatively shows the

three fused layers, with a potential void between the interface between layers. However, the SEM is only capable of showing structure on the surface of a part. Furthermore, it is difficult to determine in the image what constitutes a void or pore, and certainly not quantitatively. On the other hand, the micro-CT image clearly shows the void structure between subsequent beads as a given cross section of the part is built up. However, the micro-CT image is a single slice of a 3D array of density data, and it was possible to take quantitative measurements from this set of data.

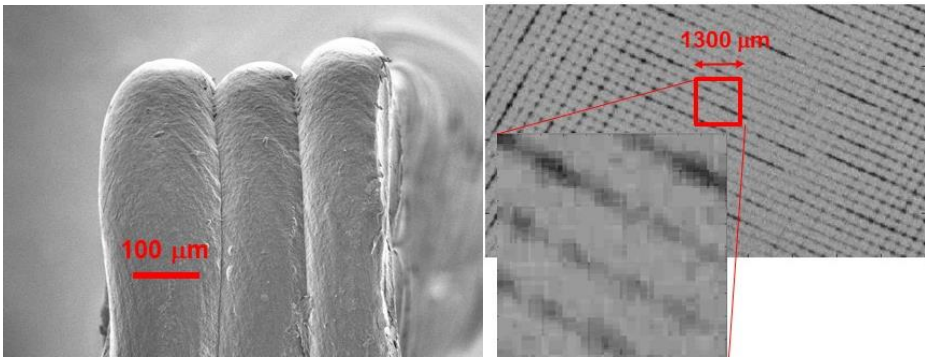

Figure 3. Left: SEM of FDM PC-ABS showing the surface of the edge of three FDM layers. Right: Micro-CT microscopy showing voids at the edge of the layers.

Figure 4 shows the results of quantitative measurements of the micro-CT data. The numbers on the *x*, *y*, and *z* axes correspond to number voxels. The physical length of each voxel was determined using a calibrated scale embedded with the data. For the data in Figure 4, the voxel length was 13.1 μm, given the overall dimensions of the cube shown to be 1,310 μm on a side. Each measurement within the void network is plotted as a point in the chart. Given that 10,000 measurements were performed, the plot shows the void network within the part volume. For each measurement, both the diameter of the void and its apparent length are measured at each randomly chosen measurement point. While it is true that the code is simplified by confining the measurement to the planes containing the Cartesian axes, nevertheless, a statistical view of the pore dimensions is determined. To demonstrate that the measurements thus obtained agree with the microscopy measurements, a sample of measured diameters and void lengths are shown in Figure 4. The diameters appear as circles and measured lengths as lines. It can be seen that the diameter and length measurements do not exceed the dimensions of the void spaces as shown by the individual measurements.

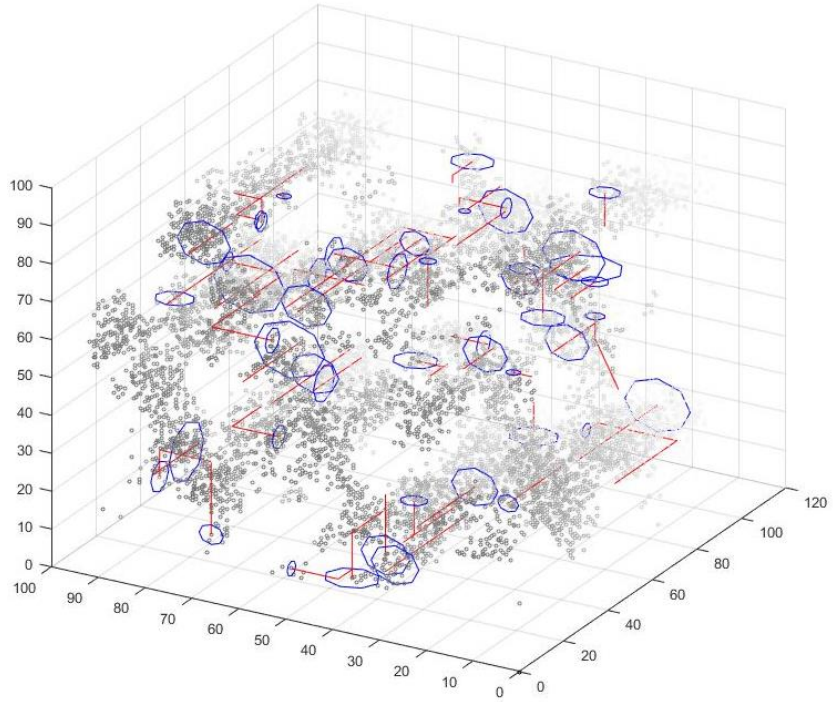

Figure 4. Representation of measurements of void structure. Circles represent the diameter measurements, and lines represent length measurements. The measurement box is 1,310 μm on a side.

Figure 5 shows the microscopy of the interface between the cylindrical handle and the prism components of a 3D-printed part. A number of observations can be made. First, the density of the handle and the base parts are different. The brightness of a voxel in the image indicates its density, and there is a clearly visible difference in intensity between different regions in the same part made by the same print method. There is also a clear difference in the apparent size of the voids between FDM beads. Towards the edges of the cylindrical component, there appears to be less void space and the FDM beads appear more tightly packed. We attribute this physical change to a change in the print conditions.

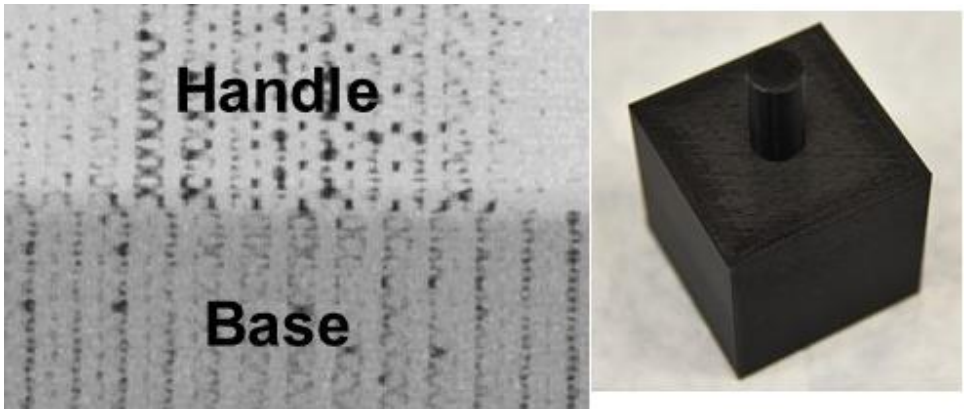

Figure 5. Left: Micro-CT micrograph of the interface between two portions of the part. Right: A photograph of the 3D-printed part.

Figure 6 shows the numerical distribution of measurements for void diameters (left) as well as void lengths (right). The distributions of void diameters for the two portions of the part are essentially identical, with an average diameter of 54.5 μm in the base and 53.9 μm in the handle. For the average void length, the base had 695.1 μm and the handle had 467.8 μm. For the case of voids in the base of the part, there appeared to be a bi-modal distribution of diameters while the distribution in the handle appeared to have a single peak, but with a tail towards the higher void lengths. An explanation for this difference is not available without additional measurements.

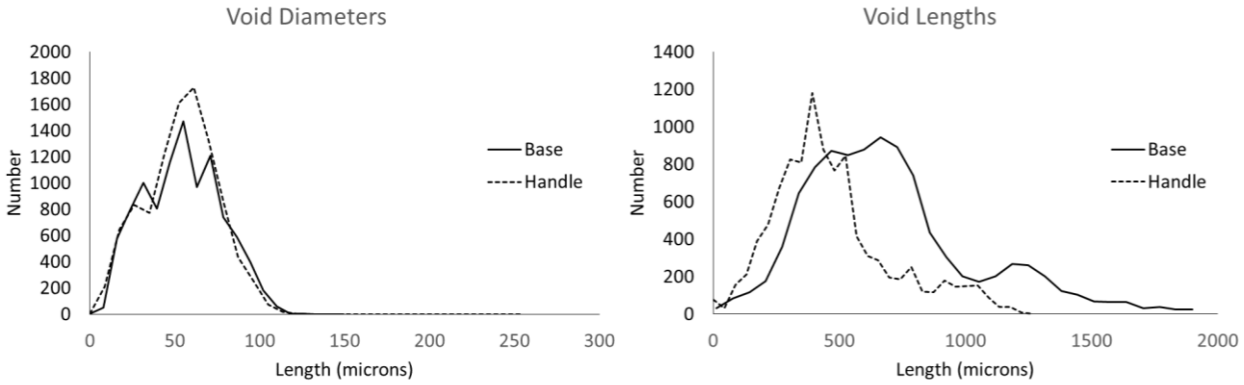

Figure 6. Left: Quantitative measurements of void diameters. Right: Void lengths for the two different regions of the same part.

Measurements were also performed for the same part design except using the SLS nylon/glass composition, with significantly different results. Voids were on average 2.2 μm in diameter and 1.23 μm long—basically spherical, on average. Additional analysis is planned when data from parts made by all three 3D printing methods becomes available.

The microscopy enabled measurements were used for the infrastructure to compare experiment to simulations. The statistical distribution of void diameters and lengths were replicated in the construction of the simulation model shown in Figure 7. The particles shown at the very top of the graphic are the solvent tracer particles used in the simulation. The number of particles could be tracked as they moved through the pore network to arrive at the opposite of the simulation box. In the left side of Figure 8, experimental data for the breakthrough of IPA through the PC-ABS sample part is shown. For the breakthrough of IPA, the mass to charge (*m/z)* 25 fragment peak in the mass spectrum was monitored as a function of time. For the PC-ABS part, the breakthrough time was nearly instantaneous, with a steep

rise time to the steady state concentration of vapor. This experimental data could be simulated. The chart on the right of Figure 8 shows the rate of solvent molecules passing through the part as a function of dimensionless time. A rise time—a period of steady state transport—and a fall time can be predicted. With scaling of the model, this predicted time can be related to the laboratory time frame. It is expected that this model will enable breakthrough times as a function of porosity structure to be simulated. Such simulations will provide detailed insight into the influence of porosity on transport.

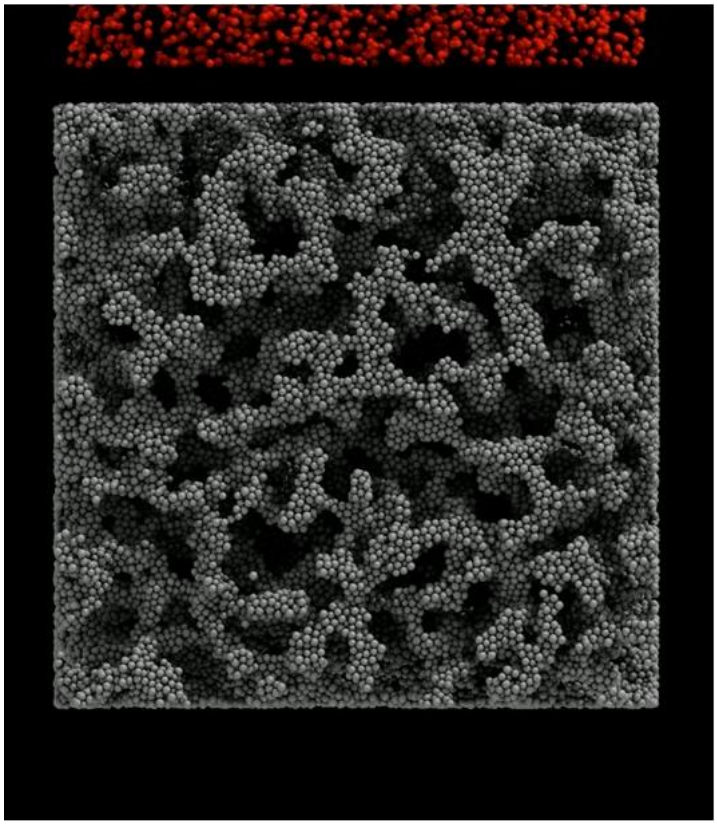

Figure 7. Pictorial representation of the porous model that has the same porosity characteristics as the microscopy measurements.

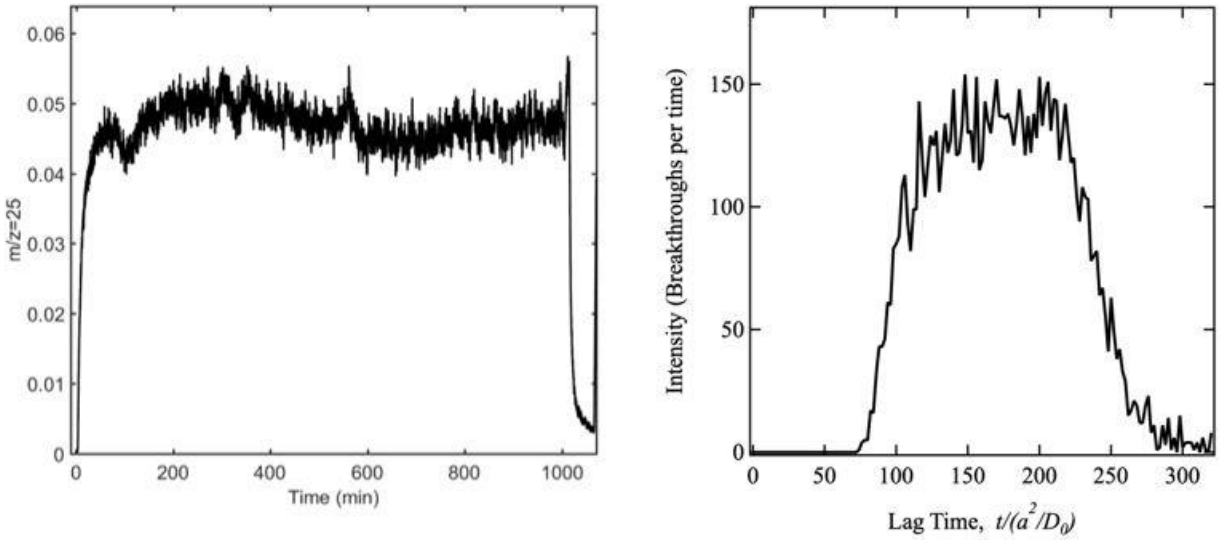

Figure 8. Left: Experimental trace of IPA ion signal as a function of time. Right: Initial results of the simulated breakthrough time in dimensionless time.

4. CONCLUSIONS

With the goal of understanding the role of porosity, voids, and defects on the transport of chemical compounds across a bulk polymeric material, three significant advances were made. First, a representation of methods of 3D printing or additive manufacturing was obtained by fabricating test parts made by FDM of PC-ABS, SLS of nylon and glass spheres, and SLA of an elastomeric material. These were then qualitatively characterized with SEM and optical microscopy, and quantitatively characterized with micro-CT X-ray imaging. Software was generated in-house to process the micro-CT data. Second, an optimal method of measuring breakthrough time was determined using mass spectrometry. An approach using ATR-IR spectroscopy was considered but was found to be ineffective. It was shown that breakthrough time was greatly affected by the 3D print method and material, and that measurements could be obtained from relevant samples. Third, significant progress was made in exploiting the quantitative measurements to build an accurate model of the voids in a 3D-printed part. Initial modeling results show that the rise and fall times can be simulated, but additional scaling is required to directly relate to experimental measurements.

ACKNOWLEDGMENTS

Funding was provided by the U.S. Army via the Surface Science Initiative Program (PE 0601102A Project VR9) at the CCDC Chemical Biological Center. The authors also thank Dr. Harvey Tsang of the CCDC ARL for assisting with the micro-CT measurements of the 3D-printed parts, as well as Dr. Anand Sampath of the CCDC ARL.

REFERENCES

[1] Mizokami, K. The U.S. Army Is Working on 3D Printed Body Armor. https://www.popularmechanics.com/military/research/a28425864/us-army-28425863d-printing-body-armor/ (accessed July 27, 2019), *Popular Mechanics*, July 18, 2019.

[2] Robson, S. Yokota airmen improve gas mask with 3D printer, potentially saving Air Force $8 million or more. https://www.stripes.com/news/yokota-airmen-improve-gas-mask-with-3d-printer-potentially-saving-air-force-8-million-or-more-1.531504 (accessed July 27, 2019), *Stars and Stripes*, June 7, 2018.

[3] Milley, M.; Esper, M. *The Army Strategy*; The U.S. Army: Washington D.C., **2018;** pp 1–11.

[4] Cerniglia, D.; Scafidi, M.; Pantano, A.; Rudlin, J. Inspection of additive-manufactured layered components. *Ultrasonics.* **2015,** *62*, pp 292–298.

[5] Lewis, G.K.; Schlienger, E. Practical considerations and capabilities for laser assisted direct metal deposition. *Mater. Des.* **2000,** *21* (4), pp 417–423.

[6] Zhang, D.; Niu, W.; Cao, X.; Liu, Z. Effect of standard heat treatment on the microstructure and mechanical properties of selective laser melting manufactured Inconel 718 Superalloy. *Mater. Sci. Eng. A.* **2015,** *644*, pp 32–40.

[7] Boudreau, B.P. The diffusive tortuosity of fine-grained unlithified sediments. *Geochim. Cosmochim. Acta.* **1996,** *60* (16), pp 3139–3142.

[8] Latour, L.L.; Kleinberg, R.L.; Mitra, P.P.; Sotak, C.H. Pore-Size Distributions and Tortuosity in Heterogeneous Porous Media. *J. Magn. Reson., Ser. A.* **1995,** *112* (1), pp 83–91.

[9] Torres-Sanchez, C.; Corney, J.R. Porosity tailoring mechanisms in sonicated polymeric foams. *Smart Mater. Struct.* **2009,** *18* (10), pp 104001–104014.

[10] Shen, L.; Chen, Z. Critical review of the impact of tortuosity on diffusion. *Chem. Eng. Sci.* **2007,** *62* (14), pp 3748–3755.

[11] Varady, M.J.; Pearl, T.P.; Bringuier, S.A.; Mantooth, B.A. Vapor emission from porous mateirals with diffusive transport in the solid-phase. *Int. J. Heat Mass Transfer.* **2017,** *114*, pp 758–768.

[12] Plimpton, S. Fast Parallel Algorithms for Short-Range Molecular Dynamics. *J. Comput. Phys.* **1995,** *117* (1), pp 1–19.

A combined density functional theory and grand-canonical Monte Carlo approach to modeling multi-component adsorption

Ivan O. Iordanov[a*], Trenton M. Tovar[b], Lawford Hatcher[c], Jared B. DeCoste[a]
[a]U.S. Army Combat Capabilities Development Command Chemical Biological Center, Research & Technology Directorate, 8198 Blackhawk Rd, Aberdeen Proving Ground, MD 21010
[b]Leidos, P.O. Box 68, Gunpowder Branch, Aberdeen Proving Ground, MD 21010
[c]Minority Undergraduate Student Internship Program, 8198 Blackhawk Rd, Aberdeen Proving Ground, MD 21010

ABSTRACT

Novel nano-scale materials often require computational support in order to provide a mechanistic understanding of their often-complex properties. Probing adsorption of gases in nanoporous materials often requires calculating both thermodynamic properties through classical methods and local binding energies calculated with quantum methods. In this work, we use grand-canonical Monte Carlo and density functional theory methods to examine the binding of small polar and non-polar gases on ZIF-8 and the binding of carfentanil in a wide variety of metal-organic frameworks. We find that the polarity of the gas does not have a significant effect on the adsorption loading in ZIF-8. We also find experimentally that there is an atypical time-gated chemisorption reaction for NO adsorbed on UiO-66-NH_2. Finally, we look at the relationship between the binding energy of the opiate carfentanil, and the size of the pores of metal-organic frameworks. The result is a volcano plot—showing the optimal pore size for binding of carfentanil to be commensurate with its size, ~4.5 Å.

Keywords: density functional theory, computational chemistry, adsorption, molecular organic frameworks, grand-canonical Monte Carlo, porous materials

1. INTRODUCTION

Adsorption in porous materials has numerous diverse applications ranging from filtration of toxic chemicals, to gas separation and CO_2 sequestration. Given the importance of porous materials, there has been significant interest in improving porous materials—such as amorphous carbons or zeolites—as well as inventing new classes of porous materials. Metal-organic frameworks (MOF) are a relatively new class of porous materials invented by the Omar Yaghi group.[1] MOFs are a modular material consisting of inorganic metallic centers called secondary building units (SBU) connected by organic linkers. By changing out the linkers or SBU, nearly infinite combinations of MOFs can be created, allowing for nearly endless variation in the properties of the material. The combination of the number of possible MOF structures, their crystallinity, as well as the intrinsic dependence of their properties on their atomistic structure make MOFs an excellent class of materials for investigation and optimization though computational means.

Extensive high-throughput computational studies have been done, searching for a MOF optimal for a particular application (e.g., CO_2 sequestration)[2,3] or property (e.g., high surface area).[4] These studies enable relatively fast screening of thousands of MOFs, which would be prohibitively difficult to do solely experimentally. It is also common practice to include hypothetical MOFs,[5] or functionalized MOFs that have not been currently synthesized, allowing computational studies to guide future synthesis when optimizing for a particular purpose. Furthermore, due to the complex geometry and chemistry of these structures, computational studies are often done in conjunction with experimental work in order to jointly provide mechanistic understanding. Classical forcefield methods, such as the grand-canonical Monte Carlo (GCMC) method, are typically used when modeling thermodynamics-related properties of MOFs, such as adsorption and diffusion, as well as structural motifs like defects that can have patterns on a multiple-unit cell-length scale. On the other hand, chemical reactions and detailed structural analysis of individual unit cells are typically done using density functional theory (DFT) due to its high accuracy and ability to handle chemical reactions. In this work, we use both methods to study adsorption within MOFs, with the goal of improving the adsorption of weakly interacting species within MOFs.

2. METHODS

2.1 Density functional theory

DFT is an *ab initio* quantum chemical method used to calculate atomic properties with high accuracy. Unlike previous quantum mechanics-based methods—such as configuration interaction—in DFT, the total energy is a functional of the total electron density instead of the multi-electron wavefunction.[6] This simplification makes much larger simulations feasible, while typically maintaining a similar level of precision as other quantum mechanics-based methods. The primary approximation in DFT is in the treatment of the exchange and correlation interactions between electrons, which is approximated through different exchange and correlation functionals. Multiple functionals have been developed over the years,[7] in an attempt to improve the accuracy of DFT for different classes of problems. Due to the large size and crystalline nature of MOFs and most other porous materials, crystalline MOF calculations are usually performed using the Perdew-Burke-Ernzerhof (PBE) functional.[8] PBE is one of the oldest, fastest, and most widely implemented generalized gradient approximation functionals, with a generally comparable accuracy to other generalized gradient approximation functionals, and we have used it in all of the calculations in this work.

Due to the crystallinity of MOFs, we have elected to use plane-wave basis sets within periodic boundary conditions to model the full unit cell of the MOF structure. The calculations were done using the open source Quantum Espresso code, which implements plane-wave DFT and many related properties calculations. The lattice vectors are taken from experimental X-ray diffraction measurements and used as-is; although, we have checked the lattice parameters by running cell relaxation calculations to confirm that there are no significant distortions. Electron orbitals are described using mixed pseudopotentials from the standard solid-state pseudopotentials (SSSP) efficiency database,[9] with 50/400 Ry cutoffs for the wavefunctions/electron density. Initially, calculations were also performed using the projector augmented wave (PAW) pseudopotentials included with Quantum Espresso. The difference in binding energies for adsorbates depending on the pseudopotential used were less than 0.01 eV. All calculations included a semi-empirical van der Waals correction due to Grimme et al.[10] because of the importance of van der Waals interactions for physisorption. Due to the size of the cells, all calculations only included the Γ k-point.

2.2 Grand-canonical Monte Carlo

While DFT has many advantages in atomistic simulations, it is difficult to run DFT simulations on time scales long enough to provide meaningful statistical ensemble averages for thermodynamic properties like temperature or pressure of gases. In order to run long/large enough simulations, the quantum interactions between electrons must be approximated using classical forcefield potentials. GCMC simulations are the primary framework for full-scale simulations of adsorption. Using classical forcefields, simulations can be run for any temperature/pressure combination, allowing for full isotherms to be simulated through a series of calculations. GCMC calculations were done using the RASPA software package,[11] using a combination of built-in and TraPPE potentials[12] for the adsorbates. The framework is kept fixed, thus not needing a forcefield parametrization, and the built-in RASPA generic MOF values are used for the Lennard-Jones parametrization.

2.3 Isotherms and synthesis

ZIF-8 was synthesized as described by Pan et al.[13] Separate aqueous solutions of $Zn(NO_3)_2{\cdot}6H_2O$ and 2-methylimidazole were mixed by stirring at room temperature for 1 hour. The product was collected by centrifuging and was washed 3 times with deionized water before methanol exchange. Isotherms for CO and NO were measured on a Micromeritics® 3Flex 3500 instrument. Before measurements, all samples were degassed under vacuum at 120 °C to remove water and record an accurate weight.

3. RESULTS

3.1 Adsorption in ZIF-8

Initial work focused on adsorption of small polar and non-polar gases in ZIF-8. ZIF-8 is a zeolitic imidazolate framework (ZIF) with small (~10 Å-diameter) pores consisting of zinc metal centers connected with imidazole linkers.[14] ZIFs can be considered a subset of MOF with more restrictive SBU/linker combinations; they have been investigated intensely due to their topological similarity to zeolites. Our initial hypothesis was that there will be stronger binding between the polar gases and the framework compared to the non-polar ones.

DFT calculations (Figure 1) show that there is no correlation between polarity of the gas and its binding energy. The most likely reason is that the van der Waals interactions dominate the overall binding, due to relatively small or inaccessible framework dipole moments. Examining the binding orientations and locations of the adsorbates (Figure 2) confirms that the optimal binding is near the linkers, optimizing the van der Waals interactions through close proximity with multiple parts of the framework. The binding geometry suggests that the binding energy could be increased by creating pores or other geometric motifs with sizes commensurate with the adsorbate size, which we will consider in section 3.3. Adsorption isotherm experiments broadly confirmed the computational results, showing that there is no particular increase in adsorption loading with polarity.

	CH_4	CO_2	CO	NO	N_2	O_2
DFT BE (eV)	0.196	0.227	0.191	0.185	0.172	0.267
Loading 0.01 bar	0.004	0.009	0.001			
Loading 0.1 bar	0.330	0.617	0.017			

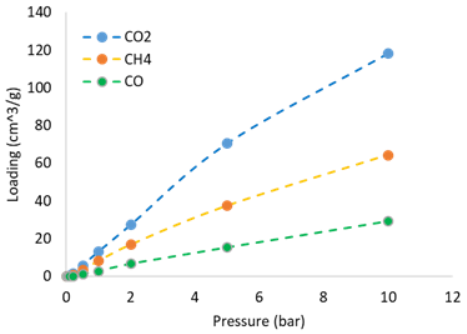

Figure 1. (Left) DFT binding energies and low pressure GCMC adsorption loadings for polar and non-polar gases. GCMC adsorption values follow same ordering as DFT binding energies. (Right) Full GCMC isotherms showing adsorption at higher pressures.

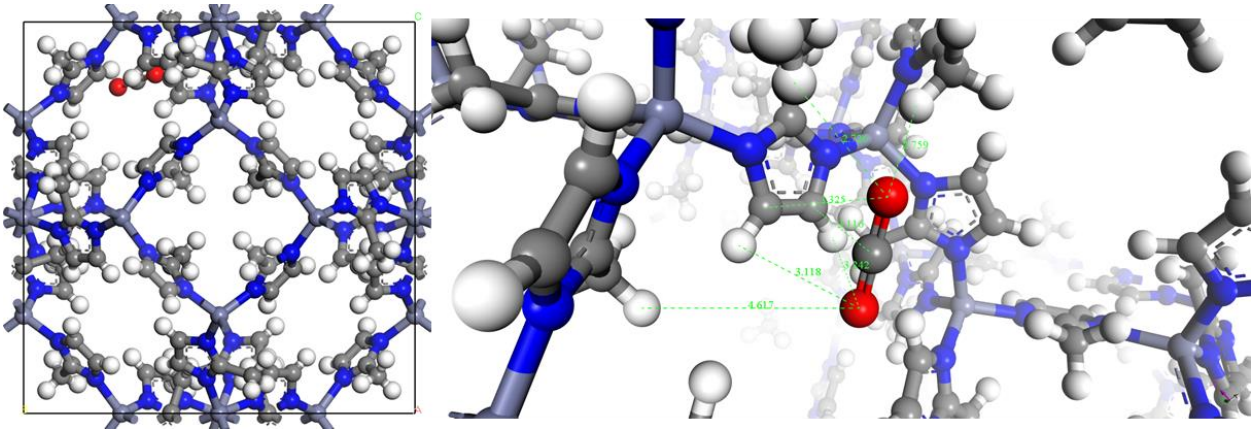

Figure 2. CO_2 adsorption in ZIF-8. Full unit cell on the left, zoom in on binding site on right. Note the close proximity of multiple linkers to the adsorbate at the binding site, showing how "enveloping" sites can improve van der Waals binding energy.

3.2 NO adsorption and reaction in UiO-66-NH_2

Subsequent to our work on adsorption of polar and non-polar gases in ZIF-8, we ran an adsorption isotherm for NO within UiO-66-NH_2, a very well-studied MOF with potential filtration applications. NO was found to have a rather peculiar isotherm (Figure 3), with very low uptake at low pressures, followed by an irreversible step uptake at higher pressures. This dynamic is in contrast to the NO isotherms on ZIF-8 and UiO-66, both of which showed reversible weak physisoprtion. The initial low uptake of the NO isotherm on UiO-66-NH_2 indicates an initiation period before chemisorption can occur. This is very different than previously reported isotherms of NO on MOFs. Typically, MOFs with coordinatively unsaturated metal sites show a step isotherm; however, the step occurs immediately at the lowest measured pressure point.[15] When the sample is re-evacuated, a second isotherm shows only reversible physisorption. Interestingly, the physisorptive uptake is higher than the initial uptake on a fresh UiO-66-NH_2 sample; meaning, the treated sample has a stronger interaction with NO.

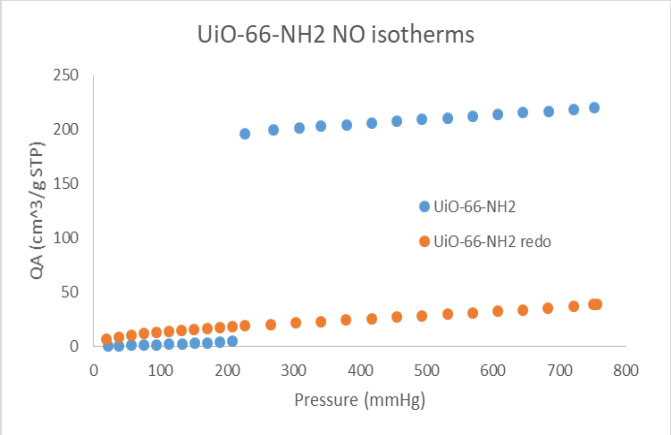

Figure 3. NO isotherms on fresh UiO-66-NH$_2$ (blue) and UiO-66-NH$_2$ already treated with NO (orange).

Reaction of NO with pendant amines has been shown for IRMOF-3 and UMCM-1-NH$_2$.[16] However, the reaction takes place at high NO pressures and an isotherm was never measured. To explore the pressure effect, UiO-66-NH$_2$ was exposed to NO at pressures of 189 mmHg (below the step) and 760 mmHg (above the step). The two samples were digested with nitric acid and the solution was measured by NMR, shown in Figure 4. For both samples, NMR shows the doublet peaks of the bdc-NH$_2$ linker shift from an untreated sample. However, the shift is different for each treatment pressure meaning that different species formed at each pressure. This indicates that the initiation phase forms a stable complex before reaction to the final product. N_2 isotherms after the reactions show only ~25 % lower surface areas, suggesting UiO-66-NH$_2$ maintains most of its structure after the reaction. *In situ* diffuse reflectance infrared fourier transform spectroscopy (DRIFTS) experiments and further DFT/GCMC calculations are planned to further explore the reaction.

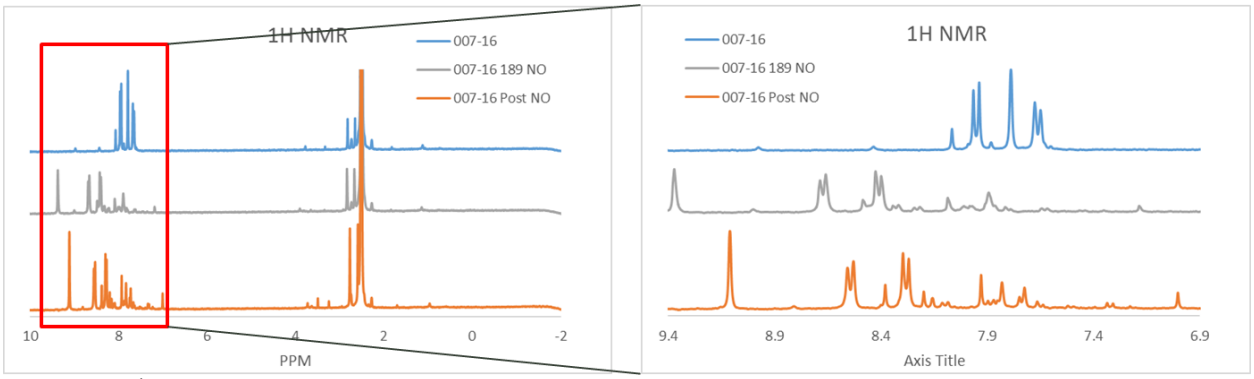

Figure 4. ^{1}H NMR of UiO-66-NH$_2$ (blue), UiO-66-NH$_2$ treated at 189 mmHg NO (gray), and UiO-66-NH$_2$ treated at 760 mmHg (orange).

3.3 Pore size effect for adsorption

Pore size effects are known to have important effects in gas adsorption and separations applications, for example in adsorption in the hierarchical pores of amorphous carbon and in the cracking of hydrocarbons using zeolites in the petrochemical industry. However, there has been comparatively little research in tailoring nano-scale pores in MOFs in order to increase phyisisorption adsorption at low pressures. Most research has focused on larger pores for increased adsorption at high pressure or chemical modifications for improved binding. In this section, we describe our initial work in investigating this approach to improve adsorption.

3.3.1 Pore size effect for carfentanil

Carfentanil is a dangerous opiate—approximately 10,000 times more potent than morphine.[17] Understanding how it interacts with surfaces and how to protect personnel or neutralize it is of general interest to the Army. Aside from its practical importance, it is also a useful test molecule for improving adsorption through pore size modulation due to its large size and generally unreactive nature. Therefore, we have done DFT binding energy calculations for carfentanil in a variety of MOFs, looking to establish a pore size verses binding energy relationship.

The results can be seen in Figure 5, which shows a typical volcano plot relationship between pore size and binding energy, centered around the approximate radius of carfentanil, ~4.5 Å. The pore sizes shown were measured as the radii of spheres contained within the pores and not allowed to overlap the van der Waals radii of the surrounding atoms. Such a measurement can lead to some discrepancy as the real pore geometry deviates from the spherical shape, but it approximates most of the cage-like pores of MOFs and provides a consistent basis for comparison. Given that the adsorbate itself does not have a perfectly spherical shape and is able to bend to accommodate geometrical features, it is not expected for there to be perfect correlation between pore size and adsorbate size, but the results are quite consistent with a pore size/adsorbate size binding improvement effect. Note that some MOFs have multiple pores with different sizes and are listed at different locations depending on each pore size.

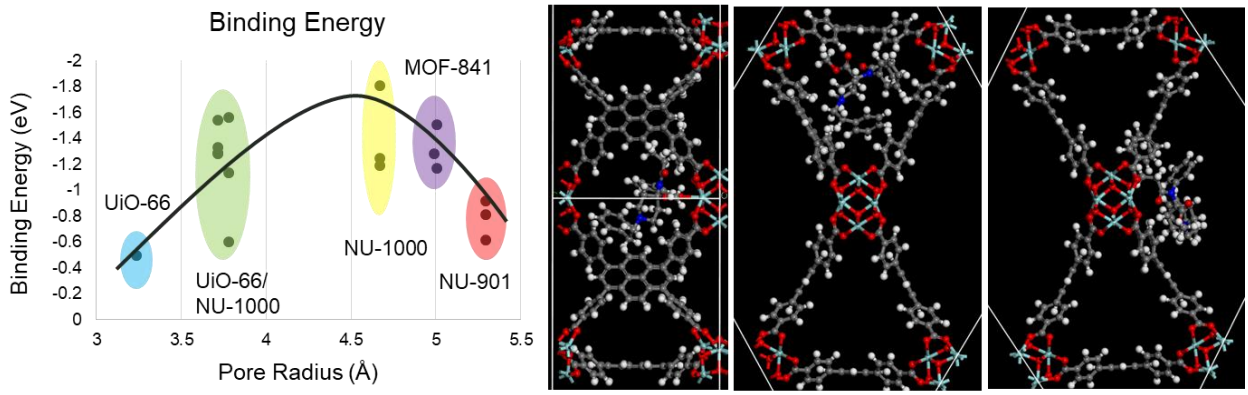

Figure 5. (Left) Binding energy of carfentanil versus MOF pore size. Volcano plot curve shows maximum near carfentanil radius (4.5 Å). Largest pore of NU-1000 is not shown, although it is consistent with the trend, with a binding energy of 0.7 eV and a 14.4 Å pore radius. (Right) Carfentanil within the three pores of NU-1000; smallest, medium, and largest from left to right.

The adsorption of carfentanil is primarily due to van der Waals interactions; however, we also find that carfentanil can create a hydrogen bond between the oxygen in the ester group and undercoordinated metal sites on Zr_6O_8 SBUs, if the geometry allows it. By twisting the carfentanil structure to allow/deny hydrogen bond formation, its contribution to the total binding can be approximated as ~0.5 eV, significant but still lower than the overall van der Waals binding. Multiple binding energies are shown in Figure 5 for most pores since multiple binding orientation converged, showing the spread in binding energy due purely to binding orientation as opposed to pore size. The inclusion of hydrogen bonding (or lack thereof) is the reason for the larger spread in binding energies shown for NU-1000 and UiO-66.

Overall, these results show a promising pathway to improving physisorption of analytes in MOFs in a way that will be size-selective as opposed to reliant on chemical reactivity. This approach could improve adsorption of chemical warfare agents in protective equipment, since chemical warfare agents have larger sizes than most ambient chemicals, and pore sizes could be tuned to improve their adsorption while allowing smaller molecules through. Future work will further investigate this possibility and use this as a basis for future projects.

3.3.2 Modifying pore size through modulators

In the previous section, we described the process of changing out different MOFs in order to optimize the pore size to bind a particular analyte with a similar size. However, instead of changing the MOF itself, there are two other options that allow for finer control of pore sizes without changing the underlying MOF structure and its topology. The first is to attach functional groups to the MOF linkers. Functional groups are typically attached to the benzene rings of the linkers in order to change the chemical reactivity of the MOF; however, attaching bulky hydrocarbons should allow for changes in pore sizes without changing the chemical properties of the material. The second option is to attach so-called "modulators" to the undercoordinated sites that are part of the normal topology of some MOFs—such as NU-901 and NU-1000. Both MOFs have four unoccupied sites, each of which allows for the attachment of a linker through two carboxylate acids. If a modulator with just one carboxylic acid is attached, we can decrease the size of the pores or change their shape without changing the connectivity of the pore network. We have already done DFT calculations on the binding energies of the modulators themselves to the SBU of previously synthesized NU-901 analogs (Figure 6) and are looking into using these optimized structures for binding energy calculations of hydrocarbons. The combination of functionalizing linkers and attaching modulators should allow for fine modulation of pore sizes and improved optimization of the binding of different analytes.

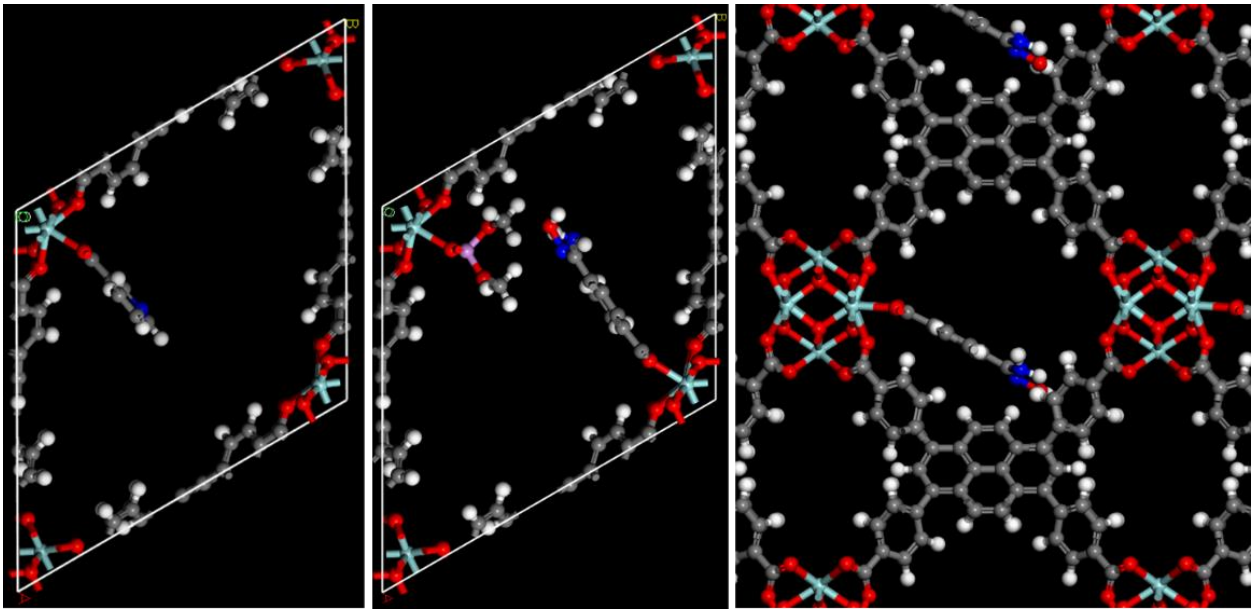

Figure 6. Modulators attached to NU-901: pyridine (left), DMP and oxime (middle), and oxime (right). Note that NU-901 has two pores and, depending on which of the four sites on the SBU the modulator is attached to, it can extend in either pore. The two figures on the left show modulators in the large pore, whereas the last rotates the view through 90 degrees to show the small pore with a modulator nearly spanning the length of the pore. Addition of modulators that are approximately as large as the pore can effectively split the pore and effectively increase the surface area of the MOF.

4. CONCLUSION

Computational and experimental methods were used to investigate and improve adsorption in MOFs. Initial work focused on small polar/non-polar gases in ZIF-8, showing that van der Waals interactions dominate adsorption even for polar gases, and that the preferred binding orientation allows for interactions with multiple linkers to improve the binding. Experimental isotherms confirmed that polarity does not have a large effect in this case, but we also found an atypical chemisorption/reaction of NO on UiO-66-NH_2. In this case, there is a delay between dosing and reaction, as well as possible pressure dependence of the products. Finally, we have looked into improving physisorption by matching pore size with adsorbate size, specifically in the case of carfentanil. A volcano plot showed the expected binding energy max near the radius of the adsorbate. Further work will focus on finer modulation of pore sizes through use of modulators and functionalization for smaller adsorbate molecules.

ACKNOWLEDGEMENTS

Funding was provided by the U.S. Army via the Surface Science Initiative Program (PE 0601102A Project VR9) at the Combat Capabilities Development Command Chemical Biological Center. This research was performed while Lawford Hatcher was a Minority Undergraduate Student Internship Program student at the Combat Capabilities Development Command Chemical Biological Center .

REFERENCES

[1] Zhou, H.-C.; Long, J.R.; Yaghi, O.M. Introduction to Metal–Organic Frameworks. *Chem. Rev.* **2012,** *112* (2), pp 673–674.

[2] Jasuja, H.; Zang, J.; Sholl, D.S.; Walton, K.S. Rational Tuning of Water Vapor and CO_2 Adsorption in Highly Stable Zr-Based MOFs. *J. Phys. Chem. C.* **2012,** *116* (44), pp 23526–23532.

[3] Han, S.; Huang, Y.; Watanabe, T.; Dai, Y.; Walton, K.S.; Nair, S.; Sholl, D.S.; Meredith, J.C. High-Throughput Screening of Metal–Organic Frameworks for CO_2 Separation. *ACS Comb. Sci.* **2012,** *14* (4), pp 263–267.

[4] Colón, Y.J.; Snurr, R.Q. High-throughput computational screening of metal–organic frameworks. *Chem. Soc. Rev.* **2014,** *43*, pp 5735–5749.
[5] Wilmer, C.E.; Leaf, M.; Lee, C.Y.; Farha, O.K.; Hauser, B.G.; Hupp, J.T.; Snurr, R.Q. Large-scale screening of hypothetical metal–organic frameworks. *Nat. Chem.* **2012,** *4*, pp 83–89.
[6] Kohn, W.; Sham, L.J. Self-Consistent Equations Including Exchange and Correlation Effects. *Phys. Rev.* **1965,** *140* (4A) pp A1133–A1138.
[7] Yu, H.S.; He, X.; Li, S.L; Truhlar, D.G. MN15: A Kohn–Sham global-hybrid exchange–correlation density functional with broad accuracy for multi-reference and single-reference systems and noncovalent interactions, *Chem. Sci.* **2016,** *7* (8), pp 5032–5051.
[8] Perdew, J.P.; Burke, K.; Ernzerhof, M. Generalized Gradient Approximation Made Simple. *Phys. Rev. Lett.* **1996,** *77* (18), pp 3865–3868.
[9] Lejaeghere, K.; Bihlmayer, G.; Björkman, T.; Blaha, P.; Blügel, S.; Blum, V.; Caliste, D.; Castelli, I.E.; Clark, S.J.; Dal Corso, A.; de Gironcoli, S.; Deutsch, T.; Dewhurst, J.K.; Di Marco, I.; Draxl, C.; Dułak, M.; Eriksson, O.; Flores-Livas, J.A.; Garrity, K.F.; Genovese, L.; Giannozzi, P.; Giantomassi, M.; Goedecker, S.; Gonze, X.; Grånäs, O.; Gross, E.K.U.; Gulans, A.; Gygi, F.; Hamann, D.R.; Hasnip, P.J.; Holzwarth, N.A.W.; Iuşan, D.; Jochym, D.M.; Jollet, F.; Jones, D.; Kresse, G.; Koepernik, K.; Küçükbenli, E.; Kvashnin, Y.O.; Locht, I.L.M.; Lubeck, S.; Marsman, M.; Marzari, N.; Nitzsche, U.; Nordström, L.; Ozaki, T.; Paulatto, L.; Pickard, C.J.; Poelmans, W.; Probert, M.I.J.; Refson, K.; Richter, M.; Rignanese, G-M.; Saha, S.; Scheffler, M.; Schlipf, M.; Schwarz, K.; Sharma, S.; Tavazza, F.; Thunström, P.; Tkatchenko, A.; Torrent, M.; Vanderbilt, D.; van Setten M.J.; Van Speybroeck, V.; Wills, J.M.; Yates, J.R.; Zhang, G-X.; Cottenier, S. Reproducibility in density functional theory calculations of solids. *Science,* **2016,** *351* (6280), pp aad3000-1–aad3000-7.
[10] Grimme, S.; Ehrlich, S.; Goerigk, L. Effect of the damping function in dispersion corrected density functional theory. *J. Comput. Chem.* **2011,** *32* (7), pp 1456–1465.
[11] Dubbeldam, D.; Calero, S.; Ellis, D.E.; Snurr, R.Q. RASPA: molecular simulation software for adsorption and diffusion in flexible nanoporous materials, *Mol. Simul.* **2015,** *42* (2), pp 81–101.
[12] Eggimann, B.L.; Sunnarborg, A.J.; Stern, H.D.; Bliss, A.P.; Siepmann, J.I. An online parameter and property database for the TraPPE force field. *Mol. Simul.* **2013,** *40* (1–3), pp 101–105.
[13] Pan, Y.; Liu, Y.; Zeng, G.; Zhao, L.; Lai, Z. Rapid synthesis of zeolitic imidazolate framework-8 (ZIF-8) nanocrystals in an aqueous system, *Chem. Comm.* **2011,** *47*, pp 2071–2073.
[14] Fairen-Jimenez, D.; Galvelis, R.; Torrisi, A.; Gellan, A.D.; Wharmby, M.T.; Wright, P.A.; Mellot-Draznieks, C.; Düren, T. Flexibility and swing effect on the adsorption of energy-related gases on ZIF-8: Combined experimental and simulation study. *Dalton Trans,* **2012,** *41* (35), pp 10752–10762.
[15] Xiao, B.; Wheatley, P.S.; Zhao, X.; Fletcher, A.J.; Fox, S.; Rossi, A.G.; Megson, I.L.; Bordiga, S.; Regli, L.; Thomas, K.M.; Morris, R.E. High-Capacity Hydrogen and Nitric Oxide Adsorption and Storage in a Metal-Organic Framework. *J. Am. Chem. Soc.* **2007,** *129* (5), pp 1203–1209.
[16] Nguyen, J.G.; Tanabe, K.K.; Cohen, S.M. Postsynthetic diazeniumdiolate formation and NO release from MOFs, *CrystEngComm.* **2010,** *12* (8), pp 2335–2338.
[17] George, A.G.; Lu, J.J.; Pisano, M.V.; Metz, J.; Erickson, T.B. Carfentanil-an ultra potent opioid. *Am. J. Emerg. Med.* **2010,** *28* (4), pp 530–532.

Probing the connection between low-frequency vibrational modes and macroscopic structural behavior of metal-organic frameworks

Neal D. Kline[a*], Bernard Goetz[b], Ashish Tripathi[a], Jose L. Mendoza-Cortes[c,d], Christian Serre[b]
[a]U.S. Army Combat Capabilities Development Command Chemical Biological Center, Research & Technology Directorate, 8198 Blackhawk Rd, Aberdeen Proving Ground, MD 21010
[b]Institut des Materiaux Poreux de Paris, CNRS Ecole Normale Superieure, Ecole Superieure de Physique et de Chimie Industrielles, PSL Research University, Paris, France 75005
[c]Florida State University, 288 Champions Way, Tallahassee, FL 32306
[d]National High Magnetic Field Laboratory, 1800 E Paul Dirac Dr, Tallahassee, FL, 32310

ABSTRACT

Metal-organic frameworks are hybrid porous materials that have been widely studied due to their promising applications in fields such as gas storage, catalysis, and sensing. Among the variety of reported metal-organic frameworks is a sub-group that have been observed to display large-scale structural flexibility. The flexibility in the metal-organic framework corresponds to a fully reversible transition between different framework conformations triggered by external stimuli including temperature, pressure, and guest molecule. This study will investigate the MIL-53 and 88 families of metal-organic frameworks by systematically varying the components (metal node, functionalization of linker) and examining the collective vibrations of the frameworks (located in the THz region) using low-frequency Raman spectroscopy. The Al^{3+}, Fe^{3+}, Cr^{3+}, and Ga^{3+} derivatives of the MIL-53 metal-organic frameworks were synthesized along with four functionalized derivatives of MIL-53 Al incorporating the $–NH_2$, $–NO_2$, $–CH_3$, and $–(COOH)_2$ functional groups on the linker. The linker molecule itself was also changed by synthesizing the MIL-88 A–C series of metal-organic frameworks. The low-frequency Raman spectra collected on the metal-organic framework samples show clearly resolved bands for all of the systems under study. Theoretical modeling is ongoing to assign the spectra.

Keywords: metal-organic frameworks, lattice dynamics, terahertz vibrations, low-frequency Raman Spectroscopy, MIL-53, MIL-88

1. INTRODUCTION

Metal-organic frameworks (MOF) are porous crystalline materials with metal ions or clusters as the nodal points and organic linkers regularly arranged in between them. The periodic and porous structures give MOFs advantages for applications such as gas storage, gas separations, catalysis, and sensing.[1,2] While MOFs are similar to other microporous materials, such as inorganic zeolites and activated carbon, they have larger surface areas and can be processed at much lower temperatures. MOFs can also be built from a wider range of constituents allowing the ability to fine tune structural aspects of the material or a specific interaction with an adsorbate. However, in contrast to the rigid structure of zeolites and carbon materials, a limited number of MOFs display large-scale structural flexibility upon the application of external stimuli that can drastically alter their characterisctics.[3,4]

This unique large-scale structural flexibility of MOFs has stimulated research to specifically study the phenomenon. Several techniques have been used including X-ray diffraction (XRD), nuclear magnetic resonance, and infrared/Raman methods.[5,6] These methods are usually implemented as an *in situ* characterization approach performed by applying an external stimulus—introducing guest molecules, applying pressure or temperature, or probing the MOF under the influence of the stimuli.

Recently, investigations studying the low-frequency vibrational modes of the zeolitic imidazolate framework family of MOFs located in the THz region (0.1–10 THz, 3–300 cm^{-1}) have been performed.[7–9] The authors discovered that the low-frequency modes of MOFs showed the standard lattice vibrations but also physical properties unique to the particular MOF included in the study. It also allowed the authors to identify possible phase change mechanisms

through which the framework may destabilize, distort, or collapse when mechanical force is applied. Several techniques were used to uncover these low-frequency vibrational modes including inelastic neutron scattering, low-frequency Raman spectroscopy, synchrotron radiation far-infrared absorption spectroscopy, and terahertz time-domain spectroscopy. The experimental investigations were also supported by theoretical density functional theory calculations in order to help assign the spectra that were obtained. Combining spectroscopic techniques capable of reaching the THz region with theoretical calculations to model the low-frequency vibrations provides an approach for a comprehensive description of MOF framework properties much more efficiently than current methods.

The structural flexibility of MOFs is associated with an anisotropic stiffness of the crystal pore which allows the material to be deformed easily in one direction but not in another. Because of this directional flexibility, the barrier between structural conformations is small, allowing the material to transition to different conformations. Férey and Serre have identified a number of structural characteristics that are indicative of framework flexibility including the nature of the organic ligand, the characteristics of the secondary building unit present in the MOF, the periodic structure of the MOF, and the coordination of the metal nodes.[4] There are also different categories of flexibility which generally illustrate the dynamic structural transformation that the MOF undergoes when exposed to the proper stimulus. One category of flexibility that will be investigated in this study is breathing (Figure 1).

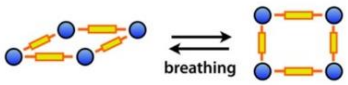

Figure 1. Structural flexibility in MOFs illustrated by the breathing phenomenon in MIL-53.[10]

Breathing is defined as reversible structural transitions between different framework conformations of a MOF during which the substantial displacement of atoms of the framework is accompanied by a change in unit cell volume.[2] In breathing, characteristic distances and angles of the unit cell change and the crystallographic space groups of the two distinct phases (narrow pore and large pore) may be different. The representative example of this kind of flexibility is the MIL-53 family of MOF ([M(bdc)(OH)] where bdc = 1,4-benzenedicarboxylate and M = Al^{3+}, Fe^{3+}, Cr^{3+}, Sc^{3+}, Ga^{3+}, In^{3+}.

Swelling (Figure 2) is characterized by a gradual enlargement of the MOF unit cell without a change in the unit cell shape and typically without a change in space group.[2] MIL-88 is the MOF that is representative of this kind of flexibility and is based on a trimeric $M_3O(H_2O)_2X^{6+}$ (M = Fe,Cr; X = F-, OH-) secondary building unit that consists of three truncated tetrahedral interconnected by dicarboxylic acids: fumaric acid (MIL-88A), bdc (MIL-88B), ndc (2,6-naphtalenedicarboxylate; MIL-88C) or bpdc (4,4'-biphenyldicarboxylate; MIL-88D).

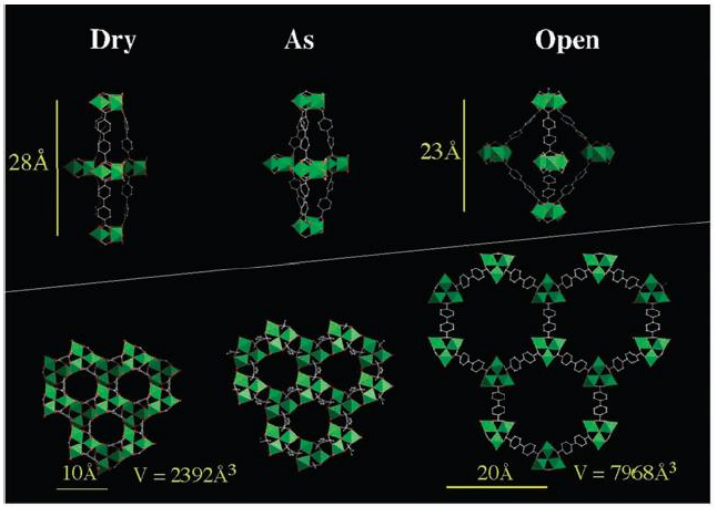

Figure 2. Simulation of pore opening for MIL-88 D for the dry, as (as synthesized), and open forms.[3]

As MOFs are considered for more large-scale applications it becomes necessary to understand their physical structure at a fundamental level and how this can determine their properties on the macroscopic scale. The methodology of interrogating the low-frequency modes of the MOF coupled with computational modeling can serve as a starting point for beginning to understand the molecular effects underpinning complex mechanisms in framework materials.

The present study reports the results of a low-frequency analysis of the Al^{3+}, Fe^{3+}, Cr^{3+}, and Ga^{3+} derivatives of the MIL-53 family along with four functionalized derivatives of MIL-53 Al incorporating the $–NH_2$, $–NO_2$, $–CH_3$, and $–(COOH)_2$ functional groups on the linker. Previous findings have indicated that changing the metal node and functionalizing the MOF can affect its macroscopic structural behavior and also the low-frequency vibrations that are intrinsically linked to the observed physical phenomena such as breathing. Our primary hypothesis is that the differences observed in the overall structural behavior of the MIL-53 MOF from changing the metal node originate in the lattice dynamics of the MOF, which can be studied using spectroscopic techniques capable of reaching very low frequencies (<100 cm^{-1}). We can then use differences in the low-frequency spectra of these MOFs to help explain their differing structural behavior.

2. EXPERIMENTAL PROCEDURE

2.1 Metal-organic framework synthesis

The various MIL-53 MOFs were synthesized according to methods reported in the literature. All chemicals were obtained from Sigma-Aldrich® and were used without further purification.

2.1.1 MIL-53(Al) $^{3+}$

MIL-53(Al) was synthesized by a solvothermal method. First 6.5 g (17.3 mmol) of aluminum nitrate nonahydrate ($Al(NO_3)_3 \cdot 9H_2O$) and 1.44 g (8.7mmol) of 1.4-benzenedicarboxylic acid (BDC) were mixed with 25-mL of deionized water in a Teflon™-lined stainless steel Parr bomb under autogenous pressure for three days at 220.0 °C for 72 hours. After the reaction, the resulting white powder was washed with deionized water. The sample was activated by heating in a furnace at 360 °C (heating rate of about 3 °C/minute) under air atmosphere for 13 hours in order to remove unreacted acid molecules.

2.1.2 MIL-53(Ga) $^{3+}$

MIL-53(Ga) was hydrothermally synthesized under mild conditions (210.0 °C, 3.5 hours). First, 0.997 g ($3.9 \cdot 10^{-3}$ mol) of $Ga(NO_3)_3 \cdot 3H_2O$ and 0.764 g ($4.6 \cdot 10^{-3}$mol) of BDC were mixed with 20 mL of deionized water in a 125-mL Teflon™-lined stainless steel Parr bomb. After the reaction, the resulting white powder was washed with 50.0 mL of dimethylformamide (DMF) in a 125-mL Teflon™-lined stainless steel Parr bomb (200 °C, 36 hours). The sample was washed again with MeOH to remove DMF and dried in a furnace at 65.0 °C.

2.1.3 MIL-53(Fe)$^{3+}$

MIL-53(Fe) was synthesized in a 250-mL laboratory flask. 6.75 g of $FeCl_3 \cdot xH_2O$ ($2.5 \cdot 10^{-3}$ mol) and 4.15 g terephthalic acid ($2.5 \cdot 10^{-3}$ mol) of each in 5 mL of DMF and 4.0 mL of hydrochloric acid (5 M) were reacted in 125.0 mL of DMF at 150.0 °C for 2 days. After filtration, the crude product was washed with 100.0 mL of MeOH at 65 °C for 12 hours and dried in an oven to remove MeOH.

2.1.4 MIL-53(Cr)

MIL-53(Cr) was synthesized by mixing chromium nitrate ($Cr(NO_3)_3 \cdot 9H_2O$) and BDC and hydrofluoric acid in a 1:1:1 molar ratio. 1.19 g of $Cr(NO_3)_3 \cdot 9H_2O$ (5 mmol), 0.83 g of BDC (5 mmol) and 1 mL of hydrofluoric acid (5 mmol from a 5 M solution) were added in 25 mL of deionized water. The mixture was stirred for about 2 hours at room temperature to homogenize. After mixing, the mixture was transferred to a Teflon™-lined stainless steel autoclave and kept at 220 °C for 72 hours. The obtained green solid was collected by filtration and washed with DMF. Subsequently, the sample was washed with MeOH to remove DMF and dried in an oven to remove MeOH.

2.1.5 MIL-53(Al)–NH_2

MIL-53(Al)–NH_2 was synthesized by mixing aluminum chloride ($AlCl_3 \cdot 6H_2O$) and benzene-2-amino-1,4-dicarboxylic acid (BDC–NH_2) and NaOH in a 1.56:1:2 molar ratio. 3.95 g (16.4 mmol) of aluminum chloride were added to 30.0 mL of water in a 100-mL round bottom flask and stirred until dissolved. Then, 1.9 g (10.5 mmol) of BDC–NH_2 dissolved in 7.5 mL of water was added, followed by 10.5 mL of NaOH solution (2 M/21 mmol). The mixture was heated in reflux conditions overnight. After the reaction, a pale-yellow powder was

collected by filtration and dried in oven at 65 °C. The solid was washed with DMF (150 °C, 8 hours) to remove non-reacted BDC–NH_2, then washed again with MeOH to remove DMF and dried in an oven to remove MeOH.

2.1.6 MIL-53(Al)–NO_2

MIL-53(Al)–NO_2 was synthesized similarly to MIL-53(Al)–NH_2, using benzene-1,4-dicarboxylic-2-nitro-acid (BDC–NO_2) as a linker. First, 3.95 g (16.4 mmol) of aluminum chloride ($AlCl_3 \cdot 6H_2O$) was added to 30 mL of water in a 100-mL round bottom flask and stirred until dissolution. 2.21 g (10.5 mmol) of BDC–NO_2 dissolved in 7.5 mL of water and 10.5 mL of NaOH solution (2 M/21 mmol) was then added to the round bottom flask and refluxed overnight. The white solid was filtered and dried at 65 °C in an oven. The sample was then washed with DMF (150 °C, 8 hours) to remove non-reacted BDC–NO_2, then washed again with MeOH to remove DMF and dried in an oven to remove MeOH.

2.1.7 MIL-53(Al)–$(COOH)_2$

MIL-53(Al)–$(COOH)_2$ was synthesized by mixing aluminum nitrate ($Al(NO_3)_3 \cdot 9H_2O$) and 1,2,4,5-benzenetetracarboxylic acid (BTEC) in a 1:1 molar ratio. 1.2 g of $Al(NO_3)_3 \cdot 9H_2O$ (3.2 mmol) and 0.53 g of BTEC (3.2 mmol) were added in 5 mL of deionized water. The mixture was stirred for about 2 hours at room temperature to homogenize. After mixing, the mixture was transferred to a Teflon™-lined stainless steel autoclave and kept at 210 °C for 24 hours. The obtained white solid was collected by filtration and washed with water. Subsequently the sample was dried in an oven and calcined at 390 °C for 10 hours to remove non-reacted linker, resulting in a beige solid.

2.1.8 MIL-53(Al)–CH_3

MIL-53(Al)–CH_3 was synthesized by mixing aluminum chloride ($AlCl_3 \cdot 6H_2O$), 2-methyl-terephthalic acid (BDC–CH_3) and NaOH in a 1.5:1.2 molar ratio. 361 mg (1.5 mmol) of aluminum chloride was added to 25 mL of water in a 50-mL round bottom flask and stirred until dissolved. Then, 180 mg (1 mmol) of BDC–CH_3 was added, followed by 1 mL of 2 M NaOH solution (2 mmol). The mixture was heated in reflux conditions overnight. After the reaction, a white powder was collected by centrifugation and dried in an oven at 65 °C. The solid was washed with DMF (150 °C, 8 hours) to remove non-reacted BDC–CH_3, then washed again with MeOH to remove DMF and dried in an oven to remove MeOH.

2.1.9 MIL-88A

MIL-88A was synthesized by mixing iron nitrate heptahydrate ($Fe(NO_3)_3 \cdot 6H_2O$) and fumaric acid in a ratio of 1.5:1. 361 mg (1.5 mmol) of iron nitrate was added to 25 mL of water in a 50-mL round bottom flask and stirred until dissolved. Then, 180 mg (1 mmol) of fumaric acid was added. The mixture was heated at 60 °C overnight. After the reaction, a dark red powder was collected by centrifugation, abundantly washed with water, and conserved in ethanol.

2.1.10 MIL-88B

MIL-88B was prepared by a procedure similar to MIL-88A. The compound is synthesized by mixing iron nitrate heptahydrate ($Fe(NO_3)_3 \cdot 6H_2O$) and terephthalic acid in a ratio 1.5:1. 361 mg (1.5 mmol) of iron nitrate was added to 25 mL of DMF in a 50 mL round bottom flask and stirred until dissolved. Then 180 mg (1 mmol) of terephthalic acid was added. The mixture was heated in reflux conditions overnight. After the reaction, a red powder was collected by centrifugation. The compound was stirred overnight in water to remove no reacted linker and DMF. The final product was conserved in ethanol.

2.1.11 MIL-88C

MIL-88C was prepared similarly to MIL-88B. The compound was synthesized by mixing iron nitrate heptahydrate ($Fe(NO_3)_3 \cdot 6H_2O$) and naphthalene dicarboxylic acid in a ratio of 1.5:1. 361 mg (1.5 mmol) of iron nitrate was added to 25 mL of water in a 50-mL round bottom flask and stirred until dissolved. Then, 180 mg (1 mmol) of naphthalene dicarboxylic acid was added. The mixture was heated in reflux conditions overnight. After the reaction, an orange powder was collected by centrifugation. The compound was refluxed overnight in ethanol to remove nonreacted linker and DMF. The final product was conserved in ethanol.

2.2 MOF characterization

2.2.1 X-Ray diffraction

Powder X-ray diffraction (PXRD) patterns of the MIL-53 and MIL-88 compounds were recorded on a high-throughput Bruker D8 Advance diffractometer working on transmission mode and using CuKα radiation (λ = 1.5418 Å) and a LYNXEYE XE-T detector. The patterns were scanned on a 2θ range from 2 to 30 ° with a typical step size of 0.02 ° in continuous mode.

2.2.2 Fourier-transform infrared spectroscopy

The infrared spectra of the various MIL-53 and MIL-88 compounds were accessed using a Perkin Elmer® Spectrum 100 Fourier-transform infrared (FTIR) spectrometer, equipped with a Universal ATR Diamond/ZnSe accessory. The spectra were acquired within a range from 400 cm^{-1} to 4,000 cm^{-1}. Each measurement results from the increment of four scans, with a scan speed of 0.2 cm/s and a resolution of 4 cm^{-1}.

2.2.3 Low-frequency Raman measurements

Samples for Raman analysis were prepared by casting thin films of the various MIL-53 MOF on aluminum-coated slides. Raman spectra were recorded using an Alpha 300R confocal microscope with a 100X objective and with a 532 nm laser with the following laser power for each sample: 2.0 mW for MIL-53 Al, 600.0 µW for MIL-53 Fe, 3.0 mW for MIL-53 Cr, 600.0 µW for MIL-53 Ga, 1.0 mW for MIL-53 Al–NH_2, 1.5 mW for MIL-53 Al–NO_2, 3.0 mW for MIL-53 Al–CH_3, 5.5 mW for MIL-53 Al–$(COOH)_2$, 100.0 µW for MIL-88B, and 0.25 mW for MIL-88C. MIL-88A Raman spectra were collected with a 633 nm laser at 3.0 mW of power. Raman spectra were acquired with a 20-second integration time with 10 co-added spectra for the high frequency (-250 cm^{-1}–2,000 cm^{-1}) portion of Raman spectra recorded using the 600 line/mm grating, while the low-frequency data (-200 cm^{-1}–1,000 cm^{-1}) were recorded using the 1,800 line/mm grating with a 30-second integration time and 15 co-added spectra.

2.3 Theoretical methods

Calculations have been performed using first-principles calculations at the level of unrestricted hybrid density functional theory, with the UB3LYP functional, as implemented in the *ab initio* CRYSTAL14 suite code. The van der Waals weak interactions were taken into account using the semi-empirical Grimme's (-D2) dispersion corrections. Triple-zeta valence with polarization quality (TZVP) Gaussian basis sets were used for light elements (H, B, C, N, O) and transition metal (TM) atoms. The convergence of energy, electron density and forces were set to 10–7 atomic units for all geometry optimizations. The spin states were allowed to relax unrestricted wave functions calculations. The harmonic vibrational frequencies at the optimized geometries were analyzed at the respective levels of theory to reveal the nature of the stable structure. This method was used for geometry optimization because densities and energies obtained with the method are less affected by spin contamination than other approaches, and it has been proven effective for related materials calculations. Integrations inside of the first Brillouin zone were sampled on 4 x 4 x 16 Monkhorst-Pack k-mesh grids for the MOF during geometry optimization. In other words, the reciprocal space for all the structures was sampled by a Γ-centered Monkhorst-Pack scheme with a resolution of around 2π x 1/60 Å-1

3. RESULTS AND DISCUSSION

3.1 X-ray diffraction and Fourier-transform infrared spectroscopy analysis

The MIL-53 family of MOFs are composed of terephthalate anions and trans chains of metal (III) octahedral-sharing –OH groups, creating a three-dimensional framework with a one-dimensional pore channel system. Their formulas are $M^{III}(OH)\cdot[O_2C\text{-}C_6H4\text{-}CO_2]H_2O$ (M^{III} = Al, Cr, Fe, Ga) for the hydrated forms (MIL-53lt; “lt”=low temperature or “np”=narrow pore) are $M^{III}(OH)\cdot[O_2C\text{-}C_6H_4\text{-}CO_2]$ for the dehydrated compounds (MIL-53ht; “ht”=high temperature or “lp”=large pore). XRD and FTIR (Figure 3) data were collected on the activated compounds and compared to literature sources to confirm their identity.[11,12] The FTIR spectra of the Cr, Fe, Ga, and Al derivatives all exhibit vibrational bands in the 1,400–1,700 cm^{-1} region which indicates the presence of a carboxylic acid functionality. The vibrational bands around 1,580 cm^{-1} and 1,403 cm^{-1} are characteristic of the $–CO_2$ asymmetric and symmetric stretching, respectively. Further confirmation of the synthesis of the MIL-53 compounds was done by collecting XRD

data (Figure 3) of the synthesized powders and comparing to literature. The XRD was performed on the powder samples after activation which would render the MOF in the hydrated "np" form. Cr, Fe, Ga, and Al analogues appear to correlate strongly with what has been reported in the literature.[11–14] The XRD pattern of the "np" form should look roughly the same for the different MIL-53 analogues as the main difference between the structures will be the metal center with minor changes in the structural parameters due to differing metal size.

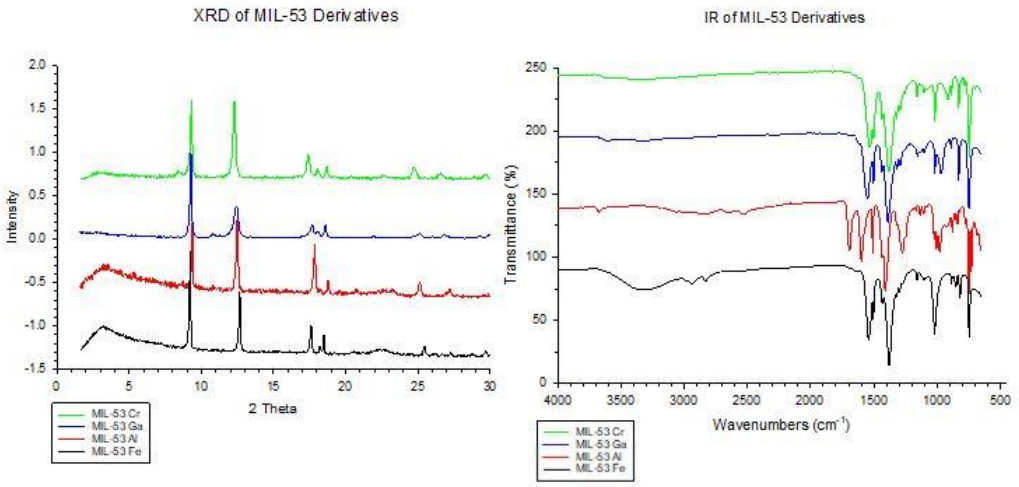

Figure 3. XRD (left) and FTIR (right) data for the Cr^{3+}, Ga^{3+}, Al^{3+}, and Fe^{3+} MIL-53 analogues.

The framework topology of the functionalized MIL-53 Al compounds is identical to the unfunctionalized parent compound. XRD and FTIR (Figure 4) data were collected on the activated functionalized MIL-53 Al MOF and compared to literature sources to confirm their identity.[15–17] The FTIR spectra of the $–NH_2$ $–NO_2$, $–CH_3$, and $–(COOH)_2$ derivatives all exhibit vibrational bands in the 1,400–1,700 cm^{-1} region which indicates the presence of a carboxylic acid functionality. The vibrational bands around 1,580 cm^{-1} and 1,403 cm^{-1} are characteristic of the $–CO_2$ asymmetric and symmetric stretching, respectively, and have small shifts from the parent compound depending on the functional group present on the linker. The XRD of the functionalized MOF is shown in Figure 6 and demonstrates that the presence of the functional group on the linker can alter the form of the MOF. The $–CH_3$ and $–NH_2$ derivatives are in the "np" form and look very similar to the XRD patterns in Figure 4 while the $–NO_2$ and $–(COOH)_2$ MOFs are in the "lp" form.

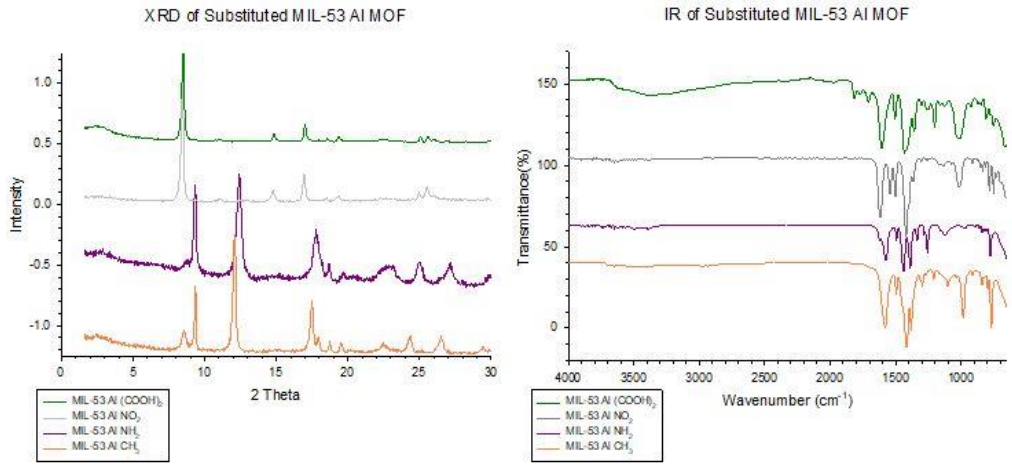

Figure 4. XRD (left) and FTIR (right) data for the functionalized MIL-53 Al MOF.

The MIL-88 family of MOF are composed of oxo-centered trinuclear iron (III) secondary building units and dicarboxylate linkers. The trimers of the octahedra are related together by *trans, trans* dicarboxylate moieties ensuring the three-dimensionality of the framework. Their formulas are [M3 IIIO(H_2O)2X(dicarbox)3]•guest (10) (M = Fe, Cr; X = F, Cl, acetate) and labeled MIL-88A to D [dicarbox = fumarate (88A); terephthalate (1,4–BDC) (88B);

2,6-naphthalenedicarboxylate (2,6-NDC) (88C); and 4-4′-biphenyldicarboxylate (4-4′-BPDC) (88D)]. XRD and FTIR data (Figure 5) were collected on the activated compounds and compared to literature sources to confirm their identity.[15–17] Like their MIL-53 counterparts, MIL-88 A–C have vibrational bands in their FTIR spectra near 1,580 cm^{-1} and 1,403 cm^{-1} that correspond to $–CO_2$ asymmetric and symmetric stretching, respectively. The XRD of the MIL-88 A–C species is presented in Figure 8 and represents the structure of the dry or closed form of each MOF.

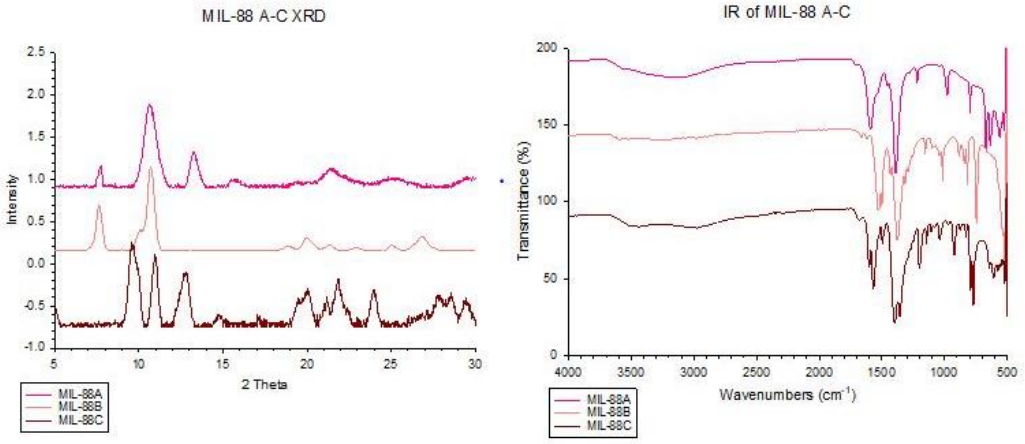

Figure 5. FTIR and XRD data for the functionalized MIL-88 A–C MOF.

3.2 Raman analysis

The Raman spectra for the Al, Fe, Ga, and Cr analogues of MIL-53 is shown in Figure 6. The low-frequency data (<200 cm^{-1}) collected is indicative of the lattice vibrations of the MOF while the higher frequency data details chemical information. In fact, the spectral features >500 cm^{-1} of the different analogues is dominated by signatures from the 1,4-benzenedicarboxylate linker indicating a very high chemical similarity between the different species. However, in the low-frequency spectra there are subtle differences between the Al, Ga, and Cr MIL-53 species while the Fe derivative displays very different low-frequency behavior.

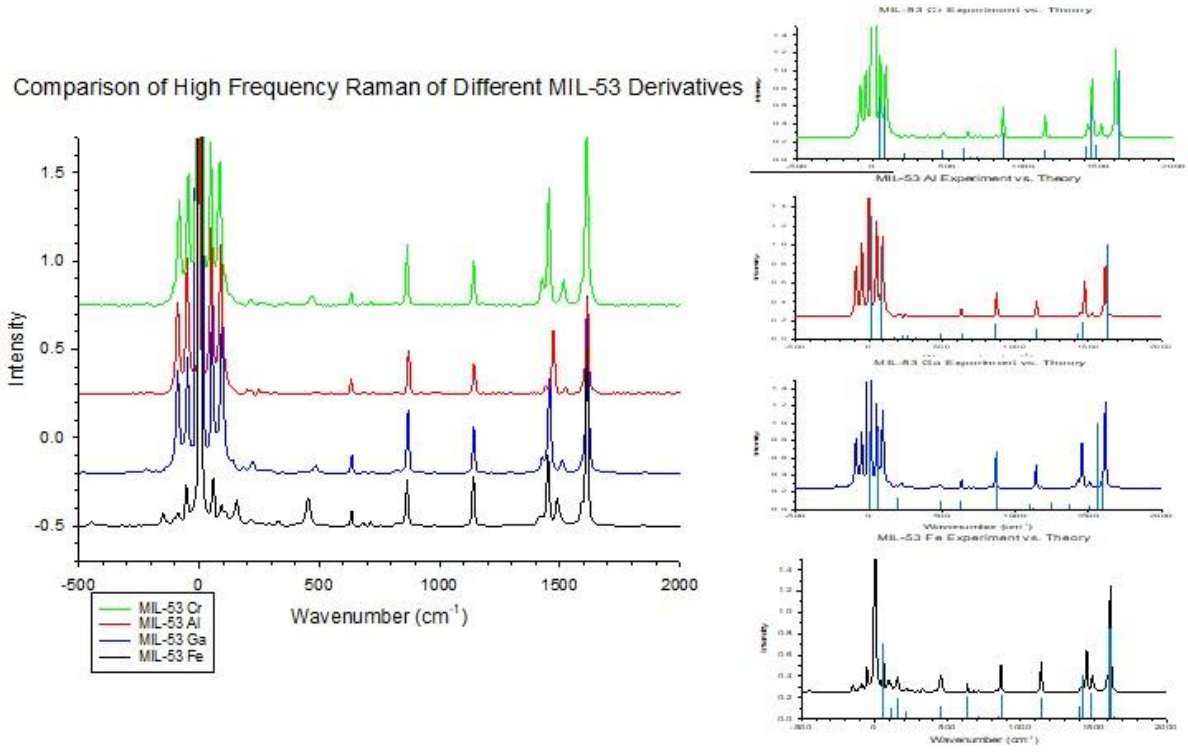

Figure 6. Experimental Raman spectra (left) and vibrational simulations with experimental Raman data (right).

Vibrational simulations were conducted for the different MIL-53 analogues after geometry optimization of the MOF in their closed pore form. The simulations are shown in the right panel of Figure 6 as the stick plots. There is excellent agreement between simulation and experiment for the Cr, Al, and Fe analogues; the simulations for the Ga MOF still match fairly well but did not predict the frequencies for the Raman bands <100 cm^{-1} as accurately as in the other derivatives and was not able to reproduce the intensity profile in the 1,400–1,600 cm^{-1} region. Vibrational band assignments < 200 cm^{-1} (we will focus on band assignments < 200 cm^{-1} for the sake of brevity) are made in Figure 7 for the Cr, Al, and Ga MIL-53 MOF. The features around 45–55 cm^{-1} correspond to out of plane phenyl ring rotation while the 85–95 cm^{-1} features appear to correspond to rotation of the entire $MO_4(OH_2)$ octahedron in addition to M-O(H)–M bending (M = Cr, Al, or Ga) and OH wagging. The observation of the phenyl ring rotation is very fascinating as phenyl ring rotation is thought to trigger the closed pore-large pore transition resulting in the macroscopic breathing that is observed in the MIL-53 systems.[18–20]

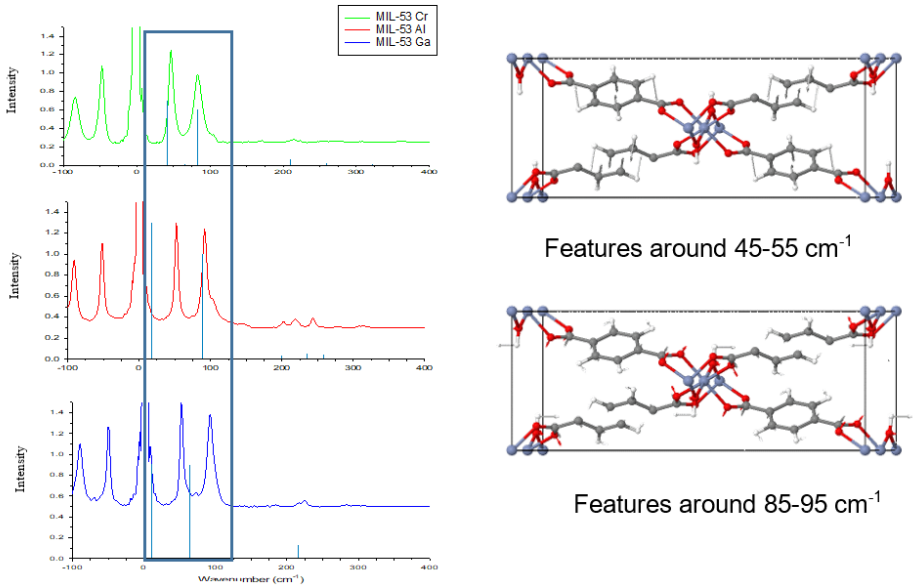

Figure 7. Vibrational band assignments below 200 cm^{-1} for MIL-53 Cr^{3+}, Ga^{3+}, and Al^{3+} MOF.

The vibrational assignments for the MIL-53 Fe MOF are shown in Figure 8. There is a slight difference in the appearance of the Raman spectrum of the Fe derivative compared to the spectra of the Cr^{3+}, Al^{3+}, and Ga^{3+} although the vibrational modes between the four MOF are very similar. The features near 55 cm^{-1} and 115 cm^{-1} correspond to phenyl ring rotation and rotation of the $FeO_4(OH_2)$ octahedron, respectively. While the feature near 155 cm^{-1} corresponds to O–Fe–O rocking which leads to a deformation of the $FeO_4(OH)_2$ octahedron.

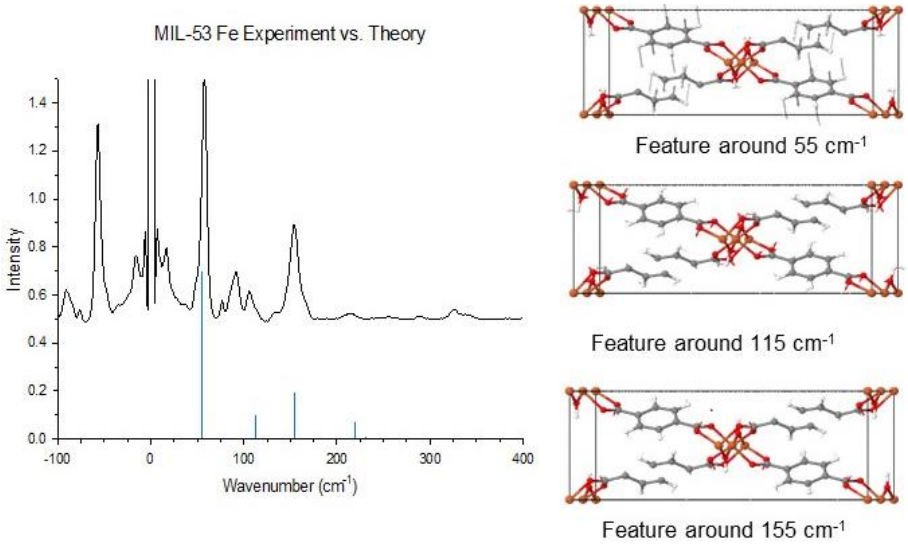

Figure 8. Vibrational band assignments below 200 cm^{-1} for MIL-53 Fe MOF.

The Raman spectra for the substituted derivatives of the Al MOF incorporating the $–NH_2$, $–NO_2$, $–CH_3$, and $–(COOH)_2$ functional groups are shown in Figure 9 along with the unsubstituted MIL-53 Al spectrum for reference. The functionalized MOF display very different spectral characteristics below 200 cm^{-1} than the original MOF, indicating a change in the breathing behavior. In all substituted MOFs, the two predominant bands below 100 cm^{-1} that are present in the parent structure have been altered. The $–NO_2$ and $–(COOH)_2$ substituted MOFs do not show much resolution in the low-frequency region while the $–CH_3$ and $–NH_2$ substituted MOFs do. Theoretical calculations are currently ongoing to make vibrational assignments to the MIL-53 Al substituted spectra and to compare the nature of the low-frequency vibrational modes of the parent structure and functionalized derivatives.

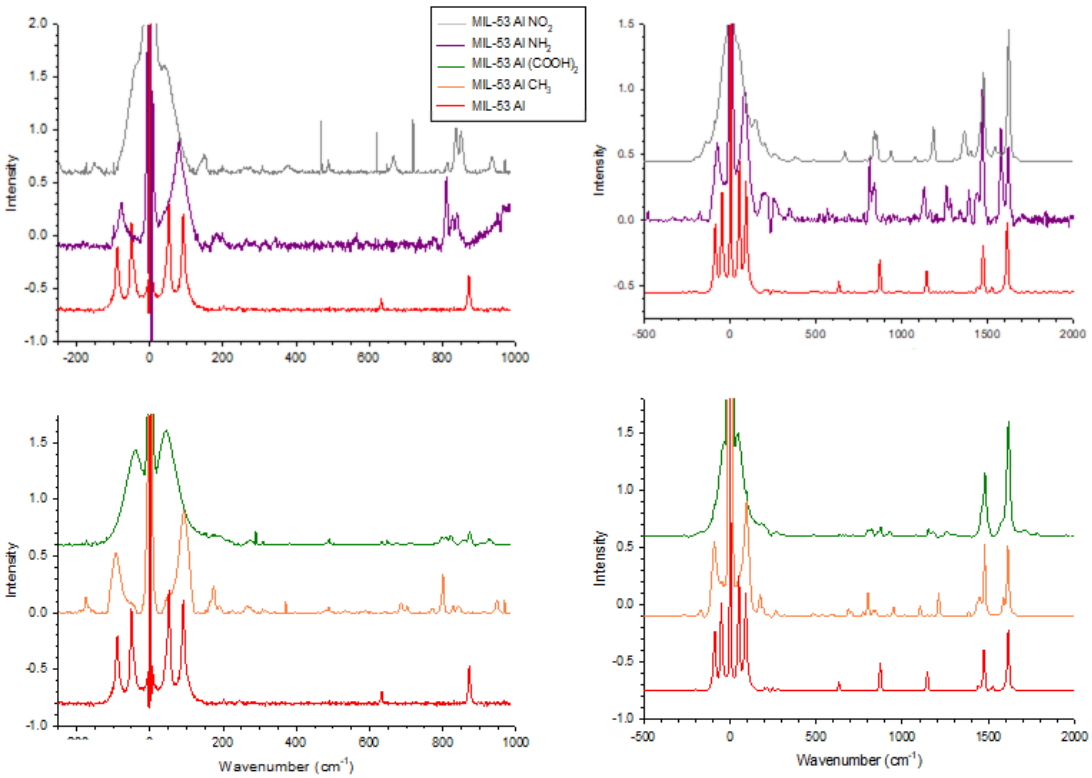

Figure 9. High frequency (right panel) and low-frequency (left panel) Raman data for substituted MIL-53 Al analogues.

The Raman spectra for the MIL-88 A–C MOFs are shown in Figure 10. There are low-frequency Raman bands present that are quite distinctive between the three species and may be related to the swelling motion of the MIL-88 MOF. Theoretical modeling is underway to aid in the band assignments of the low-frequency features.

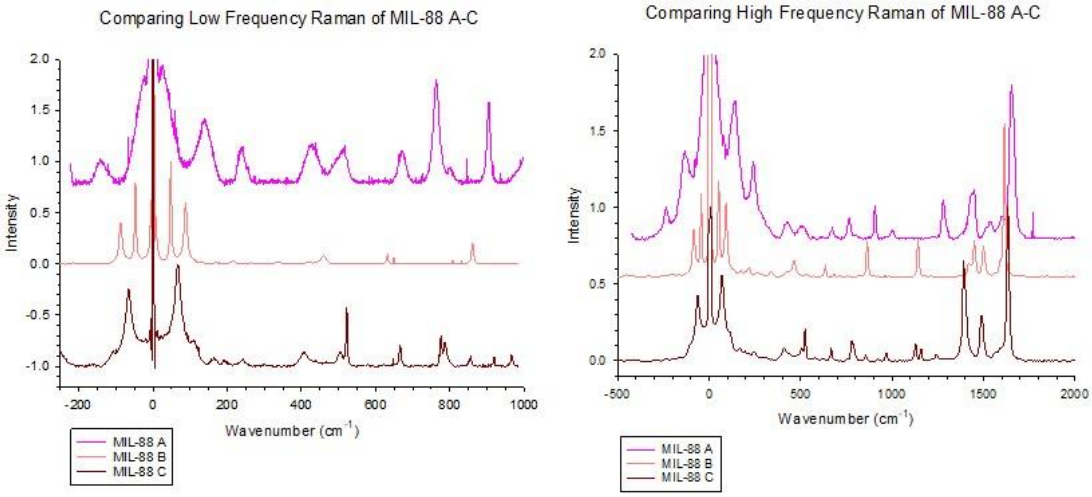

Figure 10. High frequency (right panel) and low-frequency (left panel) Raman data for substituted MIL-53 Al analogues.

4. CONCLUSIONS

Several MIL-53 and MIL-88 derivatives were synthesized and characterized in this investigation to study their low-frequency vibrational modes. The low-frequency Raman data collected shows that there are signatures related to collective lattice vibrations in both families of MOFs. The Al, Fe, Ga, and Cr MIL-53 derivatives, four substituted Al MIL-53 MOFs, and MIL-88 A–C MOFs were synthesized, and their low-frequency data compared. There were subtle differences related to peak positioning and line shape in the low-frequency data when comparing the Al, Ga, and Cr MOFs, while the Fe MOF gave very different low-frequency spectra. Incorporating the functional groups into the Al analogue also dramatically changed the low-frequency behavior. According to previous research, these changes in low-frequency behavior can be linked to changes in the macroscopic properties of the MOF. Modeling is underway which will help to assign the Raman spectra and elucidate the lattice dynamics of these species.

ACKNOWLEDGMENTS

Funding was provided by the U.S. Army via the Surface Science Initiative Program (PE 0601102A Project VR9) at the Combat Capabilities Development Command Chemical Biological Center.

REFERENCES

[1] Furukawa, H.; Cordova, K.E.; O' Keefe, M.; Yaghi, O.M. The Chemistry and Applications of Metal-Organic Frameworks. *Science*. **2013,** *341* (6149), pp 1230444.

[2] Kuppler, R.J.; Timmons, D.J.; Fang, Q-R.; Li, J-R.; Makal, T.A.; Young, M.D.; Yuan, D.; Zhao, D.; Zhuang, W.; Zhou, H-C. Potential applications of metal-organic frameworks. *Coord. Chem. Rev*. **2009,** *253* (23–24), pp 3042–3066.

[3] Schneeman, A.; Bon, V.; Schwedler, I.; Senkovska, I.; Kaskel, S.; Fischer, R.A. Flexible metal-organic frameworks. *Chem. Soc. Rev*. **2014,** *43* (16), pp 6062–6096.

[4] Férey, G.; Serre, C. Large breathing effects in three-dimensional porous hybrid matter: facts, analyses, rules and consequences. *Chem. Soc. Rev*. **2009,** *38* (5), pp 1380–1399.

[5] Miller, S.R.; Wright, P.A.; Devic, T.; Serre, C.; Férey, G.; Llewellyn, P.L.; Denoyel, R.; Gaberova, L.; Filinchik, Y. Single Crystal X-ray Diffraction Studies of Carbon Dioxide and Fuel-Related Gases Adsorbed on the Small Pore Scandium Terephthalate Metal Organic Framework, $Sc_2(O_2CC_6H_4CO_2)_3$. *Langmuir*. **2009,** *25* (6), pp 3618–3626.

[6] Klein, N.; Herzog, C.; Sabo, M.; Senkovska, I.; Getzschmann, J.; Paasch, S.; Lohe, M.R.; Brunner, E.; Kaskel, S. Monitoring adsorption-induced switching by ^{129}Xe NMR spectroscopy in a new metal–organic framework Ni_2(2,6- ndc)$_2$(dabco). *Phys. Chem. Chem. Phys*. **2010,** *12* (37), pp 11778–117784.

[7] Ryder, M.R.; Civalleri, B.; Bennett, T.D.; Henke, S.; Rudić, S.; Cinque, G.; Fernandez-Alonso, F.; Tan, J-C. Identifying the Role of Terahertz Vibrations in Metal-Organic Frameworks: From Gate-Opening Phenomenon to Shear-Driven Structural Destabilization. *Phys. Rev. Lett*. **2014,** *113* (21), pp 215502–215508.

[8] Ryder, M.R.; Civalleri, B.; Cinque, G.; Tan, J-C. Discovering connections between terahertz vibrations and elasticity underpinning the collective dynamics of HKUST-1 metal-organic framework. *Cryst. Eng. Comm*. **2016,** *18* (23), pp 4303–4312.

[9] Tan, N.Y.; Ruggiero, M.T.; Orellana-Tavra, C.; Tian, T.; Bond, A.D.; Korter, T.M.; Fairen-Jimenez, D.; Zeitler, J.A. Investigation of the terahertz vibrational modes of ZIF-8 and ZIF-90 with terahertz time-domain spectroscopy. *Chem. Comm*. **2015,** *51* (89), pp 16037–16040.

[10] Coudert, F-X.; Boutin, A.; Fuchs, A.H.; Neimark, A.V. Adsorption Deformation and Structural Transitions in Metal-Organic Frameworks: From the Unit Cell to the Crystal. *J. Phys. Chem. Lett.* **2013,** *4* (19), pp 3198–3205.

[11] Horcajada, P.; Serre, C.; Maurin, G.; Ramsahye, N.A.; Balas, F.; Vallet-Regí, M.; Sebban, M.; Taulelle, F.; Férey, G. Flexible Porous Metal-Organic Frameworks for a Controlled Drug Delivery. *J. Am. Chem. Soc*. **2008,** *130* (21), pp 6774–6780.

[12] Loiseau, T.; Serre, C.; Huguenard, C.; Fink, G.; Taulelle, F.; Henry, M.; Bataille, T.; Férey, G. A Rationale for the Large Breathing of the Porous Aluminum Terephthalate (MIL-53) Upon Hydration. *Chem. Eur. J*. **2004,** *10* (6), pp 1373–1382.

[13] Li, Z.; Wu, Y.; Li, J.; Zhang, Y.; Zou, X.; Li, F. The Metal-Organic Framework MIL-53 (Al) Constructed from Multiple Metal Sources: Alumina, Aluminum Hydroxide, and Boehmite. *Chem. Eur. J*. **2015,** *21* (18), pp 6913–6920.

[14] Volkringer, C.; Loiseau, T.; Guillou, N.; Férey, G.; Elkaïm, E.; Vimont, A. XRD and IR structural investigations of a particular breathing effect in the MOF-type gallium terephthalate MIL-54(Ga). *Dalton Trans*. **2009,** (12) pp 2241–2249.

[15] Biswas, S.; Ahnfeldt, T.; Stock, N. New Functionalized Flexible Al-MIL-53-X (X = -Cl, -Br, $-CH_3$, $-NO_2$, $-(OH)_2$) Solids: Synthesis, Characterization, Sorption, and Breathing Behavior. *Inorg. Chem.* **2011,** *50* (19), pp 9518–9526.

[16] Volkringer, C.; Loiseau, T.; Guillou, N.; Férey, G.; Haouas, M.; Taulelle, F.; Elkaim, E.; Stock, N. High-Throughput Aided Synthesis of the Porous Metal-Organic Framework-Type Aluminum Pyromellitate, MIL-121, with Extra Carboxylic Acid Functionalization. *Inorg. Chem*. **2010,** *49* (21), pp 9852–9862.

[17] Ahnfeldt, T.; Gunzelman, D.; Loiseau, T.; Hirsemann, D.; Senker, J.; Férey, G.; Stock, N. Synthesis and Modification of a Functionalized 3D Open-Framework Structure with MIL-53 Topology. *Inorg. Chem*. **2009,** *48* (7), pp 3057–3064.

[18] Hoffman, A.E.J.; Wieme, J.; Rogge, S.M.J.; Vanduyfhuys, L.; Van Speybroeck, V. The impact of lattice vibrations on the macroscopic breathing behavior of MIL-53(Al). *Z. Kristallogr*. **2019,** *234* (7–8), pp 529–545.

[19] Hoffman, A.E.J.; Vanduyfhuys, L.; Nevjestić, I.; Wieme, J.; Rogge, S.M.J.; Depauw, H.; Van Der Voort, P.; Vrielinck, H.; Van Speybroeck, V. Elucidating the Vibrational Fingerprint of the Flexible Metal-Organic Framework MIL-53(Al) Using a Combined Experimental/Computational Approach. *J. Phys. Chem. C*. **2018,** *122* (5), pp 2734–2746.

[20] Liu, Y.; Her, J-H; Dailly, A.; Ramirez-Cuesta, A.J.; Neumann, D.A.; Brown, C.M. Reversible Structural Transition in MIL-53 with Large Temperature Hysteresis. *J. Am. Chem. Soc.* **2008,** *130* (35), pp 11813–11818.

SEEDLING PROJECTS

Vertically aligned 2D nano-sheets: Chemical protection at the edge

John M. Landers[a,b], Matthew A. Browe[a]*, Christopher J. Karwacki[a]
[a]U.S. Army Combat Capabilities Development Command Chemical Biological Center, Research & Technology Directorate, 8198 Blackhawk Rd, Aberdeen Proving Ground, MD 21010
[b]National Research Council, 500 5th St NW, Washington, DC 20001

ABSTRACT

Vertical alignment of graphene sheets was attempted using methods of applied magnetic field from benchtop-strength magnets and unidirectional freezing. Applied magnetic field generated alignment but failed to result in homogeneous dispersion of the graphene sheet components. Unidirectional freezing generated more uniform dispersion of the graphene sheets, as verified by scanning electron microscopy. Additionally, cyclic voltammetry methods were established through this project.

Keywords: graphene, oxygen reduction reaction, catalysis, anisotropic, peroxide, iron oxide, magnetic, unidirectional freezing

1. INTRODUCTION

Current research thrusts in chemical and biological defense have centered on translating solution-based chemistries to a solid substrate. Further, recent efforts have involved usage of anisotropic structures, such as the laponite-polyethylene oxide system, to demonstrate high breathability and permselectivity when measuring barrier data against water vapor and vesicants. Graphene sheets provide the potential to combine both properties, as their edges have shown to be thermodynamically favorable for producing peroxide via the oxygen reduction reaction[1] (ORR), as depicted in Figure 1, serving as a favorable oxidation catalyst. Also, they have shown to be magnetically anisotropic and thus capable of alignment upon applied magnetic field (Figure 1);[2] however, superconducting magnets were required for producing this effect. Deposition of iron nanoparticles onto the graphene sheets, though, has shown to result in achieving magnetic properties via benchtop-strength magnets.[3] Lastly, unidirectional freezing has shown to produce alignment via application of a thermal gradient.[4] These two methods were investigated to elucidate their ability for producing homogeneously-aligned graphene sheets.

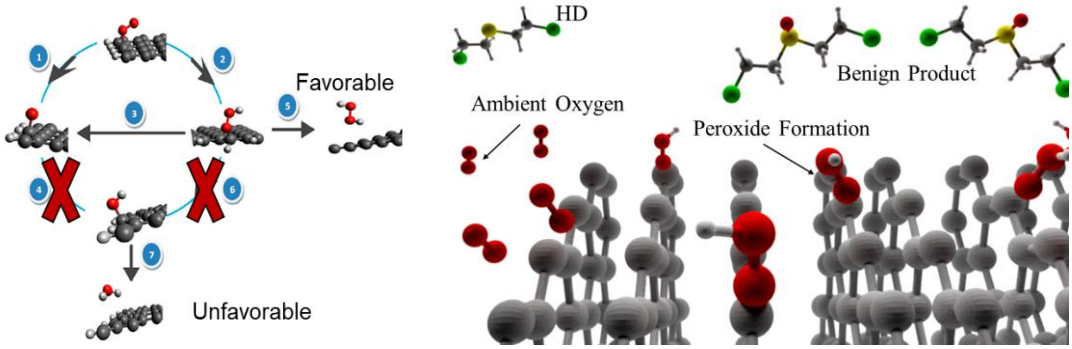

Figure 1. (left) ORR pathway and (right) HD oxidation reaction on graphene sheets via the ORR.

2. MATERIALS AND METHODOLOGY

2.1 Materials

Graphene powder (G), graphene oxide powder (GO), iron oxide-deposited graphene powder (Fe–G), and iron oxide-deposited graphene oxide powder (Fe–GO) were acquired from U.S. Research Nanomaterials, Inc. Graphene oxide solution (GO–aq) was acquired from Graphene Supermarket. Polyvinyl alcohol (PVA) powder, hydroxyethyl

methacylate solution (HEMA; 97 %), ethylene glycol dimethacrylate solution (EGDMA; 98 %), and 4-4'-azobis(4-cyanovaleric acid) powder (ACVA; 98 %) were acquired from Sigma-Aldrich®.

2.2 Methodology

2.2.1 Materials synthesis

Synthesizing films via magnetic alignment involved precursor solutions of weight ratio, 100:10:1:0.2 HEMA:EGDMA:ACVA:Fe-G, with a baseline film without aligned component synthesized in weight ratio, 100:10:1 HEMA:EGDMA:ACVA. The overall synthesis procedure is depicted in Figure 2 and consisted of pipetting 7 mL of the precursor solution into a 4-inch diameter polytetrafluoroethylene dish. The precursor solution was then cured via application of ultraviolet (UV) light to the films using a Cole-Parmer® EW-97600-00 UV lamp, with a listed wavelength of 365 nm, a power of 100 W, and a voltage of 115 V, utilizing an irradiation distance of approximately 6 inches between the bulb and film. A ring magnet with 53 lb of force was used for aligning the sheets during the curing process; vertical alignment was attempted by placing the magnet below the dish, and horizontal alignment was attempted by placing the magnet to the side of the dish. The cured films were then dried overnight and etched with O_3 the following day using an OZX-300 ozone generator, applied to the films for one hour each, while simultaneously exposing them to UV light using the same procedure employed during the curing process.

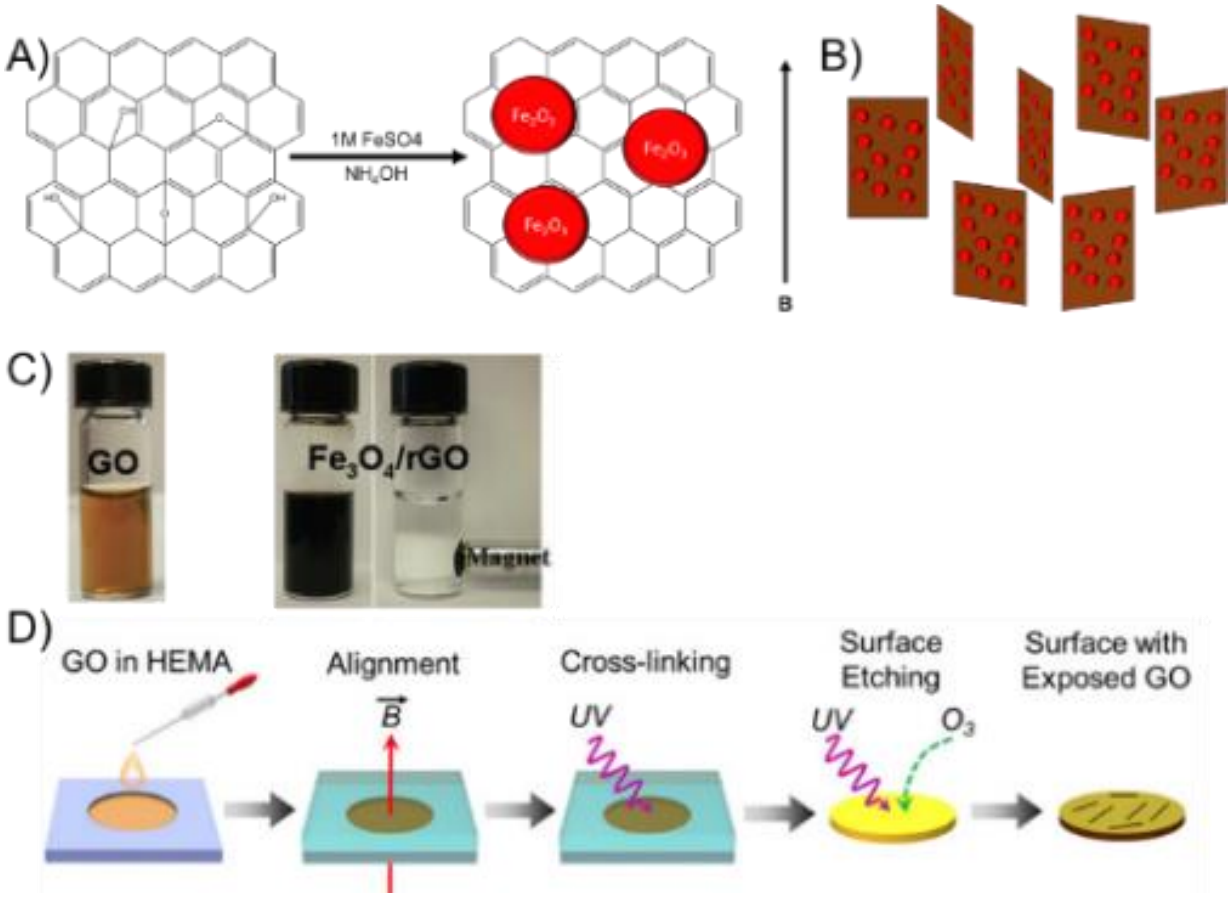

Figure 2. Magnetic alignment synthesis.

The unidirectional freezing synthesis, depicted in Figure 3, consisted of synthesizing films using graphene oxide solution and 4 wt% PVA solution in GO:PVA ratios of 10:1 and 1:10 via pipetting 1 mL total solution into a 0.5-inch-diameter plastic cap. A thermal gradient was then applied to the cap via placing it on top of a copper rod immersed in liquid nitrogen for 10 minutes. The resulting film was then freeze-dried overnight using a SP Scientific VirTis Wizard 2.0 lyophilizer.

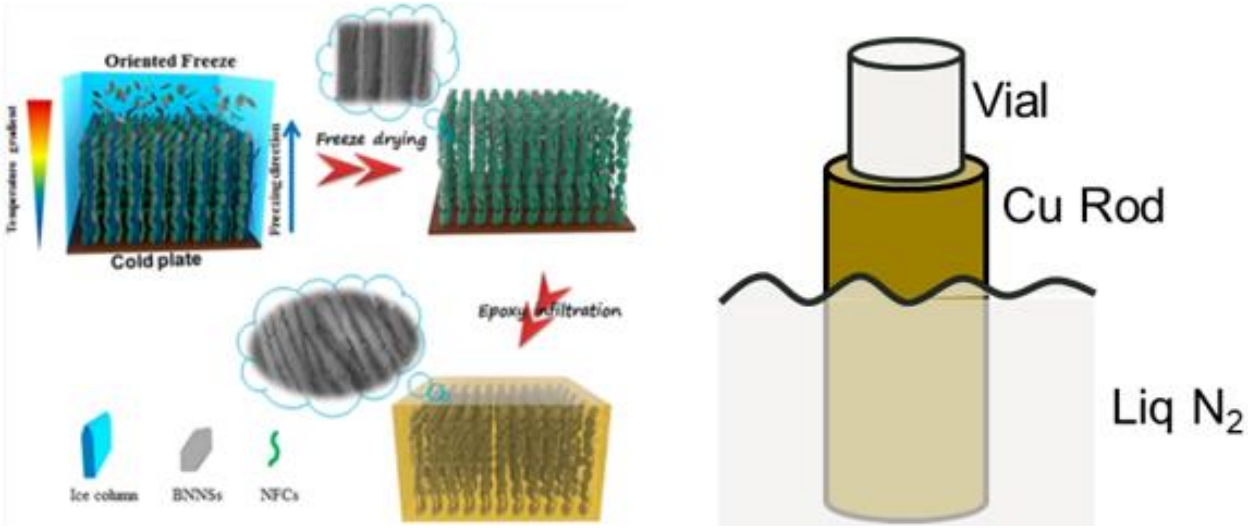

Figure 3. Unidirectional freezing synthesis.

2.2.2 X-ray diffraction

X-ray diffraction (XRD) measurements were collected using a Rigaku® Miniflex™ 600 X-ray powder diffractometer with a D/Tex detector. Samples were scanned at 40 kV and 15 mA, using Cu Kα radiation (λ = 1.54 Å) at a scan rate of 5 °min^{-1}, over a 2θ range of 2–50 °. Zero-background discs were used for XRD measurements. A background correction was performed in the Rigaku® PDXL analysis software (version 2.1.3.6).

2.2.3 Raman spectroscopy

Raman spectroscopy experiments were performed on the powder materials using a JASCO NRS-3200 Raman system. A wavelength of 785 nm was used for excitation, with a power of ~4 mW incident on the substrate. The Raman-scattered light was collected in the backscattering configuration and transmitted through a 100-μm slit to a 600 grooves/mm grating, which dispersed the light onto a thermoelectrically-cooled Andor charge-coupled device detector (Oxford Instruments). A spectral resolution of approximately 8 cm^{-1} was obtained.

2.2.4 Cyclic voltammetry

Cyclic voltammetry (CV) experiments were performed on the baseline powders using a Keithley 2450-EC potentiostat (Tektronix, Inc.) in a 3-electrode setup utilizing a 3-mm glassy carbon working electrode, an Ag/AgCl reference electrode, and a Pt wire counter electrode. A precursor slurry of each material was first prepared by mixing 50 mg of the powder with 10 mL of a 3:1 water:isopropanol mixture and 1 mL of a 15 wt% Nafion™ solution (LIQUion LQ-1115, 1100 EW). A 1-μL aliquot of the resulting solution was drop cast onto the working electrode and dried. Subsequently, CV scans were conducted in 0.1 M H_2SO_4 solution using a scan rate of 10 mV/s and three cycles per scan, with the third cycle utilized for data reporting.

2.2.5 Scanning electron microscopy

Scanning electron microscopy (SEM) images were obtained using a Phenom ProXGSR desktop SEM. Samples were gold-sputtered and then mounted on double-sided carbon tape. Data collection occurred at 15 kV in analysis mode and 1,024 cm^{-1} resolution.

2.2.6 Chloroethyl ethyl sulfide permeation

Chloroethyl ethyl sulfide (CEES) permeation testing was conducted in accordance with ASTM F739-12. Briefly, a 1.25-inch x 1.25-inch segment of film was cut, weighed, and measured for thickness with a micrometer caliper, and placed in a 1-inch-diameter Pesce PTC 700 permeation test cell. An equal countercurrent flow of 0 % relative humidity and 300 mL min^{-1} air was applied to both sides of the swatch with a feed side concentration of 300 mg/m^3 of CEES. The chemical concentration was monitored at three locations in the PTC 700 cell: the inlet stream to the cell apparatus (designated as the feed line), the outlet stream from the cell apparatus (designated as the retentate line), and the outlet

stream from the cell apparatus on the opposite side of the swatch (designated as the permeate line). The test was considered complete when the two outlet stream concentrations summed to equal the value of the feed concentration, closing the mass balance and satisfying the condition of

$$C_{feed} - C_{retentate} - C_{permeate} = 0. \quad (1)$$

The steady state permeation rate was recorded upon completion of the test.

3. RESULTS

3.1 Magnetic alignment

3.1.1 Materials synthesis

Films synthesized via magnetic alignment are shown in Figure 4. The graphene-based sheets demonstrated a strong response to a low-strength magnetic field and ostensible alignment, but it was very heterogeneous in nature. The vertically-aligned sheets migrated radially outward from the center of the magnet, and the horizontally-aligned sheets migrated toward the magnet source.

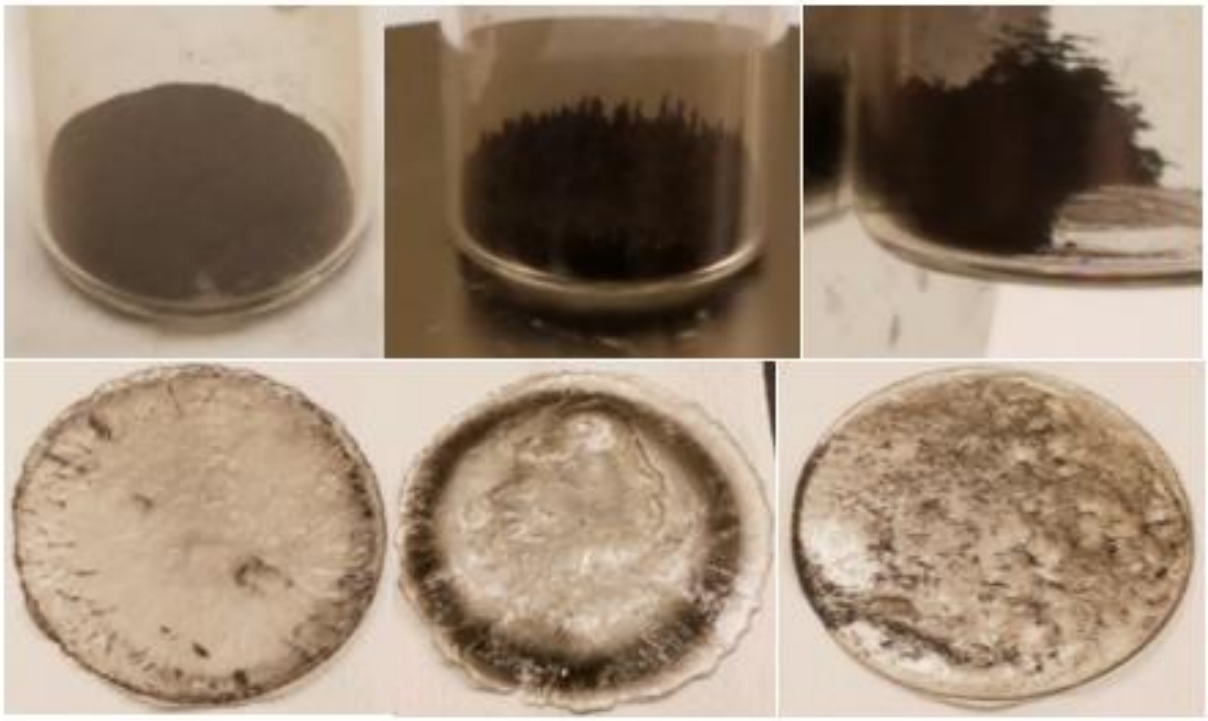

Figure 4. Precursor Fe–G powders (top) and composite films (bottom) in random (left), vertical (middle), and horizontal (right) orientation.

3.1.2 X-ray diffraction

Peaks for the Fe–G-HEMA composites samples are depicted in Figure 5. It is shown that the characteristic peaks of Fe–G, at 2-theta values of 27 ° and 36 °, are present in the aligned composite samples. The vertically-aligned composite film displayed the strongest peak intensity; although, this is likely an artifact of the higher sample density within the film.

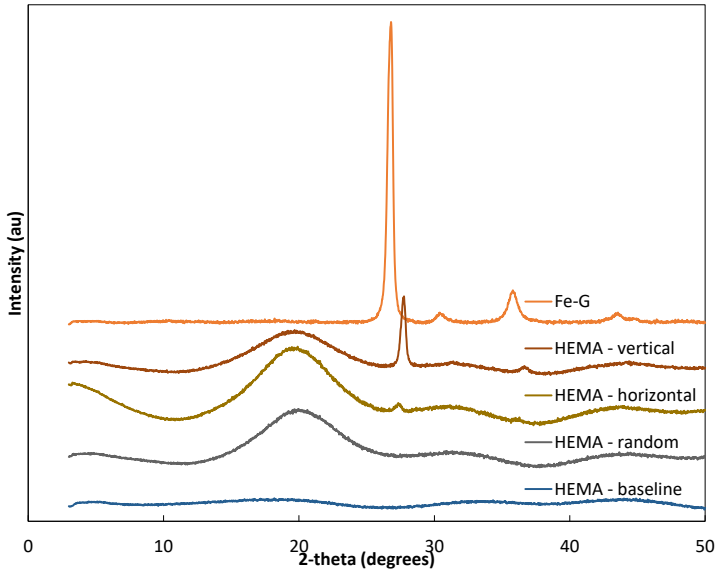

Figure 5. XRD patterns of HEMA-Fe-G composite films.

3.1.3 Raman spectroscopy

Raman spectra of the graphene sheet-based powders are depicted in Figure 6. The spectra of the graphene oxide samples exhibit characteristic D and G band peaks at 1,350 cm^{-1} and 1,580 cm^{-1}, respectively, and these are largely maintained upon iron oxide incorporation. The spectra of the graphene samples show the characteristic G and 2D peaks located at 1,580 cm^{-1} and 2,690 cm^{-1}, respectively, though these peaks are greatly diminished upon incorporation of iron oxide—indicative of significant disruption in the order of the material from the iron oxide.

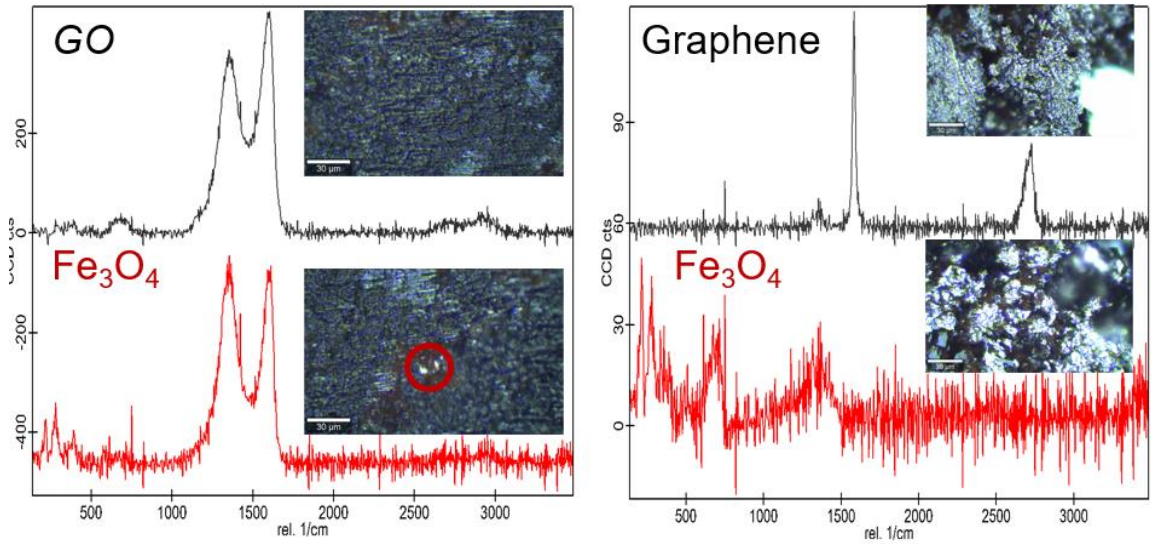

Figure 6. Raman spectra of graphene-based composite films (top) and their corresponding iron oxide-impregnated analogues (bottom).

3.1.4 Cyclic voltammetry

CV efforts commenced with a baseline control experiment to verify proper function and execution of the instrument, as this technique was a new capability developed under this project. The control experiment involved utilizing 10 mL of an electrolyte solution containing 0.2 mL of 0.1 $K_3Fe(CN)_6$ and 9.8 mL of 1.0 M KNO_3, a scan rate of 10 mV/second, and a bare working electrode. Results, depicted in Figure 7, show strong agreement with data provided by Keithley technical support and indicate successful implementation of the technique.

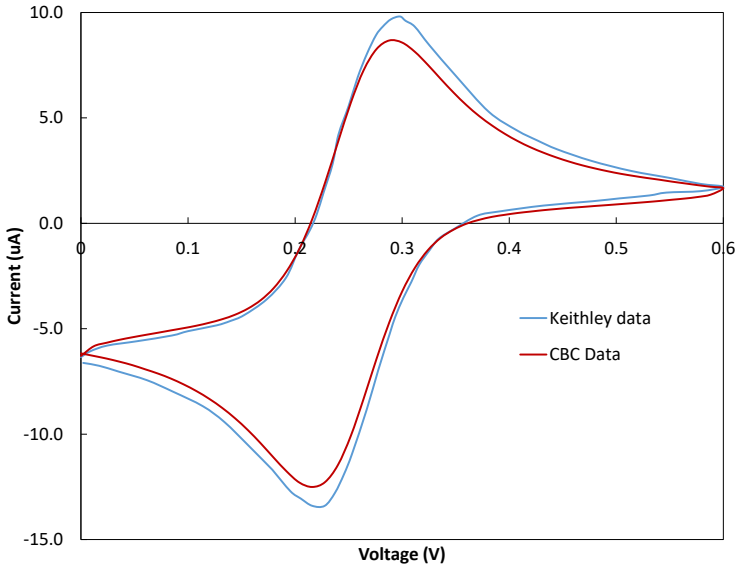

Figure 7. Comparison of CV control experiment with data provided by Keithley technical support.

Subsequently, CV scans were executed through depositing a slurry of the G and Fe–G powders onto the working electrode, as described previously, and results are depicted in Figure 8. It is seen that the iron-impregnated graphene sheets show a much greater differential between the cathodic and anodic scans than the graphene sheets alone, indicative of greater capacitance in the iron-impregnated analogue and consistent with previously published results.[3] Methods were established for bubbling the electrolyte solution with nitrogen and oxygen gas, with the intent of collecting subsequent CV scans of each material in each setting and using the differentials between the oxygen- and nitrogen-saturated scans as quantification of the propensity of the material for participating in the oxygen reduction reaction. However, results were inconclusive as of the end of the funding period for this project.

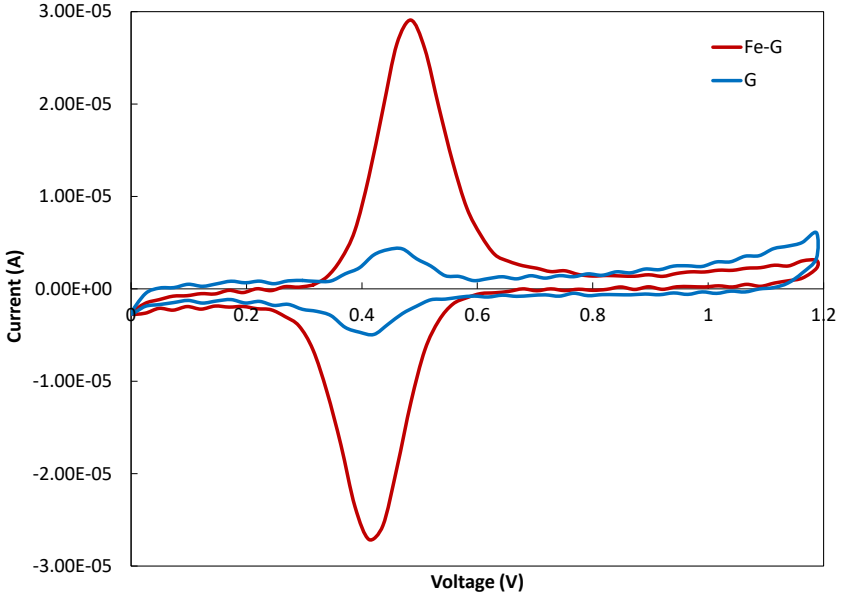

Figure 8. Voltammograms of graphene and iron-impregnated graphene sheets.

3.1.5 Chloroethyl ethyl sulfide permeation

CEES permeation data of the magnetically-aligned composite films are depicted in Figure 9. All cured polymers were approximately 1.5 mm in thickness. It is shown that, in general, incorporation of graphene sheet composite fillers had a minimal but measurable impact on the barrier properties of the film. The composites with randomly-aligned and horizontally-aligned sheets exhibited similar permeate concentration profiles, likely due to the uneven distribution of

the graphene sheet components in the film with horizontally-aligned sheets. The film with vertically-aligned sheets yielded the best barrier properties, likely due to a benefit it received from uneven sheet distribution, resulting in more clustering of the graphene component in this case and greater impedance of permeating chemical.

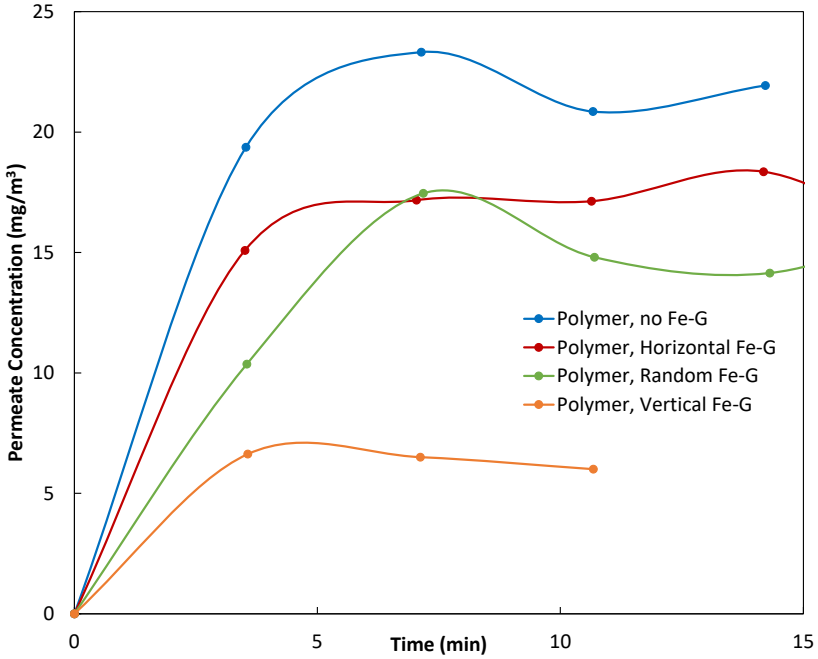

Figure 9. CEES permeation data of Fe–G-based composite films.

3.2 Unidirectional freezing

3.2.1 Materials synthesis

Films synthesized using unidirectional freezing are depicted in Figure 10. This method generated ostensibly better dispersion of the graphene component. Further, vertical alignment of ice crystals on the film surface provided additional insight of anisotropic behavior in the film.

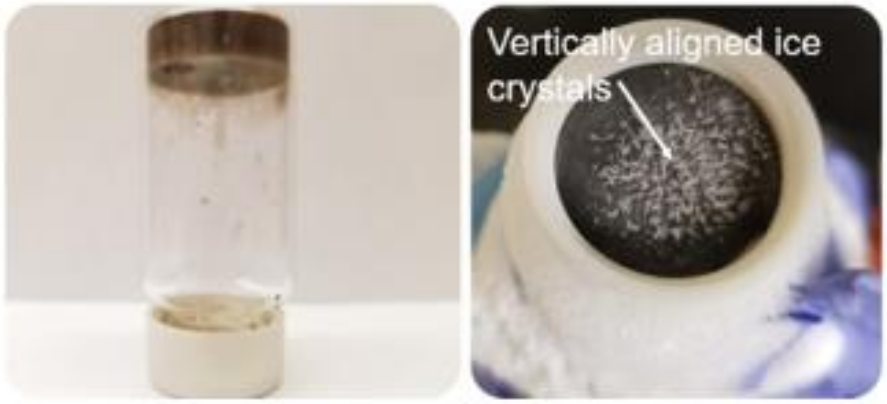

Figure 10. Unidirectionally frozen film.

3.2.2 Scanning electron microscopy

SEM data was collected to evaluate resulting alignment, and images of the graphene solution-PVA composite aerogels are depicted in Figure 11. The unidirectional freezing method was indeed found to produce aligned and homogeneously-dispersed graphene sheets. This is likely due to the greater homogeneity of the applied thermal gradient, as opposed to the heterogeneous nature of the applied magnetic field.

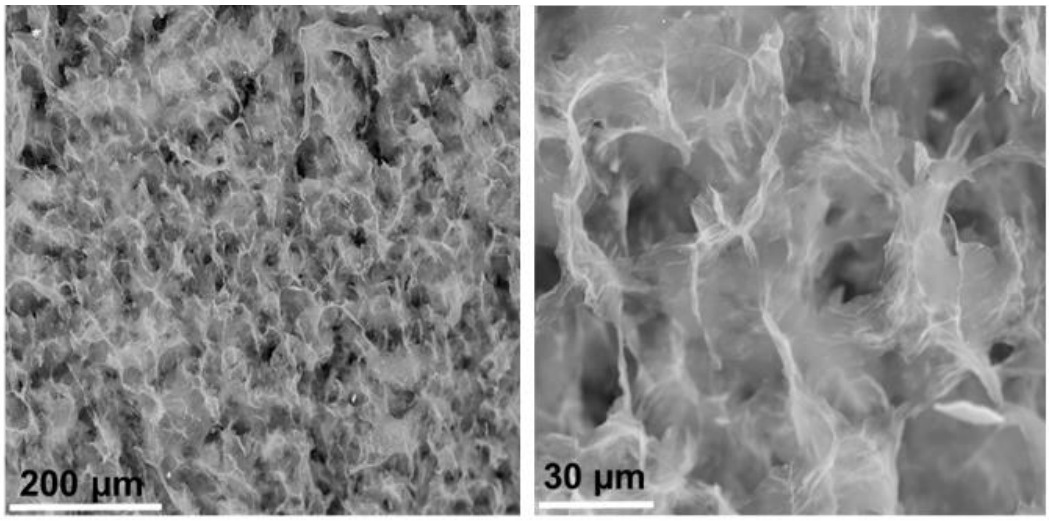

Figure 11. SEM images of the unidirectionally-frozen 10:1 GO:PVA film.

Performance evaluation of the unidirectionally-frozen film against vesicant was not conducted during the funding period for this project. However, future work is expected to elucidate the feasibility of this system for serving as an oxidation catalyst and will serve as a springboard for follow-on efforts if verified as successful.

4. CONCLUSIONS

Alignment of graphene and graphene-oxide-based nanosheets in polymer-based composite films was attempted via methods of applied magnetic field and unidirectional freezing. Applied magnetic field demonstrated alignment, but the resulting distribution of the sheets was highly heterogeneous in nature and did not yield an effective barrier material. Unidirectional freezing generated much more homogeneous dispersion of the graphene sheet component. Performance evaluation of the unidirectionally-frozen film was not performed under the funding period for this project but will be elucidated under separate efforts.

ACKNOWLEDGMENTS

Funding was provided by the Director, Combat Capabilities Development Command Chemical Biological Center under the authorities and provisions of Section 2363 of the FY 2018 NDAA to develop new technologies, engineer innovations, and introduce game-changing capabilities.

REFERENCES

[1] Ly, Q.; Merinov, B.V.; Xiao, H.; Goddard III, W.A.; Yu, T.H. The Oxygen Reduction Reaction on Graphene from Quantum Mechanics: Comparing Armchair and Zigzag Carbon Edges. *J. Phys. Chem. C*. **2017,** *121* (44), pp 24408–24417.

[2] Lu, X.; Feng, X.; Werber, J.R.; Chu, C.; Zucker, I.; Kim, J.-H.; Osuji, C.O.; Elimelech, M. Enhanced antibacterial activity through the controlled alignment of graphene oxide nanosheets. *Proc. Natl. Acad. Sci. U. S. A.* **2017,** *114* (46), pp E9793–E9801.

[3] Xue, Y.; Chen, H.; Yu, D.; Wang, S.; Yardeni, M.; Dai, Q.; Guo, M.; Liu, Y.; Lu, F.; Qu, J.; Dai, L. Oxidizing metal ions with graphene oxide: the in situ formation of magnetic nanoparticles on self-reduced graphene sheets for multifunctional applications. *Chem. Comm*. **2011,** *47* (42), pp 11689–11691.

[4] Wang, X.; Wu, P. 3D Vertically Aligned BNNS Network with Long-Range Continuous Channels for Achieving a Highly Thermally Conductive Composite. *ACS Appl. Mater. Interfaces*. **2019,** *11*, pp 28943–28952.

Probing the root cause of UiO-66-NH_2 metal-organic framework darkening upon exposure to light and ambient contaminants

Gregory W. Peterson*, Monica L. McEntee, Erin M. Durke
U.S. Army Combat Capabilities Development Command Chemical Biological Center, Research & Technology Directorate, 8198 Blackhawk Rd, Aberdeen Proving Ground, MD 21010

ABSTRACT

The metal-organic framework UiO-66-NH_2 has shown significant promise for filtration, protection, and decontamination applications; however, the material darkens upon exposure to light. The underlying mechanism of this color change is unknown and has not been studied in the literature. In this project, we exposed the UiO-66-NH_2 to potential contaminants (dimethylformamide from synthesis and carbon dioxide from the atmosphere) and then exposed the material to light (white ambient light and ultraviolet light) to understand the mechanism associated with color change. Results will inform the continuing maturation and transition of this material to military applications.

Keywords: metal-organic framework, light exposure, contamination, *in situ*

1. INTRODUCTION

The metal-organic framework (MOF) UiO-66 family is one of the most versatile and stable MOFs studied today. In particular, UiO-66-NH_2 has demonstrated the ability to efficiently react with toxic industrial chemicals–such as chlorine[2] and nitrogen dioxide[3]–and chemical warfare agents.[4] This MOF has been synthesized, engineered, scaled, matured, and transitioned from the Joint Science and Technology Office to the Joint Program Executive Office for use in novel filters. Yet, as investigations have begun exploring other technologies—such as protective suits and sensors that may see constant exposure to light—a color change of the material over time has been observed. Even though this MOF was developed over a decade ago, there has been no research published on the underlying phenomena responsible for this behavior. This study plans to more fully understand the change in color and determine if the color change is indicative of a poisoning or degradation of the MOF.

UiO-66-NH_2 is synthesized from zirconium chloride and aminoterephthalic acid (ATA), resulting in a 3D structure with high surface area and robust stability (Figure 1). The material has been investigated for, among other things, photocatalytic purposes, and has been shown to generate electron-hole pairs upon visible light irradiation and efficiently photooxidize a number of organic species. Researchers have found the origin of the photocatalytic nature of this MOF to be a transfer of π electrons from the aryl amine moiety to the zirconium oxide secondary building unit (SBU).[1]

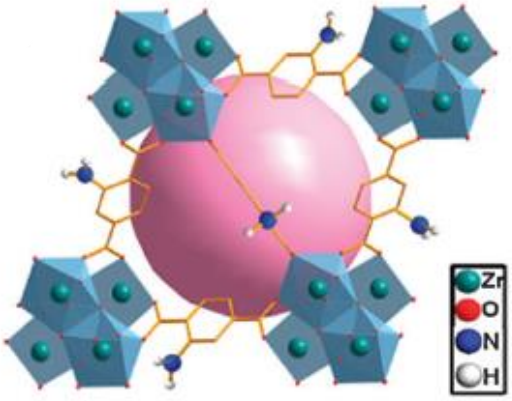

Figure 1. UiO-66-NH_2 MOF.

The UV-vis spectrum (Figure 2i) indicates that UiO-66 absorbs photons in the UV range while UiO-66-NH_2 absorbs both UV and violet light, causing the material to appear yellow according to the color wheel (Figure 2ii). Figure 2iii shows how a jar of UiO-66-NH_2 turned partially brown (note: the bottom half was exposed to light for extended periods of time while the top half was covered). Other empirical evidence has been collected showing no change in color when the MOF is exposed to a laboratory atmosphere in the dark even after one year (Figure 2iv). As mentioned above, UiO-66-NH_2 is known to be photoactive. A first hypothesis was that these oxygen radicals may cleave the C–N bond of the aryl amine; however, this would result in a hypsochromic shift (i.e., blue-shift), resulting in less absorption in the visible range and a general lightening of the material similar to UiO-66 (see Figure 2i insets). To achieve a darkening of the material, a bathochromic shift (i.e., red-shift) must occur, absorbing more in the blue-green (~450–560 nm) region such that the material darkens to orange-red. Literature suggests that multiple amine-based species are capable of absorbing light in the blue-green region. Azarifar and coworkers demonstrated the conversion of the aryl amine to an imine, which resulted in higher molar absorptivity at longer wavelengths.[5] The lack of atmospheric carbonyl required for imine formation makes this hypothesis seem unlikely; however, UiO-66-NH_2 is synthesized with dimethylformamide and frequently exchanged with acetone, both of which may be present in quantities sufficient for conversion.

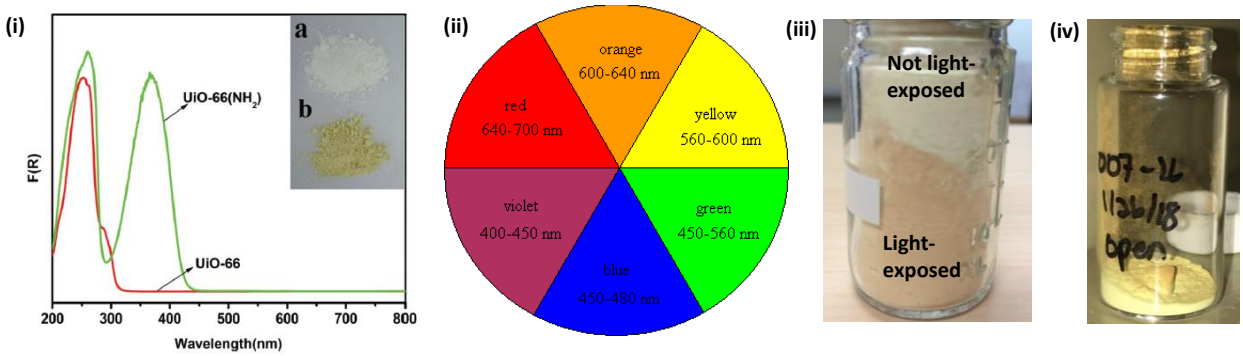

Figure 2. (i) The UV-vis spectrum of UiO-66 and UiO-66-NH_2.[1] The inset shows (a) UiO-66 and (b) UiO-66-NH_2 appearing white and yellow in color, respectively. (ii) The color wheel, in which the reflected (observed) wavelength is opposite of the absorbed wavelength. (iii) A closed jar of UiO-66-NH_2 that was partially protected from light on top. (iv) An open vial of UiO-66-NH_2 that has been stored in a dark cabinet for over 1 year.

Alternatively, carbamate may form in the MOF due to interactions with atmospheric CO_2 and the aryl amine group on the MOF linker;[6] it is possible that this reaction results in a red-shift in the absorption spectra. However, CO_2 alone cannot account for this reaction, since the MOF open to the atmosphere in dark conditions does not change color (Figure 2iv). Thus, we hypothesize that the color change is due to a chemical reaction at the amine group that is activated by exposure to light.

2. METHODOLOGY

2.1 Metal-organic frameworks

UiO-66-NH_2 was obtained from TDA under a Rapid Innovation Project. Two sets of materials were made from the mother powder. The first set was washed and rinsed three times with ethanol to remove as much dimethyl formamide (DMF) as possible. The second set was rinsed with excessive DMF. Both samples were exposed to ambient (white) and UV light for up to 7 days in sealed and open containers.

Sample nomenclature below shows the material (UiO-66-NH_2) followed by ethanol or DMF treatment followed by time and type of light exposure. Finally, some samples were tested in an open environment and are therefore denoted as "_open".

2.2 Materials characterization

A variety of techniques were used to characterize electrospun nanofibers and films developed. This section summarizes each technique.

2.2.1 Nitrogen isotherm

Nitrogen uptake was measured at 77 Kelvin (K) using a Micromeritics® ASAP™ 2040. Samples were off-gassed at 120 °C overnight under vacuum. Surface area measurements were calculated using the Brunauer-Emmett-Teller method, and total pore volumes were calculated at a relative pressure of 0.975 atm.

2.2.2 Powder X-ray diffraction

Powder X-ray diffraction (PXRD) measurements were conducted using a Rigaku® Miniflex™ 600 X-ray powder diffractometer with a D/Tex detector. Samples were scanned at 40 kV and 15 mA using Cu Kα radiation, a scan rate of 5 ° min^{-1}, over a 2θ range of 3 °C to 50 °C. Data were plotted relative to the highest intensity peak and offset on the *y*-axis to show differences between each sample.

2.2.3 Scanning electron microscopy

Scanning electron microscopy (SEM) images were obtained using a Phenom GSR desktop SEM. Samples were supported on double-sided carbon tape and sputter-coated with gold prior to analysis. Typical settings for the instrument used an accelerating voltage of 15 kV at a nominal working distance of 10 mm. Specific operating conditions are listed with each image for clarity (Figure 4).

2.2.4 Transmission infrared spectroscopy

Transmission infrared spectroscopy (TIR) experiments were performed in a vacuum chamber with a base pressure of ~$3x10^{-9}$ Torr. Approximately 0.003 g of UiO-66-NH_2 powder was pressed into a W-grid attached to copper leads to allow for resistive heating and cooling of the surface in a temperature range from ~85–1,000 K at 0.1 K resolution. As a control, the sample was preheated to 400 K for ~45 minutes in vacuum to remove any solvent from the surface. After 45 minutes, the sample was cooled back down to room temperature (300 K). An infrared (IR) spectrum was then taken before CO_2(g) or UV exposure with an average of 256 scans at a 2 cm^{-1} resolution. The background spectrum used was the W-grid without MOF or the W-grid with MOF before exposure. Either CO_2(g) or UV light was then exposed to the sample, and an IR spectrum was taken over time at separate intervals. For comparison, the samples were exposed to CO_2(g) and UV without any pretreatment heating, in order to see if the solvents had any interactions with the UV light and/or CO_2(g).

2.2.5 Ultraviolet-visible spectroscopy

Ultraviolet-visible (UV-vis) spectra were measured using a JASCO V-650 spetrophotometer with an ILV-754 150 mm integrating sphere with a 5 nm band width at 400 nm/min in the range of 200–800 nm scan with a 340 nm source.

3. RESULTS AND DISCUSSION

3.1 Materials characterization

The materials first were characterized to determine differences in structure due to the various exposures. PXRD and nitrogen isotherm data are shown in Figure 3 for representative samples. In all cases, there was no noticeable change to the X-ray patterns, indicating the crystalline structure remained intact. Furthermore, only slight decreases in nitrogen uptake were observed, again indicating minimal degradation to the structure. BET surface area measurements indicated only slight decreases in surface area as compared to the native materials (Table 1). Visually, SEM images showed no change in morphology (Figure 4).

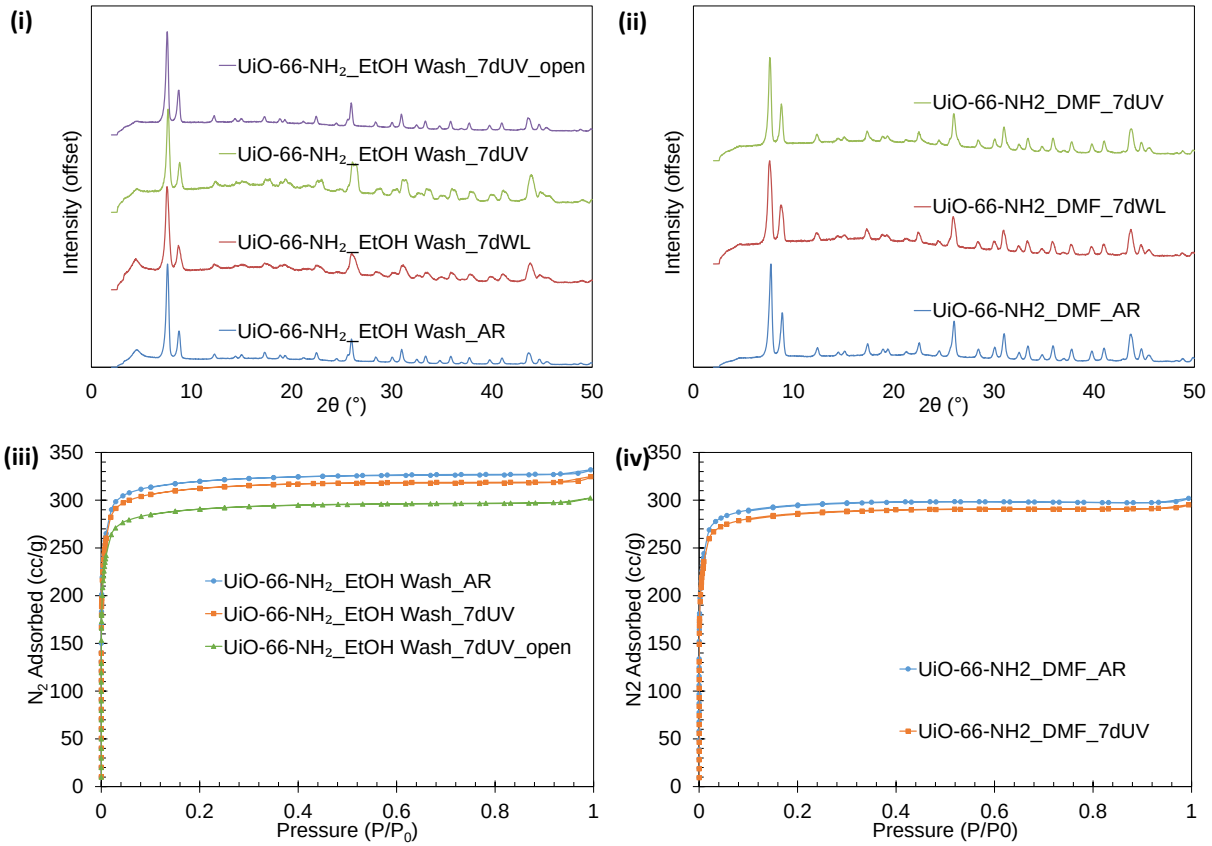

Figure 3. PXRD data for (i) ethanol and (ii) DMF washed samples. N_2 isotherms for (iii) ethanol and (iv) DMF washed samples.

Table 1. BET surface areas for select samples.

Sample	BET Surface Area (m^2/g)
UiO-66-NH_2_EtOH Wash_AR	1320
UiO-66-NH_2_EtOH Wash_7dUV	1160
UiO-66-NH_2_EtOH Wash_7dUV_open	1200
UiO-66-NH_2_DMF_AR	1220
UiO-66-NH_2_DMF_7dUV	1190

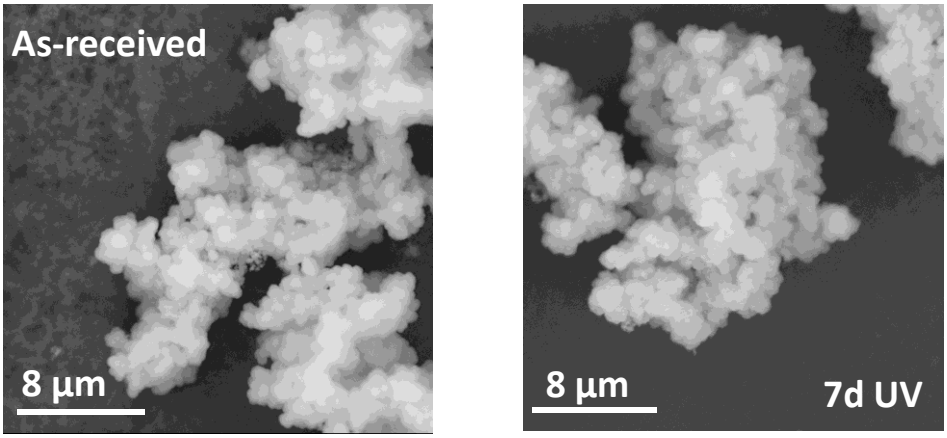

Figure 4. SEM images for (left) AR and (right) 7d UV exposed UiO-66-NH_2 washed with ethanol.

UV-vis data are presented in Figure 5 for ethanol-washed samples. A clear change in spectra occurs as samples are dosed with UV—the spectra correlate directly with changes to the sample color upon exposure. While the changes are noticeable from a visual and spectrophotometric perspective, the resulting band gap energies are virtually identical. Thus, the change in color likely does not change the electronic (or catalytic) properties of the material significantly.

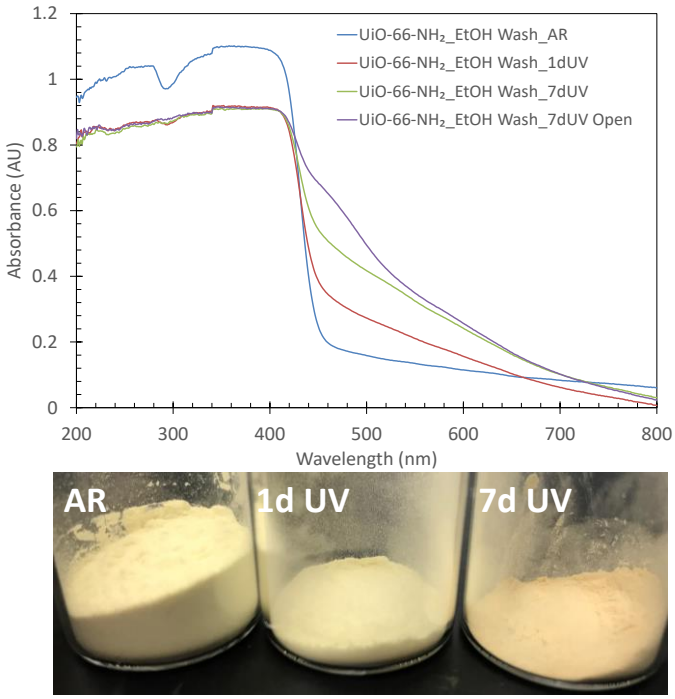

Figure 5. UV-vis spectra for select samples.

3.2 *In situ* infrared experiments

The hypothesis of this work was that the darkening of the material was directly related to the formation of imine or carbonate species due to interactions with DMF and carbon dioxide within (or after) the synthesis process. These changes could be measured spectroscopically through changes in the amine group according to Figure 6. Thus, we turned to *in situ* dosing of CO_2 and the introduction of light to measure responses on the material. Figure 7 shows the spectra prior to measurement. The amine group is clearly visible at ~1,630 cm^{-1}. DMF is also present in both samples at ~1,670 cm^{-1}, indicating that, even after excessive washing with ethanol, DMF remained. Interestingly, the peak at ~1,700 cm^{-1} corresponds well to the proposed imine stretch due to DMF interacting at the linker.

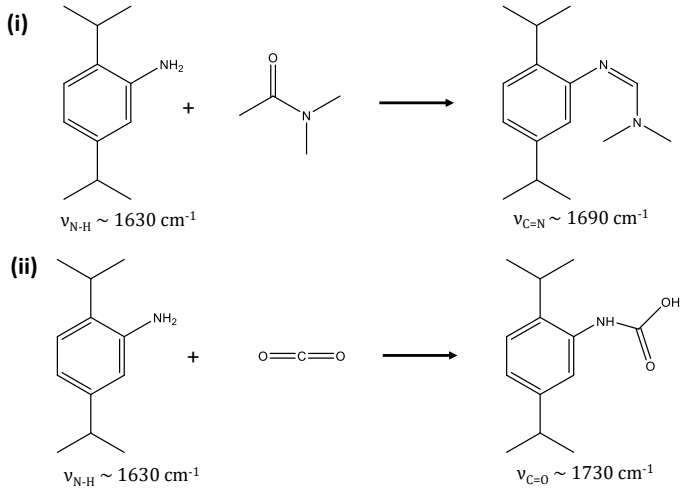

Figure 6. Potential chemistry occurring on the amine group of the linker of UiO-66-NH_2.

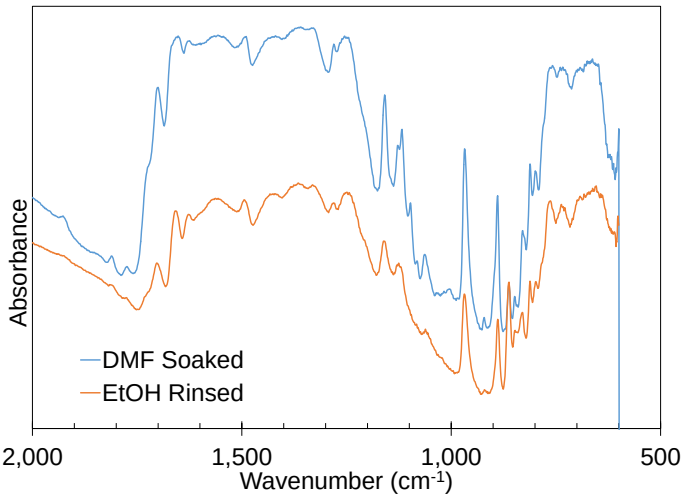

Figure 7. Spectra for UiO-66-NH_2 prior to introduction of light or CO_2.

In situ experiments carried out in TIR (Figure 8) were conducted for a variety of conditions. Simple exposure to UV light seemed to have limited effect on the material. UV exposure with and without CO_2 to DMF-washed UiO-66-NH_2 was difficult to interpret as peaks increased and decreased around 1,700 cm^{-1}. Thus, it was difficult to monitor the formation of imine functionality; however, the losses could correspond to liberation of DMF due to localized heating of the structure during UV exposure. On the CO_2-exposed, ethanol-washed UiO-66-NH_2, it appears carbamate species may have formed on the surface but were liberated upon UV exposure as seen by the disappearance of the ~1,730 cm^{-1} peak and the appearance of amine peaks at ~1,630 cm^{-1}.

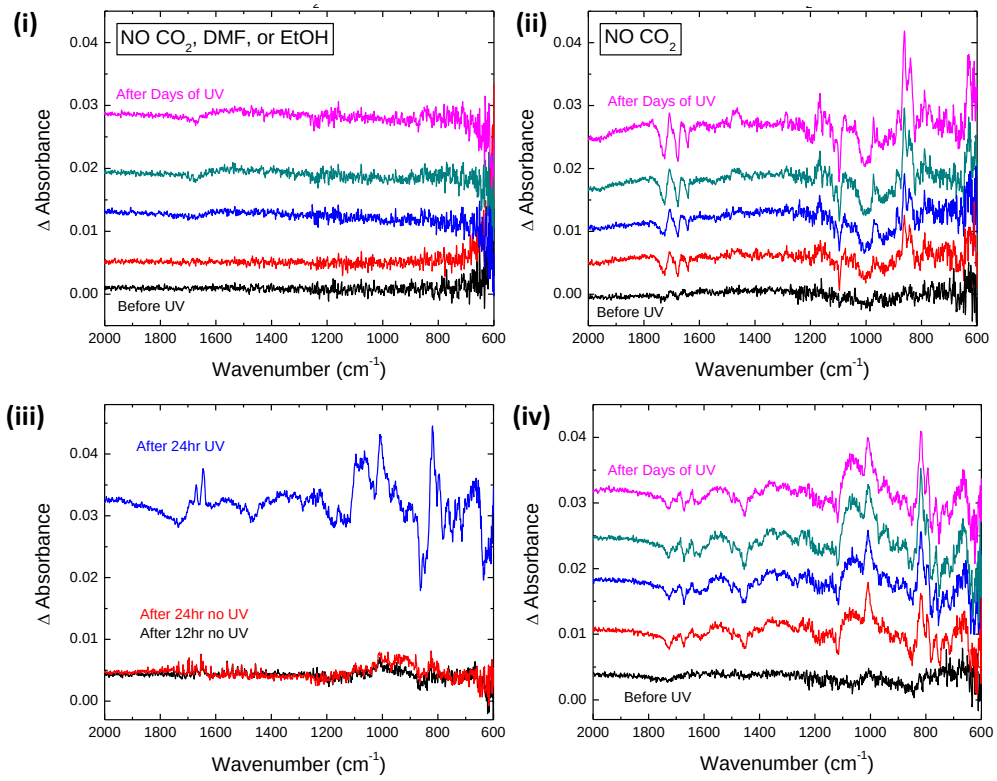

Figure 8. TIR spectra for (i) samples exposed to only UV light, (ii) DMF-washed UiO-66-NH_2 during exposure to UV light, (iii) ethanol-washed UiO-66-NH_2 during exposure to CO_2 and UV light, and (iv) DMF-washed UiO-66-NH_2 during exposure to CO_2 and UV light.

While there were observable changes to the linker during exposure to CO_2 and UV light, the underlying reactivity has yet to be determined. Chlorine breakthrough capacities are summarized in Table 2. Initial results indicate that the combination of UV and CO_2 hinder chlorine removal, which is removed by an electrophilic aromatic substitution reaction activated by the amine. Conversely, the initial results with the DMF sample indicates UV helps chlorine removal. These trends correspond well with the hypothesized mechanism of UV "cleaning" DMF off the system and a reduced reactivity due to carbamate formation.

Table 2. Chlorine loading of select samples.

Sample	Cl_2 loading (mol/kg)
UiO-66-NH_2_EtOH Wash_AR	11.7
UiO-66-NH_2_EtOH Wash_7dUV	5.8
UiO-66-NH_2_EtOH Wash_7dWL	9.2
UiO-66-NH_2_DMF_AR	3.6
UiO-66-NH_2_DMF_7dUV	10.0

4. CONCLUSIONS

UiO-66-NH_2 was dosed with DMF and CO_2 and exposed to white and UV light to determine potential degradation mechanisms due to color change. The structure remained intact based on PXRD, SEM, and nitrogen porosimetry characterization; however, clear changes were seen during *in situ* infrared experiments. Preliminary analysis suggests that UV may clean the structure after exposure to CO_2 and localized heating may off-gas DMF; however, the full mechanism has yet to be determined.

ACKNOWLEDGMENTS

Funding was provided by the Director, Combat Capabilities Development Command Chemical Biological Center under the authorities and provisions of Section 2363 of the FY 2018 NDAA to develop new technologies, engineer innovations, and introduce game-changing capabilities. The author thanks Matthew Browe and Amedeo Napolitano for running microbreakthrough experiments and Dr. Trent Tovar for conducting nitrogen isotherm experiments.

REFERENCES

[1] Long, J.; Wang, S.; Ding, Z.; Wang, S.; Zhou, Y.; Huang, L.; Wang, X. Amine-functionalized zirconium metal-organic framework as efficient visible-light photocatalyst for aerobic organic transformations. *Chem. Comm.* **2012,** *48* (95), pp 11656–11658.

[2] De Coste, J.B.; Browe, M.A.; Wagner, G.W.; Rossin, J.A.; Peterson, G.W. Removal of chlorine gas by an amine functionalized metal-organic framework via electrophilic aromatic substitution. *Chem. Commun.* **2015,** *51* (62), pp 12474–12477.

[3] Peterson, G.W.; Mahle, J.J.; DeCoste, J.B.; Gordon, W.O.; Rossin, J.A. Extraordinary NO_2 Removal by the Metal-Organic Framework UiO-66-NH_2. *Angew. Chem., Int. Ed.* **2016,** *55* (21), pp 6235–6238.

[4] Peterson, G.W.; Destefano, M.R.; Garibay, S.J.; Ploskonka, A.; McEntee, M.; Hall, M.; Karwacki, C.J.; Hupp, J.T.; Farha, O.K. Optimizing Toxic Chemical Removal through Defect-Induced UiO-66-NH_2 Metal-Organic Framework. *Chem. – Eur. J.* **2017,** *23* (63), pp 15913–15916.

[5] Azarifar, D.; Ghorbani-Vaghei, R.; Daliran, S.; Oveisi, A.R. A Multifunctional Zirconium-Based Metal-Organic Framework for the One-Pot Tandem Photooxidative Passerini Three-Component Reaction of Alcohols. *ChemCatChem.* **2017,** *9* (11), pp 1992–2000.

[6] McCann, N.; Phan, D.; Wang, X.; Conway, W.; Burns, R.; Attalla, M.; Puxty, G.; Maeder, M. Kinetics and Mechanism of Carbamate Formation from CO_2(aq), Carbonate Species, and Monoethanolamine in Aqueous Solution. *J. Phys. Chem. A.* **2009,** *113* (17), pp 5022–5029.

Enhancement of singlet oxygen generation via metal-organic framework functionalization

Ann M. Kulisiewicz[a], Sergio J. Garibay[a,b], Jared B. DeCoste[a]
[a]U.S. Army Combat Capabilities Development Command Chemical Biological Center, Research & Technology Directorate, 8198 Blackhawk Rd, Aberdeen Proving Ground, MD 21010
[b]National Research Council, 500 5th St, NW, Washington, D.C. 20001

ABSTRACT

Metal-organic frameworks are highly versatile materials that have shown great promise in chemical warfare agent adsorption and decontamination. Sulfur mustard has been one of the most prominently used chemical warfare agents over the last century; therefore, the development of effective detoxification strategies is of utmost importance. However, typical routes of detoxification are slow and/or result in the production of harmful by-products. NU-1000 has previously shown promise as a "soft" oxidizer that can readily detoxify sulfur mustard and its simulant 2-chloroethyl ethyl sulfide through the generation of singlet oxygen in the presence of either ultraviolet (396 nm) or blue (465 nm) light. We hypothesized that by employing electron-withdrawing functional groups on the linker in a position closest to the photoactive pyrene moiety, the photocatalytic rate of NU-1000 would be enhanced. Several variants of NU-1000 were synthesized (MOF-R, R = –Cl, $–NO_2$, $–NH_2$, $–CH_3$) with functional groups positioned either *ortho*- or *meta*- to the carboxylic acid on the linker. NU-1000-*o*-Cl and NU-1000-*m*-Cl showed significant enhancement of photooxidation of 2-chloroethyl ethyl sulfide in ultraviolet and blue light over the baseline material while the remaining NU-1000 derivatives showed little to no reaction. We propose that halogen functionalization enhances the intersystem crossing of the metal-organic framework to the triplet state by spin-orbit coupling, thereby enhancing the photocatalytic rate.

Keywords: metal-organic framework, photocatalysis, singlet oxygen, 2-chloroethyl ethyl sulfide

1. INTRODUCTION

The use of chemical warfare agents (CWA) has posed a critical challenge to both military and civilian populations over the last two centuries. Sulfur mustard has been the CWA predominantly used in modern warfare since its first use during WWI.[1] Three major routes of detoxification have been developed for sulfur mustard—hydrolysis, oxidation, and dehydrohalogenation.[2] The hydrolysis and dehydrohalogenation pathways are both very slow, especially due to the insolubility of sulfur mustard in water. Therefore, oxidation is a promising pathway. Most oxidants, however, are too harsh and may over-oxidize sulfur mustard to the sulfone derivative that has a toxicity analogous to that of sulfur mustard.

Metal-organic frameworks (MOF) are highly porous crystalline structures that offer a wide array of physical adsorption and chemical reactivity capabilities. These tunable structures that have shown promise for a number of applications in recent years including toxic gas removal, sensing, gas storage, and catalysis.[3] Photocatalysis by MOF has been a newly emerging application in recent years and offers an opportunity for a novel "soft" oxidation pathway for sulfur mustard and its simulant, 2-chloroethyl ethyl sulfide (2-CEES).[4] MOF have three components that can be tuned for photocatalysis—the metal nodes, the organic linkers, and molecules encapsulated in the crystalline structure. The metal nodes can either be directly excited by light or by the excitement of adjacent linker molecules that can then transfer that energy to the metal node in an antenna-like fashion.[5,6] The linkers can be readily tuned by developing linker molecules that have absorption profiles for the wavelengths of interest (e.g., solar light, red light).[7,8] Lastly, chromophores can be incorporated into the MOF structure by chemical attachment through post-synthetic modification of the linker or metal node.[9–12]

NU-1000 has previously been studied as a photooxidation catalyst for the degradation of sulfur mustard and 2-CEES.[13] The conjugated pyrene linker (1,3,6,8-tetrakis-(*p*-benzoic acid)pyrene, H_4TBAPy) has the ability to absorb

UV (396 nm) and blue (465 nm) light, which excites the MOF to the singlet state, which can transition to its triplet state via an inter-system crossing. The excited triplet state MOF can then interact with oxygen and convert it from the ground triplet state to the excited singlet state (Figure 1). Since NU-1000 contains open metal sites that are able to readily undergo solvent assisted linker incorporation, previous studies have been done exploring the effect of incorporating photosensitizers onto these sites. The goal of these endeavors was to either enhance the photocatalytic reaction rate or to extend the UV-vis absorption profile of NU-1000 so that the MOF catalyst is able to perform photocatalysis in the visible region of the spectrum.[13,14]

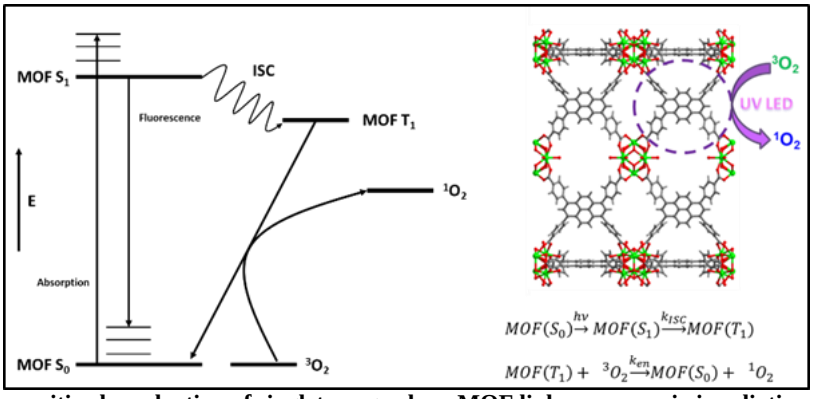

Figure 1. The photosensitized production of singlet oxygen by a MOF linker occurs via irradiation of light to excite an electron into an excited state for the MOF linker. This is followed by an intersystem crossing to the MOF linker triplet state. Returning of the electron to the ground state releases a photon of appropriate energy to excite the oxygen from its triplet state to singlet state.

However, there has been very limited work done with respect to synthesis of pyrene linker derivatives of NU-1000 and there have been no systematic studies detailing its effects on photocatalysis. To date, the only reported functionalization of H_4TBAPy within a MOF was in the form of an amine functionalization on the benzoic acid portion of the linker.[15] Derivatives of the H_4TBAPy linker can be readily synthesized via the conventional palladium cross-coupling reaction between 1,3,6,8-tetrabromopyrene and functionalized 4-methylcarbonylphenylboronic acid derivatives, followed by deprotection of the ester (Figure 2). By modifying the C and D positions on the H_4TBAPy linker, we can determine the effect of substituents that vary in electronegativity on the generation of singlet oxygen as determined by the photocatalytic half-life when reacted with 2-CEES (Figure 3). We show here that heavy halogen groups will increase the reaction rate of the catalyst and that heavy halogen groups *ortho-* to the pyrene will have the largest enhancement on the reactivity as previously observed with tetraphenylporphyrins.[16]

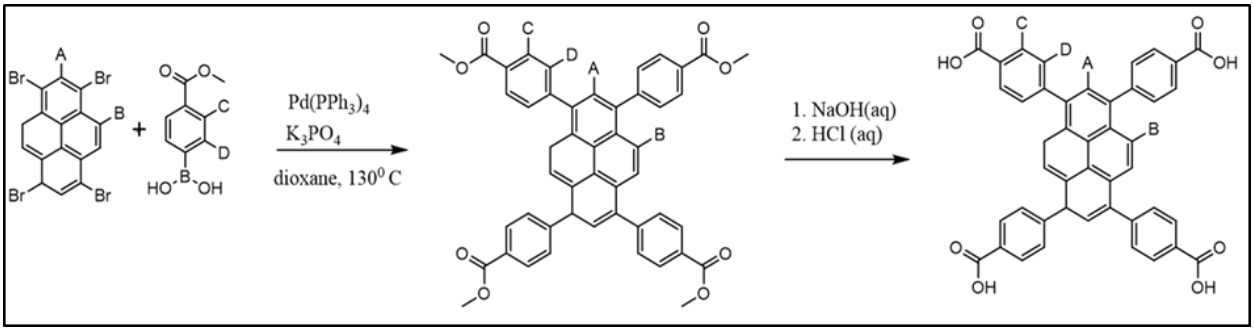

Figure 2. Synthesis of the tetratopic H4TBAPy linker found in NU-1000 and NU-901 occurs through a palladium cross-coupling reaction followed by a deprotection workup. Positions A and B on the pyrene ring and C and D on the benzoic acid ring are hydrogen atoms in H4TBAPy; however, these locations can be functionalized prior to the cross-coupling reaction leading to a variety of functionality that may alter the photophysics of the pyrene system.

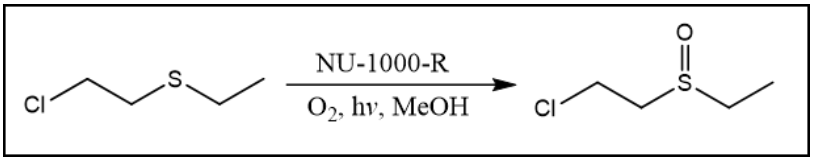

Figure 3. Reaction scheme of 2-CEES with a functionalized NU-1000 photosensitizer to form its sulfoxide oxidation product.

2. EXPERIMENTAL METHODS

2.1 Synthesis

2.1.1 Linker synthesis

All reagents were purchased from commercial sources and used without further purification. H_4TBAPy and functionalized (–CH_3, –NO_2, –NH_2) derivatives were synthesized following published procedures.[15]

2.1.2 Representative synthesis of functionalized H_4TBAPy linkers

150 mL of 1,4-dioxane was added to 250 mL Schlenk flask reactor and purged with N_2 for 1.5 hours using a syringe needle. While still purging tetrabromopyrene (0.5 g, 0.96 mmol), 4-ethoxycarbonyl-3-chlorophenylboronic acid (0.97 g, 4.25 mmol), K_3PO_4 (1.65 g, 7.77 mmol), and Pd $(PPh_3)_4$ (0.08 g, 0.07 mmol) were added into the reactor. The system was sealed and purged with N_2 before heating to 90 °C for 72 hours. The reaction was quenched with 100 mL of water and filtered. The resulting solid was washed twice with 100 mL water and with 200 mL of methanol. The crude product on the filter was purified by recrystallization. The crude product was dissolved in hot chloroform (300 mL) on the frit. The volume of the solution was reduced to 25 mL by evaporating the chloroform and the product was precipitated with 300 mL of methanol. The solid product was collected via filtration and dried in vacuum oven at 70 °C for 12 hours resulting in 0.59 g, 69 % yield. The ester precursors were hydrolyzed with KOH in a 1,4-dioxane aqueous solution and precipitated with concentrated HCl.

2.1.3 Representative synthesis of functionalized NU-1000

$ZrOCl_2 \cdot 8H_2O$ (98 mg, 0.3 mmol) and benzoic acid (2 g, 16.4 mmol) were mixed in 8 mL of DMF in an 8-dram vial and ultrasonically dissolved. The clear solution was incubated in an oven at 100 °C for 1 hour. After cooling down to room temperature, H_4-TBAPy (40 mg, 0.06 mmol) and trifluoro acetic acid (50 µL, 0.65 mmol) were added and ultrasonically mixed. The solution was incubated in an oven at 100 °C for 18 hours. The MOF was isolated by centrifuge (5 minutes, 7,500 rpm) and solvent exchanged with fresh DMF three times (10 mL each) followed by methanol or acetone three times (10 mL). The material was dried in a vacuum oven at 80 °C for 1 hour, and then activated at 120 °C for 18 hours.

2.2 Characterization

2.2.1 Powder X-ray diffraction

Powder X-ray diffraction (PXRD) patterns were measured on a Rigaku® MiniFlex™ 600 diffractometer equipped with a D/teX Ultra detector with Cu-Kα radiation (λ = 1.5418 Å) over a range of 2θ = 3-50° at a scan rate of 5 deg/min^{-1}.

2.2.2 Attenuated total reflectance-infrared

Attenuated total reflectance-Fourier transform infrared (ATR-FTIR) spectra were measured on a Bruker Tensor 27 spectrometer from 4,000–400 cm^{-1} at a resolution of 2 cm^{-1}.

2.2.3 N_2 physisorption

N_2 isotherms were measured using a Micromeritics® ASAP™ 2420 analyzer at 77 K. Samples were off-gassed at 120 °C under vacuum for ~16 hours. The Brunauer-Emmett-Teller method was used to calculate specific surface area in m^2/g.

2.2.4 UV-vis spectroscopy

Solid state UV-vis measurements of MOF samples from 200–800 nm were collected on a JASCO® V-650 UV-vis spectrophotometer equipped with a 150-mm integrating sphere.

2.3 Photocatalysis experiments

For CEES oxidation experiments, 2.2 mg of the MOF was dispersed in 1 mL anhydrous methanol and sealed in a 17-mm x 83-mm glass microwave vial. After purging with O_2 for 20 minutes, 23 µL (0.2 mmol) 2-CEES and 5 µL (0.04 mmol) internal standard (1-bromo-3,5-difluorobenzene) were added to the microwave vial with a 25-µL glass syringe. The vial was then exposed to either UV (396 nm) or blue (465 nm) LED irradiation using an LED setup constructed from solderless LEDs purchased from RapidLED that were then mounted onto a U-shaped aluminum sheet (Figure 4). 25-µL aliquots from the reaction vial were withdrawn using a syringe at 5-minute intervals, filtered, and diluted with 1 mL of methanol into a gas chromatography vial. The samples were then subjected to gas chromatography flame-ionization detection to monitor the reaction progress.

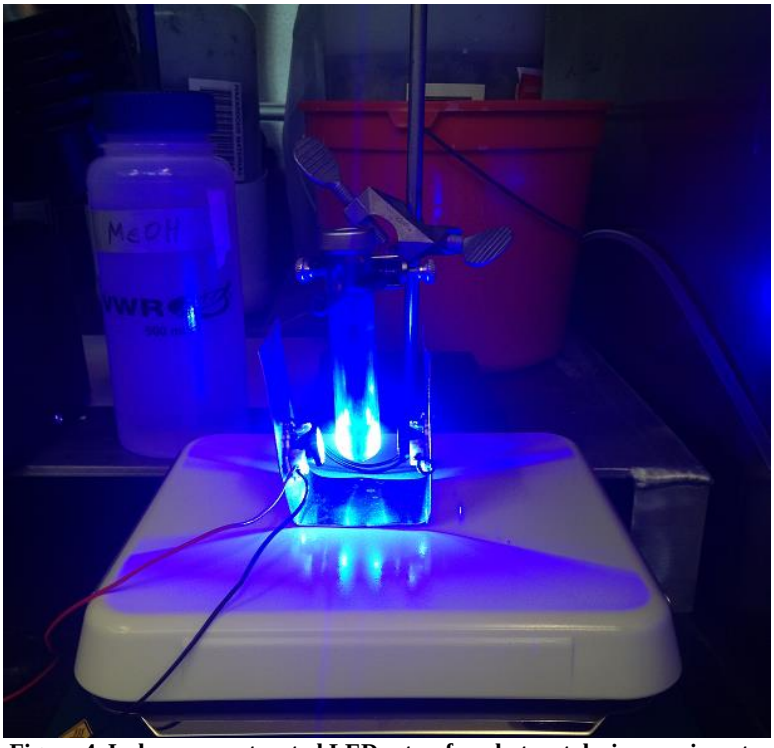

Figure 4. In-house constructed LED setup for photocatalysis experiments.

3. RESULTS

Under similar reaction conditions, the majority of functionalized H_4TBAPy linkers generated MOFs with **csq** topology that were analogous to NU-1000. However, both *meta*- and *ortho*- nitro functionalized H_4TBAPy linkers generated MOFs with **scu** and **she** topologies characteristically similar to NU-901 and PCN-224 respectively. While PXRD can clearly distinguish the **she** MOF from **csq**/**scu** topologies (Figure 5), the **scu** topology was confirmed through nitrogen adsorption experiments (Figure 6 and Figure 7).[16,17] The solid-state UV-vis spectra was collected for each functionalized MOF derivative that was synthesized (Figure 8). The addition of chlorine groups onto the linker appears to narrow the absorption spectra of the material while the addition of the nitro, amino, and methyl groups appear to broaden the absorption spectra of the material. In particular, NU-901-*m*-$(NO_2)_4$ shows a particularly large absorption profile as compared to the other synthesized NU-1000 derivatives. This material also appears much darker in color than the other synthesized materials—a dark brown powder as compared to powders that vary from light tan-yellow (PCN- 224-*o*-(NO_2) NU-1000-*m*-Cl_4, NU- 1000-*o*-$(CH_3)_4$) in color.

While the NU-1000-*o*-$(NH_2)_4$ and PCN-224-*o*-$(NO_2)_4$ derivatives also widen the absorption spectrum, they do not broaden the absorption spectrum as much as the NU-901-*m*-$(NO_2)_4$ derivative, likely leading to the lighter color of those powders as compared to NU-1000-*m*-$(NO_2)_4$.

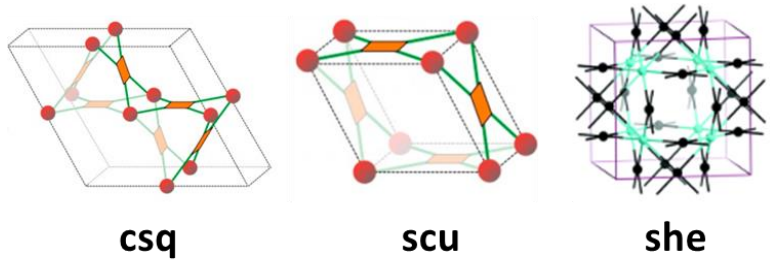

Figure 5. MOF topologies for NU-1000, NU-1000-*o*-Cl_4, NU-1000-*m*-Cl_4, NU-1000-*o*-$(CH_3)_4$, NU-1000-*o*-$(NH_2)_4$ (csq), NU-901-*m*-$(NO_2)_4$ (scu), and PCN-224-*o*-$(NO_2)_4$ (she). The csq and scu topologies have similar PXRD patterns but can be distinguished through nitrogen adsorption experiments.

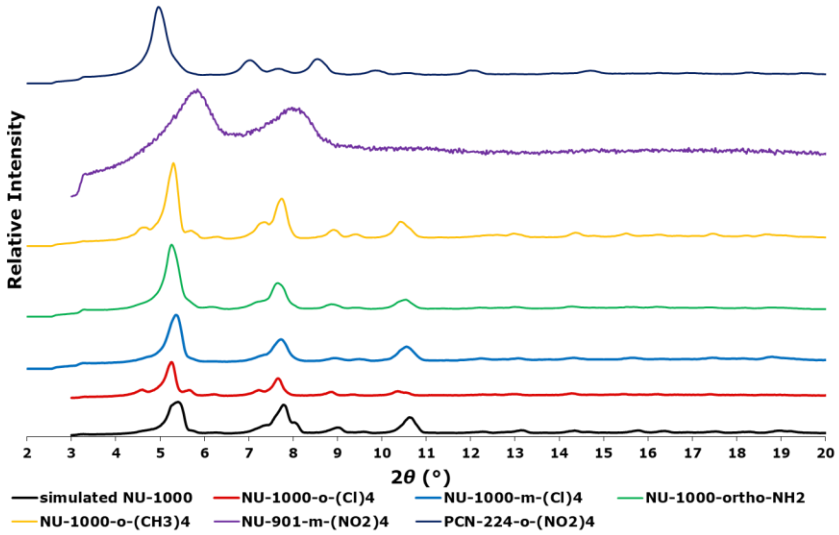

Figure 6. PXRD pattern for the synthesized MOF derivatives.

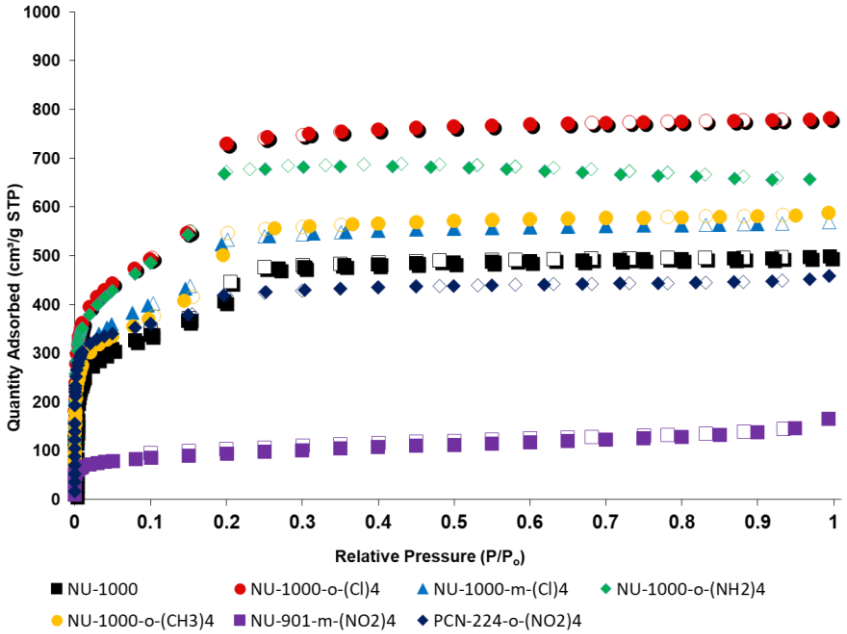

Figure 7. Nitrogen adsorption isotherms of the synthesized MOF derivatives.

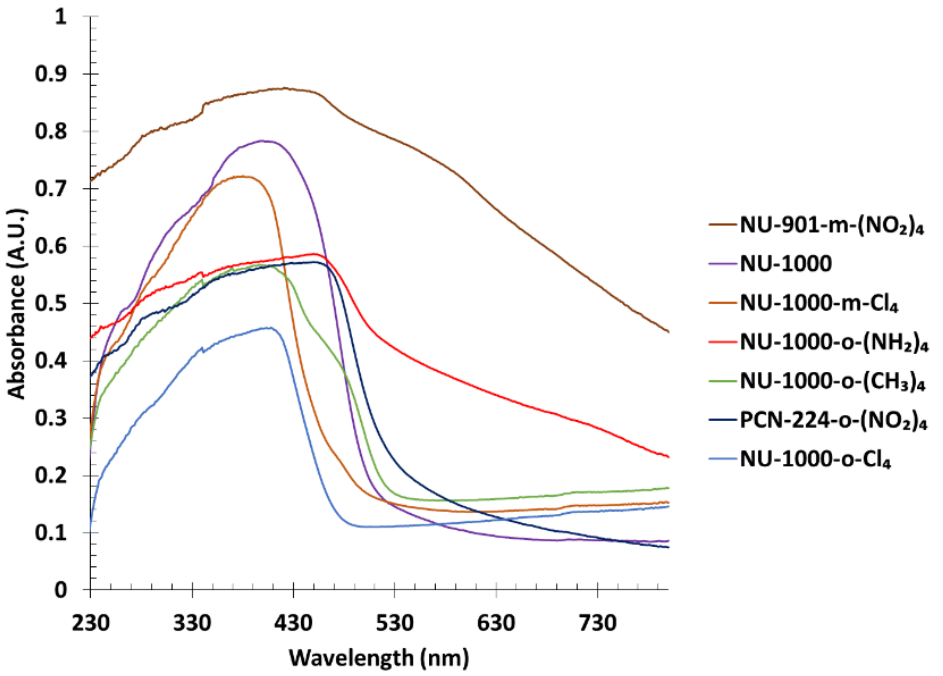

Figure 8. Solid-state UV-vis spectra for the synthesized MOF derivatives.

Each functionalized MOF was reacted with 2-CEES in the presence of either UV (396 nm) or blue (465 nm) LED light. The reactions were conducted so that there was a catalytic amount of MOF present relative to the amount of 2-CEES present in the reaction solution (approximately 100:1, 2-CEES:H_4TBAPy). PCN-224-*o*-$(NO_2)_4$, NU-901-*m*-$(NO_2)_4$, and NU-1000-*o*-$(NH_2)_4$ showed very little to no reaction under both UV and blue light conditions as compared to the baseline material. NU-1000-*o*-$(CH_3)_4$ showed reactivity in both light conditions; however, its reactivity was similar to the baseline material. NU-1000-*o*-Cl_4 and NU-1000-*m*-Cl_4 showed marked enhancement in reactivity in both UV and blue light conditions (Table 1 and Figure 9). Interestingly, these materials showed a narrower absorption spectrum as compared to the less reactive derivatives. The enhancement in reactivity is hypothesized to be a result of the heavy chlorine atoms facilitating the intersystem crossing that leads to the reactive triplet state of the MOF as previously observed in TCPP linkers.[18] The ability to reach the triplet state of the MOF is one of the primary factors for the production of singlet oxygen and enhancement of photocatalytic reactivity (Figure 1). While the more darkly colored materials (NU-901-*m*-$(NO_2)_4$, PCN-224-*o*-$(NO_2)_4$, and NU-1000-*o*-$(NH_2)_4$) have overall wider absorption spectra, this spectral enhancement does not appear to translate into an enhancement of the excitement of the material to the triplet state as evident by the lack of reactivity of these materials with 2-CEES. Rather, it is hypothesized that these materials absorb a great deal more light over a wider range of wavelengths but proceed to undergo a self-quenching mechanism as adjacent functionalized linkers can then absorb any transferred energy rather than using it to promote the MOF to the excited triplet state, particularly in the case of NU-901-*m*-$(NO_2)_4$ and PCN-224-*o*-$(NO_2)4$ as their topology causes the linkers to be in closer proximity to each other than the **csq** topology of NU-1000.

Table 1. Calculated half-lives for the oxidation of 2-CEES by the synthesized NU-1000 derivatives.

MOF	UV LED ($t_{1/2}$, min)	Blue LED ($t_{1/2}$, min)
NU-1000	3	40
NU-1000-*o*-Cl	5.5	7.5
NU-1000-*m*-Cl	1	25
NU-901-*m*-$(NO_2)_4$	N.R.	N.R.
PCN-224-*o*-$(NO_2)_4$	N.R.	N.R.
NU-1000-*o*-$(NH_2)_4$	45	N.R.
NU-1000-*o*-$(CH_3)_4$	11	40

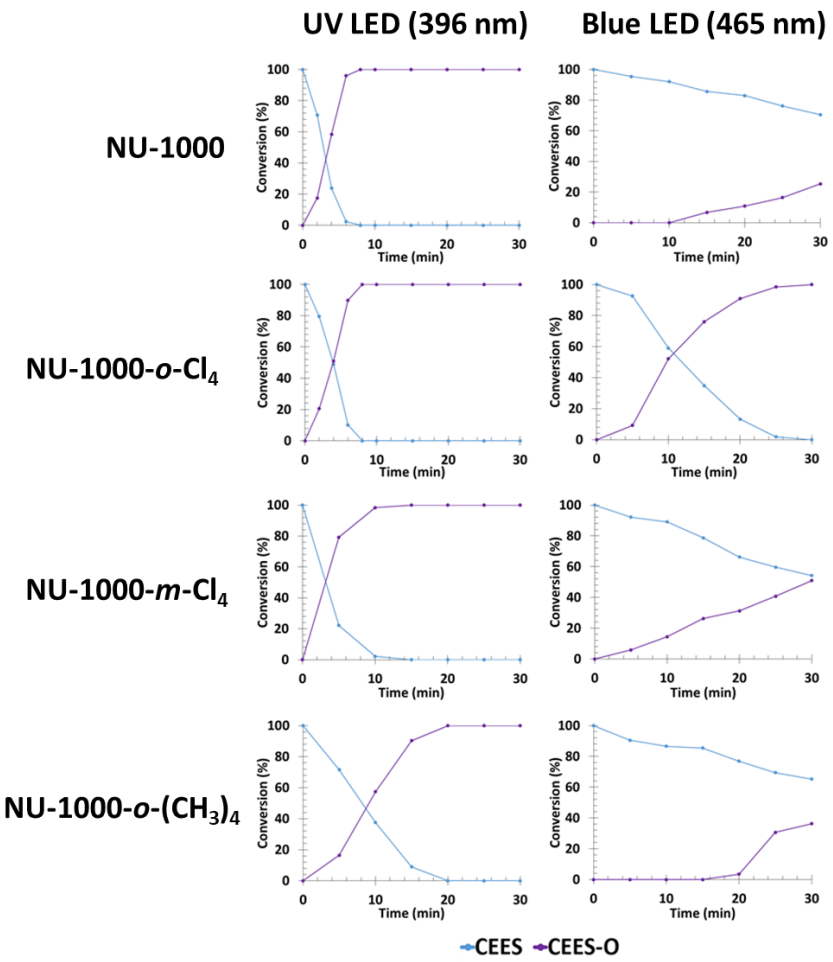

Figure 9. Reaction profiles for the reactive NU-1000 derivatives.

4. CONCLUSIONS/FUTURE WORK

Several novel MOF variants were successfully synthesized with functional groups (–Cl, $–NO_2$, $–NH_2$, $–CH_3$) positioned either *ortho*- or *meta*- to the carboxylic acid on the linker. Photocatalytic experiments showed that chlorine atoms significantly improve the photocatalytic reactivity of the material consistent with our hypothesis that heavy halogen groups would enhance the triplet state of the MOF, thereby enhancing photocatalytic reactivity. Interestingly, it was found that PCN-224-*o*-$(NO_2)_4$, NU-901-*m*-$(NO_2)_4$, and NU-1000-*o*-$(NH_2)_4$ absorb more light than the more reactive chlorine derivatives but do not enhance photocatalytic reactivity. This might indicate a quenching mechanism particularly in the case of PCN-224-*o*-$(NO_2)_4$ and NU-901-*m*-$(NO_2)_4$ as their topologies result in the linkers being closer to each other within the crystalline structure thereby facilitating self-quenching. These results not only enhance the knowledge of these materials but also contribute toward their potential use for the mitigation of toxic chemicals susceptible to oxidation including sulfur mustard, hydrogen sulfide, and other organic pollutants.

ACKNOWLEDGMENTS

Funding was provided by the Director, Combat Capabilities Development Command Chemical Biological Center under the authorities and provisions of Section 2363 of the FY 2018 NDAA to develop new technologies, engineer innovations, and introduce game-changing capabilities. This research was performed while Sergio J. Garibay held a National Research Council post-doctoral research associateship award at the Combat Capabilities Development Command Chemical Biological Center.

REFERENCES

[1] Ghabili, K.; Agutter, P.S.; Ghanei, M.; Ansarin, K.; Panahi, Y.; Shoja, M.M. Sulfur mustard toxicity: History, chemistry, pharmacokinetics, and pharmacodynamics. *Crit. Rev. Toxicol.* **2011,** *41* (5), pp 384–403.

[2] Wang, Q.-Q.; Begum, R.A.; Day, V.W.; Bowman-James, K. Sulfur, oxygen, and nitrogen mustards: stability and reactivity. *Org. Biomol. Chem.* **2012,** *10* (44), pp 8786–8793.

[3] Gangu, K.K.; Maddila, S.; Mukkamala, S.B.; Jonnalagadda, S.B. A review on contemporary Metal–Organic Framework materials. *Inorg. Chim. Acta.* **2016,** *446* (Supplement C), pp 61–74.

[4] Dhakshinamoorthy, A.; Li, Z.; Garcia, H. Catalysis and photocatalysis by metal organic frameworks. *Chem. Soc. Rev.* **2018,** *47* (22), pp 8134–8172.

[5] Bordiga, S.; Lamberti, C.; Ricchiardi, G.; Regli, L.; Bonino, F.; Damin, A.; Lillerud, K.P.; Bjorgen, M.; Zecchina, A. Electronic and vibrational properties of a MOF-5 metal–organic framework: ZnO quantum dot behaviour. *Chem. Commun.* **2004,** *20*, pp 2300–2301.

[6] Wang, C.; Xie, Z.; 'deKrafft, K. E.; Lin, W. Doping metal–organic frameworks for water oxidation, carbon dioxide reduction, and organic photocatalysis. *J. Am. Chem. Soc.* **2011,** *133* (34), pp 13445–13454.

[7] Goh, T.W.; Xiao, C.; Maligal-Ganesh, R.V.; Li, X.; Huang, W. Utilizing mixed-linker zirconium based metal-organic frameworks to enhance the visible light photocatalytic oxidation of alcohol. *Chem. Eng. Sci.* **2015,** *124*, pp 45–51.

[8] Sun, D.; Gao, Y.; Fu, J.; Zeng, X.; Chen, Z.; Li, Z. Construction of a supported Ru complex on bifunctional MOF-253 for photocatalytic CO_2 reduction under visible light. *Chem. Commun.* **2015,** *51* (13), pp 2645–2648.

[9] He, J.; Wang, J.; Chen, Y.; Zhang, J.; Duan, D.; Wang, Y.; Yan, Z. A dye-sensitized Pt@UiO-66(Zr) metal-organic framework for visible-light photocatalytic hydrogen production. *Chem. Commun.* **2014,** *50* (53), pp 7063–7066.

[10] Zhang, H.; Wei, J.; Dong, J.; Liu, G.; Shi, L.; An, P.; Zhao, G.; Kong, J.; Wang, X.; Meng, X.; Zhang, J.; Ye, J. Efficient visible-light-driven carbon dioxide reduction by a single-atom implanted metal–organic framework. *Angew. Chem. Int. Edit.* **2016,** *55* (46), pp 14310–14314.

[11] Zhou, T.; Du, Y.; Borgna, A.; Hong, J.; Wang, Y.; Han, J.; Zhang, W.; Xu, R. Post-synthesis modification of a metal–organic framework to construct a bifunctional photocatalyst for hydrogen production. *Energy Environ. Sci.* **2013,** *6* (11), pp 3229–3234.

[12] Maza, W.A.; Morris, A.J. Photophysical characterization of a ruthenium(II) tris(2,2′-bipyridine)-doped zirconium UiO-67 metal–organic framework. *J. Phys. Chem. C.* **2014,** *118* (17), pp 8803–8817.

[13] Howarth, A.J.; Buru, C. T.; Liu, Y.; Ploskonka, A.M.; Hartlieb, K.J.; McEntee, M.; Mahle, J.J.; Buchanan, J.H.; Durke, E.M.; Al-Juaid, S.S.; Stoddart, J.F.; DeCoste, J.B.; Hupp, J.T.; Farha, O.K. Postsynthetic incorporation of a singlet oxygen photosensitizer in a metal–organic framework for fast and selective oxidative detoxification of sulfur mustard. *Chem. Eur. J.* **2016,** *23* (1), pp 214–218.

[14] Lee, M.S.; Garibay, S.J.; Ploskonka, A.M.; DeCoste, J.B. Bioderived protoporphyrin IX incorporation into a metal-organic framework for enhanced photocatalytic degradation of chemical warfare agents. *MRS Commun.* **2019,** *9* (2), pp 464–473.

[15] Islamoglu, T.; Ortuño, M.A.; Proussaloglou, E.; Howarth, A.J.; Vermeulen, N.A.; Atilgan, A.; Asiri, A.M.; Cramer, C.J.; Farha, O.K. Presence versus proximity: the role of pendant amines in the catalytic hydrolysis of a nerve agent simulant. *Angew. Chem.Int. Edit.* **2018,** *57* (7), pp 1949–1953.

[16] Kirchon, A.; Feng, L.; Drake, H.F.; Joseph, E.A.; Zhou, H.C. From fundamentals to applications: a toolbox for robust and multifunctional MOF materials. *Chem. Soc. Rev.* **2018,** *47* (23), pp 8611–8638.

[17] Gomez-Gualdron, D.A.; Gutov, O.V.; Krungleviciute, V.; Borah, B.; Mondloch, J.E.; Hupp, J.T.; Yildirim, T.; Farha, O.K.; Snurr, R.Q. Computational design of metal-organic frameworks based on stable zirconium building units for storage and delivery of methane. *Chem. Mater.* **2014,** *26*, pp 5632–5639.

[18] Nifiatis, F.; Athas, J.C.; Gunaratne, D.D.; Gurung, Y.; Monette, K.M.; Shivokevich, P.J. Substituent effects of porphyrin on singlet oxygen generation quantum yields. *Open Spect. J.* **2011,** *5*, pp 1–12.

Photonic polymerase chain reaction for ultrafast biological identification

Katherine M. Broadway[a], Dean P. Kleinfelder[b], R. Cory Bernhards[d], Phillip M. Mach[d], Bryan Rivers[d]*
[a]Oak Ridge Institute for Science and Education, P.O. Box 117, Oak Ridge, TN 37831
[b]United States Military Academy, 606 Thayer Rd, West Point, NY 10996
[c]Defense Threat Reduction Agency, 8725 John J. Kingman Rd, Fort Belvoir, VA 22060
[d]U.S. Army Combat Capabilities Development Command Chemical Biological Center, Research & Technology Directorate, 8198 Blackhawk Rd, Aberdeen Proving Ground, MD 21010

ABSTRACT

Currently fielded analytical devices require approximately one to two hours from sample collection to identification of the biological agent. We aim to dramatically shorten the time from sample to answer by developing a rapid, high-confidence, low-size, low-weight, and low-power surveillance device capable of biothreat identification within five minutes. The device will utilize ultrafast photonic polymerase chain reaction, a novel biological identification method currently in development. The method uses gold nanoparticles and light emitting diodes for plasmonic photothermal light-to-heat conversion. When the light-emitting diodes are turned on and off, the surrounding solution is rapidly heated and cooled respectively, drastically reducing the time requirement for thermal cycling. We currently have a breadboard design operating by way of a microcontroller using scripts developed in-house. The system controls light-emitting diodes for photothermal heating of gold nanoparticles at their absorption wavelength. Another set of light-emitting diodes are used for fluorescent reporter excitation, which in turn generates emission spectra that are monitored in real-time using an RGB sensor. Finally, a read-out detailing assay results and analysis is produced. Overall, the exploitation of gold nanoparticles and light-emitting diodes is a low cost and light weight answer to deployable biothreat identification that promises to dramatically change the use of biological sensors in the field.

Keywords: polymerase chain reaction, extreme polymerase chain reaction, biothreat detection, light-emitting diodes

1. INTRODUCTION

Ultrafast biological identification is essential for rapid response to environmental biothreats in order to reduce exposure, alter operations, and identify when a threat has passed or has been mitigated. While optical trigger sensors have been developed to identify potential biothreats, only DNA-based analyses provide sufficient confidence to take high-regret actions. High-confidence biological identification has been traditionally limited by the biochemical activity of the enzymes used in polymerase chain reaction (PCR) which requires repeated cycles of heating and cooling to amplify the unique DNA sequence of a targeted biothreat agent. Using commercial PCR systems detection efforts are time consuming requiring an hour alone for detection of amplification products, not to mention DNA preparation from sample 1. Recently, several unique methods for rapid temperature control have been reported, resulting in nucleic acid amplification to detectable levels in a matter of minutes. The novelty of our method is the use of light-emitting diodes (LED) and gold nanoparticles to drive temperature control of the DNA amplification assay (Figure 1).

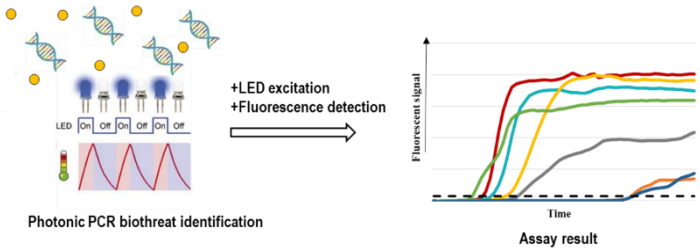

Figure 1. Depiction of photonic PCR and assay results for biothreat identification.

Recently, unique methods for rapid cycling—DNA denaturation, primer annealing, extension—have been reported such that nucleic acid amplification can be detected in a matter of minutes. One method, named "extreme PCR" uses 10- to 20-fold increases in primer and polymerase concentrations as well as heating cycles of 0.4–2 seconds, for amplified DNA detection in approximately 1 minute.[2] While this concept is novel, the technology used to achieve heating is a water bath incubator and electric hot plates and is far from fieldable.[2] Another innovative concept is called Laser PCR® (GNA Biosolutions), which utilizes gold nanoparticles and a high-powered laser beam to rapidly cycle heating and cooling. Gold nanoparticles have high heat conductivity, leading to fast heating and cooling.[3] The drawback of this approach is that lasers are expensive and do not make for a ruggedized platform. Finally, rapid PCR cycling using LEDs for heating a thin gold film has been developed and named Photonic Ultrafast PCR.[1,4] Plasmonic photothermal light-to-heat conversion occurs when light generated by the LED is absorbed by the gold surface. When photons from the LED source reach the gold surface, electrons are excited to higher energy states, generating hot electrons within 100 femtoseconds (fs).[1,5,6] The surrounding solution containing the PCR mixture is then heated over the time scale of 100 picoseconds (ps). When the LED light source is turned off, rapid cooling at the gold surface is achieved. Together, this means 30 full PCR cycles can occur in under 5 minutes.[1] The photonic PCR approach using LEDs is a low cost, light weight solution to Laser PCR. A drawback is the gold surface—it limits the variety of devices and applications with which photonic PCR can be combined. We aimed to develop a breadboard based on our innovative method, capable of identifying a biological agent within five minutes.

2. MATERIALS AND METHODS

The principle of photothermal light-to-heat conversion governs the operation of photonic DNA amplification. Absorption of photons from an excitation source, LEDs, by interacting materials, and gold nanoparticles, results in the emission of heat when photons from the LED source reach the gold surface, electrons are excited to higher energy states, generating hot electrons and heating the surrounding solution containing the DNA amplification reaction. When the LED source is turned off, rapid cooling at the gold surface is achieved. This results in low power consumption and a simple configuration for temperature control of targeted DNA amplification for the identification of biological threats in the field.

2.1 DNA amplification assays and sample preparation

An ultrafast PCR assay has been designed and initially analyzed using a standard real-time PCR instrument. Primers were tested along with all other necessary reagents including KAPA2G Fast PCR enzyme, specifically for ultrafast applications. The target for the ultrafast PCR assay is specific for identification of *Escherichia coli* and has already been validated in the context of photonic PCR.[4] The biomaterial was prepared for PCR using a kit we routinely employ called Arcis Sample Extraction Kit (Daresbury, United Kingdom) which includes reagents to effectively lyse cells and neutralize PCR inhibitors in just 1 minute. In addition to PCR, an isothermal amplification strategy was applied. Loop mediated isothermal amplification (LAMP) typically takes 10–15 minutes for a positive result. We used a published assay for the detection of the BSL-2 surrogate *Yersinia pestis* Harbin 35.[7] By incorporating the LAMP assay, we were able to use photothermal heating to maintain a constant temperature and simultaneously assess the breadboard optics.

2.2 DNA amplification and signal reporting

The breadboard consisted of ultrafast heating achieved only by LEDs and gold nanoparticles, as well as optics for DNA amplification detection. Briefly, LEDs with a focus wavelength were used for plasmonic photothermal heating of gold nanoparticles. Then, the gold nanoparticles were introduced in solution with PCR reagents and Arcis reagent prepared sample. LED light was focused using fiber coupling optic. An insulated thermocouple controlled by scripts developed at Combat Capabilities Development Command Chemical Biological Center was used for real-time temperature monitoring. Amplification of the PCR product was signified by an increase in detectable fluorescence. Therefore, a fluorescence signal detection module was implemented for tracking of an amplification product. The module consisted of LEDs focused at a wavelength to excite fluorescence for our reporter (SYTO 9). Fluorescence wavelength emission was then detected using an RGB sensor and the signal output displayed as an amplification curve. We ensured that the LED wavelength used for heating did not match the fluorescence excitation wavelength used for the reporter, which would have made detection differentiation difficult. Finally, we developed a breadboard to facilitate the control of LED-driven heating of gold nanoparticles and fluorescence real-time monitoring. Red or infrared LEDs were used for photon interaction with nanorods or nanourchins, respectively, based on their absorption

spectra and size (Figure 2). Blue LEDs were used for fluorescence excitation, an RGB sensor for fluorescence emission detection, and an Arduino with scripts developed for power, control and data acquisition (Figure 3).

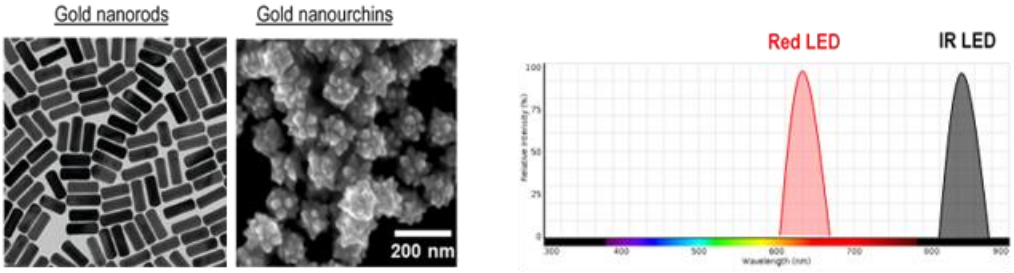

Figure 2. Spectral wavelength of light source required for absorption and heating of gold nanorods or nanourchins.

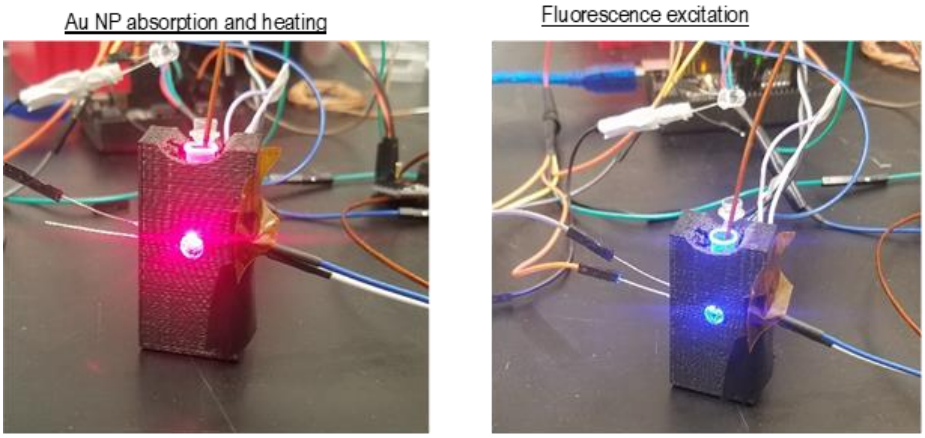

Figure 3. (Left) Heating LED active, creating red light absorbed by the NPs and converted to thermal energy. (Right) Excitation of the fluorophore for emission observation, quantifying amplified DNA.

3. RESULTS

The breadboard was developed for photothermal heating, as well as assay fluorescence detection. A housing unit to maintain positioning of circuitry was designed and 3D printed (Figure 4).

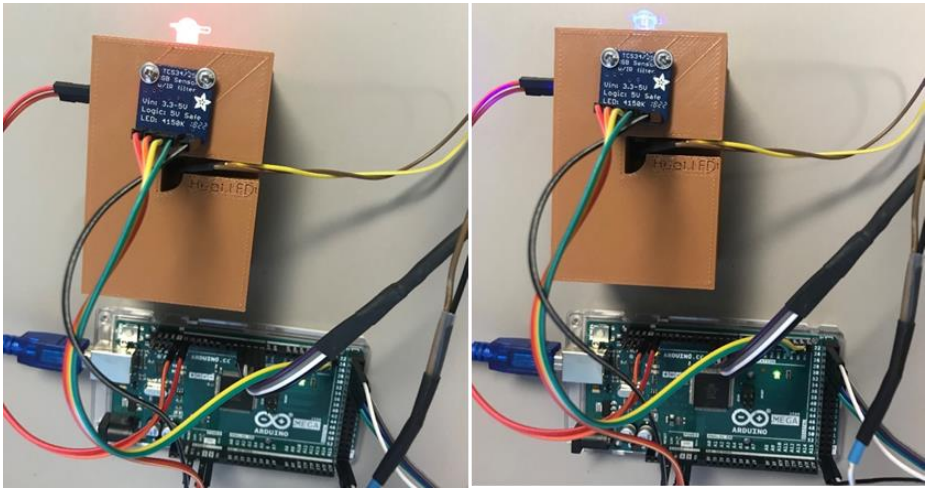

Figure 4. Additively manufactured test rig to align optics for optimal excitation observation. Associated microcontrollers shown, including Arduino and RGB light sensor.

We established real-time assay execution and monitored the LAMP assay using our breadboard to detect *Y. pestis*. Raw fluorescence data was first normalized as the ratio of the green/blue channel values to minimize detection of the

blue excitation LED from the data. Then, a curve fit function was applied to the spectral data and graphed (OriginLab®). Peak fluorescence in the positive control sample (*Y. pestis* DNA added) occurred in 8 minutes, while the negative control sample (without *Y. pestis* DNA) did not significantly change over time (Figure 5). The LAMP assay performance in our system is significantly faster from conventional strategies used for eliciting isothermal conditions, such as a heat block.[7] Importantly, the fitted amplification curve indicates an increase in slope well before 8 minutes. More understanding of the real-time photonic LAMP amplification curve could yield even lower detection time and faster identification of a biological sample.

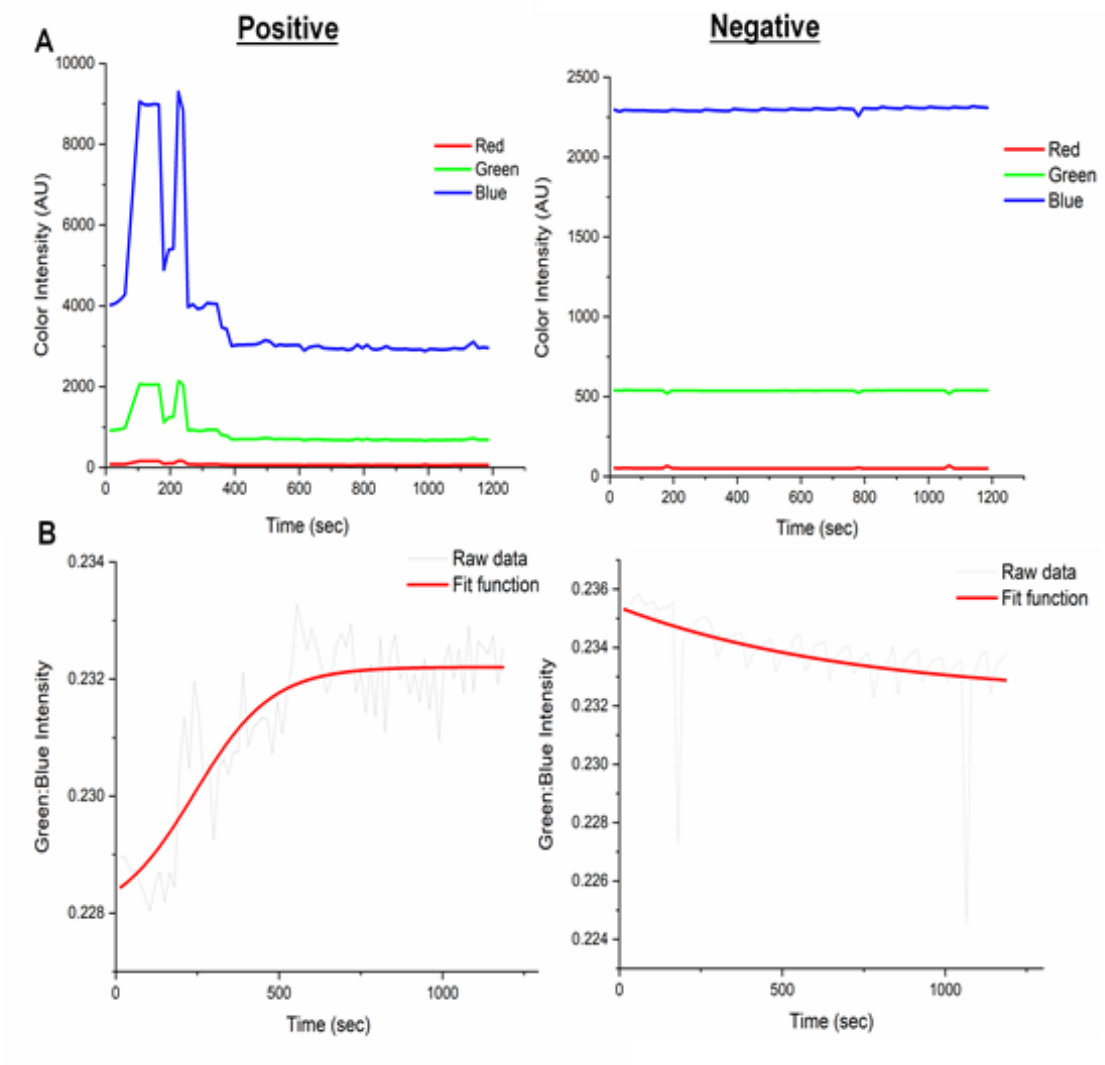

Figure 5. Real-time fluorescence monitoring of the photonic LAMP assay. A) Raw color and B) normalized color intensity values.

4. DISCUSSION

We proposed a novel, DNA amplification-based biological identification assay using LEDs and gold nanoparticles for low cost and light weight photothermal rapid heating. This would allow easy integration into a variety of devices and applications. The fundamental understanding of how gold nanoparticles and LEDs can be applied for ultrafast temperature control of DNA amplification reactions could dramatically change the use of biological sensors in the field.

Real-time temperature monitoring was not feasible with current resources. However, with proper equipment, such as a National Instruments™ (Austin, TX) thermocouple module,[1] ultrafast photonic PCR could be accomplished. Sensitive equipment to detect temperature changes is important to not only monitor the temperature of the overall reaction mix, but also the surface of the gold nanoparticles and microgradient of heat resulting from photon absorption. Importantly, once these temperatures are known and established, the temperature-monitoring equipment would not be a permanent addition to the breadboard or overall system, maintaining the low SWaP (size, weight, and power) properties of photonic PCR.

Here, we have validated the use of LEDs and gold nanoparticles for the exclusive heating of a LAMP assay to identify *Y. pestis* in a real-time assay. To our knowledge, this is the first time photothermal heating has been utilized to maintain isothermal conditions, much less for biothreat identification. Through the described effort, photonic LAMP and biological sample identification was accomplished in under 8 minutes with an in-house developed device for under $50.00. This is a promising strategy for rapid and fieldable biological detection in future.

5. SUMMARY AND FUTURE WORK

We have successfully developed a novel real-time photonic LAMP assay platform and detected *Y. pestis* in significantly less time than conventional isothermal condition-inducing equipment. In the future, this strategy could be incorporated to Warfighter standard issue equipment—such as the PEQ-15, which uses an IR laser as an advanced target pointer—to heat gold nanoparticles, thus utilizing existing Warfighter equipment to drive an isothermal detection. The photonic device would be designed as a lightweight attachment that the Warfighter could clip to their existing PEQ-15 (Figure 6).

Figure 6. Proposed integration of the photonic PCR device as an attachment to the PEQ-15. A green light will illuminate if the area is safe from biological agents and a red light will illuminate if the area is not safe.

The PEQ-15 ultrafast photonic LAMP set up would allow the analysis to run utilizing existing Warfighter equipment to provide results in under 5 minutes.

ACKNOWLEDGMENTS

Funding was provided by the Director, Combat Capabilities Development Command Chemical Biological Center under the authorities and provisions of Section 2363 of the FY 2018 NDAA to develop new technologies, engineer innovations, and introduce game-changing capabilities. This research was also made possible with the support from the Oak Ridge Institute for Science and Education postdoctoral research fellowship program. The authors would like

to thank SFC Olson for operational discussion and feedback. The views expressed in this report are those of the authors and do not necessarily reflect the official policy or position of the Department of Defense or the U.S. Government.

REFERENCES

[1] Son, J.H.; Cho, B.; Hong, S.; Lee, S.H.; Hoxha, O.; Haack, A.J.; Lee, L.P. Ultrafast photonic PCR. *Light: Sci. Appl.* **2015,** *4* (7), pp 1–7.

[2] Farrar, J.S.; Wittwer, C.T. Extreme PCR: efficient and specific DNA amplification in 15–60 seconds. *Clin. Chem.* **2015,** *61* (1), pp 145–153.

[3] Cheong, K.H.;Yi, D.K.; Lee, J.G.; Park, J.M.; Kim, M.J.; Edel, J.B.; Ko, C. Gold nanoparticles for one step DNA extraction and real-time PCR of pathogens in a single chamber. *Lab. Chip.* **2008,** *8* (5), pp 810–813.

[4] Kim, J.; Kim, H.; Park, J.H.; Jon, S. Gold nanorod-based photo-PCR system for one-step, rapid detection of bacteria. *Nanotheranostics.* **2017,** *1* (2), pp 178–185.

[5] Clavero, C. Plasmon-induced hot-electron generation at nanoparticle/metal-oxide interfaces for photovoltaic and photocatalytic devices. *Nat. Photonics.* **2014,** *8*, pp 95.

[6] Inouye, H.; Tanaka, K.; Tanahashi, I.; Hirao, K. Ultrafast dynamics of nonequilibrium electrons in a gold nanoparticle system. *Phys. Rev.* **1998,** *57* (18), pp 11334–11340.

[7] Feng, N.; Zhou, Y.; Fan, Y.; Bi, Y.; Yang, R.; Zhou, Y.; Wang, X. Yersinia pestis detection by loop-mediated isothermal amplification combined with magnetic bead capture of DNA. *Braz. J. Microbiol.* **2018,** *49* (1), pp 128–137.

Investigation of the effect of JP-8 fuel on the evaporation rate of aerosolized chemical agent simulant

John A. Tokarz III[a]*, Monica L. McEntee[a], Jason K. Navin[b], James H. Buchanan[a], Matthew B. Hart[c], Erin M. Durke[a]
[a]U.S. Army Combat Capabilities Development Command Chemical Biological Center, Research & Technology Directorate, 8198 Blackhawk Rd, Aberdeen Proving Ground, MD 21010
[b]National Research Council Research Associateship Program Supported by U.S. Army Combat Capabilities Development Command Chemical Biological Center, Research & Technology Directorate, 8198 Blackhawk Rd, Aberdeen Proving Ground, MD 21010
[c]U.S. Naval Research Laboratory, 4555 Overlook Ave SW, Washington, DC 20375

ABSTRACT

This work investigated how the presence of JP-8 fuel impacted the evaporation rates of aerosolized liquid chemical agent simulants by utilizing a Linear Electrodynamic Quadrupole system. The linear electrodynamic quadrupole system uses a quadruple to trap single micron-sized aerosol particles for direct measurements of evaporation rates using a Mie scattering technique. Two chemical agent simulants were evaluated: 1) 2-chloroethyl ethyl sulfide, a sulfur mustard simulant; and 2) pinacolyl methylphosphonate, a simulant of soman. Separate solutions of these simulants were made up along with varying amounts of JP-8 jet fuel, aerosolized, and the Mie scattering was plotted as a function of time. The results showed that JP-8 affected the evaporation rate of each simulant differently. Aerosolized 2-chloroethyl ethyl sulfide did not show any significant Mie scattering. Aerosol particles of JP-8 and pinacolyl methylphosphonate showed slightly different Mie scattering plots but were similar in evaporation rates. However, when mixed together, the evaporation rate slowed down by approximately half. These results indicate that chemical agents could persist for longer periods of time if fuels are present in the environment. JP-8 and 2-chloroethyl ethyl sulfide mixed together showed two distinct Mie scattering patterns for the same aerosol particle, which indicated that the separate components within the mixture evaporated sequentially at different rates.

Keywords: aerosol, evaporation rate, refractive index, JP-8 jet fuel, linear electrodynamic quadrupole, simulant, pinacolyl methylphosphonate, 2-chloroethyl ethyl sulfide

1. INTRODUCTION

Aerosol particles can exist in various forms: solids, liquids, and particulates that comprise a mixture of the two. The state and composition of an aerosol particle dictates how it interacts with the surrounding environment. A major property of aerosol particles, particularly liquid droplets, is their evaporation rate. The rate at which the particle evaporates will determine the distance traversed, and in a threat scenario, the extent of the incident. Often in the literature, the evaporation rate determined for the bulk phase liquid is applied to describe the aerosolized state.[1] However, this is potentially problematic as there is a significant difference in heat transfer at the surface during evaporation in bulk liquid versus a single aerosol particle.[1] During liquid evaporation, with a smaller surface-to-volume ratio, as in the bulk scenario, there is a less pronounced surface cooling effect. The cooling effect creates deviations in the measured liquid temperature and, ultimately, large discrepancies in the measured and theoretical evaporation rate value.

To mitigate this effect, our lab uses a custom single particle levitation device equipped with a Mie scattering technique. The system, known as the linear electrodynamic quadrupole (LEQ),[2-4] is capable of directly measuring the evaporation rate of a single micron-sized aerosol particle in real-time. The setup permits studies which investigate the impact of changes in temperature, relative humidity, and the presence of vaporous contaminants (e.g., pollutants, toxic industrial chemicals, toxic industrial materials, etc.). Previous research[2–4] using the LEQ has shown that the inclusion of water (i.e., higher relative humidity environment) can significantly impact the rate at which a particle of pinacolyl

methylphosphonate (PMP), a hydrolysis product of soman (GD), evaporates. Figure 1 shows that increasing the relative humidity from 8 % to 21 % results in the particle existing for seven times longer in the atmosphere.

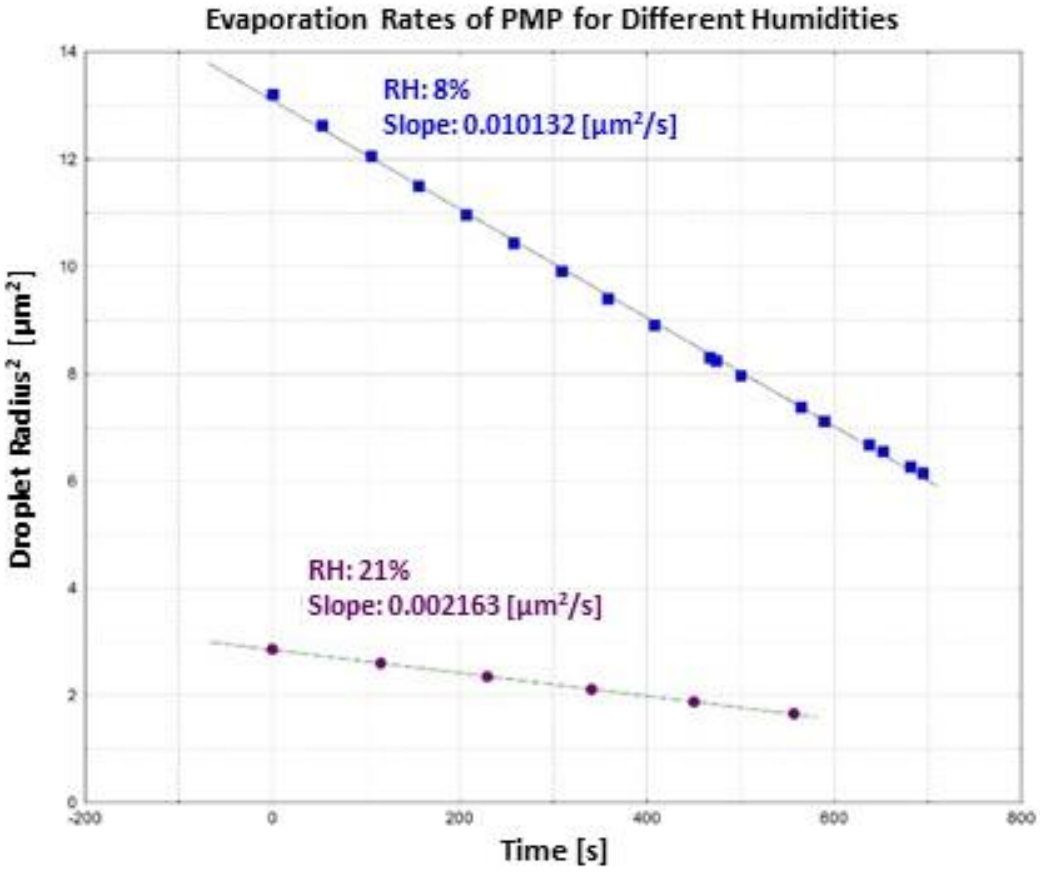

Figure 1. Comparison of the evaporation rates of PMP for two separate humidity conditions.

Understanding how aerosolized particles behave in the environment can aid in hazard prediction and decontamination efforts. The work herein investigates the evaporation rates of aerosolized liquid agent simulants and how the rates are impacted by the presence of JP-8 fuel. JP-8 fuel was chosen since it is used for jets in the U.S. Air Force, for construction and tactical equipment in the U.S. Navy, and for heaters, stoves, and tanks for all of the U.S. military and NATO allies as a replacement for diesel fuel.[5] Thus, the interaction between JP-8 and chemical agent aerosols is crucial information and can be utilized to enhance current modeling techniques for hazard prediction capabilities.

2. METHODS

2.1 Characterization of chemicals and combinations of chemicals

2.1.1 Information on reagents

All chemical reagents used were obtained from Sigma-Aldrich® (MilliporeSigma, St. Louis, MO) with the exception of JP-8 aviation turbine fuel, which was obtained with the help of Specialist Ward from the Weide Army Heliport (Edgewood, MD). PMP, CAS# 616-52-4, Sigma-Aldrich® 386588; 2-Chloroethyl ethyl sulfide (CEES), CAS# 693-07-2, Sigma-Aldrich® 242640; Water, CAS# 7732-18-5, Sigma- Aldrich® 34877; Kerosene, CAS# 8008-20-6, Sigma-Aldrich® 329460; glycerol, CAS# 56-81-5, Sigma-Aldrich® G5516; and Methanol, CAS# 67-56-1, Sigma-Aldrich® 650609.

2.1.2 Characterization of neat chemicals by gas chromatography-mass spectrometry

Neat chemicals (CEES, kerosene, and JP-8) were analyzed on an Agilent gas chromatography-mass spectrometry (GC-MS) system (Agilent Technologies, Inc.; Santa Clara, CA). A small amount of neat liquid sample (0.1 µL) was injected via an auto-sampler into a heated (250 °C) inlet, then split at a 400:1 ratio before entering into an Agilent HP-5 MS semi-volatile capillary column (30.0 m in length, a nominal inner diameter of 250.00 µm, and a 50-µm film thickness). The oven was ramped from 90 °C up to 250 °C at a rate of 10 °C/minute with an initial hold time of 2 minutes for a total run time of 18 minutes. PMP is not amenable to GC-MS techniques and therefore was not measured.

2.1.3 Obtaining accurate measurements of the refractive indices of test chemicals

Accurate measurements of the refractive indices of all the chemicals and combinations of chemicals to be tested were obtained by using a Reichert® (Reichert Technologies®; Depew, NY) AR200 Full-Range Digital Refractometer (Figure 2). The refractometer features automatic temperature compensation from 15–40 °C and measures refractive indices from 1.3300 to 1.5600 using a 589 nm LED (nD = 589 nm Sodium D Line) corrected to a reference temperature reading of 20 °C. A daily single point calibration was performed using distilled water (Sigma-Aldrich®). Liquid samples were allowed to equilibrate to room temperature, then 100–250 µLs were added to the refractometer's sample well. The refractive index was then measured and recorded. Each chemical was run in triplicate and the average was recorded. The refractometer's sample well was cleaned using methanol in between calibrations and chemicals as recommended in the user guide.

Figure 2. Reichert AR200 digital refractometer.

2.2 Obtaining Mie scattering plots of test chemicals using the LEQ

The LEQ system (Figure 3) was chosen to directly measure a single aerosol particle's evaporation rate. The LEQ uses a quadruple to trap single micron-sized aerosol particles with high efficiency for direct measurements of chemicals in their aerosolized states. The alternating high voltage of the poles traps the particle—aligning it in the center of the system—and a balancing voltage on the bottom of the system holds the particle in place. A N_2 (or air) purge is continuously flowing from top to bottom through the system to allow for the evaporation of the aerosol over time. While suspended, the aerosol particle's diameter is measured using a Mie scattering technique to determine the evaporation rate in real time (Figure 4). Separate solutions of CEES and PMP simulants were made up along with varying amounts of JP-8 jet fuel, aerosolized, and the Mie scattering was plotted as a function of time by the LEQ. The Mie scattering plots allowed us to visually infer information about the evaporation rates of the individual aerosol particles.

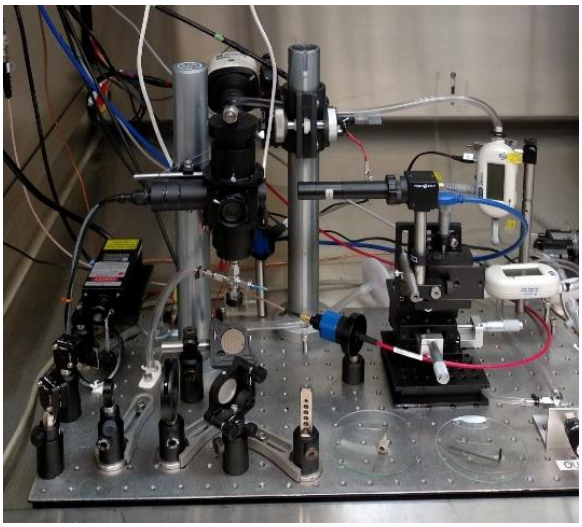

Figure 3. Picture of the LEQ test system.

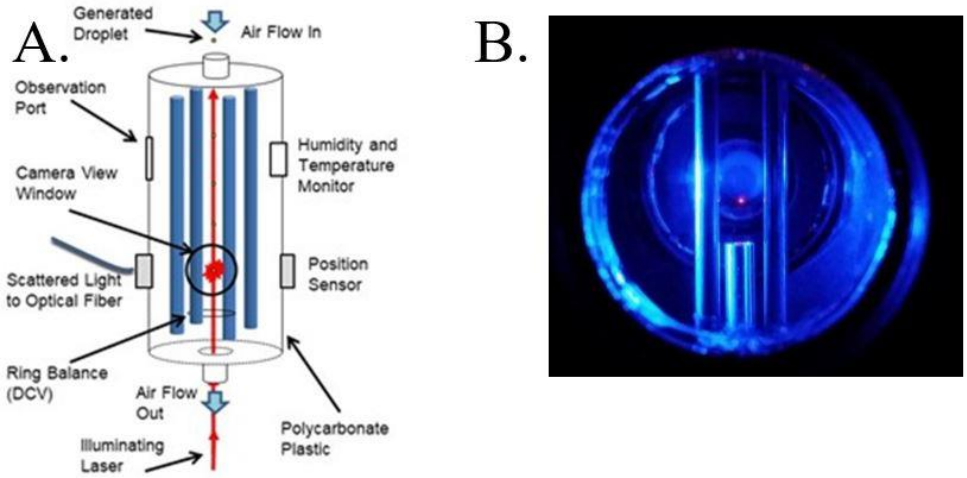

Figure 4. A.) Diagram of the LEQ apparatus. B.) View through the observation port on the LEQ.

Glycerol was used to verify that the LEQ instrument was working properly. The Mie scattering spectrum (blue curve in Figure 5) has a specific pattern, which indicates when the aerosol particle is a particular size. Pictures (direct imaging) of the aerosol particle were taken using a standard camera throughout the test. The black and white pictures visually show how the particle shrinks as it evaporates over time (Figure 5).

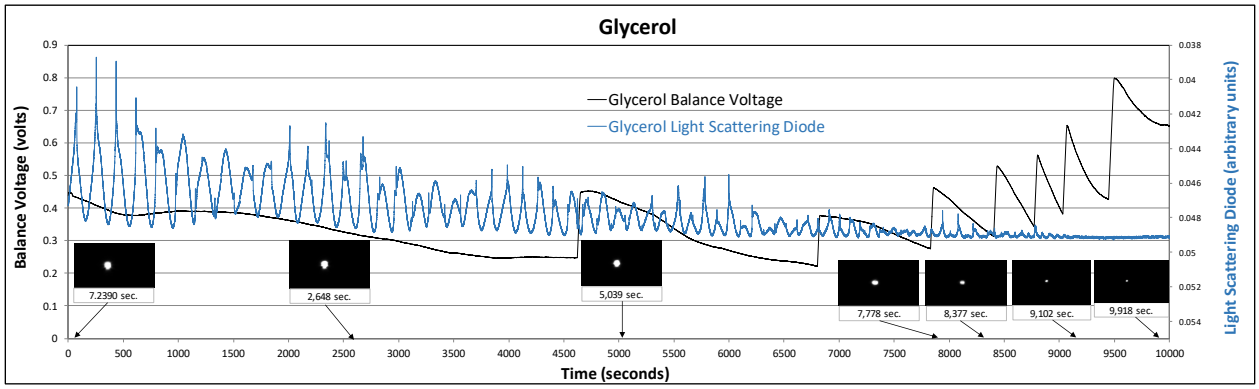

Figure 5. Mie scattering data for a glycerol standard.

3. RESULTS AND DISCUSSION

3.1 Characterization of neat chemicals by gas chromatography-mass spectrometry

Neat chemicals (CEES, kerosene, and JP-8) were analyzed on an Agilent GC-MS system. A total ion chromatogram was obtained to observe all of the separate constituents present within each starting material. Figures 6, 7, and 8 show the total ion chromatograms for CEES, kerosene, and JP-8 fuel, respectively. CEES is a pure compound as represented by the single peak in the total ion chromatogram (Figure 6). In contrast, kerosene is a mixture of C_{11} through C_{15} hydrocarbons as is evident by the many peaks in the total ion chromatogram (Figure 7). The total ion chromatogram for JP-8 is a mixture of hydrocarbons from C_6 through C_{18} as shown in Figure 8. These chromatograms might give insight into the evaporation rate changes in the mixtures. For example, the many different species in JP-8 fuel may evaporate at different times and slow the evaporation rate of an aerosol particle compared to a pure chemical, which would evaporate at a constant rate.

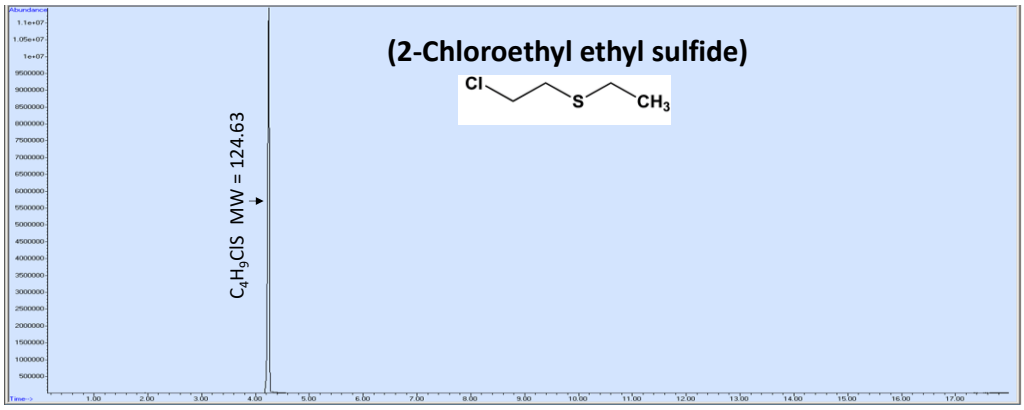

Figure 6. Total ion chromatogram of 2-CEES.

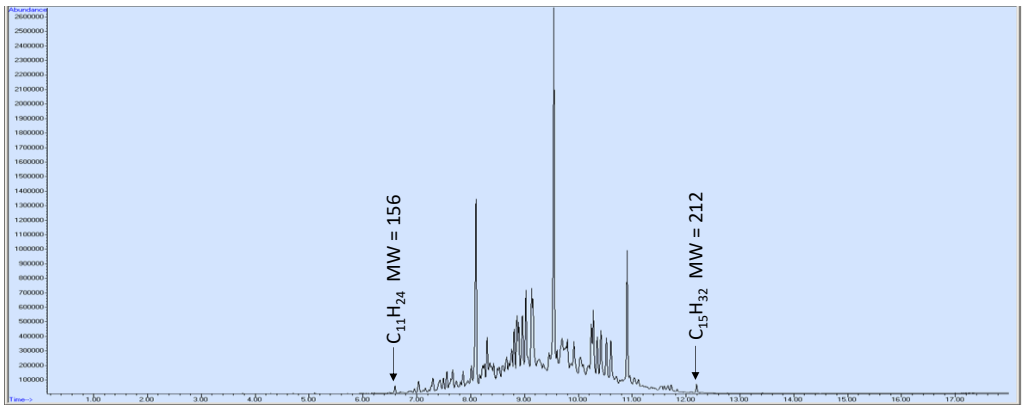

Figure 7. Total ion chromatogram of kerosene.

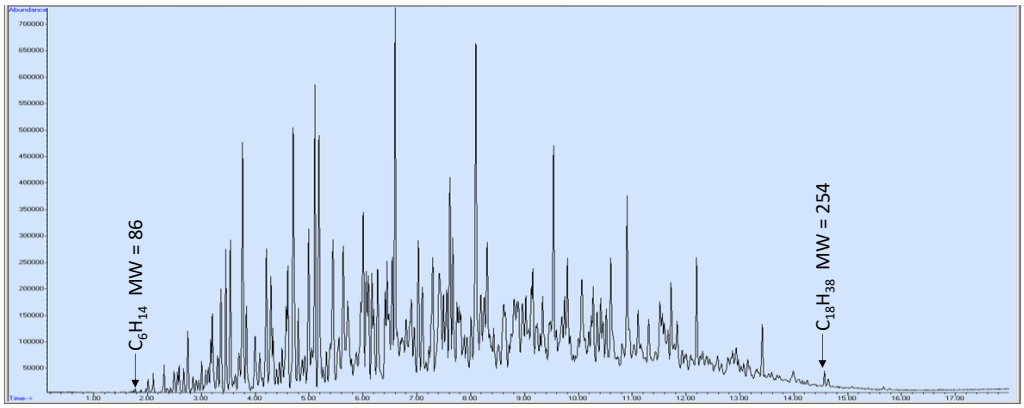

Figure 8. Total ion chromatogram of JP-8.

3.2 Measurements of the refractive indices of test chemicals

Refractive indices of neat chemicals and mixtures were measured in the laboratory at ambient conditions using a digital refractometer. The results are summarized in Table 1. The refractive indices will be used in the future to calculate the evaporation rates of these mixtures.

Table 1. Refractive indices

Literature Values	Pure Chemical	1.34[a]	1.436[a]	1.4447[b] 1.4432[b]	1.4885[a]	1.434[a]
Percentages		90%	90%	90%	90%	90%
	Chemical	Water	Kerosene	JP-8	CEES	PMP
10%	Water	**1.3328**	1.4401	1.4496	1.4876	1.4289
10%	Kerosene	1.3328	**1.4403**	---	1.4821	1.4339
10%	JP-8	1.3329	---	**1.4489**	1.4834	1.4351
10%	CEES	1.3361	1.4428	1.4519	**1.4879**	---
10%	PMP	1.3383	1.4386	1.4470	---	**1.4344**

[a] Listed on the manufacturer's bottle; [b] Energy & Fuels 2007, 21, pp.2853–2862[6]

3.3 Mie scattering plots of test chemicals using the LEQ

The Mie scattering pattern is dependent on the particle size; thus, the pattern is the same for all aerosol particles. The only thing that changes is the time it takes the Mie scattering pattern to be measured. If an aerosol particle is evaporating at a fast rate, the peaks and valleys (of the Mie scattering plot) will be close together. The opposite is true for a particle that evaporates at a slower rate; the peaks and valleys (of the Mie scattering plot) will be further apart. Aerosol particles that contain many chemical constituents may have a mixture of patterns as different chemical species evaporate at different rates over time. The experiments run and the Mie scattering plots generated allowed us to visually infer information about the evaporation rates of the individual aerosol particles. The results showed that JP-8 affected the evaporation rate of each chemical agent simulant differently. Neat aerosolized CEES and CEES mixed with a low percentage of JP-8 did not show any significant Mie scattering (Figure 9 and Figure 10).

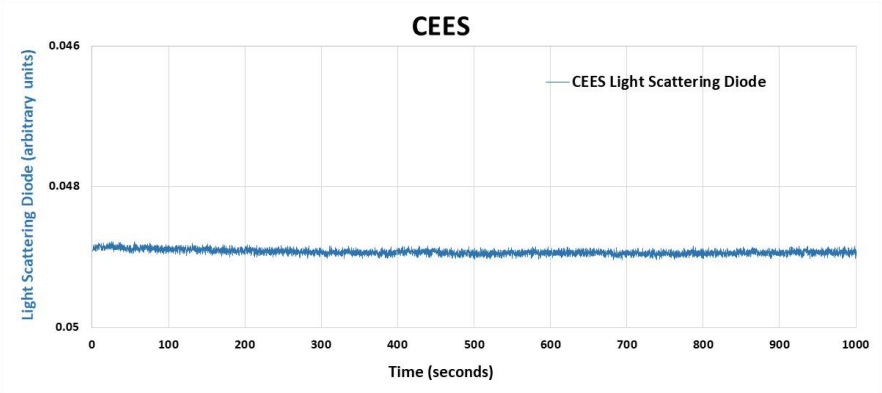

Figure 9. Mie scattering data for neat CEES.

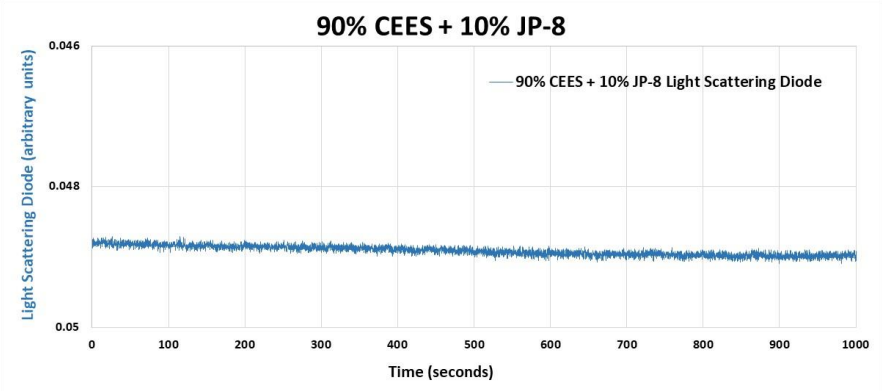

Figure 10. Mie scattering data for a high percentage of CEES and a low percentage of JP-8.

No Mie scattering could mean that the aerosol particle is not evaporating at a significant, measurable rate. This might have been due to the way that the CEES was introduced into the LEQ instrument. The interior volume of the LEQ may have been saturated with CEES vapor, thus hindering the evaporation of the aerosolized CEES particle. This phenomenon will have to be investigated further, as sample introduction is a component of system design and will have to be rectified in future experiments, either through instrument redesign, or by placing more stringent controls on the generation of the aerosols. Aerosol particles composed of a mixture of a high percentage of JP-8 and low percentage of CEES (Figure 11 and Figure 12) behaved much differently. The mixture seemed to show two distinct Mie scattering patterns for the same aerosol particle. This pattern indicated that the separate components within the mixture evaporated sequentially, but at different rates.

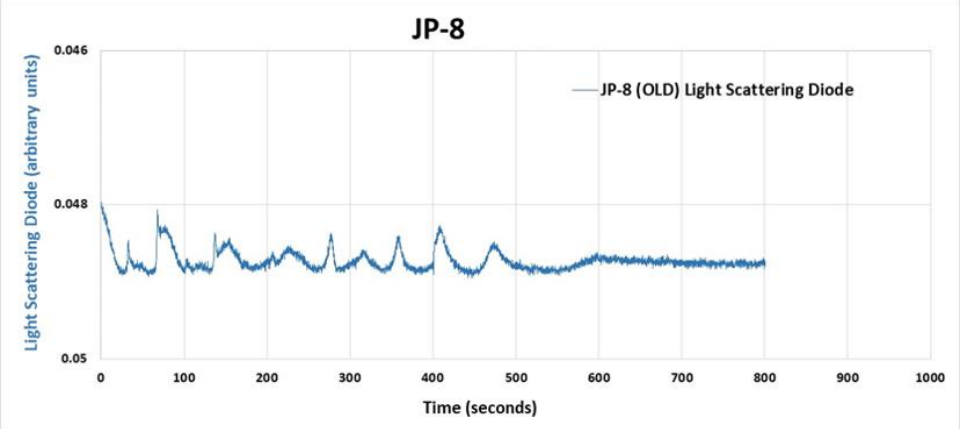

Figure 11. Mie scattering data for neat JP-8.

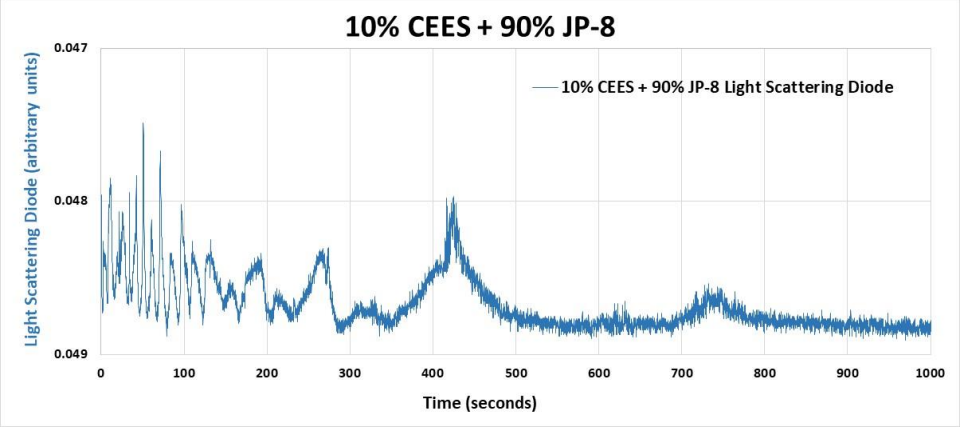

Figure 12. Mie scattering data for a low percentage of CEES and a high percentage of JP-8.

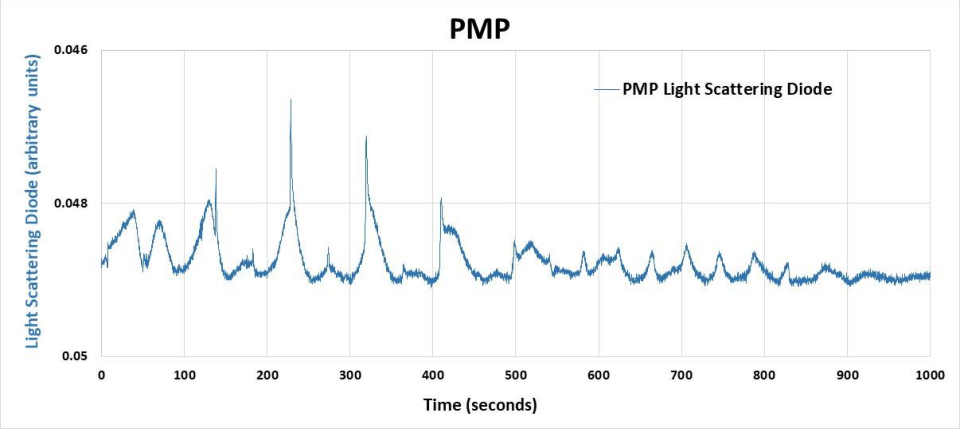

Figure 13. Mie scattering data for neat PMP.

Aerosol particles of neat JP-8 (Figure 11), neat PMP (Figure 13), and a low percentage of JP-8 and a high percentage of PMP (Figure 14) exhibited slightly different Mie scattering plots but were very similar in evaporation rates. However, when solutions of a high percentage of JP-8 and a low percentage of PMP (Figure 15) were mixed together, the evaporation rate slowed down by approximately half. These results indicate that aerosolized chemical agents could persist in the environment significantly longer in the presence of fuels. The quantitative evaporation rates were not calculated due to time constraints.

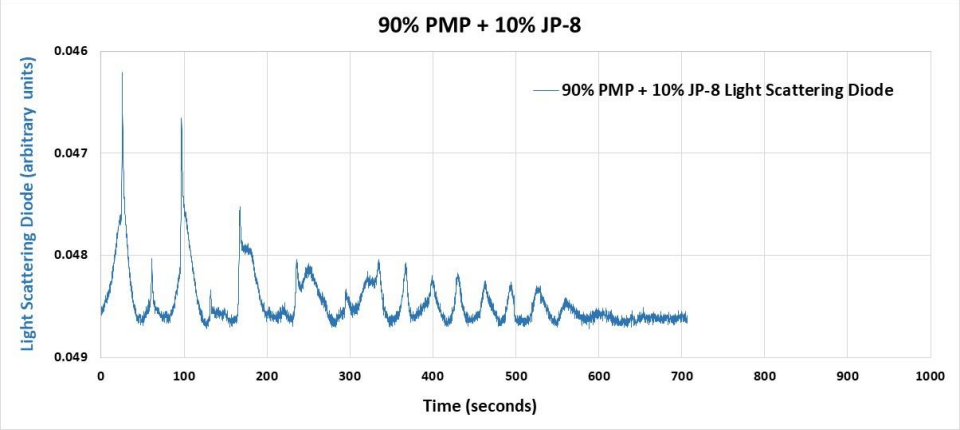

Figure 14. Mie scattering data for a high percentage of PMP and a low percentage of JP-8.

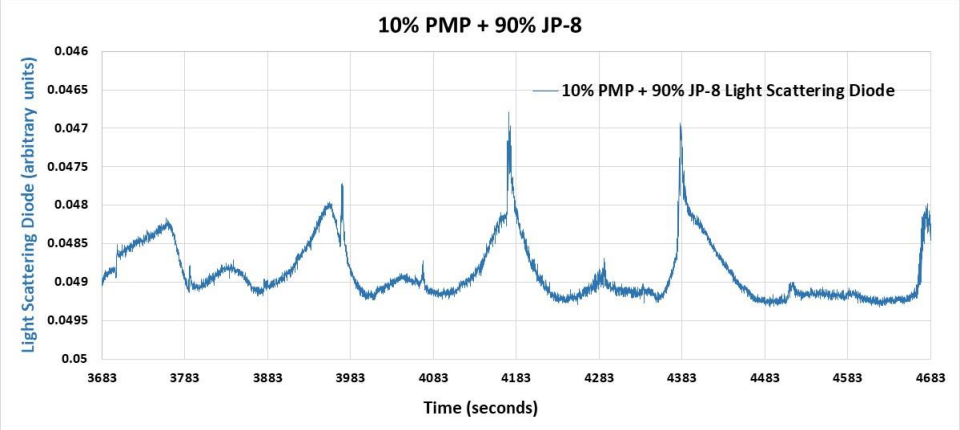

Figure 15. Mie scattering data for a low percentage of PMP and a high percentage of JP-8.

4. CONCLUSIONS

The generated Mie scattering data allowed us to visually infer information about the evaporation rates of the individual aerosol particles. The results showed that JP-8 affected the evaporation rate of each chemical agent simulant differently. Neat aerosolized CEES and CEES mixed with a low percentage of JP-8 did not show any significant Mie scattering. No Mie scattering likely means that the aerosol particle is not evaporating at a significant, measurable rate. Aerosol particles of neat JP-8 and PMP exhibited very similar evaporation rates. However, when solutions of a high percentage of JP-8 and low percentage of PMP were mixed together, the evaporation rate slowed down by approximately half the value. These results indicate that aerosolized chemical agents could persist in the environment significantly longer in the presence of fuels. Aerosol particles composed of a mixture of a high percentage of JP-8 and CEES behaved much differently. This mixture seemed to show two distinct Mie scattering patterns for the same aerosol particle, indicating that the separate components within the mixture evaporated sequentially at two distinct rates. The quantitative evaporation rates were not calculated due to time constraints.

ACKNOWLEDGMENTS

Funding was provided by the Director, Combat Capabilities Development Command Chemical Biological Center under the authorities and provisions of Section 2363 of the FY 2018 NDAA to develop new technologies, engineer innovations, and introduce game-changing capabilities. The authors would like to thank Specialist Ward from the Weide Army Heliport for providing a sample of JP-8.

REFERENCES

[1] Eames, I.W.; Marr, N.J.; Sabir, H. The evaporation coefficient of water: a review. *Inter. J Heat Mass Tran.* **1997,** *40* (12), pp 2963–2973.

[2] Hart, M.B.; Sivaprakasam, V.; Eversole, J.D.; Johnson, L.J.; Czeged, J. Optical measurements from single levitated particles using a linear electrodynamic quadrupole trap. *Appl. Opt.* **2015,** *54* (31) pp F174–F181.

[3] Hart, M.B.; Sivaprakasam, V.; Czege, J.; Eversole, J.D. Using a Linear Electrodynamic Quadrupole as a Particle Trap. *Proceedings of the Optical Trapping Applications.* San Diego, CA, **2017;** pp 2–5.

[4] Eversole, J.D.; Hart, M. Aerosol Threat Detection: Single Particle Spectroscopy and Scattering. In *Optical Chemical and Biological Sensors*, Proceedings of Imaging and Applied Optics Technical Papers, Monterey, California, United States, June 24–28, 2012; OSA Publishing Technical Digest (online); STh1B.3.

[5] British Petroleum. The History of Jet Fuel. https://web.archive.org/web/20121018042938/http://www.bp.com/sectiongenericarticle.do?categoryId=4503664&contentId=57733 (accessed October 1, 2019).

[6] Smith, B.L.; Bruno T.J. Composition-Explicit Distillation Curves of Aviation Fuel JP-8 and a Coal-Based Jet Fuel. *Energy Fuels.* **2007,** *21* (5), pp 2853–2862.